

Study of heavy flavour decay muons at forward  
rapidity in proton-proton and heavy-ion collisions  
at LHC energies

*By*

MD SAMSUL ISLAM

PHYS05201604010

Saha Institute of Nuclear Physics, Kolkata

*A thesis submitted to the  
Board of Studies in Physical Sciences  
In partial fulfillment of requirements  
for the Degree of*

DOCTOR OF PHILOSOPHY

*of*

HOMI BHABHA NATIONAL INSTITUTE



July, 2022



# Homi Bhabha National Institute

## Recommendations of the Viva Voce Committee

As members of the Viva Voce Committee, we certify that we have read the dissertation prepared by MD SAMSUL ISLAM entitled “Study of heavy flavour decay muons at forward rapidity in proton-proton and heavy-ion collisions at LHC energies” and recommend that it may be accepted as fulfilling the thesis requirement for the award of Degree of Doctor of Philosophy.

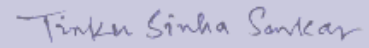
---

Chairman - Prof. Sukalyan Chattopadhyay



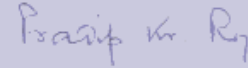
---

Guide / Convener - Prof. Tinku Sinha Sarkar



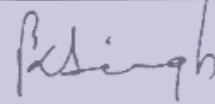
---

Co-guide - Prof. Pradip Kumar Roy



---

Examiner - Prof. Bhartendu K. Singh



---

Member 1 - Prof. Munshi G. Mustafa



---

Member 2 - Prof. Debasish Das



---

Member 3 - Dr. Partha Pratim Bhaduri



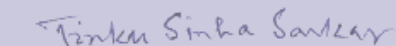
---

Final approval and acceptance of this thesis is contingent upon the candidate's submission of the final copies of the thesis to HBNI.

I hereby certify that I have read this thesis prepared under my direction and recommend that it may be accepted as fulfilling the thesis requirement.

Date: 07/10/2022

Place: SINP, Kolkata



Prof. Tinku Sinha Sarkar  
(Guide)





## STATEMENT BY AUTHOR

This dissertation has been submitted in partial fulfillment of requirements for an advanced degree at Homi Bhabha National Institute (HBNI) and is deposited in the Library to be made available to borrowers under rules of the HBNI.

Brief quotations from this dissertation are allowable without special permission, provided that accurate acknowledgement of source is made. Requests for permission for extended quotation from or reproduction of this manuscript in whole or in part may be granted by the Competent Authority of HBNI when in his or her judgement the proposed use of the material is in the interests of scholarship. In all other instances, however, permission must be obtained from the author.

*Md. Samsul Islam*

Md Samsul Islam



## DECLARATION

I, hereby declare that the investigation presented in the thesis has been carried out by me. The work is original and has not been submitted earlier as a whole or in part for a degree / diploma at this or any other Institution / University.

*Md. Samsul Islam*

Md Samsul Islam



## List of Publications arising from the thesis

### Journal:

#### a. Published

1. “Study of heavy-flavor decay muon production in proton–proton and heavy-ion collisions using the Angantyr model at LHC energies”  
\*Md. Samsul Islam, Tinku Sinha, Pradip Roy and Partha Pratim Bhaduri,  
Int. J. Mod. Phys. E 31 (2022) 2250007 [DOI:[10.1142/S0218301322500070](https://doi.org/10.1142/S0218301322500070)].

#### b. Submitted

1. “Charged-particles distribution in proton-proton and heavy-ion collisions using PYTHIA8 Angantyr model at LHC energies”  
\*Md. Samsul Islam, Tinku Sinha, Pradip Roy and Partha Pratim Bhaduri,  
Eur. Phys. J. Plus

### Conference/Symposium

1. “Heavy flavor decay muon production in proton-proton collisions at  $\sqrt{s} = 13$  TeV”  
\*Islam, M.S., Roy, P., Sinha, T.  
DAE Symp. Nucl. Phys. **63** (2018) 972. [[proceedings/63/E28](#)]
2. “Study of open heavy-flavour hadron decay muons in pp collisions with ALICE at the LHC”  
\*Islam, M.S. [ALICE Collaboration]  
DAE Symp. Nucl. Phys. **63** (2018) 984. [[proceedings/63/E34](#)]
3. “Study of Heavy flavor decay muons in PP and Pb-Pb collisions at LHC energies using Angantyr model for heavy-ion collisions in PYTHIA8”  
\*Md. Samsul Islam, Tinku Sinha, and Pradip Roy  
XXIV DAE-BRNS High Energy Physics Symposium 2020  
Springer Proceedings in Physics, pp 397–401 [[https://doi.org/10.1007/978-981-19-2354-8\\_72](https://doi.org/10.1007/978-981-19-2354-8_72)]

## Other Publications:

### a. Analysis note:

1. “Production of muons decaying from heavy flavour hadrons at forward rapidity in pp collisions at  $\sqrt{s} = 13$  TeV with ALICE”  
Md. Samsul Islam, Tinku Sarkar - Sinha  
ALICE Collaboration, ANA-1168 [[alice-notes.web.cern.ch/node/1168](https://alice-notes.web.cern.ch/node/1168)].

*Dedicated to*  
*My Parents*  
*And*  
*My Family Members*





## ACKNOWLEDGEMENTS

I express my sincere thanks and gratitude to my supervisor Prof. Tinku Sinha Sarkar. I am grateful for her continuous guidance for the completion of this PhD work. I appreciate her constant motivation, help, moral support and fruitful discussions throughout this journey of PhD. I shall remain obliged to her for valuable suggestions, comments and additional inputs in preparing this thesis. Without the support of Prof. Sinha Sarkar, this thesis work would not have been completed successfully. It was a great time indeed for learning and working under her supervision.

I am also very much thankful to my co-supervisor Prof. Pradip Kumar Roy, for his continuous support, suggestions, discussions. His guidance, encouragement and motivation helped to accomplish this doctoral work. I am grateful to him for the discussions and valuable comments which helped me to write this thesis.

My special thanks goes to Dr. Partha Pratim Bhaduri who assisted me with several value added inputs while framing my research papers. I have also learned a lot from him during our discussions.

I am also very much thankful to Prof. Sukalyan Chattopadhyay who constantly supported me throughout my work. I acknowledge his valuable suggestions, discussions and advice whenever I needed.

I sincerely thank to Prof. Munshi G. Mustafa & Prof. Debasish Das who are the members of my doctoral committee. I acknowledge their suggestions and inputs during my PhD work.

I would like to convey my sincere thanks to Dr. Antonio Uras, Dr. Xiaoming Zhang and Dr. Zuman Zhang for their valuable suggestions and support for my data analysis work with ALICE. I am very much thankful to Dr. Stefano Panebianco who guided and supervised me for the MFT-ladder Quality Assurance Test at CERN. His generous and caring character inspired me a lot. I would like to express my gratitude to Cyrille Vuillemin, Andry Rakotozafindrabe, Charlotte Riccio for helping me to understand the MFT-ladder test procedures. I am thankful to my collaborator Shaista Khan for discussing about the writing of MFT ladder QA test Internal Note. My special thanks to Sibaliso who always helped for my data analysis work. I am very much grateful to her for the discussions and suggestions she provided.

I must express thank to Wadut Shaikh for his insightful remarks and discussions about my work. He continuously encouraged me and gave useful advice, which helped to keep going with my work.

I would like to express my gratitude to Dr. Ankhi Roy who introduced me to this wonderful and fascinating field of High Energy Physics. I am very much grateful to her for guiding me during the time at IIT Indore and teaching me specially C++ coding which greatly assisted me in doing data analysis with ALICE. I always remember her

for her simplicity, honesty and generosity.

I am very much admired by Prof. Abhik Kumar Sanyal who inspired me to learn physics during my college days. I remember, he is the first person for me who presented the insightful physics and discoveries by the experiments at CERN. I shall remain grateful to him for all his support and encouragement. I would like to express my respect to my college teachers Furkan Sir, Pahari Babu, Goutam Sir, Susmita Ma'am and others for their tireless efforts in teaching me during my B.Sc.

I can not forget my primary and high school teachers, whose unwavering support and love encouraged me to go for higher education. I want to express my gratitude specially to Sujoy Mukherjee Sir, Kadam Rasul Sir, Luky Sir, Naser Sir and Giyasuddin Sir. I always admire them for their moral teaching and guidance. I am extremely grateful to all my beloved teachers.

I would like to express my thanks to all the scholars of 249, without them these years of PhD would have been very difficult. My special thanks goes to Gourab, Pritam, Wadut, Debabrata, Sweta, Anindita, Sumon, Rajarshi, Shamik, Arghya, Ashim Roy, Suvankar da, Arnab da, Kuntal da, Biswarup da, Anisa, Hushnud di and others for their support and friendship. I appreciate Gourab and Pritam for their support and discussions at all means. I always remember Ashim Roy for all his kind help and nice gesture during my stay at CERN. I must acknowledge the support of my friend Vishal who always encouraged and motivated me. All of you are wonderful person and thanks to all for being a part of my PhD journey.

I would like to thank all the staff members of SINP. My special thanks to the members of HENPP division: Sudam da, Pappu da, Rijwan da and others for all their support and help. My sincere thanks to the staff members of Library, specially Lun Maam. I would like to express my thanks to all the security guards, gardeners, housekeeping members for making SINP a very safe and secured place, a very clean and wonderful campus.

This life would have been meaningless without my beloved childhood friends especially Ibrahim, Mofi, Masiul, Obydur, Sahid. I remember, Ibrahim is the first friend who gifted me a physics book during my high school days. Mofi is the boss whose presence of mind is appreciable. I am eternally grateful to them for their unconditional love, cheering me during my off time and supporting me when I needed them most. All of you are really amazing, unforgettable and have made my life easier. My sincere thanks goes to all my school and college friends for their love and support.

Finally, I must express my sincere gratitude and respect to my Amma (Mother) and Abba (Father) whose constant support helps me to continue my education. I must mention about my all family members whose love and care made my life joyful. I can not express in words about their cumulative contributions and supports for the progress of my life. I shall remain grateful to them forever.

There are many other people who always loved and encouraged me. I apologizes to them for not being able to mention here specifically.

Thank you all.

---

# Contents

---

<b>List of Publications</b>	<b>vii</b>
<b>List of Figures</b>	<b>xvii</b>
<b>List of Tables</b>	<b>xxxii</b>
<b>1 Introduction</b>	<b>1</b>
1.1 The Standard Model of Particle Physics . . . . .	2
1.2 Quantum Chromodynamics . . . . .	3
1.3 QCD phase transition . . . . .	5
1.4 Heavy-ion collisions . . . . .	7
1.4.1 Space-time evolution of Heavy-ion collision . . . . .	7
1.4.2 Collision geometry of heavy-ion collision . . . . .	9
1.4.3 Kinematic variables in relativistic collision . . . . .	10
1.4.4 Experimental observables for QGP . . . . .	12
1.5 Heavy flavour production . . . . .	17
1.5.1 Heavy flavour production in hadronic collisions . . . . .	17
1.5.2 Open heavy flavour in pp and nucleus-nucleus collisions . . . . .	21
1.6 Open heavy flavour measurements at LHC . . . . .	23
1.6.1 Charm measurement . . . . .	24
1.6.2 Bottom measurement . . . . .	26
1.6.3 Semi-leptonic decay of open heavy flavour hadron . . . . .	27
1.7 Scope of this thesis . . . . .	32

<b>2</b>	<b>The ALICE detector at the LHC</b>	<b>41</b>
2.1	The Large Hadron Collider . . . . .	41
2.1.1	The LHC experiments . . . . .	43
2.2	A Large Ion Collider Experiment . . . . .	44
2.2.1	The ALICE coordinate system . . . . .	45
2.2.2	The ALICE detector . . . . .	45
2.2.3	Central Barrel Detectors . . . . .	48
2.2.4	Global Detectors . . . . .	53
2.2.5	The ALICE Muon Spectrometer (MS) . . . . .	55
2.2.6	The ALICE upgrade for Run 3 . . . . .	66
<b>3</b>	<b>Experimental measurements of Heavy Flavour decay Muon production in pp collisions at <math>\sqrt{s} = 13</math> TeV with ALICE</b>	<b>75</b>
3.1	Data Samples . . . . .	76
3.2	Event and track selection cuts . . . . .	77
3.2.1	Subtraction of hadronic and beam induced background . . . . .	79
3.3	Inclusive muon distribution . . . . .	83
3.4	Normalization procedure for the single muon triggered events . . . . .	85
3.4.1	Correction for pile-up events . . . . .	87
3.4.2	Offline method . . . . .	89
3.4.3	Online method . . . . .	90
3.4.4	Results on normalization procedure . . . . .	91
3.5	Acceptance times efficiency . . . . .	92
3.6	Correction of inclusive muon $p_T$ distribution. . . . .	96
3.7	Estimation of background contributions . . . . .	98
3.7.1	Primary charged pion and kaon decay muon . . . . .	99
3.7.2	Secondary Muons . . . . .	112
3.7.3	Muons decaying from W and $Z/\gamma^*$ . . . . .	114
3.7.4	Jpsi decay muon background contribution . . . . .	117
3.8	Systematic uncertainty . . . . .	120

3.8.1	Detector response . . . . .	120
3.8.2	Systematic uncertainty from background sources . . . . .	124
3.9	Results . . . . .	126
3.10	Summary . . . . .	131
<b>4</b>	<b>Heavy Flavour decay muon and charged particles production using Angantyr model at LHC energies</b>	<b>135</b>
4.1	Angantyr model . . . . .	137
4.1.1	Physics processes in PYTHIA8 . . . . .	139
4.1.2	Features of Angantyr model using PYTHIA8 . . . . .	141
4.2	Centrality Class using Monte-Carlo Glauber (MCG) Model . . . . .	144
4.3	Production of Heavy Flavour decay muon using Angantyr model . . . . .	148
4.3.1	Event generation for HFM simulation . . . . .	148
4.3.2	Results on HFM simulations . . . . .	149
4.4	Charged particles production using Angantyr model . . . . .	159
4.4.1	Event generation for charged particle . . . . .	160
4.4.2	Results on charged particle . . . . .	161
4.5	Summary . . . . .	169
<b>5</b>	<b>MFT-Ladder Assembly and Quality Assurance Test</b>	<b>177</b>
5.1	The basic structure of MFT . . . . .	178
5.2	ALPIDE sensor . . . . .	180
5.3	Ladders Assembly . . . . .	183
5.4	Ladder Qualification Test . . . . .	184
5.4.1	Smoke Test . . . . .	185
5.4.2	Functional Test . . . . .	187
5.4.3	Basic Arrangement of Functional Test Bench . . . . .	188
5.4.4	Steps of Functional Test . . . . .	189
5.4.5	Eye diagram scan . . . . .	192
5.5	Ladder qualification analysis . . . . .	193
5.5.1	Electrical Test characteristics . . . . .	194

5.5.2	Threshold-Noise scan characteristics . . . . .	195
5.5.3	Dead and noisy pixel . . . . .	197
5.6	Full MFT installation . . . . .	197
5.7	Summary . . . . .	198
<b>6</b>	<b>Outlook</b>	<b>201</b>

---

# List of Figures

---

1.1	The summary of elementary particles in Standard Model. . . . .	2
1.2	Summary of measurements of QCD coupling constant ( $\alpha_s$ ) as a function of momentum transfer ( $Q$ ) from various experimental measurements [4]. . . . .	4
1.3	The pressure, energy density and entropy density as a function of temperature obtained with Lattice QCD calculations [7]. . . . .	5
1.4	A representation of the experimental and theoretical exploration of the QCD phase diagram in temperature ( $T$ ) and baryon chemical potential ( $\mu_B$ ) plane [9]. . . . .	6
1.5	A schematic representation of various stages in relativistic Heavy-ion collision (top) [13]. A schematic diagram of the space-time evolution of a heavy-ion collision (bottom) [11]. . . . .	8
1.6	A schematic representation of nucleus-nucleus collision. . . . .	9
1.7	Measurements of $R_{AA}$ as a function of $p_T$ for $\pi^\circ$ and charged hadrons ( $h^\pm$ ) in central heavy-ion collisions at SPS, RHIC, and the LHC energies [22]. . . . .	16
1.8	$R_{AA}$ of prompt D0, D+ and $D^*$ mesons at midrapidity ( $ y  < 0.5$ ) for 0-10% centrality class in Pb-Pb collisions by ALICE [24]. . . . .	17

1.9	Fractional energy loss via collisional and radiative process for charm and beauty quark at an effective temperature $T = 304$ MeV using Djordjevic model [25]. . . . .	22
1.10	$p_T$ distribution of prompt $D^0$ (top left), $D^+$ (top right), $D^{*+}$ (bottom left) and $D_s^+$ (bottom right) in Pb-Pb collision at midrapidity ( $ y  < 0.5$ ) for three centrality classes (0-10%, 30-50%, 60-80%) [24]. . . . .	25
1.11	Average of $R_{AA}$ of non-strange prompt $D^0$ , $D^+$ , $D^{*+}$ for three centrality classes (0-10%, 30-50%, 60-80%) (left) and strange prompt $D_s^+$ (right) for 0-10% centrality class in Pb-Pb collision at midrapidity ( $ y  < 0.5$ ) [24, 38].	25
1.12	Average of $R_{AA}$ of non-strange prompt $D^0$ , $D^+$ , $D^{*+}$ for three centrality classes (0-10%, 30-50%, 60-80%) (left) and strange prompt $D_s^+$ (right) for 0-10% centrality class in Pb-Pb collision at midrapidity ( $ y  < 0.5$ ) [39]. .	26
1.13	$p_T$ -differential production cross section of electrons from semileptonic heavy flavour hadron decays (HFE) in pp collisions at $\sqrt{s} = 5.02$ TeV by ALICE and compared with theoretical model FONLL calculation (left). The $p_T$ -differential invariant yield of HFE in central (0–10%), semi-central (30–50%) and peripheral (60–80%) Pb–Pb collisions at $\sqrt{s_{NN}} = 5.02$ TeV (right) [42]. . . . .	28
1.14	Nuclear modification factor $R_{AA}$ of heavy flavour hadron decay electrons measured in Pb–Pb collisions at $\sqrt{s_{NN}} = 5.02$ TeV for three centrality classes (0-10%, 30-50%, 60-80%) [42]. . . . .	28
1.15	$p_T$ -differential production cross section of muons from heavy flavour hadron decays at forward rapidity ( $2.5 < y < 4$ ) in pp collisions at $\sqrt{s} = 2.76$ TeV (left), 5.02 TeV (right) and 7 TeV (right) [45–47]. The production cross sections are compared with the FONLL predictions at their corresponding energies. . . . .	30



1.16	$R_{AA}$ as a function of $p_T$ at $\sqrt{s} = 2.76$ and 5.02 TeV in 0-10% central Pb-Pb collisions [48] (left) and in 0-10% central Xe-Xe collisions at $\sqrt{s} = 5.44$ TeV [49] (right).	31
2.1	The CERN accelerator complex.	42
2.2	Definition of the ALICE coordinate system axis, angles and detector sides [12].	46
2.3	The schematic layout of the ALICE.	47
2.4	A schematic view of Inner Tracking System (ITS) of ALICE.	49
2.5	The Layout of Time Projection Chamber of ALICE.	50
2.6	The Layout of Muon Spectrometer of ALICE.	56
2.7	The Layout of front absorber of the Muon Spectrometer [9].	57
2.8	The Dipole Magnet of the Muon Spectrometer.	58
2.9	The quadrant type geometry of station 2 (left) and slat type geometry of station 4 and 5 (right).	59
2.10	The schematic of read out for the Tracking System of the ALICE Muon Spectrometer [26].	60
2.11	The basic geometry of Cathod Pad Chamber [27].	61
2.12	The schematic layout of the muon trigger system (left) and Resistive Plate Chamber (right).	63
2.13	Sketch to calculate track transverse momentum by ALICE muon trigger system.	64

3.1	$p_T$ -distribution of muons from different sources using MC PYTHIA simulation. . . . .	80
3.2	DCA distribution of muons from various sources using MC simulation without (left) and with (right) track-trigger matching condition. . . . .	81
3.3	DCA distribution of muons as a function of momentum (p) before (left) and after (right) track-trigger matching condition. . . . .	81
3.4	pDCA distribution of muons as a function of transverse momentum ( $p_T$ ) before (left) and after (right) applying pDCA cut of $6\sigma$ in pp collisions at $\sqrt{s} = 13$ TeV using realistic PYTHIA simulation. . . . .	83
3.5	pDCA distribution of muons as a function of transverse momentum ( $p_T$ ) before (left) and after (right) applying pDCA cut of $6\sigma$ in pp collisions at $\sqrt{s} = 13$ TeV using ALICE data sample. . . . .	83
3.6	Transverse momentum distributions of inclusive muons with different track selection cuts in pp collisions at $\sqrt{s} = 13$ TeV for MB (top), MSL (bottom, left) & MSH (bottom, right) triggered events. . . . .	84
3.7	Transverse momentum distributions of inclusive muons after all event and track selection cuts in pp collisions at $\sqrt{s} = 13$ TeV for MB, MSL & MSH triggered events (left). The corresponding statistical uncertainties are also shown (right). . . . .	85
3.8	Transverse momentum distributions of inclusive muons in five sub-pseudorapidity intervals after applying all selection cuts for MSL triggered events in pp collisions at $\sqrt{s} = 13$ TeV (left). The corresponding statistical uncertainties are also shown (right). . . . .	86

3.9	Transverse momentum distributions of inclusive muons in five sub-pseudorapidity intervals after applying all selection cuts for MSH triggered events in pp collisions at $\sqrt{s} = 13$ TeV (left). The corresponding statistical uncertainties are also shown (right).	86
3.10	L0b trigger rates, number of colliding bunches ( $N_b$ ), purity factor (PF) and pile-up correction factor ( $CF_{pile-up}$ ) for the MB triggers (CINT & C0TVX) as a function of run numbers.	89
3.11	Normalization factor ( $F_{norm}$ ) for muon triggers MSL (left) and MSH (right) as a function of run number.	91
3.12	$p_T$ -distribution in pp collisions at $\sqrt{s} = 13$ TeV corresponding to MSL (left) and MSH (right) predicted by FONLL. The fit functions are also shown for $p_T$ distribution.	93
3.13	y-distribution in pp collisions at $\sqrt{s} = 13$ TeV corresponding to MSL (left) and MSH (right) predicted by FONLL. The fit functions are also shown for y distribution.	94
3.14	Acceptance times efficiency ( $A \times \epsilon$ ) as a function of $p_T$ for two muon triggers MSL(left) and MSH (right) within the full acceptance ( $-4 < \eta < -2.5$ ) at $\sqrt{s} = 13$ TeV.	94
3.15	Acceptance times efficiency ( $A \times \epsilon$ ) as a function of $p_T$ for MSL trigger at five rapidity intervals.	95
3.16	Acceptance times efficiency ( $A \times \epsilon$ ) as a function of $p_T$ for MSH trigger at five rapidity intervals.	95
3.17	Inclusive muons $p_T$ -distribution for MSL and MSH triggered events before (left) and after (right) normalization correction.	96

3.18	The comparison of normalized and $A \times \epsilon$ corrected $p_T$ -distributions of inclusive muons for MSL and MSH triggered events at different rapidity intervals. . . . .	97
3.19	The ratio of the corrected (normalized and $A \times \epsilon$ ) $p_T$ distributions of inclusive muons of MSH with respect to that of MSL triggered events for the full rapidity range (left) and various sub-rapidity intervals (right). . .	97
3.20	The $p_T$ distributions of inclusive muons obtained by mixing MSL ( $2 < p_T < 7$ GeV/ $c$ ) and MSH ( $7 < p_T < 30$ GeV/ $c$ ) triggered events. . . . .	98
3.21	Extrapolated $p_T$ -distribution of charged pion (left) and kaon (right) at mid-rapidity in pp collisions at $\sqrt{s} = 13$ TeV. . . . .	100
3.22	Relative uncertainties for extrapolated $p_T$ -distribution of charged pion (left) and kaon (right) at mid-rapidity in pp collisions at $\sqrt{s} = 13$ TeV using Tsallis distribution and power law function. . . . .	101
3.23	Rapidity distributions of charged pion and kaon with $p_T > 2$ GeV/ $c$ obtained from PYTHIA8 (left panel) and PHOJET (right panel). . . . .	102
3.24	Ratio of the fitted function with that simulated rapidity distributions of charged pion and kaon with $p_T > 2$ GeV/ $c$ obtained from PYTHIA8 (left panel) and PHOJET (right panel). . . . .	102
3.25	Ratio of the rapidity distributions of charged pion and kaon between PYTHIA8 and PHOJET. . . . .	103
3.26	Generated $p_T$ -distribution of $\pi^\pm$ (left panel) and $K^\pm$ (right panel) at different rapidity intervals with respect to that at mid-rapidity ( $ y  < 0.5$ ) and rescaled to that with first $p_T$ bin for two colour reconnection schemes available in PYTHIA8. . . . .	103

3.27	Generated $p_T$ - distribution of $\pi^\pm$ and $K^\pm$ at different rapidity intervals with respect to that at mid-rapidity ( $ y  < 0.5$ ) and rescaled to that with first $p_T$ bin for two colour reconnection schemes CR=0 (left panel) and CR=1 (right panel) available in PYTHIA8. . . . .	104
3.28	Relative production probability of muons from charged pion and kaon decay as a function of $V_z$ in forward rapidity ( $-4 < \eta < -2.5$ ) with different $p_{T,hadron}$ cuts. . . . .	105
3.29	The relative production probability of muons from charged pion (left panel) and kaon (right panel) decay using full PYTHIA simulation. The corresponding fit functions are indicated (solid line) also. . . . .	105
3.30	The parametrizaion for the relative production of muons from charged pion and kaon decay as a function of $V_z$ in forward rapidity ( $2.5 < y < 4$ ) for muons with $p_T > 2$ GeV/ $c$ . . . . .	106
3.31	Comparison of $p_T$ -distribution of muons decaying from charged pion (left) and kaon (right) obtained using rapidity extrapolation with PYTHIA and PHOJET. . . . .	107
3.32	$p_T$ -distribution of muons decaying from charged pion (left) and kaon (right) for different $p_T$ -dependent rapidity extrapolation cases. . . . .	108
3.33	A comparison of $p_T$ -distribution of muons decaying from charged pion (left) and kaon (right) with CR=0 (MPI) and CR=1 (new QCD) colour reconnection schemes. . . . .	108
3.34	Comparative study of $p_T$ -distribution of muons decaying from charged pion (left) and kaon (right) with the absorber parametrization and with vertex cut $V_z < 130$ cm on muon production. . . . .	109

3.35	Comparison of decay muons $p_T$ -distribution from charged pion (left) and kaon (right) is obtained with the $p_T$ -extrapolation using Tsallis distribution and a polynomial function. . . . .	110
3.36	Systematic uncertainties for the measurement of decay muons during the $p_T$ -extrapolation process for pion (left) and kaon (right). . . . .	110
3.37	$p_T$ -distribution of muons decaying from charged pion and kaon (left) in forward rapidity ( $-4 < \eta < -2.5$ ) and the corresponding systematic uncertainties (right). . . . .	111
3.38	The ratio of decay muons $p_T$ -distribution from charged pion (left) and kaon (right) with respect to the inclusive muons at different pseudorapidity intervals. . . . .	111
3.39	$p_T$ -distribution of muons decaying from various sources using full MC PYTHIA8 simulation with GEANT3 in the range $-4 < \eta < -2.5$ (left). The fractional contribution of secondary muons with respect to the inclusive muons at different rapidity intervals (right). . . . .	112
3.40	Comparison of $p_T$ -distributions of secondary muons between PYTHIA8 and PHOJET simulation using GEANT3 in the range $-4 < \eta < -2.5$ (left). The same comparison between GEANT3 and GEANT4 simulation with PYTHIA8 (right). . . . .	113
3.41	The ratio in the $p_T$ -distribution of secondary muons with respect to the decay muons using the MC simulations of PHOJET with GEANT3 (top), PYTHIA8 with GEANT3 (bottom left) and PYTHIA8 with GEANT4 (bottom right) at the forward rapidity ( $-4 < \eta < -2.5$ ). . . . .	114
3.42	$p_T$ - (top) and $y$ - (bottom) distribution of muons decaying from $W^\pm$ and $Z/\gamma^*$ for two Parton Distribution Functions (PDF) CT10nlo (left) and CTEQ6l (right) respectively using POWHEG simulation. . . . .	115

3.43	Comparison of $W^\pm$ & $Z/\gamma^*$ decay muons production at different rapidity intervals with respect to the mid-rapidity ( $ y  < 1$ ) for two Parton Distribution Functions (PDF) CT10nlo and CTEQ6l (left panel) and two center-of-mass energies $\sqrt{s} = 5.02$ TeV and 13 TeV (right panel) respectively. . . . .	116
3.44	The ratio of $W^\pm$ & $Z/\gamma^*$ decay muons relative to the inclusive muons as a function of $p_T$ at different intervals in the range $-4 < \eta < -2.5$ (left). The same is for the full acceptance $-4 < \eta < -2.5$ (right). . . . .	116
3.45	The extrapolated $p_T$ - (left) and $y$ - (right) differential production cross-section of $J/\psi$ in pp collisions at $\sqrt{s} = 13$ TeV. . . . .	118
3.46	The estimated $p_T$ -differential production cross-section of muons decaying from $J/\psi$ ( <b>red line</b> ) and inclusive single muons ( <b>black line</b> ) in pp collisions at $\sqrt{s} = 13$ TeV. . . . .	119
3.47	The $p_T$ -distribution of muons decaying from $J/\psi$ (left panel) and the corresponding fraction relative to the inclusive single muons (right) at different intervals in the range $-4 < \eta < -2.5$ . . . . .	119
3.48	The $p_T$ -distribution of muons decaying from $J/\psi$ using $p_T$ -extrapolation with Tsallis, Polynomial function1 and Polynomial function2 (left panel). The total systematic uncertainties with various contributions for $p_T$ -extrapolation of $J/\psi$ (right panel). . . . .	120
3.49	Ratio of the $p_T$ -distribution of muons using $\sigma_{shift} = 3.25$ with respect to $\sigma_{shift} = 0$ at forward rapidity ( $-4 < \eta < -2.5$ ). . . . .	124

3.50	The estimated background contribution from various sources (left) and their corresponding ratio with respect to the inclusive muons (right) as a function of $p_T$ at forward rapidity ( $-4 < \eta < -2.5$ ). The vertical error bars and open boxes are representing their corresponding statistical and systematic uncertainties respectively. . . . .	124
3.51	Contribution of systematic uncertainties from various sources as function of $p_T$ in the full acceptance ( $-4 < \eta < -2.5$ ). . . . .	125
3.52	The $p_T$ -differential production cross-section of muons decaying from heavy flavour hadrons at forward rapidity ( $2.5 < y < 4$ ) in pp collisions at $\sqrt{s} = 13$ TeV and compared with FONLL calculations. The bottom panel presents the data to FONLL ratio. . . . .	127
3.53	The $p_T$ -differential production cross-section of muons decaying from heavy flavour hadrons for five rapidity intervals in the full range of $2.5 < y < 4$ . The results are compared with FONLL calculations. The bottom panel presents the ratios of the data to FONLL. . . . .	129
3.54	Production cross section of muons from heavy flavour hadron decays as a function of rapidity for the $p_T$ intervals $2 < p_T < 7$ GeV/ $c$ (left) and $7 < p_T < 30$ GeV/ $c$ (right). Statistical and systematic uncertainties are represented by the vertical bars (smaller than symbols) and open boxes respectively. The production cross sections are compared with FONLL predictions (top). The ratios of the data to FONLL calculations are shown also (bottom). . . . .	130



3.55	The production cross section of muons from heavy flavour hadron decays in forward rapidity ( $2.5 < y < 4$ ) at $\sqrt{s} = 13$ TeV. The result is compared with the previous ALICE measurements at $\sqrt{s} = 2.76, 5.02$ and $7$ TeV respectively. The statistical and systematic uncertainties are represented by the vertical bars and open boxes respectively. . . . .	130
3.56	The ratio of production cross section of muons from heavy flavour hadron decays in forward rapidity in pp collision at $\sqrt{s} = 13$ TeV with respect to that at $\sqrt{s} = 5.02$ TeV (left) and at $\sqrt{s} = 7$ TeV (right) respectively. The statistical (vertical bars) and systematic (open boxes) uncertainties are indicated. The results are compared with the FONLL calculations. . . . .	131
4.1	A Schematic representation of a heavy-ion collision using the hydrodynamical approach considering a thermalised medium creation (right side of the figure) and the PYTHIA/Angantyr model with no-QGP baseline method (left side of the figure) [14]. . . . .	138
4.2	A schematic representation of a HI collision at an impact parameter (b). The two colliding nuclei A and B are Lorentz contracted [29]. . . . .	145
4.3	Comparison of the HFM $p_T$ -spectra in p-p collisions at $\sqrt{s} = 2.76, 5.02, 7$ and $13$ TeV between default PYTHIA8 and Angantyr model calculations. . . . .	150
4.4	The $p_T$ -distribution of heavy flavour decay muons at forward rapidity ( $2.5 < y < 4$ ) in pp collisions (left panel) and for most central (0-10%) Pb-Pb collisions (right panel) at $\sqrt{s} = 5.02$ TeV respectively. The results with different PhaseSpace:pTHatMin cuts are compared. . . . .	151

4.5	The simulated $p_T$ -differential cross-section of muons from heavy flavour hadron decays in pp collisions are shown at $\sqrt{s} = 2.76$ TeV, 5.02 TeV, 7 TeV and 13 TeV. Comparisons are done between simulation results and ALICE data [39–41]. At $\sqrt{s} = 13$ TeV, the comparison is done with FONLL calculation. . . . .	152
4.6	The simulated $y$ -distribution of HFM in pp collisions at $\sqrt{s} = 5.02$ TeV (top) and 7 TeV (bottom) are shown. The simulated results are compared with the corresponding ALICE data [39, 41]. The bottom panels describe the ratio of the simulation with respect to data. . . . .	153
4.7	The $p_T$ -differential yield of HFM with Angantyr simulation at forward rapidity ( $2.5 < y < 4$ ) and compared with the ALICE data [43] at various centrality classes (0–10%, 10–20%, 20–40% & 40–60%) in Xe-Xe collisions at $\sqrt{s_{NN}} = 5.44$ TeV. . . . .	154
4.8	The $p_T$ -differential yield of HFM at forward rapidity ( $2.5 < y < 4$ ) in Pb–Pb collisions at $\sqrt{s_{NN}} = 2.76$ TeV (left) for most central collision (0–10%) and at $\sqrt{s_{NN}} = 5.02$ TeV (right) for three centrality classes (0–10%, 20–40% and 60–80%) respectively. The simulated results are compared with the corresponding ALICE measurement [44]. . . . .	156
4.9	The $p_T$ differential yield of HFM using Angantyr simulation at forward rapidity ( $2.5 < y < 4$ ) for 0–10% central O-O collisions at $\sqrt{s_{NN}} = 6.37$ TeV (left). The rapidity distribution for 0–10% central collision within $2 < p_T < 20$ GeV/ $c$ (right). . . . .	157
4.10	Angantyr simulation results for $R_{AA}$ of Heavy Flavour decay Muons at forward rapidity ( $2.5 < y < 4$ ) in central (0–10%) Pb-Pb collisions at $\sqrt{s_{NN}} = 2.76$ TeV (left) and 5.02 TeV(right). The simulated $R_{AA}$ are compared with ALICE data [44]. . . . .	159

4.11	A comparison of charged-particle multiplicity distribution ( $N_{ch}$ ) at mid-rapidity ( $ y  < 0.5$ ) in pp collisions at $\sqrt{s} = 2.76$ TeV between the standalone PYTHIA8 and Angantyr model. . . . .	161
4.12	Transverse momentum spectra of charged-particle in pp collisions at $\sqrt{s} = 2.76, 5.02$ and 13 TeV with Angantyr model. A comparison of model results (full circle) and ALICE data (open circle) [52] is done for $\sqrt{s} = 2.76$ TeV (red), 5.02 TeV (blue) and 13 TeV (magenta). . . . .	162
4.13	Transverse momentum of charged particles at mid-rapidity $ \eta  < 0.8$ in Xe-Xe collisions at $\sqrt{s_{NN}} = 5.44$ TeV for nine centrality classes. Comparisons are done between the simulation (full circle) and ALICE data (open circle). The centrality classes are described with different colors. . . . .	163
4.14	Transverse momentum of charged particles at mid-rapidity $ \eta  < 0.8$ in Pb-Pb collisions at $\sqrt{s_{NN}} = 2.76$ TeV (left) and 5.02 TeV (right) in nine centrality classes respectively. Comparisons are done between the simulation (full circle) and ALICE data (open circle). The centrality classes are described with different colors. . . . .	164
4.15	The $\frac{2}{\langle N_{part} \rangle} N_{ch}^{tot}$ as a function of $\langle N_{part} \rangle$ for Xe-Xe at $\sqrt{s_{NN}} = 5.44$ TeV and Pb-Pb collisions at $\sqrt{s_{NN}} = 2.76$ TeV and 5.02 TeV respectively. The comparison of Angantyr model calculation are done with ALICE data [55].	165
4.16	$R_{AA}$ of charged-particles as a function of $p_T$ at mid-rapidity ( $ \eta  < 0.8$ ) in Pb-Pb collisions at $\sqrt{s_{NN}} = 2.76$ TeV (left) and 5.02 TeV (right) respectively. Comparison of simulated $R_{AA}$ are done with ALICE data at three centrality classes (0-5%, 10-20% and 50-60%). . . . .	165

4.17	Mean transverse momentum ( $\langle p_T \rangle$ ) as function of charged particle multiplicity ( $N_{ch}$ ) in pp collisions at $\sqrt{s} = 0.9, 2.76$ and 7 TeV. Comparison of simulations with ALICE data are done (left). Simulation results at $\sqrt{s} = 0.9, 2.76, 5.02$ and 7 TeV are compared with respect to the result of 13 TeV (right). . . . .	167
4.18	The mean transverse momentum ( $\langle p_T \rangle$ ) as function of charged particle multiplicity ( $N_{ch}$ ) in Xe-Xe at $\sqrt{s_{NN}} = 5.44$ TeV and in Pb-Pb collisions at $\sqrt{s_{NN}} = 2.76$ and 5.02 TeV respectively. Comparison of simulation with ALICE data [57] (Pb-Pb at $\sqrt{s_{NN}} = 2.76$ TeV). . . . .	168
4.19	The profile of the charged-particles production at mid-rapidity ( $ \eta  < 0.8$ ) in O-O collisions at $\sqrt{s_{NN}} = 6.37$ TeV for four centrality classes: 0-5%, 5-10%, 10-20% and 20-100% using Angantyr simulation (left). The $\langle p_T \rangle$ as a function of $N_{ch}$ ( $0.15 < p_T < 10$ GeV/c) at mid-rapidity $ \eta  < 0.3$ (right).168	168
5.1	The schematic layout of MFT integrated with ALICE. . . . .	179
5.2	The schematic view of MFT detector [2]. . . . .	180
5.3	The arrangement of ladders and chips at different zones of MFT half-disks [4]. . . . .	181
5.4	A Schematic cross-sectional view of a pixel of ALPIDE chip with Tower-Jazz CMOS technology. . . . .	181
5.5	The Architecture of ALPIDE pixel-matrix (left) and ALPIDE readout block diagram (right). . . . .	182
5.6	A view of ladders equipped with 4 chips along with FPC (top) and the back side of the same ladder with the integrated chips (bottom). . . . .	184

5.7	The Lid of a transportation box (upper). A ladder including an ICL board inside the transportation box (lower). . . . .	185
5.8	Basic arrangement of smoke test bench [8]. . . . .	186
5.9	Visualisation of the GUI based software (left) and activity diagram (right) for smoke test [8]. . . . .	187
5.10	The basic arrangement of Functional Test without back-bias voltage (top) and with back-bias voltage (bottom). . . . .	188
5.11	The Eye diagram for ideal high speed digital waveform signal. . . . .	192
5.12	Two examples of Eye diagram obtained from the eye diagram scan of ladder. . . . .	193
5.13	Classification cuts during functional test. . . . .	194
5.14	Power consumption of ladders per chip during electrical test A (left), B (middle), and C (right). . . . .	195
5.15	Statistics on threshold values: mean without back-bias (top left), mean with back-bias (top right), rms without back-bias (bottom left) and rms with back-bias (bottom right). . . . .	196
5.16	Statistics on noise values: mean without back-bias (top left), mean with back-bias (top right), rms without back-bias (bottom left) and rms with back-bias (bottom right). . . . .	196
5.17	The rear view of MFT half-cone assembled inside the barrel (left). The MFT detector in at final position where the beam pipe goes in the center of MFT (right) [2]. . . . .	197



---

# List of Tables

---

1.1	The fundamental interactions with their corresponding theory, strength and mediators. . . . .	3
2.1	ALICE data taking in Run 1 (2009-2013) and Run 2 (2015-2018). . . . .	45
2.2	Summary of ALICE central barrel detectors [10]. . . . .	53
3.1	Number of events and tracks after various selection cuts for MB, MSL and MSH trigger. . . . .	84
3.2	Normalization factor, cross-section and Integrated Luminosity for MSL and MSH data sample. . . . .	92
3.3	The comparison of $\mu^+/\mu^-$ ratio obtained in data (LHC16k) and in FONLL based full MC simulation for various tuned values of $\sigma_{shift}$ in two selected $p_T$ ranges. . . . .	123
3.4	Systematic uncertainties associated to the various sources in the measurement of $p_T$ -differential production cross-section of heavy flavour decay muons at $-4 < \eta < -2.5$ in pp collisions at $\sqrt{s} = 13$ TeV. . . . .	125
4.1	Various geometric quantities in Pb-Pb collisions at $\sqrt{s_{NN}} = 2.76$ TeV obtained with the MCG model for the centrality class used in this work. . .	146

4.2	Various geometric quantities in Pb-Pb collisions at $\sqrt{s_{NN}}=5.02$ TeV obtained with the MCG model for the centrality class used in this work. . .	147
4.3	Various geometric quantities in Xe-Xe collisions at $\sqrt{s_{NN}}=5.44$ TeV obtained with the MCG model for the centrality class used in this work. . .	147
4.4	Comparison of mean of $N_{part}$ ( $\langle N_{part} \rangle \pm rms$ ) in Pb-Pb collisions at $\sqrt{s_{NN}}=2.76$ TeV & 5.02 TeV and in Xe-Xe collisions at $\sqrt{s_{NN}}=5.44$ TeV obtained from MCG, ALICE and Angantyr (this work). . . . .	155
5.1	Various geometrical parameters of each half-disk of MFT [3, 4]. . . . .	180
5.2	The nominal power consumption of ladders during electrical test. . . . .	190
5.3	Summary of the assembled and tested ladders. . . . .	194



# CHAPTER 1

---

## Introduction

---

The exploration of high energy physics (HEP) allows to identify the most fundamental building blocks of matter and to probe the interactions between them. The discoveries of such elementary constituents of matter are supported by HEP theoretical and experimental research including fundamental accelerator science and technology. As per our current knowledge, the dynamics of all matter are govern by four different types of fundamental interactions: electromagnetic, strong, weak and gravitational. The electromagnetic force is experienced by charged particles separated by some distance. The theory of electromagnetic interaction is called Quantum ElectroDynamics (QED). The gravitational force is the most common universal force which is experienced by any massive particle. Strong force binds the constituents of nucleus together. Weak force is responsible for beta decay and some other phenomena. The theory describing weak interaction is called Quantum FlavourDynamics (QFD). Among all the four fundamental forces, the strength of the strong force is strongest and the gravitational force is the most feeble one.

The Standard Model provides the basic understanding of the elementary particle physics and describe the interactions among them [1, 2]. The underlying theoretical construct of Standard Model is based on three fundamental forces of interactions. These

are electromagnetic force, strong force and weak force. In the following section, a brief description of the SM is given.

## 1.1 The Standard Model of Particle Physics

The Standard Model (SM) is the most successful theory of particle physics describing the best understanding of the fundamental particles and their association with three (electromagnetic, strong and weak interactions) out of the four fundamental forces of the universe. All elementary particles in SM are characterised by their mass and a set of quantum numbers such as charge, spin and baryon and lepton numbers etc. The elementary particles in SM are summarised as shown in Figure 1.1.

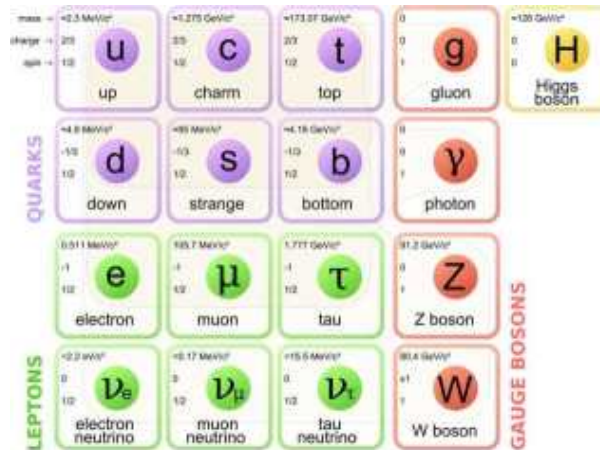


Figure 1.1: The summary of elementary particles in Standard Model.

The elementary particles are classified into two groups based on their intrinsic spin: half-integer spin fermion and integer spin boson. The fermions are further classified into lepton and quark. There are three generations of leptons: electron ( $e^-$ ), muon ( $\mu^-$ ) and tau ( $\tau^-$ ) each carrying one unit of negative charge with their corresponding left-handed leptonic neutrinos electron neutrino ( $\nu_e$ ), muon neutrino ( $\nu_\mu$ ) and tau neutrino ( $\nu_\tau$ ). Each lepton is associated to their counterpart antiparticles carrying one unit of positive charge anti-leptons ( $e^+$ ,  $\mu^+$ ,  $\tau^+$ ) and their corresponding right-handed anti-neutrinos

$(\bar{\nu}_e, \bar{\nu}_\mu, \bar{\nu}_\tau)$ . There are six quarks: up (u), down (d), charm (c), strange (s), bottom (b) and top (t). The SM includes an anti-quark associated with each of the quarks and hence there are six anti-quarks ( $\bar{u}, \bar{d}, \bar{c}, \bar{s}, \bar{t}, \bar{b}$ ). The model is described with four spin-1 gauge bosons (photon, gluon,  $W^\pm$  and Z) and one spin-0 Higgs boson. Moreover, the elementary particles can interact with each other by three different kind of forces: electromagnetic, strong and weak associated with the exchange of a specific boson. A strong force is governed by the exchange of gluons, electromagnetic by photons and weak interaction is associated with  $W^\pm$  and Z boson respectively. The Gravitational force is not included in the SM. The fundamental interactions with their corresponding theory, strength and mediators have been listed in Table 1.1.

Table 1.1: The fundamental interactions with their corresponding theory, strength and mediators.

Interaction	Theory	strength	Mediator
Strong	Quantum Chromodynamics	1	Gluons
Weak	Quantum Flavourdynamics	$10^{-13}$	$W^\pm$ & Z bosons
Electromagnetic	Quantum Eelectrodynamics	$10^{-2}$	Photons
Gravitational	Quantum Gravity	$10^{-38}$	Graviton

In the next section, the Quantum Chromodynamics theory of standard model is discussed in a nutshell.

## 1.2 Quantum Chromodynamics

The Quantum Chromodynamics (QCD) is the theory of strong interaction between quarks and gluons. Quarks and gluons are the basic constituents of free hadron. A hadron made up of two valence quarks is called meson ( $q\bar{q}$ ) and of three valence quark (qqq) is called baryon. The quarks are characterised by a quantum property called color charge analogous to the electric charge and thus the name of the theory Quantum Chromodynamics. The quarks and gluons are often called together as partons. According to QCD, each quark can be described by three color charges (red, green, blue) and a

hadron made up of quarks should be colorless. The potential of the QCD interaction is given by

$$V_{QCD}(r) = -\frac{4}{3} \frac{\alpha_s}{r} + kr \quad (1.1)$$

where  $\alpha_s$  is the running QCD coupling constant,  $r$  is the distance between two interacting partons and  $k$  is the color string tension.  $\alpha_s$  depends on the momentum transfer ( $Q^2$ ) between the two interacting partons and can be described as

$$\alpha_s(Q^2) = \frac{12\pi}{(11N_c - 2N_f) \ln\left(\frac{Q^2}{\lambda_{QCD}^2}\right)} \quad (1.2)$$

$N_c$  is the number of color charges,  $N_f$  is the number of quark flavours and  $\lambda_{QCD}$  is the non-perturbative QCD scaling parameter. A Summary of the measurements of  $\alpha_s$  as a function of momentum transfer ( $Q$ ) is presented in Figure 1.2 [3, 4].

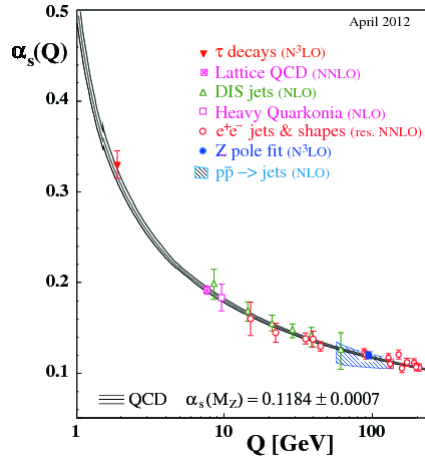


Figure 1.2: Summary of measurements of QCD coupling constant ( $\alpha_s$ ) as a function of momentum transfer ( $Q$ ) from various experimental measurements [4].

Equation 1.2 describes that at small momentum transfer or at large distance,  $\alpha_s$  becomes very strong. This results the quarks and gluons are bound together and confined inside hadrons. This is called Quark Confinement. In contrary, at large momentum transfer ( $Q^2 \gg \lambda_{QCD}^2$ ) or at a scale of small distance,  $\alpha_s$  becomes relatively very small

and the quarks and gluons behave as free particles. This property of QCD matter is known as asymptotic freedom. In this energy scale, the perturbative QCD (pQCD) calculations are allowed to describe the partons. The phenomena of asymptotic freedom of QCD was discovered by David Gross, Frank Wilczek and David Politzer and they awarded the Nobel prize in Physics for year 2004.

### 1.3 QCD phase transition

A hot and dense matter of free quarks and gluons can be created at a very high density and/or temperature environment over a relatively large volume. Such a state of matter is known as Quark-Gluon Plasma (QGP). The lattice QCD (LQCD) calculations also predict the existence of such QGP phase at high temperature [5–7]. The pressure, energy density and entropy density of QCD matter obtained by LQCD calculations with different quark flavours are shown in Figure 1.3. A rapid increase in energy density at  $\sim T_c = 145\text{--}164$  MeV suggests an increase in number of degrees of freedom. Therefore, a possible phase transition from hadronic matter to a quark matter is expected within this narrow temperature range.

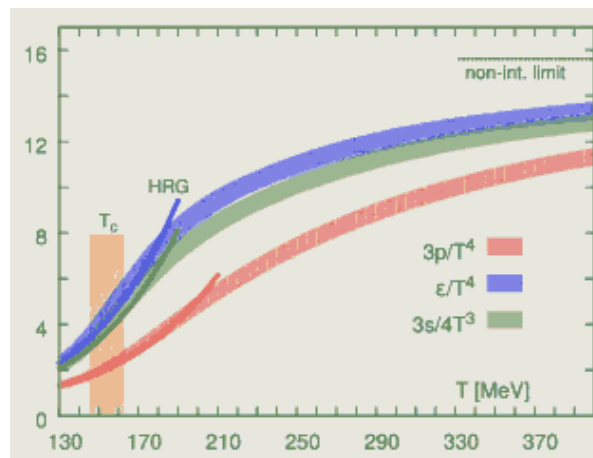


Figure 1.3: The pressure, energy density and entropy density as a function of temperature obtained with Lattice QCD calculations [7].

The phase diagram of QCD matter based on the knowledge obtained by both mapping experimentally and qualitatively fundamental description of QCD in the standard model is schematically shown in Figure 1.4. This figure illustrates the existence of various phases of nuclear matter depending upon the temperature and baryon chemical potential ( $\mu_B$ ) of the system. This QCD phase diagram describes the distribution of ordinary matter (hadronic matter), the QGP and other possible phases of QCD such as color superconductivity. The baryon chemical potential ( $\mu_B$ ) is the measure of imbalance between matter and antimatter. A value of  $\mu_B = 0$  corresponds to equal contributions of matter and antimatter, which is thought to have existed in the early universe. The deconfined state of nuclear matter (quarks and gluons) are expected to exist at high temperature and relatively lower  $\mu_B$  and also at low T and high  $\mu_B$ . However, the nuclear matter is expected to be confined inside hadrons at lower T and low  $\mu_B$ . The critical point indicates where hadronic and QGP phases can co-exist. The LQCD calculations predict a smooth crossover between hadronic phase and QGP phase at high T and low  $\mu_B$ . To establish the position of the critical point, the energy of the heavy-ion collider experiment is tuned across the region where it is likely to lie. However, at higher  $\mu_B$ , the transition between the phases is of first order. At low T and very high  $\mu_B$ , there is possible region of color superconductivity which arises due to the diquark Cooper pair [8].

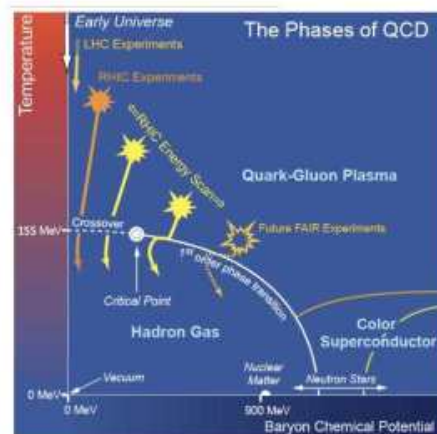


Figure 1.4: A representation of the experimental and theoretical exploration of the QCD phase diagram in temperature ( $T$ ) and baryon chemical potential ( $\mu_B$ ) plane [9].

## 1.4 Heavy-ion collisions

Scientists do believe that the QGP phase is expected to have existed in the early universe in the first few microseconds after the Big Bang [10, 11]. A QGP like phase of nuclear matter can be formed in laboratory at very high temperature and/or very high density. In order to produce such deconfined state (QGP) in the laboratory, the only known way is to collide heavy ions at relativistic energies. Therefore, little bangs are created in relativistic heavy-ion collisions at many experimental facilities like Relativistic Heavy Ion Collider (RHIC) at Brookhaven National Laboratory, the Large Hadron Collider (LHC) at European Organization for Nuclear Research (CERN). There are future experiments such as the Facility for Anti-proton and Ion Research (FAIR) in Darmstadt, Germany and the Nuclotron-based Ion Collider fAcility (NICA) in Dubna, Russia, designed to study the QCD matter in heavy-ion collisions [12]. All these Heavy-Ion Collision (HIC) experimental facilities are motivated to explore the possibility of QCD phase transition and formation of QGP.

In the following section, a discussion about the space-time evolution of heavy-ion collisions is done.

### 1.4.1 Space-time evolution of Heavy-ion collision

Two heavy nuclei relativistically accelerated are longitudinally Lorentz contracted and made to collide each other. In Figure 1.5, a schematic view of the various stages of the relativistic heavy-ion collisions is shown (top). The bottom part of the Figure 1.5 represents the space-time evolution of a heavy-ion collision based on the understanding of relativistic hydrodynamic model. The two Lorentz contracted nuclei collide at time  $t=0$  and deposite a large amount of energy within a very small volume in a very short time interval. In this HI collision, several nucleon-nucleon hard collisions result to many

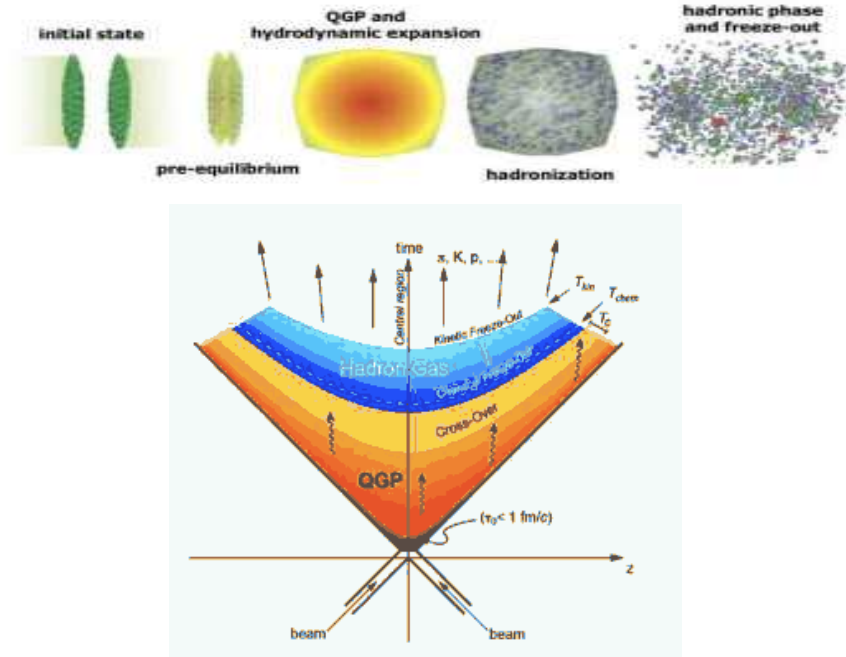


Figure 1.5: A schematic representation of various stages in relativistic Heavy-ion collision (top) [13]. A schematic diagram of the space-time evolution of a heavy-ion collision (bottom) [11].

number of partons. If the energy density produced in the collision is very high, then a deconfined state of partons are formed after the collision. Initially, it is in non-equilibrium state. As the system expands and the parton's are continuously interacting each other, local equilibrium takes place within the time scale of  $1 \text{ fm}/c$  [14]. This deconfined state of quarks and gluons in a local equilibrium state is called QGP. The QGP medium expands due to the pressure gradient generated by partons momenta and cools down further. As the medium expands, the energy density of the system reduces. At a critical temperature ( $T_c$ ), the energy density of the system reduces below a critical density  $\rho_{crt} \approx 1 \text{ GeV}/\text{fm}^3$  and then partons starts to hadronise. During the initial stage of this hadronisation, a coexistence of hadrons and free partons is expected which gradually vanishes with time and the system left with hadron gas only. As the system keeps expanding, at temperature  $T=T_{ch}$ , the probability of inelastic interaction among the hadrons is almost zero. This temperature ( $T_{ch}$ ) is known as chemical freeze-out temperature. After the chemical freeze-out, the relative abundance of different type of hadrons produced remain same.



As the system expands further and cools down, the inter-hadronic distance surpasses the range of strong interaction which reduces the probability of elastic scattering. At temperature  $T=T_{fo}$ , all the elastic interactions between the hadrons ceases, is known as kinetic freeze-out temperature. At this kinetic freeze-out phase, the system can not maintain the thermal equilibrium anymore. Finally, the hadrons freely travel to the detector.

### 1.4.2 Collision geometry of heavy-ion collision

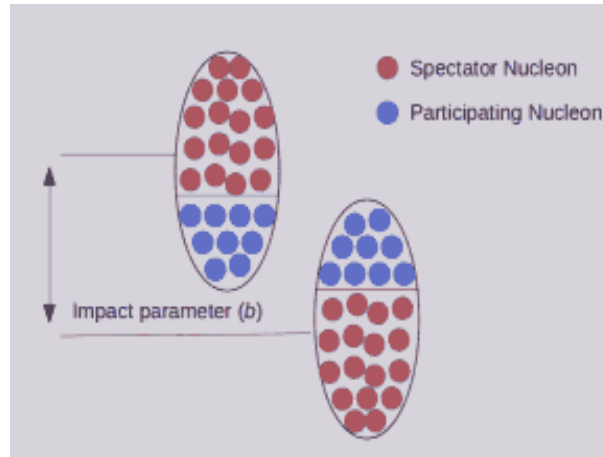


Figure 1.6: A schematic representation of nucleus-nucleus collision.

The overlap region of two colliding nuclei is defined by the impact parameter ( $b$ ) which is the perpendicular distance between the centers of two colliding nuclei at the time of collision (see Figure 1.6). A collision is said to be most central when the two nuclei suffers complete overlap ( $b=0$ ) for a head-on collision. The nucleons within the overlap region take part in the collisions and called as participants (wounded nucleons), whereas the nucleons outside the overlap region just move away in the beam direction without colliding each other, called as spectators. In addition to several nucleon-nucleon (NN) collisions, many simultaneous sub-nucleonic collisions may also occur in a heavy-ion collision. The geometrical properties of this overlap region in HI collision is characterised by the impact parameter ( $b$ ), the number of participants ( $N_{part}$ ) and the number of binary

nucleon-nucleon collisions ( $N_{coll}$ ). These geometrical quantities are calculated by means of Monte-Carlo simulation based on Glauber formalism [15]. A detail description of the Glauber Model is discussed in section. 4.2.

### 1.4.3 Kinematic variables in relativistic collision

The coordinate system of a collider experiment is described by the orthogonal Cartesian coordinate system and the origin (0, 0, 0) is set at the interaction point of the two colliding beams. The z-axis is usually along the beam direction and  $x$ - $y$  plane is the perpendicular plane to the beam direction. The kinematic variables such as transverse momentum ( $p_T$ ), rapidity ( $y$ ), pseudorapidity ( $\eta$ ) etc are used very commonly in high energy physics experiments.

- **Transverse momentum**

The total momentum of a particle can be described into two parts. One of them is the longitudinal momentum ( $p_z$ ) along the beam direction and the other one is projection of the momentum in the  $x$ - $y$  transverse plane, called transverse momentum ( $p_T$ ) which is defined by

$$p_T = \sqrt{p_x^2 + p_y^2} \quad (1.3)$$

where  $p_x$  and  $p_y$  are the components of the momentum along the  $x$  and  $y$  direction.

- **Rapidity**

The rapidity of a particle of energy  $E$  is defined as

$$y = \frac{1}{2} \ln \left( \frac{E + p_z c}{E - p_z c} \right) \quad (1.4)$$

where  $c$  is the velocity of light. The rapidity is the relativistic realization of velocity of a particle. In a collider experiment, the lab frame (LS) is boosted along the beam

direction with a velocity  $v_z = \beta c$  with respect to the center of mass frame (CM). Therefore, the transformation of rapidity under Lorentz boosts along the beam direction (z-axis) is given by

$$\begin{aligned} y_{particle}^{LS} &= y_{particle}^{CM} + y^{CM} \\ &= y_{particle}^{CM} + \ln \sqrt{\frac{1+\beta}{1-\beta}} \end{aligned} \tag{1.5}$$

where,  $y_{particle}^{LS}$  and  $y_{particle}^{CM}$  are the rapidities of a particle in Lab frame and CM frame respectively. The advantage of using rapidity that it is invariant under longitudinal Lorentz transformation.

- **Pseudorapidity**

The rapidity is hard to measure for highly relativistic particles. In particle physics experiment, the identification of a particle requires to measure the energy and total momentum ( $p$ ). In some cases, where such particle identification is difficult, a quantity easier than rapidity can be defined based on the angle ( $\theta$ ) at which the particle is detected with respect to the beam axis. This quantity is called pseudorapidity ( $\eta$ ) and can be described as

$$\begin{aligned} \eta &= \frac{1}{2} \ln \left( \frac{p + p_z}{p - p_z} \right) \\ &= \frac{1}{2} \ln \left( \frac{p + p \cos \theta}{p - p \cos \theta} \right) \end{aligned} \tag{1.6}$$

For highly relativistic particles,  $p_z = p \cos \theta$ ,

$$\eta = -\ln \left[ \tan \left( \frac{\theta}{2} \right) \right] \tag{1.7}$$

### 1.4.4 Experimental observables for QGP

In relativistic heavy-ion collision, the produced hot and dense medium (QGP) is very short lived ( $\sim 1\text{fm}/c$ ). Experimentally, this QGP medium cannot be detected directly and many indirect measurements are done to probe the signature of QGP. The probes are broadly categorised as

- Strangeness enhancement
- Anisotropic flow
- Electromagnetic probe
- Jet Quenching
- Quarkonia suppression

Few of the experimental probes for the creation of hot and dense nuclear medium (QGP) in heavy-ion collisions are discussed below:

#### Strangeness Enhancement

The enhancement of strange particle (particle containing ‘s’ quark) production in heavy-ion collision is a very primary signature of QGP formation [16]. The net strangeness is zero before and after the collision in both pp and A-A. Therefore, the production of any strange particle in the collision must be accompanied by its antiparticle. The production of strange quarks are mainly from two types of processes:  $q\bar{q} \rightarrow s\bar{s}$  and  $gg \rightarrow s\bar{s}$ . The QGP is very gluon rich medium, so the production of  $s\bar{s}$  pair is more favourable in the gluon-gluon interactions compared to the quark-antiquark annihilation. Therefore, an enhancement in the production of strange hadrons is expected for the QGP medium in the heavy-ion collision compared to the pp collisions.

## Anisotropic flow

The anisotropic flow of particles produced in the heavy-ion collision, is one of the key probe to study the existence of QGP medium. In a non-central heavy-ion collisions, the shape of the overlapping region between the two colliding nuclei is almond-like. After the collision, if a QGP like medium is formed, then it expands under large pressure gradients. This momentum anisotropy transfers the inhomogeneous initial conditions into azimuthal anisotropy of the particles produced. This azimuthal distribution of the produced particles can be expressed as

$$\frac{dN}{d\phi} \propto \left[ 1 + 2v_1 \cos(\phi - \psi) + 2v_2 \cos(2(\phi - \psi)) + \dots \right] \quad (1.8)$$

where  $\phi$  is the azimuthal angle of the particle produced and  $\psi$  is the reaction plane angle which is the angle made by the reaction plane with the x-axis. The reaction plane is defined by the beam direction and impact parameter vector in a collision. The anisotropic flow coefficient  $v_n$  can be expressed as  $v_n = \langle \cos(n(\phi - \psi)) \rangle$  where  $\langle \rangle$  stands for the average over the particles in all events. The anisotropic flow coefficient  $v_n$  echoes the rescattering among the constituents after the collision and hence indicates the “degree of thermalisation” of the QGP medium. Therefore in a heavy-ion collision, the spatial anisotropy is transferred to momentum anisotropy via the rescattering of the particles produced and thermalizes the system. In isotropic emission, each coefficient in the expansion (Eq. 1.8) is equal to zero, leaving only the radial flow. The flow coefficients  $v_1$  and  $v_2$  are called directed and elliptic flow coefficients respectively. The strategy and techniques for analyzing anisotropic flow in relativistic heavy-ion collisions can be found in Ref [17, 18].

## Electromagnetic probe

The photons and lepton pairs or dilepton ( $e^+e^-$  and  $\mu^+\mu^-$ ) play important role to probe the earliest and hottest phase of the QGP medium. The photons and leptons interact with the system only electromagnetically and hence they can escape the dense and hot fireball with very negligible final state interactions [19]. On the other hand, hadrons are emitted from the freeze-out surface after undergoing extreme rescattering, they lose initial information of the system. Therefore, the photons and leptons carry the full information about the state of the medium from where they are produced. The photons and dileptons are produced in all stages of the nuclear collisions: from the pre-equilibrium stage, from QGP phase, from hadronic phase and from the decay of hadrons produced at the time of freeze-out. The search for the photons from QGP can be identified in a region of phase space ( $p_T$  window) where the photons from QGP is dominated over all other sources. Photons from QGP could be visible in the transverse momentum range  $2 < p_T < 5$  GeV/c [20].

## Nuclear Modification Factor

To quantify the various probes for the hot and thermalised medium formation in heavy-ion collisions, it is very common to measure the  $p_T$  dependent nuclear modification factor ( $R_{AA}$ ) as given below:

$$R_{AA} = \frac{1}{N_{coll}} \frac{(dN/dp_T)_{AA}}{(dN/dp_T)_{pp}} \quad (1.9)$$

where  $(dN/dp_T)_{AA}$  and  $(dN/dp_T)_{pp}$  are the transverse momentum spectra of particles in nucleus-nucleus (A-A) and proton-proton (pp) collisions and  $N_{coll}$  is the number of binary nucleon-nucleon collisions for the particular overlap region in the collision. For  $R_{AA} < 1$  indicates a suppression while  $R_{AA} > 1$  is an enhancement. If heavy-ion collision is a simple superposition of pp collisions and in the absence of any medium formation,

the  $R_{AA}$  is expected to be almost equal to one. Therefore, any deviation of  $R_{AA}$  from unity indicates an in-medium modification in nucleus-nucleus collisions.

The following probes are used to study the hot and dense medium produced in the heavy-ion collision where the nuclear modification factor is the measurable quantity.

#### a) **Jet Quenching**

In relativistic heavy-ion collision, the high momentum partons are produced mainly in initial hard scattering process. These high  $p_T$  partons are fragmented into a collimated spray of hadrons which are known as jets. Jets are created when a nucleon's parton scatters off of another nucleon's parton. The  $2 \rightarrow 2$  hard scattering is a dominant process of a collisions and hence a jet should have a partner jet moving exactly in a opposite direction ( $180^\circ$  in azimuth) [21]. When high  $p_T$  partons are propagated through the hot and dense medium, it interacts with the medium constituent. These interactions lead to loss of energy via collisions and in-medium gluon radiation process. According to Bjorken theory [11], high momentum partons loses more energy in QGP than in hadronic medium and leads to a suppression. This is known as jet quenching. Generally, jet emitted from the surface of the medium should not have back-to-back correlated jet because one of the correlated jet must go through the medium and hence be quenched. Experimentally, the jet quenching in heavy-ion collisions can be measured by using correlated high momentum inclusive or single hadrons.

In Figure 1.7, the  $R_{AA}$  as a function  $p_T$  in central A-A collision for neutral pion ( $\pi^0$ ) and inclusive charged hadrons at SPS (Pb-Pb at  $\sqrt{s} = 17.3$  GeV), RHIC (Au-Au at  $\sqrt{s} = 200$  GeV) and LHC (Pb-Pb at  $\sqrt{s} = 2.76$  & 5.02 TeV) are shown. The suppression of high  $p_T$  charged hadrons is clearly seen at both RHIC and LHC energies which is the effect of jet quenching.

#### b) **Quarkonia suppression**

In high energy collision, the heavy quarks ( $c, \bar{c}, b, \bar{b}$ ) are produced in the early stages

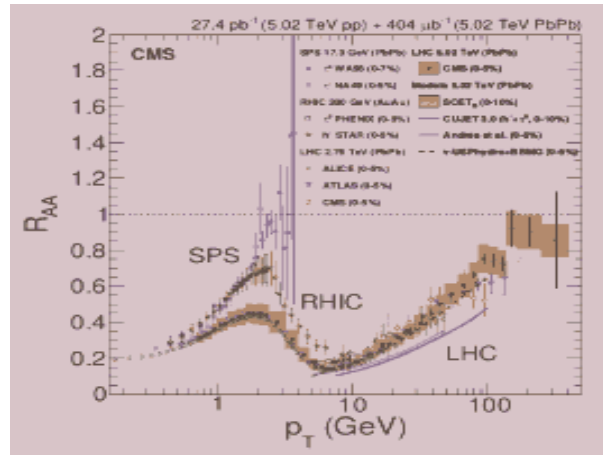


Figure 1.7: Measurements of  $R_{AA}$  as a function of  $p_T$  for  $\pi^0$  and charged hadrons ( $h^\pm$ ) in central heavy-ion collisions at SPS, RHIC, and the LHC energies [22].

of the collision via hard parton-parton scattering. The bound states of charm and bottom quarks and their antiquarks are called quarkonia ( $c\bar{c}$  or  $b\bar{b}$ ). When a very large number of heavy quark and antiquarks are produced in heavy-ion collisions, quarkonia could also be formed by recombining a heavy quark antiquark pair. This is known as regeneration. The production of the quarkonia is supposed to be suppressed due to the presence of color screening in a deconfined QGP medium. However, other mechanisms such as absorption of quarkonia in cold nuclear matter or the breaking-up of quarkonia due to interaction with other hadrons (co-movers) could also be responsible for quarkonia suppression.

### c) Open heavy flavour hadron suppression

In high energy collisions, heavy quarks and antiquarks individually fragmented into hadrons. An open heavy flavour hadron containing one charm quark is called D hadron and containing one beauty quark is called B hadron respectively. Due to the dead cone effect, the quarks with higher mass exhibits smaller radiative energy loss [23]. Therefore, a distinct mass hierarchy is expected for the high  $p_T$  open heavy flavour hadron suppression in heavy-ion collision. In Figure 1.8, the  $R_{AA}$  for prompt D-mesons ( $D^0$ ,  $D^+$  and  $D^{*+}$ ) is shown as a function of  $p_T$  at midrapidity ( $|y| < 0.5$ ) for 0-10% central Pb-Pb collisions measured by ALICE experiment [24]. A strong



suppression of the D-mesons over a wide range of transverse momentum upto  $p_T = 50 \text{ GeV}/c$  is seen.

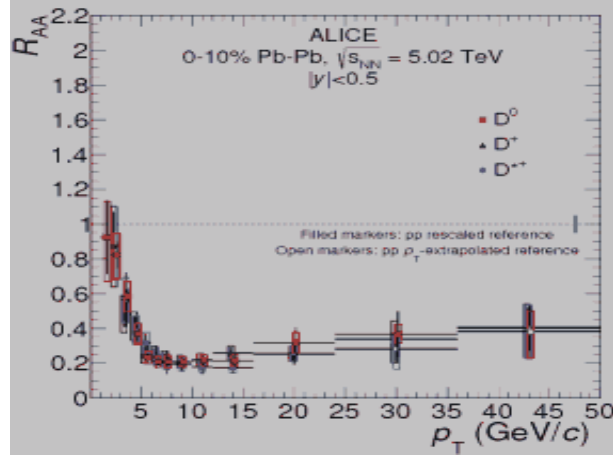


Figure 1.8:  $R_{AA}$  of prompt  $D^0$ ,  $D^+$  and  $D^{*+}$  mesons at midrapidity ( $|y| < 0.5$ ) for 0-10% centrality class in Pb-Pb collisions by ALICE [24].

This thesis is mainly focused on the production of muons from the semi-muonic decay of open heavy flavour hadrons in pp and A-A collisions. Therefore a detail description for the production and decays of open heavy flavour hadrons is discussed in the following sections.

## 1.5 Heavy flavour production

### 1.5.1 Heavy flavour production in hadronic collisions

The production of open heavy flavour in hadronic collisions provides important tests to understand the various aspects of Quantum Chromodynamics (QCD). The heavy quark mass ( $m_Q$ ) allows the relevant calculations in perturbative QCD (pQCD) framework down to low  $p_T$ . Multiple hard scales ( $m_Q, p_T$ ) of heavy quarks allow to study pQCD at various kinematic regimes ( $p_T < m_Q, p_T \sim m_Q, p_T \gg m_Q$ ). Thus the experimental measurement of heavy flavour production provides an important test to the theoretical

understanding of QCD. The inclusive differential production cross-section of a heavy-quark  $Q$  in a hadronic collision can be calculated as follows [25],

$$\begin{aligned} \frac{d\sigma^{Q+X}}{dp_T}(s, p_T, y, m_Q) &\simeq \sum_{i,j} \int_0^1 dx_i \int_0^1 dx_j f_i^A(x_i, \mu_F) f_j^B(x_j, \mu_F) \\ &\times \frac{d\hat{\sigma}_{i,j \rightarrow Q+X}}{dp_T}(x_i, x_j, s, p_T, y, m_Q, \mu_F, \mu_R) \end{aligned} \quad (1.10)$$

or

$$\frac{d\sigma^{Q+X}}{dp_T} \simeq \sum_{i,j} f_i^A \otimes f_j^B \otimes \frac{d\hat{\sigma}_{i,j \rightarrow Q+X}}{dp_T} \quad (1.11)$$

where, a heavy quark  $Q$  of transverse momentum  $p_T$  and rapidity  $y$  is produced in a collision between hadrons  $A$  and  $B$  at centre-of-mass energy  $\sqrt{s}$ .  $f_i^A$  ( $f_j^B$ ) is the parton distribution functions (PDFs) of the parton of flavour  $i$  ( $j$ ) inside the hadron  $A$  ( $B$ ) which carries a momentum fraction  $x_i$  ( $x_j$ ) of the hadron  $A$  ( $B$ ) at the factorisation scale  $\mu_F$ . The parton flavour  $i$  and  $j$  corresponds to the parton species ( $q, \bar{q}, g$ ).  $\frac{d\hat{\sigma}_{i,j \rightarrow Q+X}}{dp_T}$  is the short distance partonic cross-section which depends on strong coupling constant  $\alpha_s(\mu_R)$  evaluated at the renormalisation scale  $\mu_R$ .

The production cross-section of a heavy flavour hadron  $H$  with momentum  $p_H$  can be written as,

$$\frac{d\sigma^H}{dp_T} = \frac{d\sigma^Q}{dp_T} \otimes D_Q^H(z) \quad (1.12)$$

where  $D_Q^H(z)$  is the fragmentation function (FF) describing a heavy flavour hadron  $H$  with momentum fraction  $z = p_H/p_Q$  formed from a heavy quark  $Q$  with momentum  $p_Q$ . The short-distance partonic cross-section can be calculated as a perturbation series in  $\alpha_s(\mu_R)$  [26].  $\mu_R$  and  $\mu_F$  are both of the order of heavy quark mass.

The scale dependences for various partonic sub-processes are discussed below:

- **Leading Order:**

At the Leading Order (LO),  $\mathcal{O}(\alpha_s^2)$ , there are mainly two subprocesses contributing to the hard scattering:

$$q + \bar{q} \rightarrow Q + \bar{Q}$$

$$g + g \rightarrow Q + \bar{Q}$$

The first process is the  $q\bar{q}$  pair annihilation and the second one is the gluon fusion.

- **Next-to-Leading Order:**

At the Next-to-Leading Order (NLO),  $\mathcal{O}(\alpha_s^3)$ , virtual corrections to the  $Q\bar{Q}$  production cross-section must be included. At NLO, the following 2→3 processes contribute:

$$q + \bar{q} \rightarrow Q + \bar{Q} + g$$

$$g + g \rightarrow Q + \bar{Q} + g$$

$$g + q \rightarrow q + Q + \bar{Q}$$

$$g + \bar{q} \rightarrow \bar{q} + Q + \bar{Q}$$

It is to be mentioned that the last two sub processes (flavour excitation and gluon splitting) for quark-gluon scattering are not present at LO.

- **FONLL:**

In the FONLL (Fixed-Order + Next-to-Leading Logarithms) framework [27], the entire approach is valid for the full kinematic range ( $p_T \ll m_Q, p_T \simeq m_Q, p_T \gg m_Q$ ). FONLL scheme is based on the massive NLO calculations in the Fixed-

Flavour-Number Scheme (FFNS) with the massless NLO in the Zero-Mass Variable-Flavour- Number Scheme (ZM-VFNS). In FFNS (=FO), the heavy quark is not an active parton in the hadron, whereas in ZM-VFNS (RS), the heavy quark is included but its mass ( $m_Q$ ) is neglected in the resummed short-distance partonic cross-section calculation as described in Eq 1.10. Typically, the FFNS at NLO can be applied in the range  $0 \leq p_T \leq 5m_Q$  and the ZM-VFNS is reliable only for very large transverse momenta ( $p_T \gg m_Q$ ). Therefore, according to FONLL [25],

$$d\sigma_{FONLL} = d\sigma_{FO} + (d\sigma_{RS} - d\sigma_{FOM0}) \times G(m_Q, p_T) \quad (1.13)$$

where  $d\sigma_{FO}$  is the cross-section in FO calculation and  $d\sigma_{FOM0}$  is the the same in the asymptotic limit  $p_T \gg m_Q$ .  $d\sigma_{RS}$  is the resummed cross-section in the massless limit following ZM-VFNS approach. The matching function  $G(m_Q, p_T)$  can be described with an interpolating function given by

$$G(m_Q, p_T) = \frac{p_T^2}{(p_T^2 + a^2 m_Q^2)} \quad (1.14)$$

where  $a$  is a constant. Therefore, at large transverse momentum range ( $p_T \gg m_Q$ ), the condition  $d\sigma_{FONLL} \rightarrow d\sigma_{RS}$  requires  $G(m_Q, p_T)$  to be unity. However, at small transverse momenta limit,  $d\sigma_{FONLL}$  approaches to the fixed-order (FO) calculation  $d\sigma_{FO}$  ( $d\sigma_{FONLL} \rightarrow d\sigma_{FO}$ ).

The general-purpose Monte-Carlo event generators (MCEG) like PYTHIA [28] and HERWIG [29] can describe the inclusive production of heavy flavour hadron or its decay products at Leading Order(LO)+Leading-Logarithmic (LL) accuracy. There are other MCEG like POWHEG [30] which are consistent with NLO calculations including parton showers.

## 1.5.2 Open heavy flavour in pp and nucleus-nucleus collisions

The experimental study of open heavy flavour production is done by measuring the hadrons carrying heavy quarks (charm and bottom) or through their leptonic decay products. Among the six quarks in the SM, u,d and s quarks have masses smaller or comparable to the nonperturbative QCD scale parameter  $\lambda_{QCD} \simeq 200$  MeV. On the other hand, the masses of the heavy quarks charm ( $m_c \simeq 1.29$  GeV) and bottom ( $m_b \simeq 4.19$  GeV) are significantly larger than the  $\lambda_{QCD}$ . Therefore, the production of heavy quarks (antiquarks) in ultra-relativistic hadron-hadron collision are expected mainly from the initial hard partonic scattering and hence their production can be calculated in the perturbative QCD (pQCD) framework. Due to the large quark mass ( $m_Q \gg \lambda_{QCD}$ ), the calculation of cross-section of heavy-quarks in pQCD is allowed over all momentum range whereas perturbative treatment of light quarks (u,d,s) and gluons are valid possibly only at high momenta [31].

The measurement of open heavy flavour in pp collisions provides a precision test to the understanding of pQCD. Furthermore, it provides a baseline for the measurement in nucleus-nucleus collisions. As we discussed in section 1.4.4, any deviation of  $R_{AA}$  from unity would indicate nuclear modifications for heavy flavour observables. Such nuclear modifications may depend on initial as well as final state effects.

- **Initial State Effect:** This effect is from the initial (non-perturbative) condition which explicitly depends on the parton distribution function (PDF)  $f(x, Q^2)$ .  $x$  is the fractional momenta carried by the interacting partons from the colliding hadrons and  $Q^2$ , is the momentum transfer between the two interacting partons. At  $x \sim 0.1$  in the antishadowing region, the parton density in nucleons is smaller than in nucleus, whereas at low  $x < 0.01$  in the shadowing region, the parton density reduces in nuclei relative to nucleons.
- **Final State Effect:** The final state effects are due to the presence of hot and

deconfined state of matter produced in the relativistic heavy-ion collisions. The partons propagating through the medium lose energy which is very sensitive to the energy density of the medium. The partons lose energy via collisional and radiative energy loss mechanisms. Moreover, the radiative energy loss is not expected to be same for all partons. A larger radiative energy loss is expected for gluons than quarks due to their larger coupling factor than quarks. The heavier quarks emit more gluons than lighter quarks due to the dead-cone effect [23].

In Figure 1.9, the fractional energy loss  $\Delta E/E$  through collisional and radiative process for charm and beauty quark at an effective temperature  $T = 304$  MeV using Djordjevic model are shown. The radiative energy loss for charm quarks dominates over collisional energy loss for  $p_T > 10$  GeV/ $c$  whereas for beauty quarks, it dominates for  $p_T > 25$  GeV/ $c$ . Therefore, the comparison of radiative energy loss for two quarks of different masses presents a clear illustration of the dead-cone effect. It also shows that the effect disappears when  $p_T \gg m_Q$ .

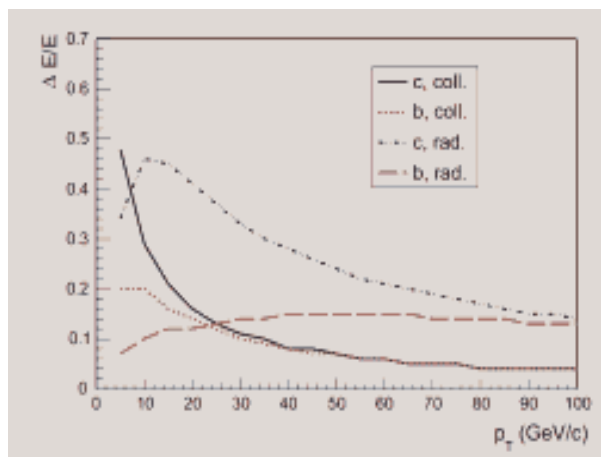


Figure 1.9: Fractional energy loss via collisional and radiative process for charm and beauty quark at an effective temperature  $T = 304$  MeV using Djordjevic model [25].

Recently, the ALICE experiment at CERN, confirms the first direct observation of the dead-cone effect in pp collision at  $\sqrt{s} = 13$  TeV [32]. ALICE applied a new iterative declustering technique to jets tagged with a reconstruction of  $D^0$ -meson to directly

observe this dead-cone effect [33].

## 1.6 Open heavy flavour measurements at LHC

Over the many years, the study of open charm and bottom production in pp collisions and nucleus-nucleus collisions are done as unique probe to test the pQCD theory and the properties of hot QCD matter respectively. The Intersecting Storage Rings (ISR) at CERN was the world's first ever hadron collider which provided two proton beam to collide in the year 1971 for the first time [34]. However, first observation of single electrons from open heavy flavour hadron decays was at ISR, CERN in the year 1974 for pp collision at  $\sqrt{s} = 52.7$  GeV [35]. The bottom production was investigated in  $p\bar{p}$  collisions at  $\sqrt{s} = 546$  GeV and 630 GeV by UA1 collaboration at CERN [36]. The result for bottom production was obtained with single muon at high  $p_T$  range ( $10 < p_T < 40$  GeV $c$ ) and compared with the pQCD calculation in the next-to-leading-order ( $\mathcal{O}(\alpha_s^3)$ ) [37]. A good agreement between the data and pQCD calculation was observed within uncertainties. The measurement of open charm was not possible at UA1 because of non availability of low  $p_T$  selective trigger and difficulties to separate them from bottom production at high  $p_T$  [31]. There are collider experiments like RHIC, PHENIX and STAR, which conducted the open heavy flavour measurements in pp and Au-Au collisions. The investigation in Cu-Cu collisions allowed to study the system size dependencies in open heavy flavour production.

The LHC provided the first ever proton-proton beam to collide at center of mass energy  $\sqrt{s} = 900$  GeV in the late 2009. In the year 2011, the ALICE, ATLAS and CMS experiments recorded data in Pb-Pb collisions at  $\sqrt{s} = 2.76$  TeV. However, all the four experiments at LHC recorded data in pp collisions at  $\sqrt{s} = 7$  TeV which served as the baseline for Pb-Pb collisions after been scaled to the lower energy  $\sqrt{s} = 2.76$  TeV.

In this section, we discuss the results related to the open heavy flavour hadron pro-

duction measured by ALICE experiment at LHC.

### 1.6.1 Charm measurement

The measurement of open charm production is being done by ALICE via the reconstruction of D-meson at mid-rapidity ( $|y| < 0.5$ ) based on the displaced-vertex topology selections. The measurements of D-meson are done via the reconstruction of the following hadronic decay channels :

$$D^0 \rightarrow K^- \pi^+ (BR = 3.95\%)$$

$$D^+ \rightarrow K^- \pi^+ \pi^+ (BR = 9.46\%)$$

$$D^{*+} \rightarrow D^0 \pi^+ (BR = 67.7\%)$$

$$D_s^+ \rightarrow \phi \pi^+ \rightarrow K^- k^+ \pi^+ (BR = 2.27\%)$$

The identification of charged pion ( $\pi^\pm$ ) and kaon ( $k^\pm$ ) via TPC and TOF detector plays significant role to reduce the combinatorial background in the measurement. The measurements of D-meson raw yields are done with an invariant-mass analysis as described in Ref. [24]. In Figure 1.10, the transverse momentum ( $p_T$ ) distribution of D-mesons ( $D^0, D^+, D^{*+}$  and  $D_s^+$ ) measured by ALICE experiment in Pb-Pb collision at midrapidity ( $|y| < 0.5$ ) are shown for three centrality classes 0-10%, 30-50% and 60-80% respectively.

In Figure 1.11 (left panel), the nuclear modification factor ( $R_{AA}$ ) of average of prompt  $D^0, D^+, D^{*+}$  mesons is shown at midrapidity ( $|y| < 0.5$ ) for three centrality classes (0-10%, 30-50%, 60-80%) in Pb-Pb collision. The average of D-mesons is calculated using the inverse of the quadratic sum of the relative statistical and uncorrelated systematic uncertainties as weights.  $R_{AA}$ s for those three prompt D-mesons are found to be compatible within uncertainties. The average  $R_{AA}$  for the D-mesons is most suppressed for



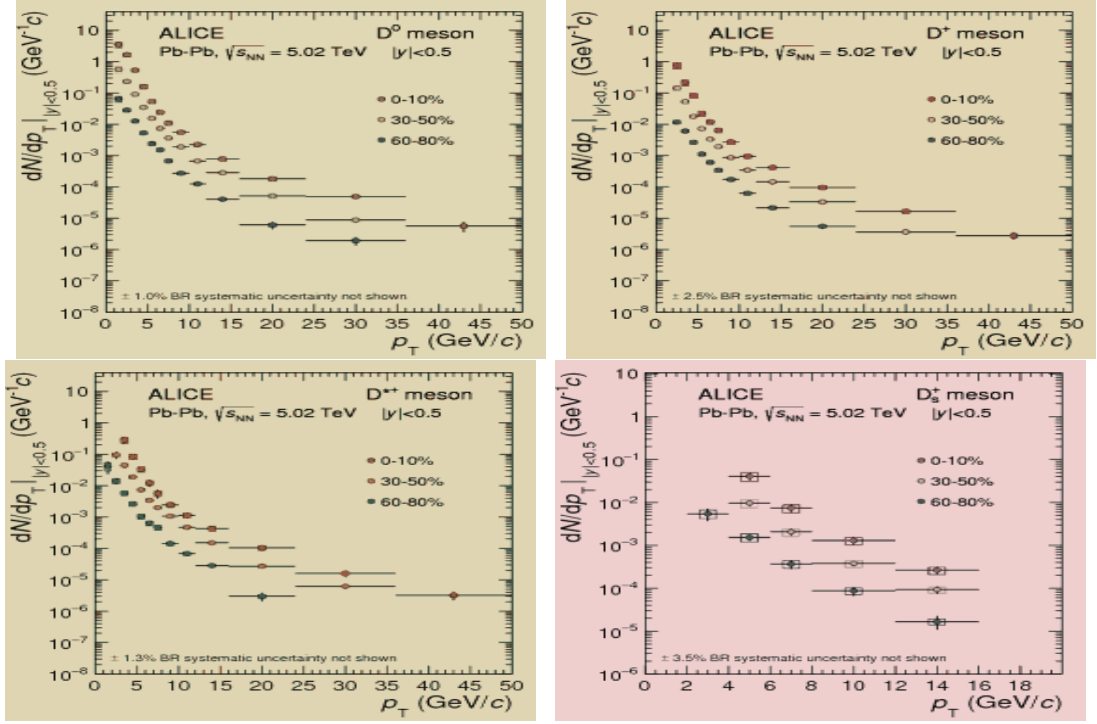


Figure 1.10:  $p_T$  distribution of prompt  $D^0$  (top left),  $D^+$  (top right),  $D^{*+}$  (bottom left) and  $D_s^+$  (bottom right) in Pb-Pb collision at midrapidity ( $|y| < 0.5$ ) for three centrality classes (0-10%, 30-50%, 60-80%) [24].

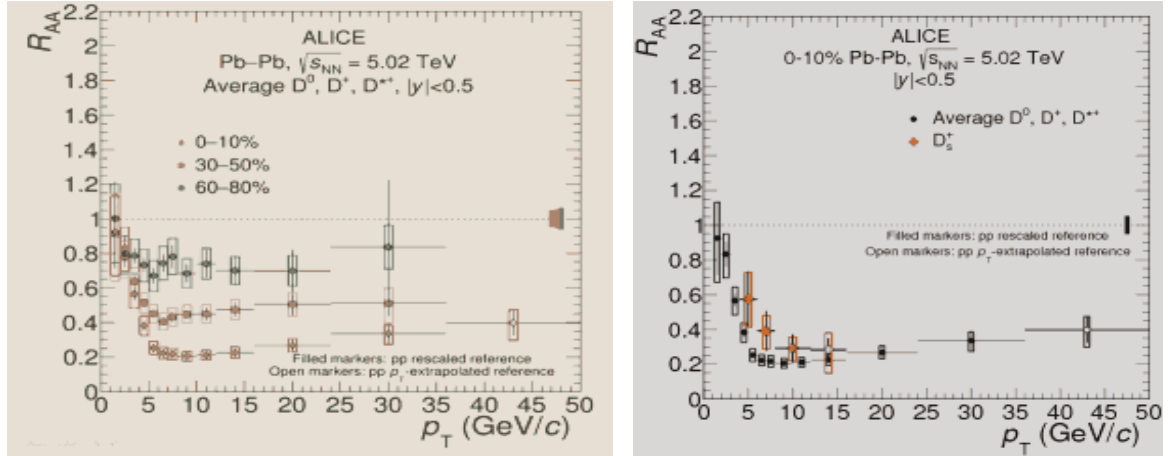


Figure 1.11: Average of  $R_{AA}$  of non-strange prompt  $D^0$ ,  $D^+$ ,  $D^{*+}$  for three centrality classes (0-10%, 30-50%, 60-80%) (left) and strange prompt  $D_s^+$  (right) for 0-10% centrality class in Pb-Pb collision at midrapidity ( $|y| < 0.5$ ) [24, 38].

0-10% centrality and the suppression is decreasing from central to peripheral collisions. The suppression is maximum at  $p_T \approx 10$  GeV/c in the case of 0-10% central collision and remains below  $R_{AA} = 0.4$  upto a high  $p_T = 50$  GeV/c. The  $R_{AA}$  of prompt  $D_s^+$  meson

for 0-10% central collision is also shown in Figure 1.11 (right panel) and compared with the average  $R_{AA}$  of the non-strange D-mesons in the interval  $2 < p_T < 15$  GeV/c. It is observed that the average  $R_{AA}$  of the non-strange D-mesons is more suppressed than the  $D_s^+$  in that  $p_T$  range.

## 1.6.2 Bottom measurement

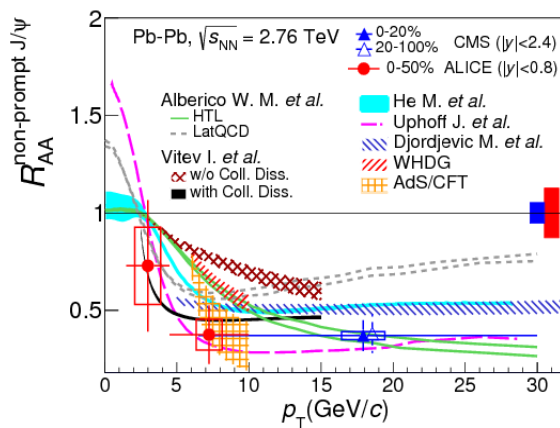


Figure 1.12: Average of  $R_{AA}$  of non-strange prompt  $D^0$ ,  $D^+$ ,  $D^{*+}$  for three centrality classes (0-10%, 30-50%, 60-80%) (left) and strange prompt  $D_s^+$  (right) for 0-10% centrality class in Pb-Pb collision at midrapidity ( $|y| < 0.5$ ) [39].

The investigation of bottom production is done via the measurement of non-prompt  $J/\psi$  measurement from the decay of bottom hadrons. The measurement of non-prompt  $J/\psi$  is done via reconstruction of displaced bottom-hadron decay vertex from the primary vertex by measuring the pseudo-proper decay length of the  $J/\psi$  mesons. The nuclear modification factor  $R_{AA}$  for non-prompt  $J/\psi$  measured by ALICE [39] together with CMS [40] are shown in Figure 1.12 for Pb-Pb collision at  $\sqrt{s_{NN}} = 2.76$  TeV. The results are presented with different centrality classes for ALICE (0-50%) and CMS (0-20% and 20-100%). The results obtained by ALICE and CMS are compared with various model calculations. The energy loss mechanism described by the models is based on either by pure collision or a combination of collisional and radiative processes. A larger  $R_{AA}$  value for most of the models are observed when compared to the ALICE and CMS

measurements. Therefore, more precise data are required to describe the discrepancies among the models.

### 1.6.3 Semi-leptonic decay of open heavy flavour hadron

ALICE has measured the open heavy flavour hadron via their semi-leptonic decay channels. The open heavy flavour production is measured via their hadronic semi-electronic decay channel at mid-rapidity ( $|y| < 0.8$ ) and through semi-muonic decay channel at forward rapidity ( $-4 < y < -2.5$ ).

#### Semi-electronic decay of open heavy flavour hadron

The production of electrons from open heavy flavour hadron decays are measured by ALICE at mid-rapidity [41–44]. The electrons are identified by the Time Projection Chamber (TPC), Time Of Flight (TOF), Transition Radiation Detector (TRD) and ElectroMagnetic Calorimeter (EMCal) detectors of ALICE. The main background contribution is from Dalitz decays of the  $\pi^0$  and  $\eta$  mesons. In addition to this, light vector mesons ( $\rho, \omega, \phi$ ) and quarkonia ( $J/\psi, \Upsilon$ ) decays also contribute to the background electrons. The Inner Tracking System (ITS) of ALICE is capable to separate the secondary vertices of bottom-hadron decay from charm-hadron decay. Therefore, it allows to measure the contribution of electron from charm and bottom hadron decays separately.

Figure 1.13 presents the production of electrons from semileptonic heavy flavour hadron decays (HFE) in pp and Pb-Pb collisions measured by ALICE experiment [27]. The  $p_T$ -differential production cross section of HFE at mid-rapidity ( $|y| < 0.8$ ) in pp collisions at  $\sqrt{s} = 5.02$  TeV is shown in the left panel of Figure 1.13. The measurement in pp collision is compared with the theoretical model FONLL calculations. The bottom panel shows the data to model ratio which describe a good agreement with the theoretical calculations especially at higher  $p_T$ -region. The right panel of Figure 1.13 shows

the  $p_T$ -differential invariant yield of HFE at mid-rapidity in Pb–Pb collisions at  $\sqrt{s_{NN}} = 5.02$  TeV. The results in Pb–Pb collisions are presented for three centrality classes: central (0–10%), semi-central (30–50%) and peripheral (60–80%).

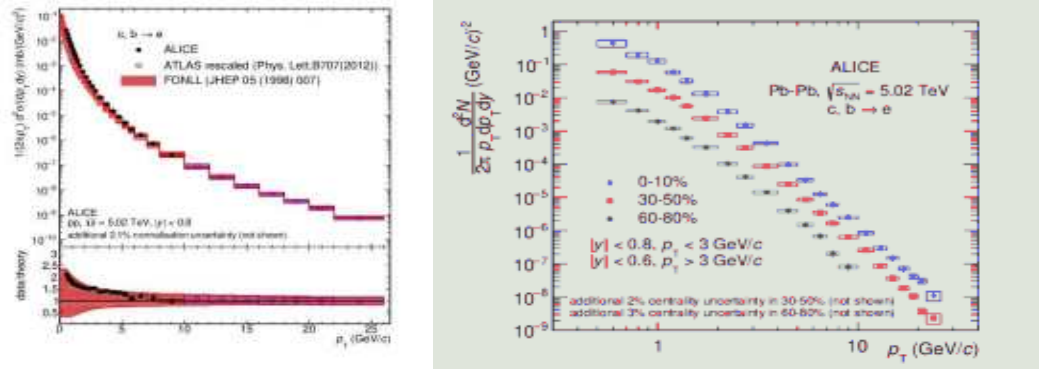


Figure 1.13:  $p_T$ -differential production cross section of electrons from semileptonic heavy flavour hadron decays (HFE) in pp collisions at  $\sqrt{s} = 5.02$  TeV by ALICE and compared with theoretical model FONLL calculation (left). The  $p_T$ -differential invariant yield of HFE in central (0–10%), semi-central (30–50%) and peripheral (60–80%) Pb–Pb collisions at  $\sqrt{s_{NN}} = 5.02$  TeV (right) [42].

The measurements of  $R_{AA}$  for electrons from semileptonic heavy flavour hadron decays are shown in Figure 1.14 for three centrality (0-10%, 30-50%, 60-80%) classes in Pb–Pb collisions at  $\sqrt{s_{NN}} = 5.02$  TeV. The measured  $R_{AA}$  is seen to be strongly dependent on the collision centrality where  $R_{AA}$  is decreasing from peripheral to central collision. This suppression of electrons describe the final state effects such as parton energy loss in the medium produced in Pb-Pb collisions.

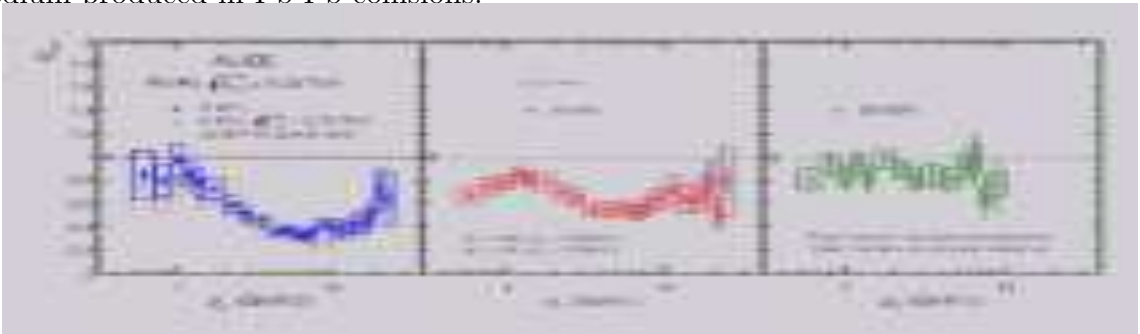


Figure 1.14: Nuclear modification factor  $R_{AA}$  of heavy flavour hadron decay electrons measured in Pb–Pb collisions at  $\sqrt{s_{NN}} = 5.02$  TeV for three centrality classes (0-10%, 30-50%, 60-80%) [42].

## Semi-muonic decay of open heavy flavour hadron

The open heavy flavour production is also measured by ALICE experiment via the semi-muonic decay of heavy flavour hadrons at forward rapidity ( $-4 < \eta < -2.5$ ) in pp and heavy-ion collisions. In this thesis, the results for the production of Heavy Flavour hadron decay Muon (HFM) in pp collisions at  $\sqrt{s} = 13$  TeV using ALICE detector is discussed.

Experimentally, ALICE measures the HFM production at forward rapidity ( $-4 < \eta < -2.5$ ) which allows to test the prediction of pQCD over a large momentum range and in a region of small Bjorken- $x$ . In ALICE, the muons are identified in the pseudorapidity range  $-4 < \eta < -2.5$  using muon spectrometer (MS) of ALICE detector. The MS consists of a front absorber, five tracking stations, a dipole magnet, two trigger stations and an iron wall in between the tracking and trigger systems. The spectrum of the inclusive muons contains background muons originating from various sources. The maximum background contribution at lower  $p_T$ -region is from the muons decaying from primary light hadrons ( $\pi^\pm, K^\pm$ ). In addition to this, there are other background contributions toward low  $p_T$  such as muons decaying from secondary light hadrons produced in the material of the front absorber and punch through hadrons escaped from the front absorber and reaching to the tracking system. The muons from quarkonia ( $J/\psi$ ) decay contribute mainly in the intermediate  $p_T$  range ( $\sim 6$ -12 GeV/ $c$ ) whereas the  $W^\pm$ , Z-boson decay background muons dominate at higher  $p_T$  region. ALICE has adopted various systematic strategies to subtract the background muons to estimate the HFM production which are discussed in details in chapter 3.

The  $p_T$ - and  $y$ -differential production cross-section of HFM have been measured by ALICE in pp collisions at  $\sqrt{s} = 2.76$  TeV [45], 5.02 TeV [46] and 7 TeV [47]. The HFM measurement has also been done in Pb-Pb collisions at  $\sqrt{s_{NN}} = 2.76$  TeV [45] and 5.02 TeV [48] and in Xe-Xe collisions at  $\sqrt{s_{NN}} = 5.44$  TeV [49].

In Figure 1.15, the  $p_T$ -differential production cross sections of HFM at forward rapidity ( $2.5 < y < 4$ ) in pp collisions at  $\sqrt{s} = 2.76$  TeV (left), 5.02 TeV (middle) and 7 TeV (right) are presented. The vertical bars and the empty boxes represent the statistical and systematic uncertainties respectively. The HFM measurement at  $\sqrt{s} = 2.76$  TeV and 7 TeV is upto  $p_T = 10$  GeV/ $c$  and  $p_T = 12$  GeV/ $c$  respectively. However, this measurement is extended upto  $p_T = 20$  GeV/ $c$  at  $\sqrt{s} = 5.02$  TeV. The measured HFM production cross-section is compared with the theoretical model FONLL calculations at their respective energies. The FONLL predictions are compatible with the ALICE data for all the three energies within the experimental and theoretical uncertainties. The measurements of HFM in pp collisions serve as references to study the hot and thermalised medium produced in Pb–Pb collisions at the same centre-of-mass energy ( $\sqrt{s} = 2.76$  and 5.02 TeV). However, the study of QCD matter produced in Xe–Xe collisions at  $\sqrt{s_{NN}} = 5.44$  TeV is done by using the pp data at  $\sqrt{s} = 5.02$  TeV which is further normalised to  $\sqrt{s} = 5.44$  TeV applying a pQCD-driven energy scaling based on FONLL calculations [50].

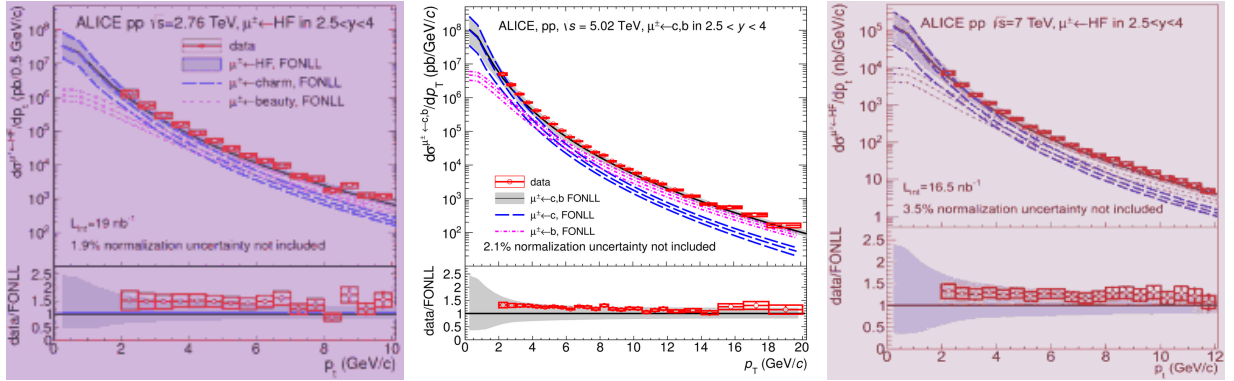


Figure 1.15:  $p_T$ -differential production cross section of muons from heavy flavour hadron decays at forward rapidity ( $2.5 < y < 4$ ) in pp collisions at  $\sqrt{s} = 2.76$  TeV (left), 5.02 TeV (middle) and 7 TeV (right) [45–47]. The production cross sections are compared with the FONLL predictions at their corresponding energies.

The  $p_T$ -differential  $R_{AA}$  of HFM at forward rapidity in Pb–Pb collisions for 0-10% centrality for two energies  $\sqrt{s_{NN}} = 2.76$  and 5.02 TeV has been compared in left panel of Figure 1.16. The result at  $\sqrt{s_{NN}} = 5.02$  TeV presents an improvement in the precision

measurement compared to that at  $\sqrt{s_{NN}} = 2.76$  TeV. It is noticed that the suppressions of  $R_{AA}$  of HFM are similar at both the energies which has also been observed for heavy flavour hadron decay electrons (HFE) in midrapidity [42]. The similarity of  $R_{AA}$  at these two energies (2.76 and 5.02 TeV) could results due to the flattening of the initial momentum distributions of charm and bottom quarks with increasing collision energy. In addition to this, an increase in medium temperature with beam energy induces more energy loss in the medium and hence more suppression with increase in energy [51].

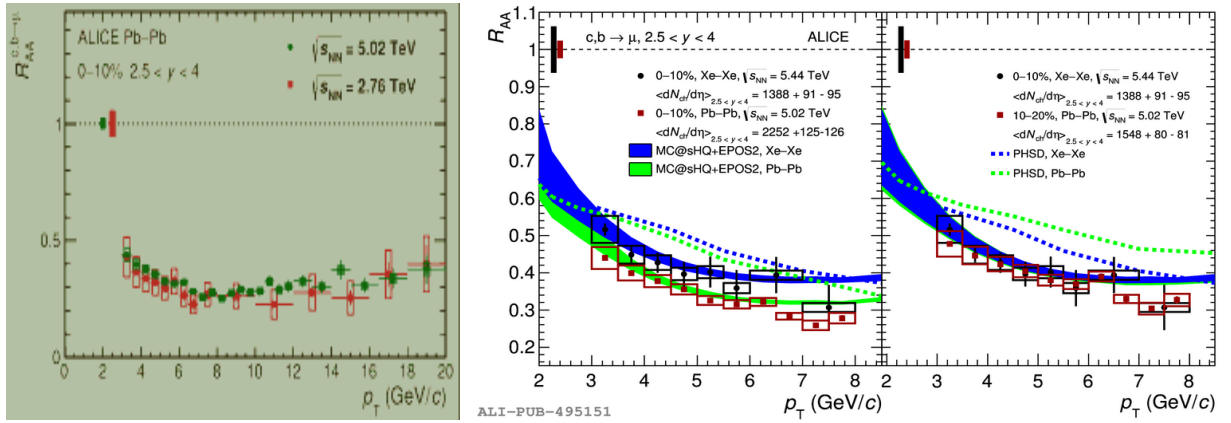


Figure 1.16:  $R_{AA}$  as a function of  $p_T$  at  $\sqrt{s} = 2.76$  and 5.02 TeV in 0-10% central Pb-Pb collisions [48] (left) and in 0-10% central Xe-Xe collisions at  $\sqrt{s} = 5.44$  TeV [49] (right).

The  $R_{AA}$  of HFM in Xe-Xe collisions at  $\sqrt{s_{NN}} = 5.44$  TeV is presented in the right panel of the Figure 1.16. This measurement of  $R_{AA}$  in 0-10% central Xe-Xe collisions is compared with the Pb-Pb collisions at  $\sqrt{s_{NN}} = 5.02$  TeV for two centrality classes 0-10% and 10-20% along with various transport models (HSD and MC@sHQ+EPOS2). It is observed that the suppression is smaller in Xe-Xe collision compared to that in Pb-Pb collision for the same centrality class. Moreover, a comparison in the Xe-Xe collision for 0-10% centrality and in Pb-Pb collision at 10-20% centrality is done where the average charged-particle multiplicity density are similar. In this case, the  $R_{AA}$  is found to be very similar for both the collision systems where the average charged-particle multiplicity densities are comparable.



## 1.7 Scope of this thesis

In chapter 2, a brief description of the ALICE (A Large Ion Collider Experiment) detector at the Large Hadron Collider (LHC) is given. In ALICE, the heavy flavour decay muon production is measured by the Muon Spectrometer (MS) which is situated in the forward direction in the range  $-4 < \eta < -2.5$ . The various sub-systems of the MS are discussed also. In the latter part of this chapter, the upgrade program for the ALICE Run 3 is discussed briefly.

In chapter 3, a report of data analysis to measure the production cross-section of muons decaying from heavy flavour hadrons in pp collision at  $\sqrt{s} = 13$  TeV using the muon spectrometer of the ALICE detector is presented. This new measurement of heavy flavour decay muons (HFM) is done at the highest available energy  $\sqrt{s} = 13$  TeV during LHC Run 2 in pp collisions with integrated luminosity of  $\sim 36$  pb<sup>-1</sup>. ALICE published the results of HFM production in pp collisions at  $\sqrt{s} = 2.76, 5.02$  and 7 TeV and in A-A collisions at  $\sqrt{s_{NN}} = 2.76$  and 5.02 TeV which have been discussed above. The measurement of HFM production in pp collisions at  $\sqrt{s} = 5.02$  TeV is extended upto 20 GeV/*c* from the earlier measurements at  $\sqrt{s} = 7$  TeV which was upto 12 GeV/*c*. The data sample collected in 2016 of Run 2 at  $\sqrt{s} = 13$  TeV allows to obtain the transverse momentum of heavy flavour decay muon upto  $p_T = 30$  GeV/*c* with high statistical precision. The various background muons originated from the light hadron decays,  $J/\psi$  decays and  $W^\pm$ , Z-boson decays are subtracted from the inclusive muons to obtain muons from heavy flavour hadron decays. The HFM production cross-section as a function of transverse momentum ( $p_T$ ) and rapidity ( $y$ ) has been reported. The  $p_T$ -differential production cross-section of HFM is obtained in the full acceptance ( $-4 < \eta < -2.5$ ) of the Muon Spectrometer. In addition to this, the same measurement has also been carried out at five equal pseudo-rapidity intervals in the range of  $-4 < \eta < -2.5$ . The  $p_T$  integrated production cross-section of HFM as a function of rapidity has been obtained



at two different  $p_T$ -region:  $2 < p_T < 7$  GeV/ $c$  and  $7 < p_T < 30$  GeV/ $c$ . The experimental measurement of HFM in pp collision by ALICE at this high energy  $\sqrt{s} = 13$  TeV provides an important test to describe the theoretical pQCD calculations. The experimental data for the production of HFM is compared to the theoretical model FONLL calculations. The measurement of HFM at  $\sqrt{s} = 13$  TeV is compared with the previous results of HFM reported by the ALICE experiment at other energies ( $\sqrt{s} = 2.76, 5.02$  and  $7$  TeV).

In chapter 4, phenomenological studies for the production of HFM and charged particles using Angantyr model in PYTHIA8 are discussed. The Angantyr model does not assume the formation of hot and thermalised medium (QGP) in heavy-ion collision. The simulation results of the HFM and charged particles using Angantyr have been presented in pp and A-A (Pb-Pb, Xe-Xe and O-O) collisions over a wide range of LHC energies. The study of HFM using Angantyr provides important understanding of the behaviour of heavy flavour production in heavy-ion collision where no hot and thermalised medium is created. In addition, it may be served as reference study of the non-collective background to the observables sensitive to the collective behaviours.

In chapter 5, the Quality Assurance (QA) test of ladders for Muon Forward Tracker (MFT) detector of ALICE is discussed. This QA test was done as a part of ALICE service-task. The basic detection element of MFT is the silicon pixel sensor, called ALPIDE (ALICE P*IX*el D*E*tector), jointly developed by the Inner Tracking System (ITS) and MFT collaborations. These silicon pixel sensors are integrated on mechanical ladder structures. The qualification tests for these ladders were carried out in the Antenna building at CERN, Geneva. I was personally involved for the qualification tests of  $\sim 230$  newly ladders. The assembled full MFT-disk was installed in ALICE cavern in November, 2020 and it started taking data from 5th July, 2022 for LHC Run 3. A brief description of the Ladder Qualification Test benches and various testing procedure for the ladder qualification is discussed in this chapter.

In chapter 6, the future outlook has been discussed.



---

# Bibliography

---

- [1] D. Griffiths, *Introduction to elementary particles* (2008). 1
- [2] M.D. Schwartz, *Quantum Field Theory and the Standard Model*, Cambridge University Press (3, 2014). 1
- [3] S. Bethke, *Experimental tests of asymptotic freedom*, *Prog. Part. Nucl. Phys.* **58** (2007) 351 [[hep-ex/0606035](#)]. 4
- [4] S. Bethke, *World Summary of  $\alpha_s$  (2012)*, *Nucl. Phys. B Proc. Suppl.* **234** (2013) 229 [[1210.0325](#)]. xvii, 4
- [5] F. Karsch, *Lattice results on QCD thermodynamics*, *Nucl. Phys. A* **698** (2002) 199 [[hep-ph/0103314](#)]. 5
- [6] F. Karsch, *Lattice QCD at nonzero chemical potential and the resonance gas model*, *Prog. Theor. Phys. Suppl.* **153** (2004) 106 [[hep-lat/0401031](#)].
- [7] H.-T. Ding, F. Karsch and S. Mukherjee, *Thermodynamics of strong-interaction matter from Lattice QCD*, *Int. J. Mod. Phys. E* **24** (2015) 1530007 [[1504.05274](#)]. xvii, 5
- [8] K. Rajagopal and F. Wilczek, *The Condensed matter physics of QCD*, in *At the frontier of particle physics. Handbook of QCD. Vol. 1-3*, M. Shifman and B. Ioffe, eds., pp. 2061–2151 (2000), DOI [[hep-ph/0011333](#)]. 6

- [9] U. Heinz et al., *Exploring the properties of the phases of QCD matter - research opportunities and priorities for the next decade*, [1501.06477](#). xvii, 6
- [10] J.P. Blaizot and A.H. Mueller, *The Early Stage of Ultrarelativistic Heavy Ion Collisions*, *Nucl. Phys. B* **289** (1987) 847. 7
- [11] J.D. Bjorken, *Highly Relativistic Nucleus-Nucleus Collisions: The Central Rapidity Region*, *Phys. Rev. D* **27** (1983) 140. xvii, 7, 8, 15
- [12] P. Senger, *Heavy-ion collisions at fair-nica energies*, *Particles* **4** (2021) 214. 7
- [13] L. McLerran, *Theoretical Concepts for Ultra-Relativistic Heavy Ion Collisions*, in *Meeting of the Division of Particles and Fields of the American Physical Society (DPF 2009)*, 11, 2009 [[0911.2987](#)]. xvii, 8
- [14] H. Shah, *The Angantyr Model For Simulating Heavy-Ion Collisions*, bachelor thesis, Lund U., 2021. 8
- [15] R.J. Glauber and G. Matthiae, *High-energy scattering of protons by nuclei*, *Nucl. Phys. B* **21** (1970) 135. 10
- [16] P. Koch, B. Muller and J. Rafelski, *Strangeness in Relativistic Heavy Ion Collisions*, *Phys. Rept.* **142** (1986) 167. 12
- [17] A.M. Poskanzer and S.A. Voloshin, *Methods for analyzing anisotropic flow in relativistic nuclear collisions*, *Phys. Rev. C* **58** (1998) 1671 [[nucl-ex/9805001](#)]. 13
- [18] ALICE collaboration, *Elliptic flow of identified hadrons in Pb-Pb collisions at  $\sqrt{s_{NN}} = 2.76$  TeV*, *JHEP* **06** (2015) 190 [[1405.4632](#)]. 13
- [19] R. Chatterjee, L. Bhattacharya and D.K. Srivastava, *Electromagnetic probes*, *Lect. Notes Phys.* **785** (2010) 219 [[0901.3610](#)]. 14

- [20] S. Chakrabarty, J. Alam, D.K. Srivastava, B. Sinha and S. Raha, *High-energy photons from expanding quark - gluon plasma and hot hadronic matter*, *Phys. Rev. D* **46** (1992) 3802. 14
- [21] C. Nattrass, *Jets in heavy ion collisions*, *J. Phys. Conf. Ser.* **832** (2017) 012001. 15
- [22] R. Pasechnik and M. Šumbera, *Phenomenological Review on Quark–Gluon Plasma: Concepts vs. Observations*, *Universe* **3** (2017) 7 [1611.01533]. xvii, 16
- [23] Y.L. Dokshitzer and D.E. Kharzeev, *Heavy quark colorimetry of QCD matter*, *Phys. Lett. B* **519** (2001) 199 [hep-ph/0106202]. 16, 22
- [24] ALICE collaboration, *Measurement of  $D^0$ ,  $D^+$ ,  $D^{*+}$  and  $D_s^+$  production in Pb-Pb collisions at  $\sqrt{s_{\text{NN}}} = 5.02$  TeV*, *JHEP* **10** (2018) 174 [1804.09083]. xvii, xviii, 16, 17, 24, 25
- [25] A. Andronic et al., *Heavy-flavour and quarkonium production in the LHC era: from proton–proton to heavy-ion collisions*, *Eur. Phys. J. C* **76** (2016) 107 [1506.03981]. xviii, 18, 20, 22
- [26] R.V. Gavai, S. Gupta, P.L. McGaughey, E. Quack, P.V. Ruuskanen, R. Vogt et al., *Heavy quark production in pp collisions*, *Int. J. Mod. Phys. A* **10** (1995) 2999 [hep-ph/9411438]. 18
- [27] M. Cacciari, M. Greco and P. Nason, *The  $P(T)$  spectrum in heavy flavor hadroproduction*, *JHEP* **05** (1998) 007 [hep-ph/9803400]. 19, 27
- [28] T. Sjostrand, S. Mrenna and P.Z. Skands, *A Brief Introduction to PYTHIA 8.1*, *Comput. Phys. Commun.* **178** (2008) 852 [0710.3820]. 20
- [29] G. Corcella, I.G. Knowles, G. Marchesini, S. Moretti, K. Odagiri, P. Richardson et al., *HERWIG 6: An Event generator for hadron emission reactions with interfering gluons (including supersymmetric processes)*, *JHEP* **01** (2001) 010 [hep-ph/0011363]. 20

- [30] S. Frixione, P. Nason and G. Ridolfi, *A Positive-weight next-to-leading-order Monte Carlo for heavy flavour hadroproduction*, *JHEP* **09** (2007) 126 [0707.3088]. 20
- [31] R. Averbeck, *Heavy-flavor production in heavy-ion collisions and implications for the properties of hot QCD matter*, *Prog. Part. Nucl. Phys.* **70** (2013) 159 [1505.03828]. 21, 23
- [32] ALICE collaboration, *Direct observation of the dead-cone effect in quantum chromodynamics*, *Nature* **605** (2022) 440 [2106.05713]. 22
- [33] C. Frye, A.J. Larkoski, J. Thaler and K. Zhou, *Casimir Meets Poisson: Improved Quark/Gluon Discrimination with Counting Observables*, *JHEP* **09** (2017) 083 [1704.06266]. 23
- [34] The Intersecting Storage Rings.  
<https://home.cern/science/accelerators/intersecting-storage-rings>. 23
- [35] F.W. Busser et al., *Observation of High Transverse Momentum Electrons at the CERN ISR*, *Phys. Lett. B* **53** (1974) 212. 23
- [36] UA1 collaboration, *Search for New Heavy Quarks at the CERN Proton - anti-Proton Collider*, *Z. Phys. C* **37** (1988) 505. 23
- [37] P. Nason, S. Dawson and R.K. Ellis, *The Total Cross-Section for the Production of Heavy Quarks in Hadronic Collisions*, *Nucl. Phys. B* **303** (1988) 607. 23
- [38] ALICE collaboration, *D-meson production in Pb-Pb collisions with ALICE at the LHC*, *Nucl. Phys. A* **1005** (2021) 121747 [2001.05949]. xviii, 25
- [39] ALICE collaboration, *Inclusive, prompt and non-prompt  $J/\psi$  production at mid-rapidity in Pb-Pb collisions at  $\sqrt{s_{NN}} = 2.76$  TeV*, *JHEP* **07** (2015) 051 [1504.07151]. xviii, 26
- [40] CMS collaboration, *Suppression of non-prompt  $J/\psi$ , prompt  $J/\psi$ , and  $Y(1S)$  in PbPb collisions at  $\sqrt{s_{NN}} = 2.76$  TeV*, *JHEP* **05** (2012) 063 [1201.5069]. 26

- [41] ALICE collaboration, *Measurements of low- $p_T$  electrons from semileptonic heavy-flavour hadron decays at mid-rapidity in  $pp$  and  $Pb-Pb$  collisions at  $\sqrt{s_{NN}} = 2.76$  TeV*, *JHEP* **10** (2018) 061 [[1805.04379](#)]. 27
- [42] ALICE collaboration, *Measurement of electrons from semileptonic heavy-flavour hadron decays at midrapidity in  $pp$  and  $Pb-Pb$  collisions at  $\sqrt{s_{NN}} = 5.02$  TeV*, *Phys. Lett. B* **804** (2020) 135377 [[1910.09110](#)]. xviii, 28, 31
- [43] ALICE collaboration, *Measurement of electrons from semileptonic heavy-flavour hadron decays in  $pp$  collisions at  $\sqrt{s} = 7$  TeV*, *Phys. Rev. D* **86** (2012) 112007 [[1205.5423](#)].
- [44] ALICE collaboration, *Measurement of electrons from heavy-flavour hadron decays in  $p-Pb$  collisions at  $\sqrt{s_{NN}} = 5.02$  TeV*, *Phys. Lett. B* **754** (2016) 81 [[1509.07491](#)]. 27
- [45] ALICE collaboration, *Production of muons from heavy flavour decays at forward rapidity in  $pp$  and  $Pb-Pb$  collisions at  $\sqrt{s_{NN}} = 2.76$  TeV*, *Phys. Rev. Lett.* **109** (2012) 112301 [[1205.6443](#)]. xviii, 29, 30
- [46] ALICE collaboration, *Production of muons from heavy-flavour hadron decays in  $pp$  collisions at  $\sqrt{s} = 5.02$  TeV*, *JHEP* **09** (2019) 008 [[1905.07207](#)]. 29
- [47] ALICE collaboration, *Heavy flavour decay muon production at forward rapidity in proton-proton collisions at  $\sqrt{s} = 7$  TeV*, *Phys. Lett. B* **708** (2012) 265 [[1201.3791](#)]. xviii, 29, 30
- [48] ALICE collaboration, *Production of muons from heavy-flavour hadron decays at high transverse momentum in  $Pb-Pb$  collisions at  $\sqrt{s_{NN}} = 5.02$  and  $2.76$  TeV*, [2011.05718](#). xix, 29, 31
- [49] ALICE collaboration, *Inclusive heavy-flavour production at central and forward*

- rapidity in Xe-Xe collisions at  $\sqrt{s_{NN}}=5.44$  TeV*, *Phys. Lett. B* **819** (2021) 136437 [2011.06970]. xix, 29, 31
- [50] R. Averbeck, N. Bastid, Z.C. del Valle, P. Crochet, A. Dainese and X. Zhang, *Reference Heavy Flavour Cross Sections in pp Collisions at  $\sqrt{s} = 2.76$  TeV, using a pQCD-Driven  $\sqrt{s}$ -Scaling of ALICE Measurements at  $\sqrt{s} = 7$  TeV*, 1107.3243. 30
- [51] M. Djordjevic and M. Djordjevic, *Predictions of heavy-flavor suppression at 5.1 TeV Pb + Pb collisions at the CERN Large Hadron Collider*, *Phys. Rev. C* **92** 024918 [1505.04316]. 31



## CHAPTER 2

---

### The ALICE detector at the LHC

---

In this chapter, the experimental set up of the ALICE (**A** **L**arge **I**on **C**ollider **E**xperiment) detector at the Large Hadron Collider (LHC) is described briefly. The LHC experimental facilities and its characteristics are mentioned. The Muon Spectrometer (MS) of ALICE detector is used to collect the data for the analysis carried out for Heavy Flavour decay Muon production in pp collisions at  $\sqrt{s} = 13$  TeV. In the later part of this chapter, special attention is given to the Muon Spectrometer while discussing the description of the different sub-detectors of ALICE.

#### 2.1 The Large Hadron Collider

The Large Hadron Collider (LHC) is the world's largest and most powerful particle accelerator. The LHC was built by the laboratory European Center for Nuclear Research (CERN), located on the French-Swiss border near the Geneva city of Switzerland. The CERN accelerator complex (Fig. 2.1) is a succession of several accelerating machines [1–3]. Each of these machines accelerates a beam of particles to a specific energy and inject that beam into a machine of higher energy in the chain. The LHC is the last part of this chain where a beam reaches at the highest energy. The size of the LHC tunnel is

very large and it is approximately a 27 km ring placed at a depth of  $\sim 100$  m from the surface. This underground tunnel is filled with several superconducting magnets with a number of accelerating structures to boost the energy of particles along the way. It can accelerate protons or ions at a ultra-relativistic high energy. Two separate ultrahigh vacuum beam pipes are present inside the LHC ring. The particles in each beam travels very close to the speed of light, but in opposite direction. The two opposite beams are made to collide at four different locations which are the positions of four different particle detectors ALICE [4], CMS [5], LHCb [6] and ATLAS [7] respectively.

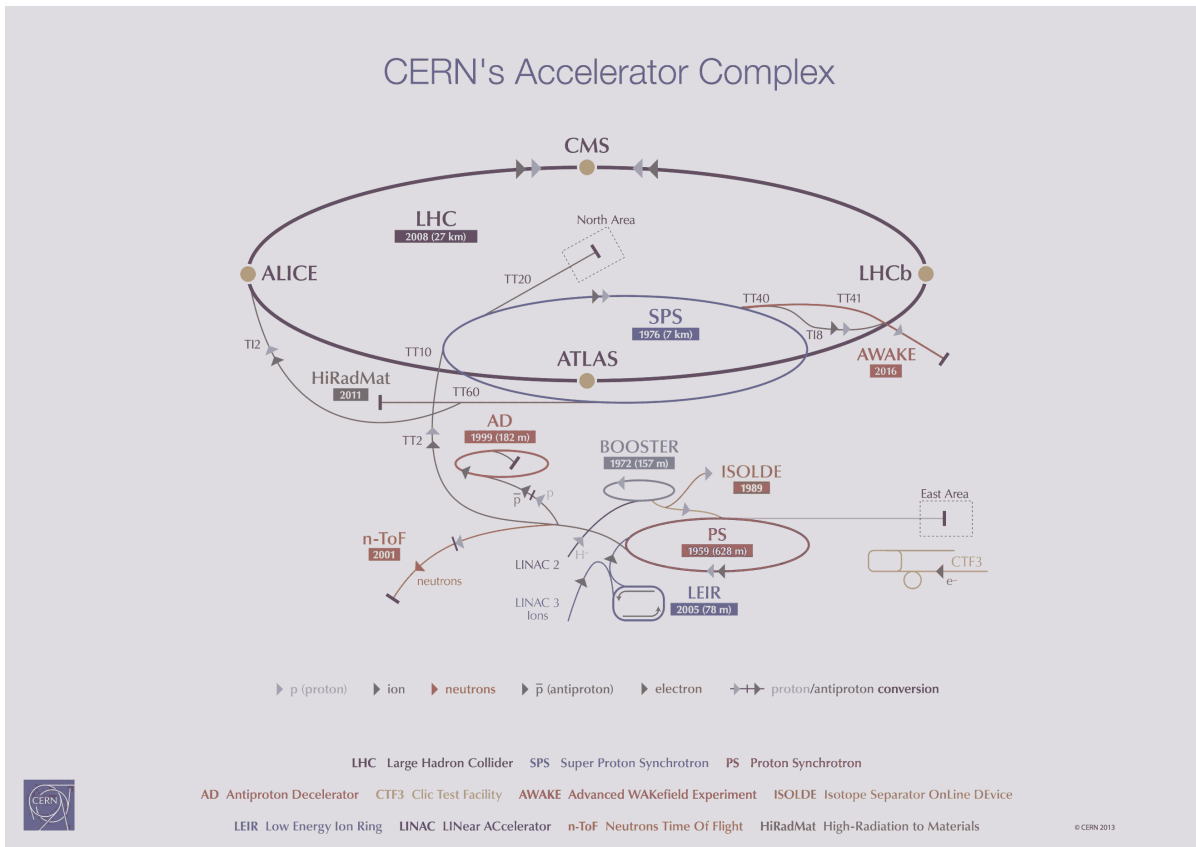


Figure 2.1: The CERN accelerator complex.

The LHC provides two types of beam facilities: proton (p) and heavy-ion (A). So, LHC can have pp, p-A and A-A type of collisions. So far, LHC used Lead ( $_{82}Pb^{208}$ ) and Xe ( $_{56}Xe^{129}$ ) as heavy-ions in Run 1 and Run 2 periods. In addition, there is a plan to have experiments with a short O-O collisions during LHC Run 3 [8]. For the

ALICE experiment, one of the main objectives of heavy-ion collisions is to investigate the evolution and properties of Quark-Gluon Plasma (QGP) which is a deconfined matter believed to be produced in such collisions at extremely high temperature and/or density. The significant part of LHC physics programme implies Pb-Pb collisions with a design of luminosity  $10^{27} \text{ cm}^{-2} \text{ s}^{-1}$ . The most massive heavy-ion source of LHC beam is Pb-ion. It is roughly 208 times massive than a proton, containing 82 protons and 126 neutrons. The lead-ion beams of LHC are generated from a highly purified piece of lead. This lead sample is heated to vaporize, further ionized by an electric current to create lead ions. These lead-ions are then successively accelerated into Linac3 (Linear Accelerator), LEIR (Low Energy Ion Ring), Proton Synchrotron (PS) and Super Proton Synchrotron (SPS). The beam is accelerated to 177 GeV per nucleon at the SPS and finally enters into the LHC ring. In the LHC, the Pb-ion can be accelerated to even more higher energy (up to 2.76 TeV per nucleon) and made to collide at the four locations of the particle detectors: ALICE, CMS, LHCb and ATLAS respectively. The LHC is designed to have a maximum possible energy of a proton beam  $E_p = 7 \text{ TeV}$ , which corresponds to a maximum possible energy for a Pb-beam is  $E_A = (Z/A).E_p \approx 2.76 \text{ TeV}$ .

### 2.1.1 The LHC experiments

There are four major experimental facilities at the LHC where the collisions take place. The name of the experiments are given as per their respective detector used. Each experiment is motivated with some physics goals which include the study of QGP, searches of Higg's boson, to test for the prediction and limit of Standard Model, searches of supersymmetric particles etc.

- **ALICE** (A Large Ion Collider Experiment) is the detector dedicated for the heavy-ion collisions. The main focus of ALICE is to study the physics of Quark-Gluon Plasma (QGP), a new state of deconfined matter formed in heavy-ion collisions. It is believed that our universe also had gone through such QGP phases during its

first few micro-second after the big bang. Hence, the study of QGP could give the information about the early stage of our universe. A more details description of ALICE detector is given in section 2.2.

- **CMS** (Compact Muon Solenoid) is one of the general-purpose particle detector at LHC which is designed to explore the physics phenomena at the LHC energies. It is very compact in respect of all the detector materials and contains most powerful solenoid magnet. It is designed to identify muon particle very accurately.
- **LHCb** (Large Hadron Collider beauty) detector is designed to study the matter-antimatter asymmetry. It is also specialized to detect the rare phenomena with decays of heavy flavours particularly B-mesons.
- **ATLAS** (A Toroidal LHC AparatuS) is another general-purpose detector used at the LHC, which is the largest in the world. The ATLAS is focused with similar physics goals as the CMS experiment. It facilitates investigation for a variety of searches for dark-matter candidates, Higgs boson, extra-dimensions of spacetime etc.

## 2.2 A Large Ion Collider Experiment

The ALICE [9] is one of the four major experiments at the LHC which focuses on the investigation of strongly interacting matter created at high temperature and/or density in ultra-relativistic heavy-ion collisions. ALICE has delivered runs for pp, p-Pb, Pb-Pb and Xe-Xe collisions at various center of mass energies ( $\sqrt{s}$ ) starting from 2.76 TeV to 13 TeV. It has plan for a short O-O collisions at  $\sqrt{s} = 6.37$  TeV during the ALICE Run 3 period [8] also. The luminosity recorded by ALICE at different collision systems during Run 1 (2009-2013) and Run 2 (2015-2018) are illustrated in Table 2.1 [10].

Table 2.1: ALICE data taking in Run 1 (2009-2013) and Run 2 (2015-2018).

System	Year	Energy (TeV)	Recorded ( $L_{int}$ )	Luminosity
pp	2009-2013	0.9, 2.76, 7, 8	$\sim 200 \mu\text{b}^{-1}$ , $\sim 100 \text{nb}^{-1}$ , $\sim 1.5 \text{pb}^{-1}$ , $\sim 2.5 \text{pb}^{-1}$	
	2015,2017	5.02	$\sim 1.3 \text{pb}^{-1}$	
	2015,2018	13	$\sim 36 \text{pb}^{-1}$	
p-Pb	2013	5.02	$\sim 15 \text{nb}^{-1}$	
	2016	5.02, 8.16	$\sim 3 \text{nb}^{-1}$ , $\sim 25 \text{nb}^{-1}$	
Xe-Xe	2017	5.44	$\sim 0.3 \mu\text{b}^{-1}$	
Pb-Pb	2010,2011	2.76	$\sim 75 \mu\text{b}^{-1}$	
	2015	5.02	$\sim 250 \mu\text{b}^{-1}$	
	2018	5.02	$\sim 536 \mu\text{b}^{-1}$	

### 2.2.1 The ALICE coordinate system

The ALICE coordinate system [11] is shown in Fig. 2.2. The origin ( $x,y,z = 0$ ) of the right handed Cartesian coordinate system of ALICE is the Interaction Point (IP) where the collision takes place. The z-axis is along the beam direction and is negative (downstream) from the origin towards the muon spectrometer placed at side C of ALICE detector and known as forward direction. The x-axis is perpendicular to the beam direction and pointing towards the center of LHC. Positive x is taken from the IP towards the accelerator center. The y-axis is perpendicular to both the x-axis and the beam direction. The positive y is upward from the origin. The azimuthal angle  $\phi$  is around the beam direction and increases counter clockwise from x( $\phi = 0^\circ$ ) to y ( $\phi = 90^\circ$ ). The full acceptance in the azimuthal angle is ranges from  $0^\circ$  to  $360^\circ$ . The polar angle  $\theta$  increases from z ( $\theta = 0^\circ$ ) through x-y plane( $\theta = 90^\circ$ ) to -z( $\theta = 180^\circ$ ).

### 2.2.2 The ALICE detector

The schematic layout of the ALICE detector is shown in Fig. 2.3. The ALICE detector is placed in cavern, at a depth of a  $\sim 50$  m from the surface. The different sub-detectors

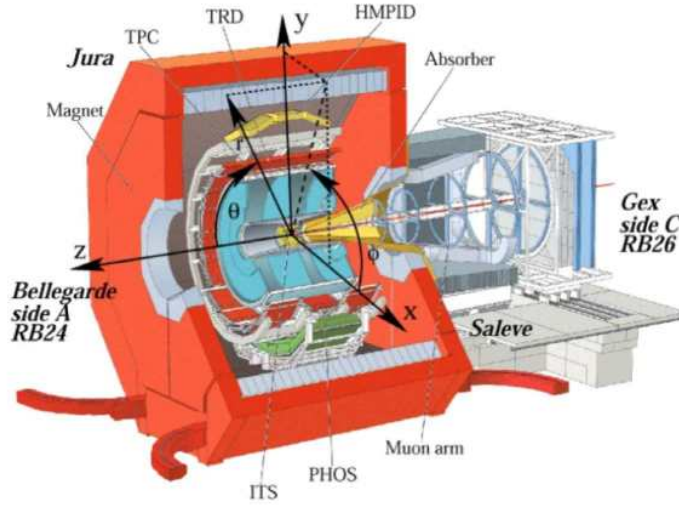


Figure 2.2: Definition of the ALICE coordinate system axis, angles and detector sides [12].

of ALICE detector are categorised mainly into three following parts:

- **Central Barrel Detectors** cover the pseudo-rapidity region  $-0.9 < \eta < 0.9$  with polar angle range  $45^\circ < \theta < 135^\circ$ . It is composed of several detectors which allow the reconstruction of primary vertex with a resolution better than  $100 \mu m$ . These detectors are used for Particle Identification (PID), e.g. electrons, photons and charged hadrons. These detectors have capability of tracking charged particles over a large momentum range from  $100 \text{ MeV}/c$  to  $\sim 100 \text{ GeV}/c$ . The central barrel consists of **I**nnear **T**racking **S**ystem (ITS), the **T**ime **P**rojection **C**hamber (TPC), the **T**ransition **R**adiation **D**etector (TRD), the **T**ime **O**f **F**light (TOF), the **H**igh **M**omentum **P**article **I**dentification **D**etector (HMPID), the **P**HOton **S**pectrometer (PHOS), the **E**lectro**M**agnetic **C**alorimeter (EMCal) and the ALICE **C**OSmic **R**ay **D**etector (ACORDE).
- **Global Detectors** are comprised of several smaller detectors placed outside the central barrel detectors to measure the global event characteristics. These are the Photon Multiplicity Detector (PMD), the Forward Multiplicity Detector (FMD), the V0 and T0 Detectors, the Zero Degree Calorimeter (ZDC). These detectors

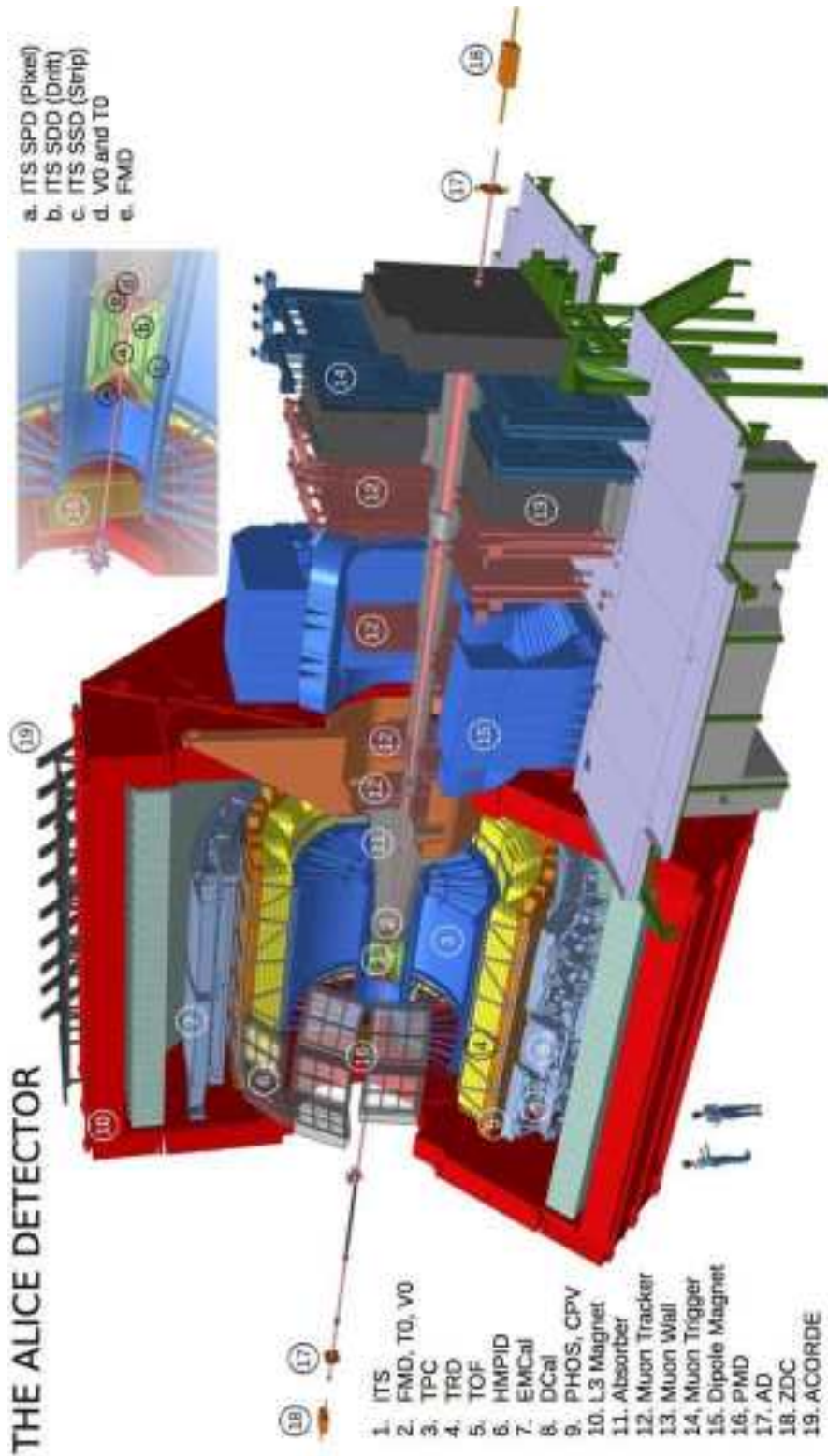


Figure 2.3: The schematic layout of the ALICE.

are used for the centrality determination, reconstruction of event reaction plane in heavy-ion collisions, charged particle multiplicity measurement and also triggering a correct decision for the beam-beam interaction.

- **Muon Spectrometer** The ALICE Muon Spectrometer is located at the forward side. It is designed to study the quarkonia production ( $J/\psi$ ,  $\psi'$ ,  $\gamma$ ,  $\gamma'$ ,  $\gamma''$ ) via the di-muon measurement. It also measures the semi-muonic decay of open heavy flavour hadrons. This detector allows to investigate the weak interactions probe by measuring the production of  $W^\pm$  and Z-boson and the measurement of low mass resonances ( $\rho$ ,  $\omega$ ,  $\phi$ ) using muonic channel.

In the following sections the brief descriptions of the central barrel and global detectors are given while the Muon Spectrometer is elaborated in details in section [2.2.5](#).

### 2.2.3 Central Barrel Detectors

#### Inner Tracking System (ITS)

The ITS [\[13\]](#) of central barrel is the innermost detector. ITS consists of six cylindrical layers of silicon detectors and covers the rapidity range of  $|\eta| < 0.9$ . A schematic view of ITS is shown in [Figure 2.4](#). The radius of the innermost layer is 3.9 cm and the outermost layer is 44 cm. The two innermost layers are made of silicon pixel detectors (SPD), the two intermediate layers are consist of drift detector (SDD) and the two outer most layers are built of strip detectors (SSD). ITS is dedicated for determining the primary vertex position and could be operated at high particle density ( $\sim 8000$  per unit rapidity) environment, since it has high granularity feature and the component detector SDD is used for high precision spatial resolution. It can measure the secondary vertices for the hyperon and charm decays also. In addition, it has excellent capability to track low momentum particle ( $< 100$  MeV/c) and particle identification.



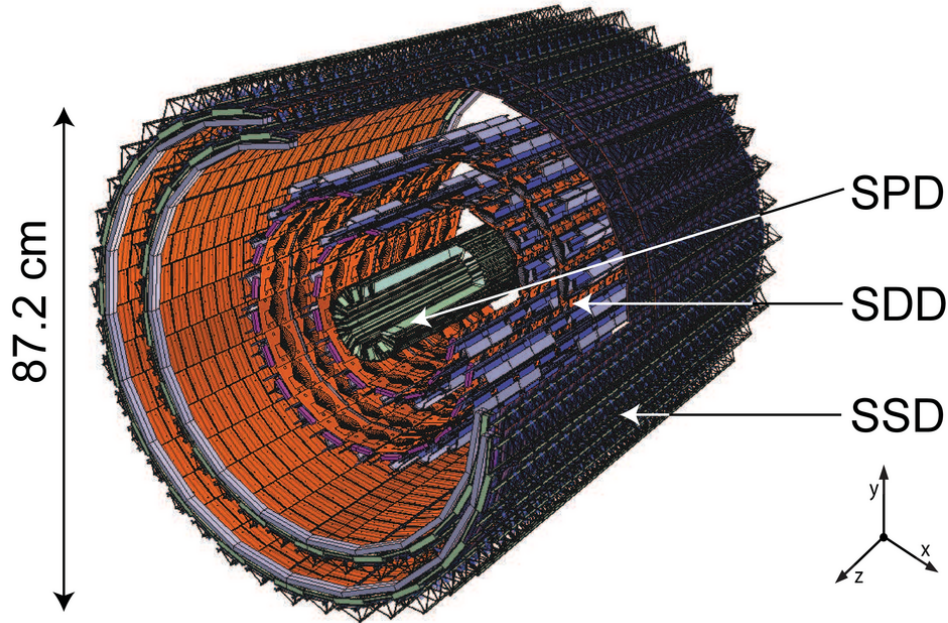


Figure 2.4: A schematic view of Inner Tracking System (ITS) of ALICE.

### Time Projection Chamber (TPC)

The Time Projection Chamber [14] is the main tracking detector of central barrel placed between the ITS and the Transition Radiation Detector (TRD). The layout of TPC is shown in Fig. 2.5. The overall acceptance ( $|\eta| < 0.9$ ) of TPC allows to study the event-by-event fluctuations in hadronic observables such as the  $K/\pi$  ratio. The TPC is of cylindrical shape with length  $\sim 500$  cm along the beam direction and with inner and outer radii of about 80 cm and 250 cm respectively. The cylindrical design of TPC is needed to cover the full azimuth and is very crucial to investigate the electron physics with high mass and/or high- $p_T$  electron pairs. It is a gas detector filled with  $\text{Ne} + \text{CO}_2 + \text{N}_2$  gas (85%+10%+5%) and operated at atmospheric pressure. The conducting electrode is charged upto 100 kV to detect charged particle trajectories inside the detector. TPC together with other central barrel detectors, can provide particle identification and precision momentum measurement of charged particles.

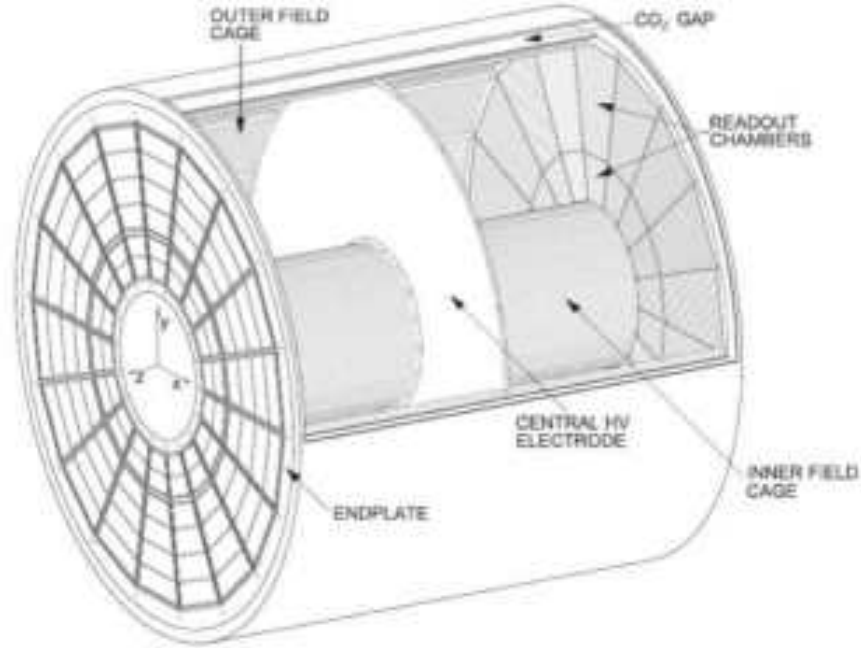


Figure 2.5: The Layout of Time Projection Chamber of ALICE.

### Transition Radiation Detector (TRD)

The TRD [15] can identify the electron for momentum above  $1 \text{ GeV}/c$  where TPC is not capable of rejecting pion through energy loss measurement. It consists of 18 sectors, each having 6 individual layers and each layer is with a 5 fold segmentation along the beam direction. Thus TRD is equipped with a total  $18 \times 6 \times 5 = 540$  detector modules. These are placed around TPC with a full azimuthal angle coverage. Each of these modules consists of a radiator of thickness 4.8 cm and a multi-wire proportional readout chamber. The Transition Radiation (TR) is used for detecting sum of ionisation loss of charged particle and TR X-rays. A xenon riched gas mixture  $\text{Xe}+\text{CO}_2$  (85%+15%) is used in the readout chambers to optimise the absorption of X-rays. The heavier particles pions do not emit TR below  $\sim 100 \text{ GeV}/c$  and thus TRD could identify pions and electrons separately. The TRD together with ITS and TPC measure the production of light and heavy meson resonances.

### **Time Of Flight (TOF) Detector**

The TOF detector [16] is a cylindrical gas detector of larger area and placed around TRD. It covers the pseudo-rapidity region of  $|\eta| < 0.9$  and have inner and outer radii of 3.7 m and 3.99 m respectively. It is comprising of Multi gap Resistive Plate Chamber (MRPC) which provides an excellent time resolution for TOF with a high efficiency. The TOF is dedicated for particle identification based on the measurement of time of flight ( $\tau_{TOF}$ ) of a particle passing through the detector. The particle mass is calculated using the time-of-flight. The particle momentum and track length are measured by the tracking detectors. The time resolution of  $\sim 100$  ps provides TOF to identify the ratios  $\pi/K$  up to 2.5 GeV/ $c$  or K/p up to 4 GeV/ $c$  respectively.

### **High-Momentum Particle Identification Detector (HMPID)**

The HMPID [17] is designed in a single arm consisting of seven Ring Imaging Cherenkov Counter (RICH) modules. The detector covers a pseudo-rapidity of  $|\eta| < 0.6$  and an azimuthal angle of  $\sim 58^\circ$ . This single arm geometry covers the 5% of the central barrel phase space and fulfils the criterion of low rate of high momentum particles in Pb-Pb collisions at the LHC energies. The performance of this detector is optimized to enhance the particle identification capabilities of ALICE by measuring  $\pi/k$  or k/p up to 3 GeV/ $c$  and 5 GeV/ $c$  respectively. The HMPID detector is also capable of measuring inclusive particle ratios and transverse-momentum spectra in the region where the pre-equilibrium stage of the nucleus-nucleus collisions is studied.

### **PHOton Spectrometer (PHOS)**

The PHOS [18] is a high resolution electromagnetic spectrometer which includes a highly segmented electromagnetic calorimeter made of lead-tungstate crystals and a Charged Particle Veto (CPV) detector comprising of a Multi-Wire Proportional Cham-

ber (MWPC) with cathode-pad readout. It covers a pseudo-rapidity range of  $|\eta| < 0.12$  and azimuthal angle of  $100^\circ$  and placed at the bottom of the ALICE set-up at a distance of 460 cm from the interaction point. PHOS can identify photon and the neutral meson ( $\pi^0$ ,  $\eta$ ) via their di-photon decay channel. In addition, it can also register charged and neutral hadrons: pions, kaon, protons, neutrons. The CPV is an essential part of the PHOS spectrometer and is placed in front of the PHOS for additional rejection of charged hadrons. The CPV detector is capable for measurement with localization accuracy of about 3 mm.

### **ElectroMagnetic CALorimeter (EMCAL)**

The technology of EMCAL [19] is based on a layered Pb- scintillator sampling calorimeter consisting of alternating layers of 1.44 mm of lead and 1.76 mm of polystyrene scintillator. The pseudo-rapidity coverage of this detector is  $|\eta| < 0.7$  in the azimuthal angle  $107^\circ$ . EMCAL provides an enhancement for the jet quenching measurement capabilities by ALICE. It improves the capabilities to measure the high momentum photons, neutral hadrons and electrons, with a particular importance for tagging the heavy flavour jets.

### **ALICE COsmic Ray DETector (ACORDE)**

ACORDE [20] is an array of plastic scintillator modules and placed on the top of ALICE L3 magnet. There are such 60 scintillator modules arranged on the three upper faces of the ALICE magnet. Each of these modules consists of two paddles ( $0.2 \times 2 m^2$ ) of plastic scintillators, arranged in a doublet configuration. The trigger hit is provided by the coincidence signal in a time window of 40 ns from the two scintillator paddles of each module. The Cosmic Ray Trigger (CRT) system acts a fast Level 0 (L0) trigger signal to the central trigger processor when an atmospheric muon hits the detector. The signal is used for the calibration and alignment of the TRD, TPC and ITS detectors. ACORDE along with these detectors, allows for performance study of high energy cosmic

rays through the detection of atmospheric muons. At least 17 GeV energy is needed for an atmospheric muon to reach the ALICE cavern.

In Table 2.2, the geometrical acceptance, position from the interaction point and the main function of different central barrel detectors are reported.

Table 2.2: Summary of ALICE central barrel detectors [10].

Detector	Acceptance		Position (cm)	main purpose
	$\eta$	$\phi$		
ITS layer 1,2 (SPD)	$ \eta  < 2.0$	full	$r = 3.9$	tracking, vertex
	$ \eta  < 1.4$	full	$r = 7.6$	tracking, vertex
ITS layer 3,4 (SDD)	$ \eta  < 0.9$	full	$r = 15.0$	tracking,PID
	$ \eta  < 0.9$	full	$r = 23.9$	tracking,PID
ITS layer 5,6 (SSD)	$ \eta  < 1.0$	full	$r = 38.0$	tracking,PID
	$ \eta  < 1.0$	full	$r = 43.0$	tracking,PID
TPC	$ \eta  < 0.9$	full	$85 < r < 247$	tracking,PID
TRD	$ \eta  < 0.8$	full	$290 < r < 386$	tracking, $e^\pm$
TOF	$ \eta  < 0.9$	full	$370 < r < 399$	PID
PHOS	$ \eta  < 0.12$	$220^\circ < \phi < 320^\circ$	$460 < r < 478$	photons
EMCal	$ \eta  < 0.7$	$80^\circ < \phi < 187^\circ$	$430 < r < 455$	photons and jets
HMPID	$ \eta  < 0.6$	$1^\circ < \phi < 59^\circ$	$r = 490$	PID
ACORDE	$ \eta  < 1.3$	$30^\circ < \phi < 150^\circ$	$r = 850$	cosmic

## 2.2.4 Global Detectors

### Photon Multiplicity Detector (PMD)

The PMD [21] is a preshower detector where granularity is optimized with low occupancy and high efficiency to detect photons. It is placed at a distance of 3.67 m from the interaction point (IP) and located in the opposite side (side-A) of the Muon Spectrometer. The detector has two planes and is made of several of honeycomb shaped gaseous proportional chambers. One of the planes is for Charged Particle Veto (CPV) and other for preshower detection. It allows the study of event shape and fluctuations by measuring the multiplicity and spatial distributions ( $\eta - \phi$ ) of photons in the for-

ward pseudo-rapidity ( $2.3 < \eta < 3.5$ ). The preshower signal of this detector helps in estimating the transverse electromagnetic energy.

### **Forward Multiplicity Detector (FMD)**

The FMD [22] is consisted of 5 ring counters equipped with total 51200 silicon strip channels. The FMD together with ITS provide a precise measurement of charged particle multiplicity distribution over a wide pseudo-rapidity interval ( $-3.4 < \eta < -1.7$  and  $1.7 < \eta < 5$ ). The electronics of FMD is the integrated preamplifiers with multiplexed readout. A readout time of  $\approx 13 \mu\text{s}$  allows it to participate in the ALICE trigger hierarchy at L2 level and higher. The azimuthal segmentation of FMD allows to study the multiplicity fluctuations and flow measurement.

### **V0 Detector**

The V0 detector [22] consists of 2 arrays, each of them contains 32 counters (scintillator material with embedded Wave Length Shifting Fibers) placed asymmetrically on each sides of the IP. The detector array installed in side-A is called V0A and in side-C is called V0C respectively. The V0A is located at a distance of 330 cm from IP and covers a pseudo-rapidity range of  $2.8 > \eta > 5.1$  while V0C is at a distance of 90 cm from IP and covers  $-3.7 < \eta < -1.7$ . The V0 detector has versatile functions. By measuring the time of flight difference between V0A and V0C, the system can reject the background events arising from beam-gas interaction. It provides minimum-bias trigger (MB) for the central barrel detectors. The V0 system can estimate the centrality of a heavy-ion collision by summing up the energy deposited in the two V0 disks. The sum of total energy scales directly with the number of primary particles generated in the collision. V0 also participates to control the luminosity. It provides a validation signal for the muon trigger to filter background in pp collision mode.

## T0 Detector

The T0 detector [22] consists of two arrays of quartz Cherenkov counters keeping the IP in-between. The array located in side-A is called T0A and the other located at side-C is called T0C. T0A is positioned at a distance of 3.6 m from IP and covers pseudo-rapidity range of  $4.5 < \eta < 5$  while T0C is kept at a distance of 70 cm from IP with a pseudo-rapidity coverage of  $-3.3 < \eta < -2.9$ . Both the T0 arrays are placed as close to the beam pipe as possible to maximize triggering efficiency according to the transverse direction. The detector provides fast signals to the ALICE L0 trigger. This detector can determine the vertex position with an accuracy of  $\pm 1.5$  cm with 50 ps time resolution. In addition, it has an excellent capability to reject events from beam-gas interactions.

## Zero Degree Calorimeter (ZDC)

ALICE has two sets of ZDCs [23]. The ZDC consists of two identical hadronic calorimeters. The ZDCs are located on both sides of the IP at a distance of  $\sim 116$  m. The insertion of ZDCs allows distance between beam pipes only  $\sim 8$  cm. The ZDC detects the energy of the spectator nucleons and hence able to calculate the number of spectator nucleons (nucleons which are not taking part in A-A collisions) by measuring the energy deposited in the detector for nucleus-nucleus collisions. This ZDC system is used for the centrality estimation and determination of the reaction plane as well.

### 2.2.5 The ALICE Muon Spectrometer (MS)

The goal of the ALICE forward Muon Spectrometer (MS) is to study the open heavy flavours (B & D) and quarkonia ( $J/\Psi$ ,  $\Psi'$  and  $\Upsilon(1S)$ ,  $\Upsilon(2S)$  and  $\Upsilon(1S)$ ) production via the muonic channel in pp, pA and AA collisions. These open heavy flavours and quarkonia production could be studied as a function of charged particle multiplicity and centrality in p-p and A-A collisions respectively using the ALICE central barrel detec-



tors. It is located in the negative Z-direction of the ALICE detector. The spectrometer acceptance is in the pseudo-rapidity range  $-4 < \eta < -2.5$  and in polar angle range  $170^\circ < \theta < 178^\circ$  over the full azimuthal ( $360^\circ$ ) coverage. The uniqueness of this spectrometer is to measure the quarkonia resonances at almost zero transverse momentum ( $p_T$ ). The invariant mass resolution is  $\sim 100 \text{ MeV}/c^2$  for upsilon ( $\Upsilon$ ) and in the order of  $70 \text{ MeV}/c^2$  for J/Psi ( $J/\Psi$ ) region. These values are good enough to resolve and measure the individual five quarkonia resonance states. The MS is comprised of front absorber, a dipole magnet, a tracking system, a muon filter and a trigger system. The layout of the Muon Spectrometer (MS) is shown in Fig. 2.6.

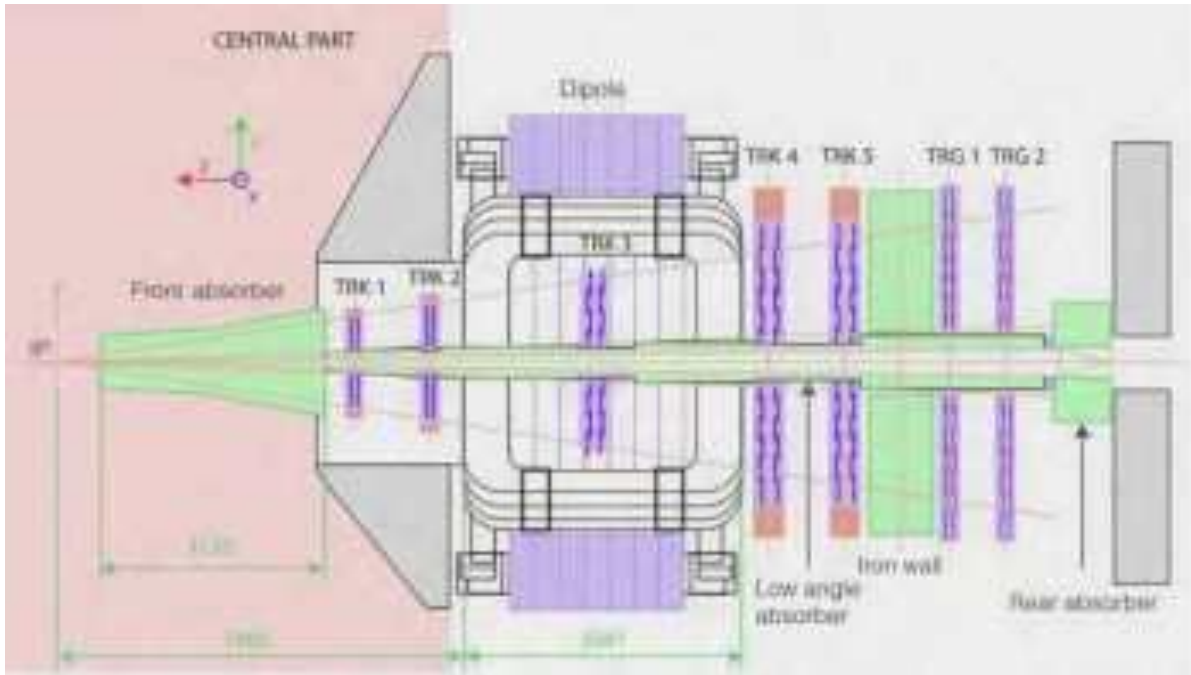


Figure 2.6: The Layout of Muon Spectrometer of ALICE.

### Front Absorber:

The front absorber is placed at a distance of 90 cm from the interaction point (IP) and extended upto 4.13 m before the tracking system starts. The layout of the front absorber is shown in Fig 2.7. It is made up of several layers of carbon, concrete, tungsten, polyethylene and lead. It reduces the initial flux of primary hadrons produced in heavy-ion



collisions by a factor of 100 and decreases muon background decaying from the primary charged pion and kaon by limiting the free path for  $\pi, K \rightarrow \mu$  in secondary collisions. A minimum distance of 90 cm between the absorber and the IP is maintained to avoid the deterioration of physics performance of ALICE central barrel detectors. The design criteria of front absorber is crucial since the invariant mass resolution of the detected particles in the muon spectrometer becomes worsen due to the straggling and multiple scattering of particles in the absorber material. So, the design and material composition of the absorber are optimised to ensure good shielding capabilities. This design criteria imposes the material budget ( $\sim 10\lambda_{int}$  and  $\sim 60X_0$ ) optimization and requires the low-Z material towards the IP and high-Z shielding material towards the tracking chambers of MS.

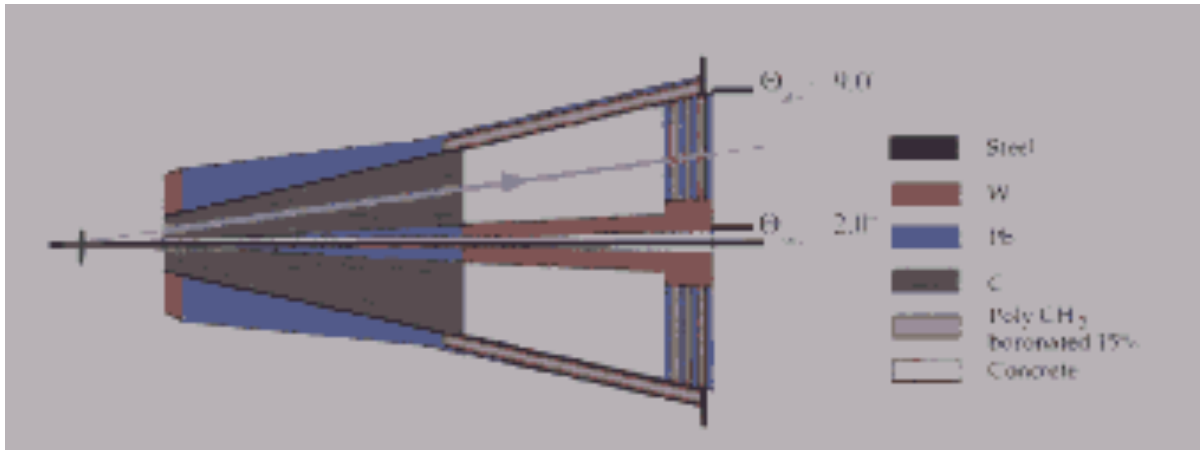


Figure 2.7: The Layout of front absorber of the Muon Spectrometer [9].

### Dipole Magnet:

The dipole magnet [24] is placed at a distance of 7m from the IP and is shown in Fig. 2.8. This is the largest warm dipole magnet with a size of 5 m long, 6.6 m wide and 8.6 m high. It has a free gap of 3.5 m between the poles and weight of 900 tons [25]. This dipole has a nominal magnetic field of 0.7 T and a field integral  $\int |B| dz \sim 3$  T-m between the IP and muon filter. This magnetic field is in a horizontal plane (x-z) perpendicular to

the beam direction. The magnetic field defines a bending plane (zy plane) by providing the bending power to measure the momentum of muons in the tracking chambers. It provides a non-bending plane (x-z plane) also.



Figure 2.8: The Dipole Magnet of the Muon Spectrometer.

### Tracking System:

The Muon Tracking system [9] is comprised of five tracking stations, each of them consists of two detection planes. The first two tracking stations are placed before the dipole magnet and at a distance of 5.4 m and 6.8 m respectively from the IP. The third tracking station is inside the dipole magnet and at a distance of 9.7 m from the IP. The last two tracking stations are placed after the dipole magnet and at a distance of 12.6 m and 14.2 m respectively from the IP.

The tracking chambers are designed to study the various resonant states of  $\Upsilon$ . A momentum resolution about 1% is needed to achieve the required invariant mass resolution of  $\sim 100 \text{ MeV}/c^2$  to resolve the  $\Upsilon$ ,  $\Upsilon'$  and  $\Upsilon''$  resonances. This can be achieved by a very good spatial resolution of about  $100 \mu\text{m}$  for the tracking chambers in the bending plane. The tracking chambers are designed to operate for a maximum hit density of  $\sim$

$5 \times 10^{-2} \text{ cm}^{-2}$  expected from a central Pb-Pb collision. In addition, the tracking chambers have high detection efficiency ( $\geq 95\%$ ) for the charged particles and low sensitivity to photon and neutron background. Each tracking station is basically a 5 mm drift multi-wire proportional chamber (MWPC) with bi-cathode pad readout (cathode pad chambers, CPC). The material budget of each chamber is restricted below 3% radiation length to limit the multiple scattering effects and hence to avoid any degradation in mass resolution. For much higher flux of particles closer to the IP, the station 1 and 2 are required to be small in size and of quadrant type with fine-granularity segmentation in the readout pads. While stations 3, 4 and 5 are larger in size and chosen for modular design consisting of rectangular CPC called slat. Figure. 2.9 shows the quadrant (left) and slat (right) type geometry of detectors for station 2 and station 4 & 5 respectively. Since the hit density of particles to the tracking chambers depend on the position of stations and pseudo-rapidity, different pad densities are present with the distance from the beam-pipe. The muon tracking system consists of about  $10^6$  readout channels to limit the occupation rate to a maximum of 5% for the full set of chambers.



Figure 2.9: The quadrant type geometry of station 2 (left) and slat type geometry of station 4 and 5 (right).

The arrangement of readout of all the stations are known as Front End Electronics (FEE). This FEE is based on a 16 channel MANAS (Multiplexed ANALogic Signal processor) chip. The Indian chip MANAS was designed by SINP, kolkata and fabricated at SCL, Chandigarh. Four such MANAS chips are mounted on an electronic board

named as MANas NUmerical (MANU) card where a 12 bit ADC is present named as Muon Arm Readout Chip(MARC). The functionalities of the MARC is for signal digitization and zero suppression of data. The noise level of the full electronics chain is  $\sim 1000$  electrons. The data of 1.08 million channels of the full tracking system are read by  $\sim 17000$  MANU cards. The data is transferred from the MANU card to the Cluster ReadOut Concentrator Unit System (CROCUS) via the Protocol for the ALICE Tracking CHamber (PATCH) buses. Each tracking chamber is connected to two CROCUS which concentrate, format the data and transfer them to the DAQ. In Fig. 2.10, the readout architecture of tracking system of MS is shown. **The second tracking system is being designed, fabricated, installed and commissioned by MUON Collaborators of India (SINP, Kolkata and AMU, Aligarh).** The second tracking system consists of total eight quadrants which are CPC detectors.

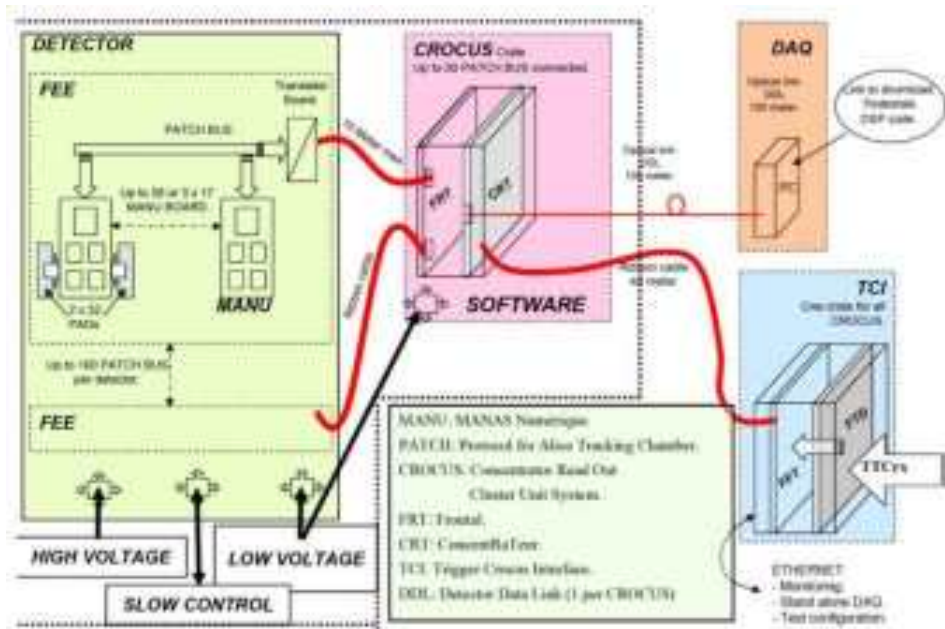


Figure 2.10: The schematic of read out for the Tracking System of the ALICE Muon Spectrometer [26].

### Cathode Pad Chamber (CPC):

Cathode pad chamber (CPC) is a multiwire proportional chamber. It has two cathode planes symmetrically separated (2.5 mm) from the anode wire plane. Each cathode plane is divided into sensitive pads of different sizes, which are used to locate the position of a particle traversing through the detector. A gas mixture of Ar (80%) and  $\text{CO}_2$  (20%) is used in CPC and it is operated at atmospheric pressure. When a charged particle travels through the active gas volume of the chamber, it creates electron-ion pairs by the ionization process. These produced primary electrons are accelerated by the action of electric field towards the nearest anode wire and avalanche takes place. The induced charges are accumulated in cathode pad and the corresponding pad coordinates are used to measure the position (x,y) of the particle passing through the chamber. The basic geometry of Cathode Pad Chamber is shown in Fig. 2.11.

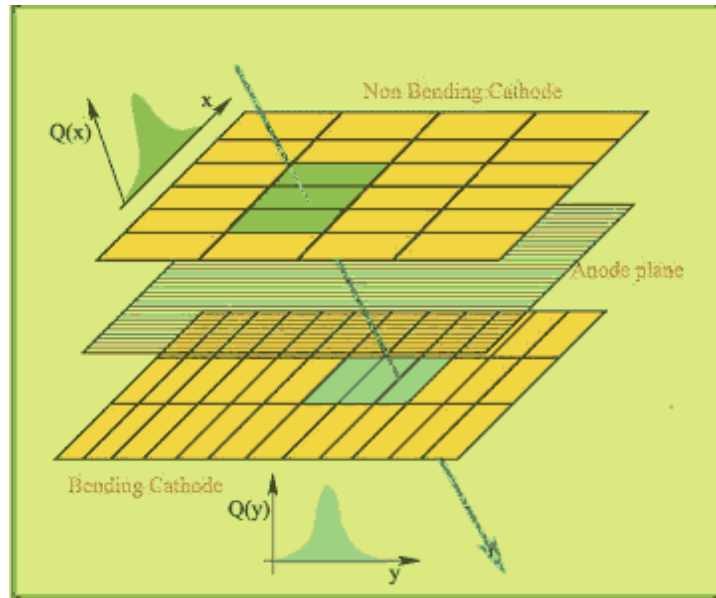


Figure 2.11: The basic geometry of Cathode Pad Chamber [27].

**Muon Filter:**

An iron wall of thickness 1.2 m is placed between the fifth tracking station and the first trigger station. The thickness of the muon filter corresponds to 7.2 interaction lengths ( $\lambda_{int}$ ). It reduces the background on the trigger stations by absorbing the punch-through hadrons (secondary hadrons produced by the primary hadrons in the detector materials) and muons having low momentum ( $\leq 4 \text{ GeV}/c$ ) from reaching the trigger system. Thus, this muon filter enhances the performance of trigger stations.

**Trigger System**

The Muon Trigger System consists of two trigger stations (MT1 & MT2) placed at distances of 16 m and 17 m respectively from the IP and it is located downstream of the muon filter. The Muon Trigger stations are operated in streamer mode and deliver information to the central trigger processors for the generation of the ALICE level 0 (L0) trigger providing the track parameters ( $p_x$ ,  $p_y$ ,  $p_z$ ) for the tracks formed in the Trigger stations. A schematic layout of the trigger system is shown in the left panel of Fig. 2.12. The design of this trigger system reduces the hadronic component background which punch through the front absorber by requiring the matching condition of muon tracks reconstructed in muon tracker and the hits in two trigger stations. Different type of muon triggers are defined at hardware level and improves the signal to background ratio. The active areas covered by the first and second trigger stations are  $6.12 \times 5.44 \text{ m}^2$  and  $6.50 \times 5.78 \text{ m}^2$  respectively. The larger dimension of the detection planes is along the bending plane (vertical direction). The acceptance of the trigger system's bending plane ranges from  $2^\circ$  to  $10^\circ$  while for the non-bending plane, it is  $2^\circ$  to  $9^\circ$ . Each trigger station is made of two detection planes perpendicular to the beam direction. Each plane is equipped with 18 single-gap Resistive Plate Chambers (RPC) separated by 15 cm and a total of 72 number of RPCs are there in the whole system. A schematic layout of the RPC is shown in the right panel of Fig. 2.12. RPC is a detector of large area and made

up of Bakelite electrodes of high resistivity ( $\sim 3\text{-}9 \times 10^9 \Omega\text{m}$ ). It is capable of having good position ( $< 1 \text{ cm}$ ) and time ( $< 2 \text{ ns}$ ) resolution.

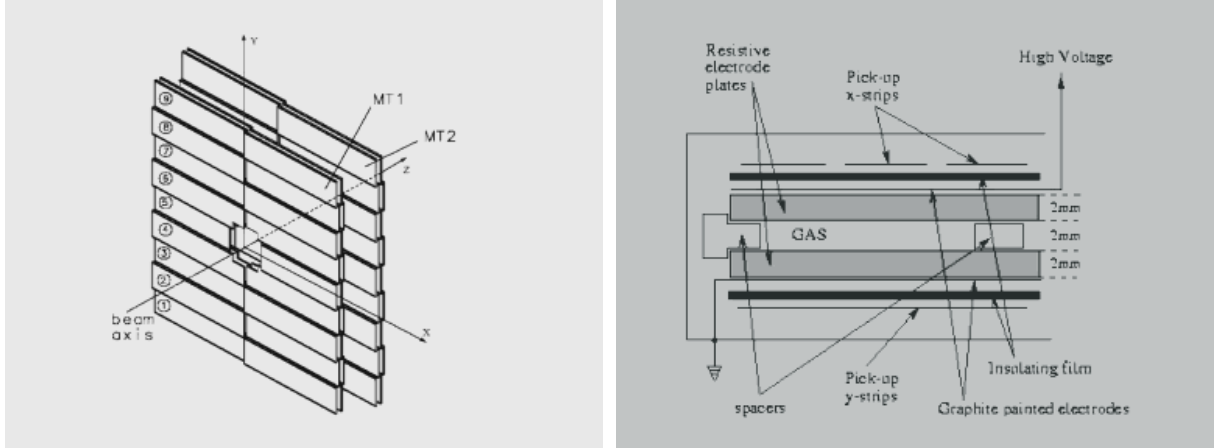


Figure 2.12: The schematic layout of the muon trigger system (left) and Resistive Plate Chamber (right).

The RPCs are gaseous detector with planar geometry, where the active gas material is flushed through the resistive electrode plates. These detectors are positioned on a mechanical structure with readout strips to provide a bi-dimensional information and the design allows to avoid any inactive zones. These readout strips collect the signals which are connected to the Front-End Electronics (FEE) consisting of a leading-edge discriminator and a shaper. A deviation is occurred due to the dipole magnetic field of muon spectrometer. The horizontal strips measure the position along y-direction (bending plane) and the vertical strips measure the position along x-direction (non-bending plane). The signals from FEE are sent to the local trigger electronics. The whole trigger system is divided into 234 detection areas where each of this is associated with a local trigger board.

### Muon Trigger decision

The muon trigger decision in the ALICE Muon Spectrometer is done using the RPC detectors of muon trigger system [28]. The trigger algorithm is performed in the electronic



level of four RPC detector planes following the track information obtained from trigger system. To define a track, both the bending and non-bending planes are required to be fired. The track deviation is computed in the bending plane while the non-bending plane is useful for background rejection. A particle of low  $p_T$  have large deviation and vice versa.

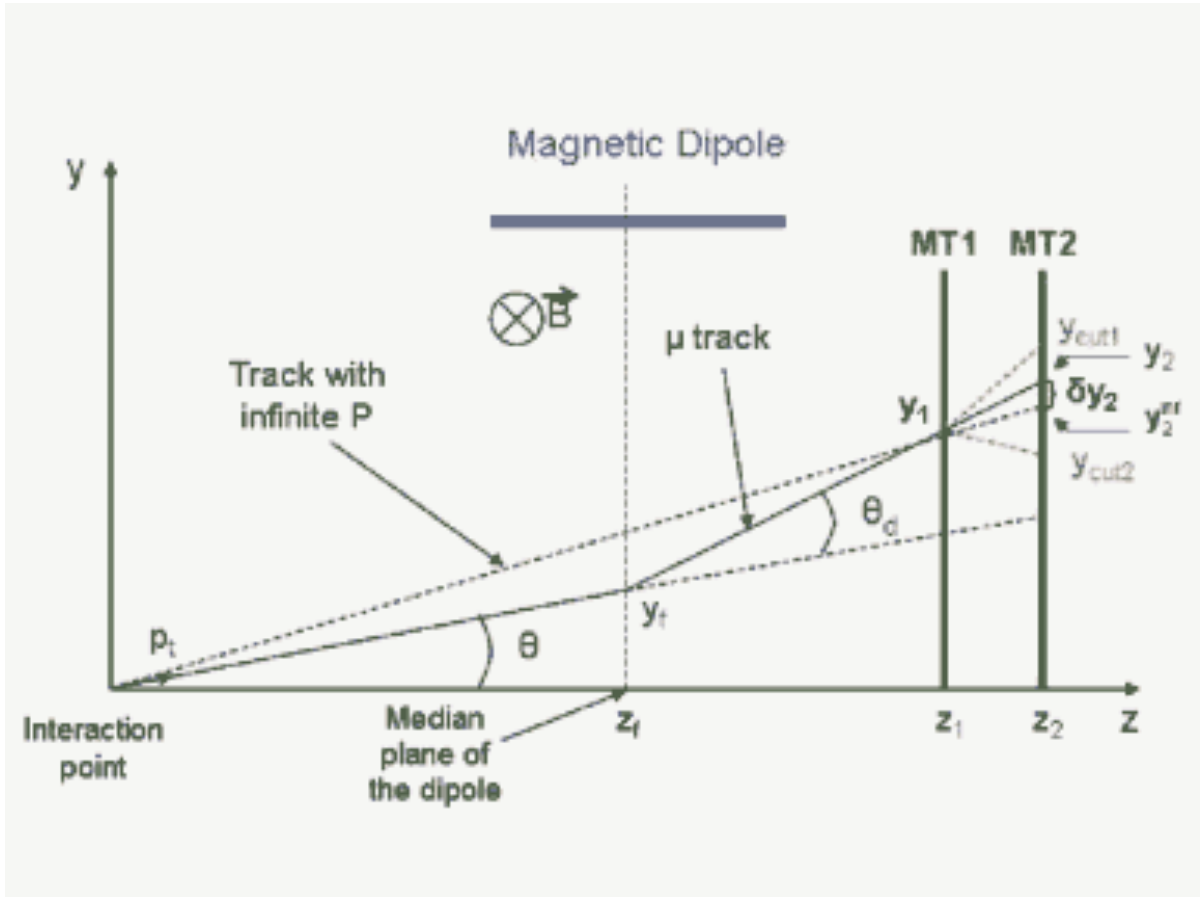


Figure 2.13: Sketch to calculate track transverse momentum by ALICE muon trigger system.

Fig. 2.13 shows the calculation of transverse momentum of the reconstructed muon tracks by ALICE muon trigger system. In Fig. 2.13,  $(y_1, z_1)$  and  $(y_2, z_2)$  are the position of the muon tracks at the first trigger station and second trigger station respectively. The coordinate of the dipole is  $(x_f, y_f, z_f)$ . The deviation in the y-plane (in second trigger station) is labelled as  $\delta y_2$ . Using these information, one can calculate the deviation ( $\theta_d$ )



of the track as:

$$\theta_d = \frac{1}{z_f} \left( \frac{z_1 y_2 - z_2 y_1}{z_2 - z_1} \right) \quad (2.1)$$

Under the small angle approximation, the transverse momentum ( $p_t$ ) can be calculated as,

$$p_t \simeq qLB \left( \frac{z_2 - z_1}{z_1} \right) \frac{\sqrt{x_f^2 + y_f^2}}{\delta y_2} \quad (2.2)$$

and

$$y_f = y_1 \frac{z_f}{z_1} - \delta y_2 \left( \frac{z_1 - z_f}{z_2 - z_1} \right) \quad (2.3)$$

Where B and L are the magnetic field and length of the dipole magnet respectively.

The muon trigger system uses a three-level electronics to fulfil the requirements of trigger decisions. First, local card receives information from the detector and take a decision within 250 ns to provide a “local trigger”. This “local trigger” can be a no trigger, a trigger for positive particle, a trigger for negative particle and a trigger without deviation. The information of the local cards are then collected by the regional cards to compute one candidate track, or two or more candidate tracks with like-sign or unlike-sign. Finally, the information of the regional cards are stored by the global card and can provide the signals of five triggers which are then further sent to the Central Trigger Processor (CTP).

The five possible muon trigger signals for the CTP are mentioned below:

- Single muon above low (high)  $p_t$  cut: Muon Single Low (High).
- Like-sign di-muon of low  $p_t$  cut: PairLikeLPt
- Like-sign di-muon of high  $p_t$  cut: PairLikeHPt
- Unlike-sign di-muon of low  $p_t$  cut: PairUnlikeLPt
- Unlike-sign di-muon of high  $p_t$  cut: PairUnlikeHPt

Muon trigger system uses two threshold values for low and high  $p_t$ -cut. The threshold for low  $p_t$  muon trigger is 1 (or 0.5) GeV/ $c$  and for high  $p_t$  muon trigger is 4 GeV/ $c$ . Since, the detector efficiency is not an ideal step function, these  $p_t$  cuts for the triggers are not sharp in practice. A  $p_t$ -cut of 0.5 GeV/ $c$  is given to define All  $p_t$  which corresponds to the maximum deviation that can be measured by the local electronics.

### 2.2.6 The ALICE upgrade for Run 3

One of the main focus to design ALICE at the LHC is to study the QGP matter created in high energy heavy-ion collisions along with in-depth research of several physics programs in proton-proton and proton-ion collisions. The ALICE upgrade strategy beyond Long Shutdown 2 (LS2) is to collect the Pb-Pb data corresponding to integrated luminosity  $L_{int} = 13 \text{ nb}^{-1}$  which is almost 10 times higher than the ALICE Run 2. Near the end of the year 2018 during Run 2, ALICE has recorded the data samples in Pb-Pb collisions with  $L_{int} = 800 \mu\text{b}^{-1}$  [29]. During Run 3, ALICE targets for data collection in p-Pb collisions with  $L_{int} = 0.6 \text{ pb}^{-1}$  which was  $L_{int} = 25 \text{ nb}^{-1}$  during Run 2. However in pp collisions, it aims to operate with a maximum integrated luminosity  $L_{int} = 200 \text{ pb}^{-1}$  compared to  $L_{int} = 36 \text{ pb}^{-1}$  during Run 2 at  $\sqrt{s} = 13 \text{ TeV}$ . There is also plan for a short period run for O-O collisions at  $\sqrt{s} = 6.37 \text{ TeV}$  with  $L_{int} \sim 1 \text{ pb}^{-1}$  during Run 3 [8]. The ALICE upgrade programs will allow for collection and inspection of a large data volume in Pb-Pb and p-Pb collisions with continuous readout mode using ALICE detectors. This will enable an increase in data samples of about 100 and 1000 times more compared to the data collected with a minimum-bias trigger during Run 2 for Pb-Pb and p-Pb respectively. Hence, Run 3 will subsequently increase the statistical significance and allow more precision measurements. Few of the ALICE upgrade programs are described as following:

### Inner Tracking System (ITS)

The main tasks of ALICE ITS are to determine the interaction vertex, tracking and identifying the particles of low transverse momentum ( $p_T$ ), to measure the distance of closest approach (DCA) of charged particles with respect to the interaction vertex etc. For the upgrade of ITS, the first detection layer becomes nearer to the interaction vertex after the reduction of the beampipe diameter at the center of ALICE. This will improve the measurement of impact parameter ( $b$ ) resolution [30]. The use of Monolithic Active Pixel Sensors (MAPS) as readout in new ITS, reduces the material budget. This upgradation will significantly improve the tracking performance and the momentum resolution. This newly designed ITS is able to read data corresponding to collision rate of 100 kHz for Pb-Pb and 400 kHz for pp collisions which is capable by a factor of 2 higher than the ALICE Run 3 upgrade requirements.

### Muon Forward Tracker (MFT)

During Run 1 & Run 2, the ALICE physics program had various limitations. One of those are due to the multiple scattering of muon tracks by the front absorber. This results a complete smearing of the primary vertex. As a consequence, it was very difficult to reject the background muon coming from semi-muonic decays of pions and kaons (at low  $p_T$ ). The large uncertainty of interaction vertex determination also prevents the separation between prompt and non-prompt  $J/\psi$  production. One of the physics challenges is to differentiate between open charm and beauty component of open heavy flavour decay muon production.

The presence of Muon Forward Tracker (MFT) in ALICE Run 3 is expected to overcome the limitations as discussed above. The MFT is equipped with high resolution silicon pixel detector (jointly developed by ITS and MFT team) and is placed upstream of the front absorber. It covers the acceptance range of  $-3.6 < \eta < -2.5$  which slightly

reduces the acceptance of muon spectrometer (MS) [31]. The presence of MFT will significantly improve the vertexing capability ( $\sim \mu m$ ) of the muon spectrometer, which was in the order of cm at Run 2. The pointing accuracy of muon tracks with respect to the interaction vertex will enhance efficiently. This will be done by matching the extrapolated muon tracks from the tracking chambers placed downstream of the front absorber and finding the clusters in MFT. A detail description of the MFT detector will be discussed in chapter 5.

### **Readout upgrade of MS**

In ALICE Run 2, the Pb-Pb collision rate was 1 kHz. The basic unit of FEE of all five tracking stations of MS was 16 channel MANAS (Multiplexed ANALogic Signal processor) chip. In Run3, ALICE will operate in higher collision rates i.e. at 50 kHz for Pb-Pb collision and 200 kHz for p-Pb (pp) collision respectively. The FEE with MANAS chip is not compatible for this high luminosity beam ( $L = 6 \times 10^{27} cm^{-2} s^{-1}$ ). Therefore, the FEE of MS is re-designed and upgraded with new 32 channel SAMPA (Serialized Analogue-digital Multi Purpose ASIC) chip replacing MANAS. The ASIC (Application Specific Integrated Circuit) chip SAMPA will comply with this high rate collision. The first prototype design of ASIC SAMPA was from Electrical Engineering-Polytechnical School, University of São Paulo, Brazil. The SAMPA chip can read detector signal in both the modes: external trigger and continuous self-trigger. The SAMPA chip contains a common digital signal processor to provide various signal filtering operations and improves the ability of data compression.

The parameters of the SAMPA chips for the Muon Chambers(MCH) are following [32]:

- 10-bit ADC resolution.
- 10 MHz sampling rate.
- shaping time of 330 ns.

- noise level below 2000 electrons (large pads) and 1000 electrons (small pads).

The new Dual SAMPA (DS) boards replace the previous MANU boards. Each DS board contains two such SAMPA chip and each board is connected to 64 readout channels of the tracking detector. The upgraded FEE will be connected via GBT (Gigabit Transceiver) optical links to the common readout unit (CRU). The data flow will be reduced by the online computing system before sending to the offline system. The new FEE for second tracking station of MS is designed, fabricated, and installed in ALICE by MUON group of SINP, Kolkata.

The upgrade strategy for Run 3 implies for no need of fast, hardware-based,  $p_T$ -dependent muon trigger signal. All muon detectors could read for each minimum bias trigger with the goal of maximising the muon physics potential and the data can be used in offline for further hadron rejection. The corresponding muon trigger system is called as the Muon Identifier (MID).

### **Online-Offline ( $O^2$ ) computing system**

$O^2$  is a major upgraded ALICE Online-Offline computing system which has been deployed during LS2. The Online-Offline ( $O^2$ ) computing system will face more challenges during Run 3 as the raw data shipped from the detector to online farm in triggerless continuous mode with a rate of  $\sim 3.3$  TB/s for heavy-ion runs[33]. A compression (by a factor of 6.6) of data volume is done by baseline correction and zero-suppression for both the collision rate 50 kHz (Pb–Pb) and 200 kHz (pp and p–Pb ) respectively. Further compression of the data with a factor of 5.5 is done by the online calibration and reconstruction. The reconstructed data goes to the data storage only [29]. The major role of the  $O^2$  system is to perform detector calibration and data reconstruction online in parallel with the storage of data while replacing the original raw data with compressed data.



---

# Bibliography

---

- [1] O.S. Bruning, P. Collier, P. Lebrun, S. Myers, R. Ostojic, J. Poole et al., *LHC Design Report Vol.1: The LHC Main Ring*, . [41](#)
- [2] O. Buning, P. Collier, P. Lebrun, S. Myers, R. Ostojic, J. Poole et al., *LHC Design Report. 2. The LHC infrastructure and general services*, .
- [3] M. Benedikt, P. Collier, V. Mertens, J. Poole and K. Schindl, *LHC Design Report. 3. The LHC injector chain*, . [41](#)
- [4] *The ALICE experiment at the CERN LHC*, *Journal of Instrumentation* **3** (2008) [S08002](#). [42](#)
- [5] *The CMS experiment at the CERN LHC*, *Journal of Instrumentation* **3** (2008) [S08004](#). [42](#)
- [6] *The LHCb detector at the LHC*, *Journal of Instrumentation* **3** (2008) [S08005](#). [42](#)
- [7] *The ATLAS experiment at the CERN large hadron collider*, *Journal of Instrumentation* **3** (2008) [S08003](#). [42](#)
- [8] ALICE collaboration, *ALICE physics projections for a short oxygen-beam run at the LHC*, . [42](#), [44](#), [66](#)
- [9] ALICE collaboration, *The ALICE experiment at the CERN LHC*, *JINST* **3** (2008) [S08002](#). [xix](#), [44](#), [57](#), [58](#)

- [10] W. Shaikh, *BOTTOMONIUM STUDIES AT LHC ENERGY USING ALICE MUON SPECTROMETER*, Ph.D. thesis, HBNI, Mumbai, 11, 2020. [xxxiii](#), [44](#), [53](#)
- [11] L.B. et al., *Definition of the ALICE coordinate system and basic rules for sub-detector components numbering*, *ALICE-INT* (2003) 038. [45](#)
- [12] ALICE collaboration, *Definition of the ALICE Coordinate System and Basic Rules for Sub- detector Components Numbering*, . [xix](#), [46](#)
- [13] ALICE collaboration, *ALICE technical design report of the inner tracking system (ITS)*, . [48](#)
- [14] ALICE collaboration, *ALICE: Technical design report of the time projection chamber*, . [49](#)
- [15] ALICE collaboration, *ALICE transition-radiation detector: Technical Design Report*, . [50](#)
- [16] ALICE collaboration, *ALICE technical design report of the time-of-flight system (TOF)*, . [51](#)
- [17] ALICE collaboration, *ALICE technical design report: Detector for high momentum PID*, . [51](#)
- [18] ALICE collaboration, *ALICE technical design report of the photon spectrometer (PHOS)*, . [51](#)
- [19] ALICE collaboration, *ALICE electromagnetic calorimeter technical design report*, . [52](#)
- [20] A. Fernandez, S. Kartal and C. Pagliarone, *ACORDE a cosmic ray detector for ALICE*, in *Summer School and Conference on New Trends in High-Energy Physics: Experiment, Phenomenology, Theory*, 12, 2006 [[physics/0612051](#)]. [52](#)



- [21] ALICE collaboration, *ALICE technical design report: Photon multiplicity detector (PMD)*, . 53
- [22] ALICE collaboration, *ALICE technical design report on forward detectors: FMD, T0 and V0*, . 54, 55
- [23] ALICE collaboration, *ALICE technical design report of the zero degree calorimeter (ZDC)*, . 55
- [24] D. Swoboda, C. De Almeida, A. Meynet, H. Taureg and A. Tournaire, *Results from the ALICE Dipole Magnet Commissioning*, *IEEE Trans. Appl. Supercond.* **16** (2006) 1696. 57
- [25] X. Zhang, *Study of Heavy Flavours from Muons Measured with the ALICE Detector in Proton-Proton and Heavy-Ion Collisions at the CERN-LHC*, Ph.D. thesis, Clermont-Ferrand U., 2012. 57
- [26] ALICE collaboration, *The electronics of ALICE dimuon tracking chambers*, in *Topical Workshop on Electronics for Particle physics*, pp. 242–246, 2008. xix, 60
- [27] <http://www.saha.ac.in/web/henppd-introduction-detector-working>. xix, 61
- [28] P. Dupieux, F. Guerin, F. Yermia, P. Rosnet and E. Vercellin, *ALICE Muon Trigger Performance*, . 63
- [29] L. Valencia Palomo, *The ALICE experiment upgrades for LHC Run 3 and beyond: contributions from mexican groups*, *J. Phys. Conf. Ser.* **912** (2017) 012023. 66, 69
- [30] ALICE collaboration, *Technical Design Report for the Upgrade of the ALICE Inner Tracking System*, *J. Phys. G* **41** (2014) 087002. 67
- [31] ALICE collaboration, *Technical Design Report for the Muon Forward Tracker*, . 68

- [32] ALICE collaboration, P. Antonioli, A. Kluge and W. Riegler, eds., *Upgrade of the ALICE Readout & Trigger System*, . [68](#)
- [33] P. Buncic, M. Krzewicki and P. Vande Vyvre, *Technical Design Report for the Upgrade of the Online-Offline Computing System*, . [69](#)

## CHAPTER 3

---

# Experimental measurements of Heavy Flavour decay Muon production in pp collisions at $\sqrt{s} = 13$ TeV with ALICE

---

In this chapter, the new measurement of Heavy Flavour decay Muon (HFM) production cross-section at forward rapidity in proton-proton (pp) collisions at  $\sqrt{s} = 13$  TeV with the ALICE detector at the LHC has been described. The measurements of HFM production in pp collisions at  $\sqrt{s} = 13$  TeV are presented as a function of transverse momentum ( $p_T$ ) and rapidity ( $y$ ) within the full acceptance ( $-4 < \eta < -2.5$ ) of ALICE muon spectrometer (MS). The measurement of  $p_T$ -differential production cross-section of HFM is also performed at five different pseudo-rapidity intervals in the range  $-4 < \eta < -2.5$ . This HFM analysis is carried out by using the data sample (LHC16k) collected in the Run 2 period of 2016. The results are obtained with high statistics data compared to the Run 1 measurements for pp collisions at  $\sqrt{s} = 2.76$  TeV [1] and 7 TeV [2] and at  $\sqrt{s} = 5.02$  TeV of Run 2 [3]. This high statistics allows to measure the production cross-section of HFM at an extended  $p_T$ -range upto 30 GeV/ $c$ . It is to be mentioned that the previous measurements of HFM in pp collisions are done at  $\sqrt{s} = 2.76$  TeV upto 10 GeV/ $c$ , at  $\sqrt{s} = 5.02$  TeV upto 20 GeV/ $c$  and at  $\sqrt{s} = 7$  TeV upto 12 GeV/ $c$  respectively. The new

measurements of the production cross-sections of HFM at  $\sqrt{s} = 13$  TeV are compared with the FONLL calculation [4]. The measured  $p_T$ -differential production cross-section of HFM at  $\sqrt{s} = 13$  TeV is compared with the previous results measured by ALICE at different center-of-mass energies.

### 3.1 Data Samples

ALICE collected data samples in pp collisions during the Run 2 period from the year of 2015 to 2018. This analysis is performed taking the data sample LHC16k (2016) based on AODs (Analysis Object Data) with muon pass1 reconstruction. The analysis is carried out with the minimum-bias (MB) trigger and two muon triggers having  $p_T$  threshold of 1 GeV/ $c$  (Muon Single Low, MSL) and 4 GeV/ $c$  (Muon Single High, MSH) respectively. The muon spectrometer (MS), SPD and V0 & T0 sub-detectors of ALICE participated during the collection of data used for this analysis. The SPD is used for the primary vertex reconstruction while the MS is used for the reconstruction of muon tracks. The V0 and T0 are used for the luminosity measurements. The 169 number of good runs of LHC16k data set are finalised for this analysis after Quality Assurance (QA). This QA checking is done taking the information from Run Condition Table (RCT) of ALICE Grid monitoring toolset MonALISA (Monitoring Agents using a Large Integrated Services Architecture):

The following are the good runs of LHC16k (pass1, AOD) data set:

258537 258499 258498 258477 258456 258454 258452 258426 258393 258391 258388 258387  
258359 258336 258332 258307 258306 258303 258302 258301 258299 258280 258278 258274  
258273 258271 258270 258258 258257 258256 258204 258203 258202 258197 258178 258117  
258114 258113 258109 258108 258107 258063 258062 258060 258059 258049 258048 258045  
258042 258041 258039 258019 258017 258014 258012 258008 257989 257986 257979 257963  
257960 257958 257957 257939 257937 257936 257932 257912 257901 257893 257892 257737  
257735 257734 257733 257727 257725 257724 257697 257694 257688 257687 257685 257684

257682 257644 257642 257636 257635 257632 257630 257606 257605 257604 257601 257595  
257594 257592 257590 257588 257587 257566 257564 257563 257562 257561 257560 257541  
257540 257531 257530 257492 257491 257490 257488 257487 257474 257468 257457 257433  
257364 257358 257330 257322 257320 257318 257260 257224 257095 257092 257086 257084  
257083 257082 257080 257077 257071 257026 257021 257012 257011 256944 256942 256941  
256697 256695 256694 256691 256684 256681 256677 256676 256658 256620 256619 256591  
256567 256565 256564 256561 256560 256557 256556 256554 256552 256512 256510 256506  
256504

## 3.2 Event and track selection cuts

Various event and track selection cuts are applied to obtain the inclusive single muon. These selection cuts are standard cuts for the single muon analysis and used in the previous measurements. These selections cuts are mentioned below:

### 1. Event Cuts:

- Physics selection
- z-component of vertex selection within  $|V_z| < 10cm$

### 2. Track Cuts:

- Pseudo-rapidity :  $-4.0 < \eta < -2.5$
- Theta :  $170^\circ < \theta < 178^\circ$
- track-trigger matching
- pDca :  $6\sigma$

An offline event selection is applied to reject any possible background events after the online event selection at the hardware level. This offline physics event selection is known as Physics selection (PS). This PS reproduces the online trigger conditions at the offline level in order

to reject background events arising from incorrect trigger decisions at hardware level due to the noise of the front-end electronics. This Physics selection also rejects beam-gas induced background events by using the event leading time distribution in V0A and V0C detectors respectively. The physics selection defines the minimum-bias trigger condition at the software level as following:

$$(FO \geq 2) \mid (FO \geq 1 \ \&(V0A \mid V0C)) \mid (V0A \ \& \ V0C) \quad (3.1)$$

where, FO is the number of SPD hits, V0A (V0C) corresponds to at least one hit in V0A (V0C) detector and the leading time is located in the beam-beam interaction window of V0A (V0C). The physics selected events are those events which pass the offline software trigger following the Eq. 3.1.

The physics selection condition can reject part of the events without reconstructed primary vertex. In our analysis, the reconstruction of muon tracks should be related to the primary vertex. The heavy flavour decay muons are produced at the position of the interaction point (about few hundred  $\mu\text{m}$ ). So, an event with a muon tracks without reconstruction of primary vertex is rejected in our analysis. This rejection is done when the number of primary vertex contributors are larger than zero. The position of the primary vertex is determined using the SPD tracklets of all the reconstructed tracks in the central barrel detector. Moreover, an additional cut ( $|V_z| \leq 10$  cm) is applied in the position of the reconstructed primary vertex along the beam-axis with respect to the center (0,0,0) of the ALICE co-ordinate system.

The muon tracks are reconstructed within the geometrical acceptance of ALICE muon spectrometer with polar angle  $170^\circ < \theta < 178^\circ$  and pseudo-rapidity coverage  $-4 < \eta < -2.5$ . There should be a matching condition with the track candidate in the tracking system and the tracklets reconstructed in the trigger stations. The track-trigger matching not only rejects the punch-through hadrons, but also removes the muon of low momentum ( $< 4$  GeV/ $c$ ). A data sample containing muon-triggered events requires the coincidence of the minimum-bias condition as described in Eq. 3.1 and at least a muon track in the muon trigger system. In this analysis for single muons, the MB trigger condition requires the coincidence of the signals in the two V0 detectors (V0A and V0C). Two single muon trigger classes based on the  $p_T$ -threshold

has been used: Muon Single Low (MSL) and Muon Single High (MSH). The MSL (MSH) is with a  $p_T$ -threshold above 1 (4) GeV/ $c$ . These two single muon trigger classes are named as CMSL-B-NOPF-MUFAST (MSL) and CMSH-B-NOPF-MUFAST (MSH) respectively whereas the MB trigger for single muon is named as CINT7-B-NOPF-MUFAST (CINT). Finally, an additional  $p \times \text{DCA}$  cut of  $6\sigma$  is applied to remove the beam-gas induced background. The Distance of Closest Approach (DCA) is the distance between the extrapolated muon track and the interaction vertex in a plane perpendicular to the beam direction and passing through the interaction vertex.  $p$  is the momentum of the reconstructed muon track.

### 3.2.1 Subtraction of hadronic and beam induced background

In order to study the contribution of muons from various background sources, a realistic Monte-Carlo (MC) simulations with the full response of detector geometry using GEANT3 is done. In Figure. 3.1, the transverse momentum ( $p_T$ ) distribution of muons from different sources using MC simulation based on PYTHIA are shown. The muons from various sources are following:

- $\mu \leftarrow$  beauty (*red*) and  $\mu \leftarrow$  charm (*green*) are the muons from the semi-muonic decay of heavy flavour hadron B and D respectively.
- primary  $\mu$  (*blue*): muons decaying from primary charged pion( $\pi^\pm$ ) and kaon ( $K^\pm$ ) produced in the collision.
- secondary  $\mu$  (*magenta*): muons decaying from secondary light hadrons produced inside the front absorber of Muon Spectrometer.
- hadrons (*cyan*): punch through hadrons and secondary light hadrons escaped from the front absorber and crossing the tracking chamber and reconstructed as muons erroneously.
- fake tracks (*grey*): tracks which are not associated to one single particle crossing the spectrometer.

In Figure. 3.2, the DCA distribution of muons from various sources are shown for without

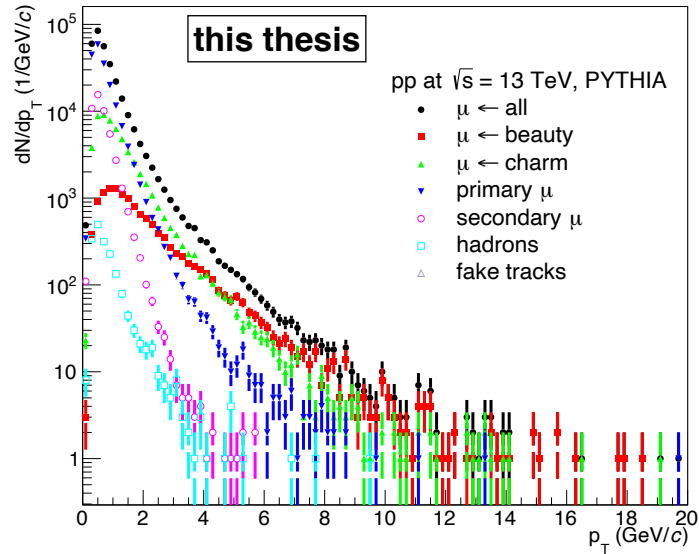


Figure 3.1:  $p_T$ -distribution of muons from different sources using MC PYTHIA simulation.

(left) and with (right) trigger matching condition with that track in tracking system. It is observed that, this trigger matching condition is very much effective to reject the tracks of high DCA values. It is evident from the Figure. 3.2 that high DCA values are corresponding to hadronic component mostly. It is also seen from figure. 3.3 that low momentum muons corresponding to the tracks of high DCA values (left) are largely rejected after the track-trigger matching condition (right). After applying this trigger matching condition, the hadronic component which is basically the punch through hadron, got rejected by  $\sim 98.5\%$ . In addition to this, the contribution of primary and secondary muons is suppressed by  $\sim 56\%$  and  $\sim 65\%$  respectively.

The origin of large values of DCA may be due to following reasons [5]:

- the production vertex of particles related to a given reconstructed track is far from the interaction vertex, such as for light hadron decay muons or beam induced particles.
- large scatterings of the primary and/or secondary muons inside the front absorber (this effect mainly affects the track in the low  $p_T$  region).

The correlation between momentum and DCA has been employed to remove the beam-



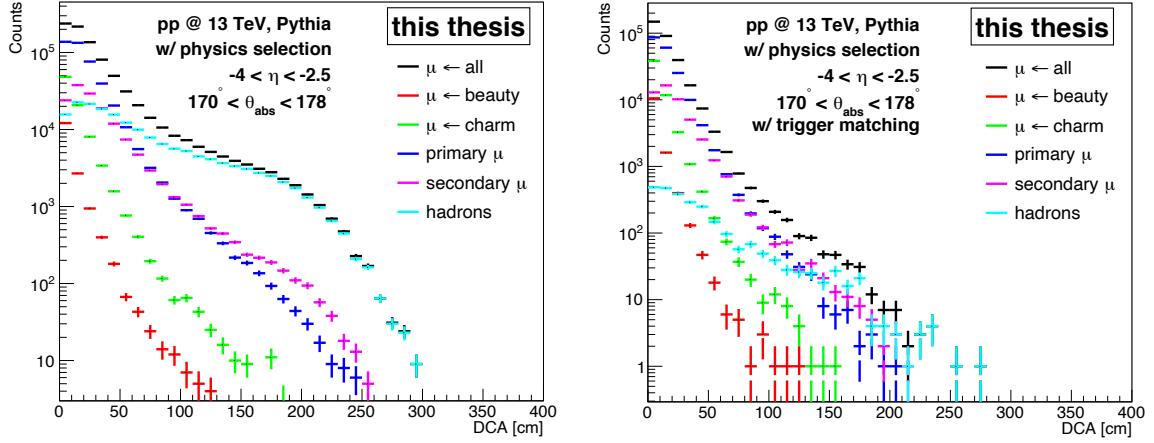


Figure 3.2: DCA distribution of muons from various sources using MC simulation without (left) and with (right) track-trigger matching condition.

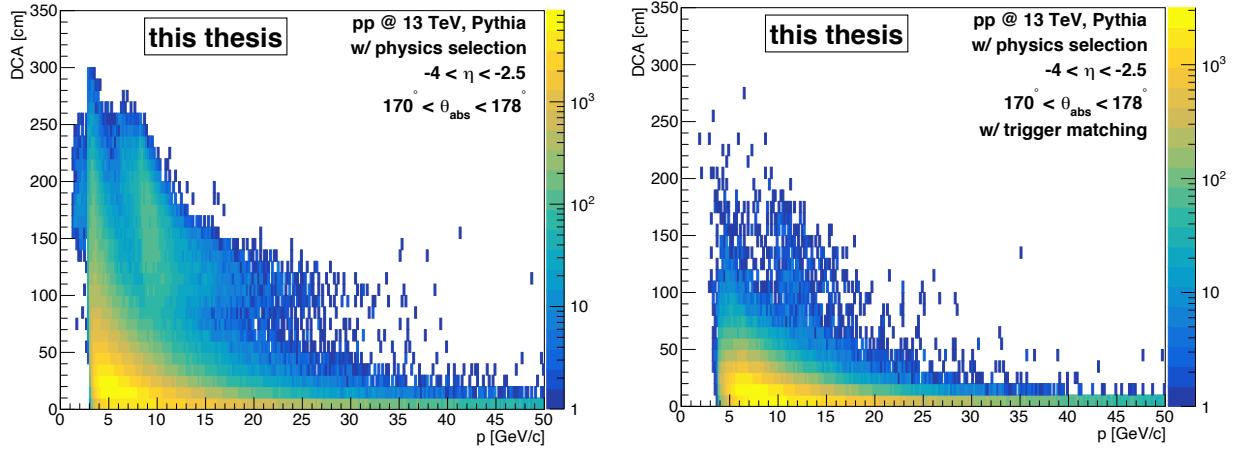


Figure 3.3: DCA distribution of muons as a function of momentum ( $p$ ) before (left) and after (right) track-trigger matching condition.

induced background muons [2]. A beam-induced background track does not point towards the interaction vertex. Due to the multiple coulomb scattering inside the front absorber, the DCA distribution of the tracks pointing toward interaction vertex can be described by a Gaussian function. The width ( $\sigma$ ) of this function can be approximated by:

$$\sigma = \frac{13.6 \text{ MeV}}{\beta c p} \times z \times \sqrt{x/X_0} \times [1 + 0.038 \ln(x/X_0)] \quad (3.2)$$

where  $p$ ,  $\beta c$  and  $z$  are the momentum, velocity and charge number of the particle and  $x/X_0$  is

the thickness of the scattering medium in the unit of radiation length respectively.

From Eq. 3.2, it is evident that the width ( $\sigma$ ) is proportional to the  $1/p$ , where  $p$  is the momentum of the particle. Thus it is proposed to study the variable pDCA ( $p$  times DCA) in order to avoid the dependence on  $p$ .

The left panel of Figure 3.3 shows that the large DCA values at low momentum are associated with the hadronic component and muons from light hadron decays. In the high  $p_T$  region, the large DCA values should not be attributed to large scatterings of light hadrons inside the front absorber. The particles of large DCA values in the high  $p_T$  regions are the background from the beam-gas induced particles. The beam induced background becomes very important in the high  $p_T$  region where the yield of physical tracks is strongly suppressed. The  $p_T$  distribution of the beam induced background does not follow the expected trend as seen for particles produced in the beam-beam collisions. Indeed, they do not follow the DCA distribution as described in Eq. 3.2 and can be rejected applying a cut of  $6\sigma$  on pDCA. The  $\sigma$  is extracted with a Gaussian fit to the pDCA distribution.

To investigate the subtraction of beam-gas induced background, a study of pDCA as a function of transverse momentum ( $p_T$ ) is done. A realistic MC simulation using PYTHIA is performed with a pDCA cut of  $6\sigma$  after the track-trigger matching condition as shown in figure. 3.4. It is observed in the simulation that a pDCA cut of  $6\sigma$  is effective to remove the beam-gas induced background while it does not affect the yield of heavy flavour decay muons, primary muons and hadrons except a reduction of secondary muons by about 1.5%.

The Figure 3.5 shows the effect of this pDCA cut of  $6\sigma$  for the data sample collected using ALICE detector in pp collisions at  $\sqrt{s} = 13$  TeV. The left panel of figure 3.5 shows a tail of beam-gas induced background upto a large  $p_T$ -range. The application of the pDCA cut removes this beam-gas induced background very efficiently which is shown in Figure 3.5 (right).

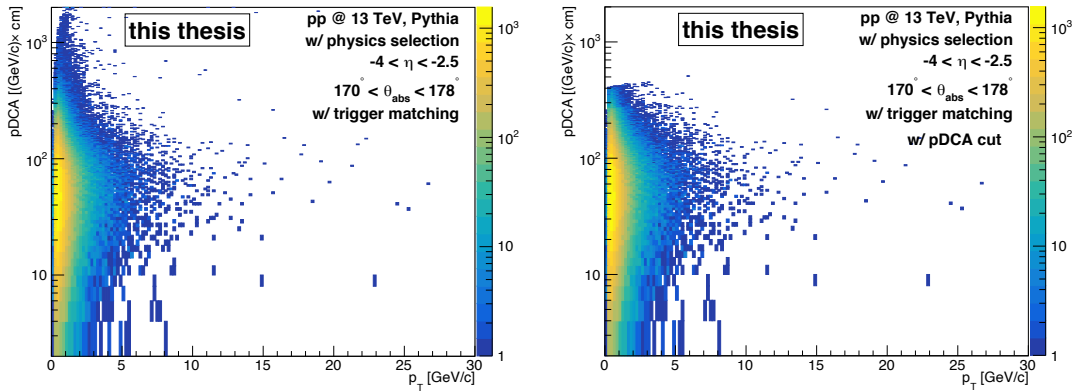


Figure 3.4: pDCA distribution of muons as a function of transverse momentum ( $p_T$ ) before (left) and after (right) applying pDCA cut of  $6\sigma$  in pp collisions at  $\sqrt{s} = 13$  TeV using realistic PYTHIA simulation.

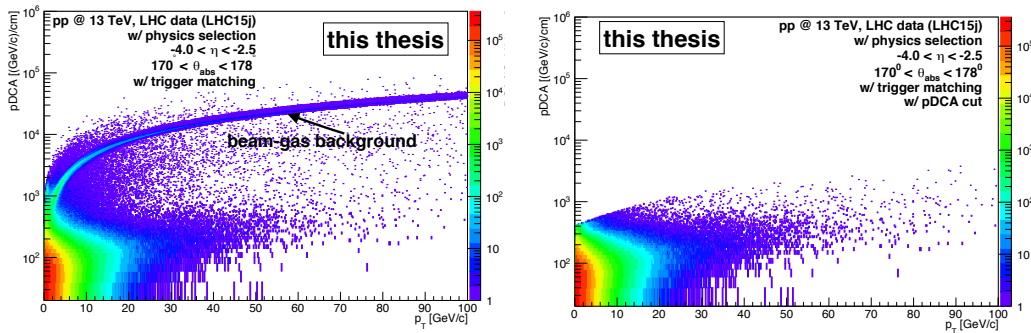


Figure 3.5: pDCA distribution of muons as a function of transverse momentum ( $p_T$ ) before (left) and after (right) applying pDCA cut of  $6\sigma$  in pp collisions at  $\sqrt{s} = 13$  TeV using ALICE data sample.

### 3.3 Inclusive muon distribution

The study of HFM production in pp collisions at  $\sqrt{s} = 13$  TeV is done by analysing the ALICE data sample (LHC16k) as mentioned in section 3.1. The reconstruction of muon tracks are done with the minimum-bias (MB) trigger along with two muon triggers MSL and MSH. The statistics of the events and the corresponding reconstructed muons after applying event and different track selection cuts are shown in Table 3.1.  $N_{evt}$  is the number of events and  $N_{trk}$  is the corresponding number of muon tracks after the event selection cuts applied as discussed in section 3.2.

Table 3.1: Number of events and tracks after various selection cuts for MB, MSL and MSH trigger.

data sample	trigger	$N_{evt}$	$N_{trk}$	w/ $\eta$	w/ $\theta_{abs}$	w/ trig matching	w/ $p \times DCA$
LHC16k	MB	$5.395 \times 10^6$	$3.067 \times 10^5$	$2.518 \times 10^5$	$2.44 \times 10^5$	$5.3522 \times 10^4$	$5.339 \times 10^4$
	MSL	$5.306 \times 10^7$	$3.541 \times 10^7$	$3.227 \times 10^7$	$3.21 \times 10^7$	$2.916 \times 10^7$	$2.909 \times 10^7$
	MSH	$2.301 \times 10^7$	$1.465 \times 10^7$	$1.327 \times 10^7$	$1.319 \times 10^7$	$1.122 \times 10^7$	$1.106 \times 10^7$

The  $p_T$ -distribution of inclusive muons after each track selection cut applied for MB (top), MSL (bottom, left ) and MSH (bottom, right) triggered events are shown in Figure. 3.6. The  $p_T$ -distribution of inclusive muons after applying all event and track selection cuts for MB, MSL and MSH are shown in Figure. 3.7 (left) and the corresponding statistical uncertainties (right) are shown also. As it is expected a higher statistical data volume at this  $\sqrt{s} = 13$  TeV, the inclusive muon  $p_T$ -spectra could be extended upto  $p_T = 40$  GeV/ $c$  with a statistical uncertainties up to 21% for MSL and 5.6% for MSH respectively at the higher  $p_T$ -region within  $36 < p_T < 40$  GeV/ $c$ . However, in the previous measurement of inclusive muons at  $\sqrt{s} = 5.02$  TeV [3] with Run 2 data, it was possible to extend upto  $p_T = 20$  GeV/ $c$  only with a statistical uncertainty of 16% within  $18 < p_T < 20$  GeV/ $c$  for MSH data sample.

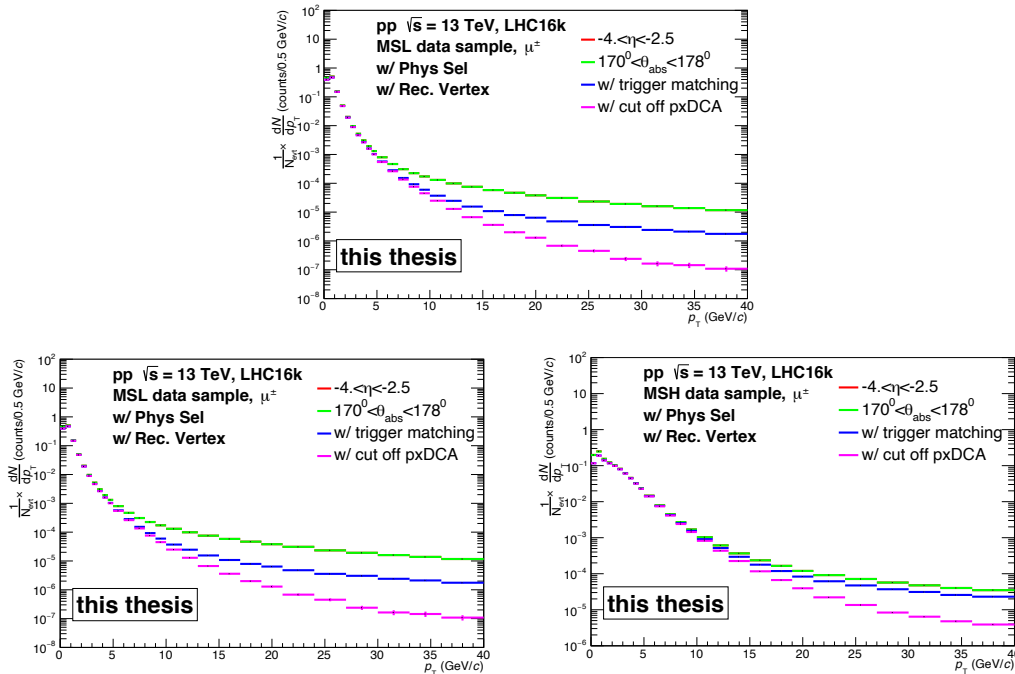


Figure 3.6: Transverse momentum distributions of inclusive muons with different track selection cuts in pp collisions at  $\sqrt{s} = 13$  TeV for MB (top), MSL (bottom, left) & MSH (bottom, right) triggered events.

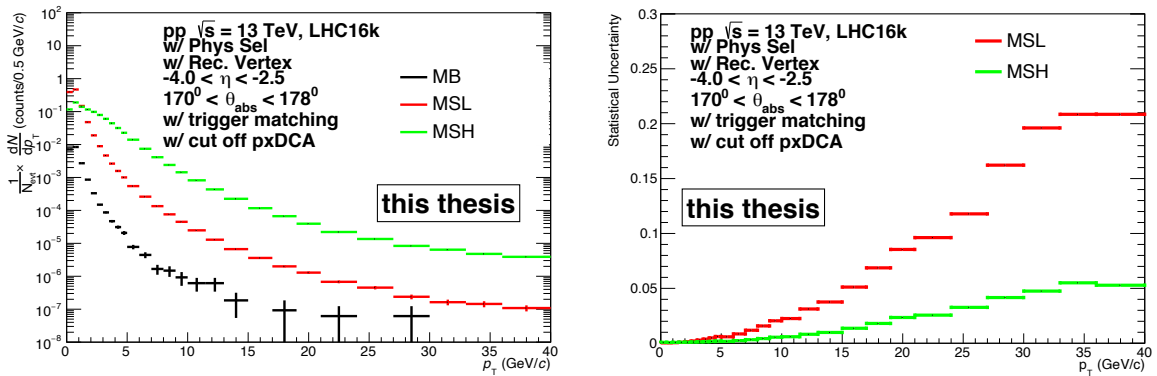


Figure 3.7: Transverse momentum distributions of inclusive muons after all event and track selection cuts in pp collisions at  $\sqrt{s} = 13$  TeV for MB, MSL & MSH triggered events (left). The corresponding statistical uncertainties are also shown (right).

The  $p_T$ -distribution of the inclusive muons at five equal pseudo-rapidity ( $\eta$ ) intervals are also shown for MSL in Figure 3.8 and for MSH in Figure 3.9 respectively. The corresponding statistical uncertainties for these two muon triggers MSL and MSH are shown at the right panel of Figure 3.8 and Figure 3.9 respectively. It is seen that a maximum statistical uncertainty of  $\sim 57\%$  ( $25\%$ ) for MSL (MSH) is associated in the case of most forward interval ( $-4 < \eta < -3.7$ ). It is observed a significantly large background contribution at the lower  $p_T$  region ( $< 2$  GeV/c) for muon decaying from primary and secondary light hadrons as described in section 3.2.1 and low statistics at higher  $p_T$  region. Therefore, the inclusive muon  $p_T$ -distribution is limited within  $2 < p_T < 30$  GeV/c to investigate the production cross-section of heavy flavour decay muon using this data sample at  $\sqrt{s} = 13$  TeV.

### 3.4 Normalization procedure for the single muon triggered events

This HFM analysis is carried out using two single muon triggers CMSL7-B-NOPF-MUFAST (MSL) and CMSH7-B-NOPF-MUFAST (MSH). The data taking with MSL and MSH trigger require one muon track fired in the trigger system in addition to the minimum-bias (MB) trigger. However, the MB triggered events were downscaled during the data taking for allowing more

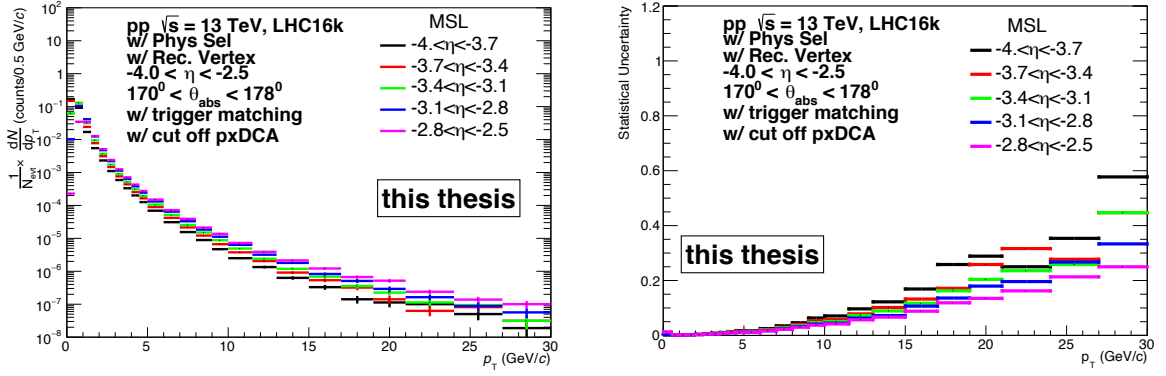


Figure 3.8: Transverse momentum distributions of inclusive muons in five sub-pseudorapidity intervals after applying all selection cuts for MSL triggered events in pp collisions at  $\sqrt{s} = 13$  TeV (left). The corresponding statistical uncertainties are also shown (right).

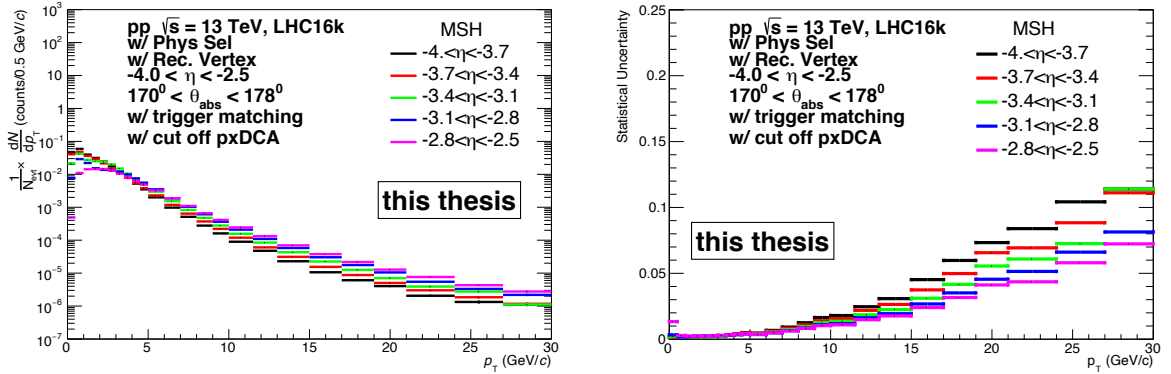


Figure 3.9: Transverse momentum distributions of inclusive muons in five sub-pseudorapidity intervals after applying all selection cuts for MSH triggered events in pp collisions at  $\sqrt{s} = 13$  TeV (left). The corresponding statistical uncertainties are also shown (right).

DAQ bandwidth with the rare triggers like CMUL used for quarkonia analysis in the di-muon channel. Hence, to measure the yield of inclusive single muons in MB triggered events, it is required to determine the equivalent number of minimum bias events corresponding to these two single muon triggered events. The estimation of the equivalent number of minimum bias collisions for a given muon triggered data sample are required for the normalization of muon triggered events. The equivalent number of minimum-bias events ( $N_{MB}^{eq}$ ) corresponding to the

muon triggered events can be calculated as :

$$N_{MB}^{eq} = F_{norm}^{MSL(MSH)} \times N_{MSL(MSH)} \quad (3.3)$$

where,  $F_{norm}^{MSL(MSH)}$  is the normalization factor and  $N_{MSL(MSH)}$  is the number of events for MSL (MSH) respectively. The normalization procedure is very similar analyses as done for  $J/\psi$  and single muons previously [6, 7]. Two method called offline and online(scalar) are adapted for the calculation of  $F_{norm}^{MSL(MSH)}$ . In Offline method, one applies the muon trigger condition on minimum-bias (CINT7) events, whereas online method uses L0b trigger rate as an input taken from Offline Conditions DataBase (OCDB).

### 3.4.1 Correction for pile-up events

It is possible to have several interactions during the integration time of readout detectors and registered as one single event for all these interactions. This is called pile-up events. The pile-up of different collisions happens in two ways: “in-bunch pile-up” where two (or more) collisions occur in the same bunch crossing, and “out-bunch pile-up” occurs where one (or more) collisions occur from neighbouring bunch-crossings. The influence of “out-bunch pile-up” is more with respect to “in-bunch pile-up” on the heavy-ion data at LHC. The pile-up events should be removed to estimate the correct number of MB events. The “out-bunch pile-up” affect detectors differently depending on their readout time and hence the data sample is not sensitive to the pile-up events from different bunch-crossings. So, the pile-up from same bunch crossing is considered only.

The number of inelastic collisions in a bunch crossing follows poisons distribution as below:

$$P(n) = \frac{\mu^n e^{-\mu}}{n!} \quad (3.4)$$

$$\mu = \frac{\sigma L}{N_b f_{LHC}} \quad (3.5)$$

where,  $P(n)$  is the probability of collisions in an event and  $\mu$  is the mean number of collisions per bunch crossing.  $L$  is the LHC instantaneous luminosity and  $\sigma$  is the inelastic cross-section. Hence, the numerator of Eq. 3.5 represents the number of interactions per unit of time.  $N_b$  is the number of bunches in the LHC ring and  $f_{LHC}$  is the LHC revolution frequency (11245 Hz). Therefore, the denominator ( $N_b \cdot f_{LHC}$ ) of Eq. 3.5 is the maximum bunch crossing rate.

The probability of having at least one MB trigger (CINT) is the ratio of the MB trigger rate ( $R_{CINT}$ ) and the rate of bunch crossing ( $N_b \cdot f_{LHC}$ ), as given by

$$P_{CINT}(n \geq 1) = \frac{R_{CINT}}{N_b f_{LHC}} \quad (3.6)$$

It is to be mentioned that  $R_{CINT} \leq N_b \cdot f_{LHC}$ . So, the probability for at least one MB collision in the case of MB trigger with offline physics selection is

$$P_{CINT}(n \geq 1) = \frac{PF_{CINT} \cdot L0bR_{CINT}}{N_b f_{LHC}} \quad (3.7)$$

where,  $PF_{CINT}$  is the purity factor corresponding to the MB trigger CINT. The purity factor (PF) is the fraction of events with offline physics selection to the total number of events for a given trigger used.  $L0bR_{CINT}$  is the rate of number of MB events recorded by the L0b counter. Now, following Eq. 3.4, the probability of having zero collisions is  $P(0) = 1 - P(n \geq 1)$ . Hence, further using Eq. 3.7, the mean number of collisions per bunch crossing is given by

$$\mu = -\ln\left(1 - \frac{PF_{CINT} \cdot L0bR_{CINT}}{N_b f_{LHC}}\right) \quad (3.8)$$

Finally, a pile-up correction factor ( $CF_{Pile-up}^i$ ) is calculated run by run as,

$$CF_{Pile-up}^i = \frac{\mu^i}{1 - e^{-\mu^i}} \quad (3.9)$$

where,  $i$  stands for the run number of the selected data sample.

The pile-up correction has been evaluated also for the MB trigger from T0 (C0TVX) along with the MB trigger from V0 (CINT) using the same procedure. The C0TVX is used for the



pile-up correction based on the L0b trigger rate, called online method. In Figure. 3.10, the L0b trigger rate corresponding to CINT and C0TVX, the number of colliding bunches ( $N_b$ ), the purity factor (PF) corresponding to CINT and the pile-up correction factor ( $CF_{pile-up}$ ) are shown as a function of run numbers. The average values of  $CF_{pile-up}$  considering all the 169 run numbers for the two MB triggers CINT and C0TVX are also displayed in Figure. 3.10 (bottom, right).

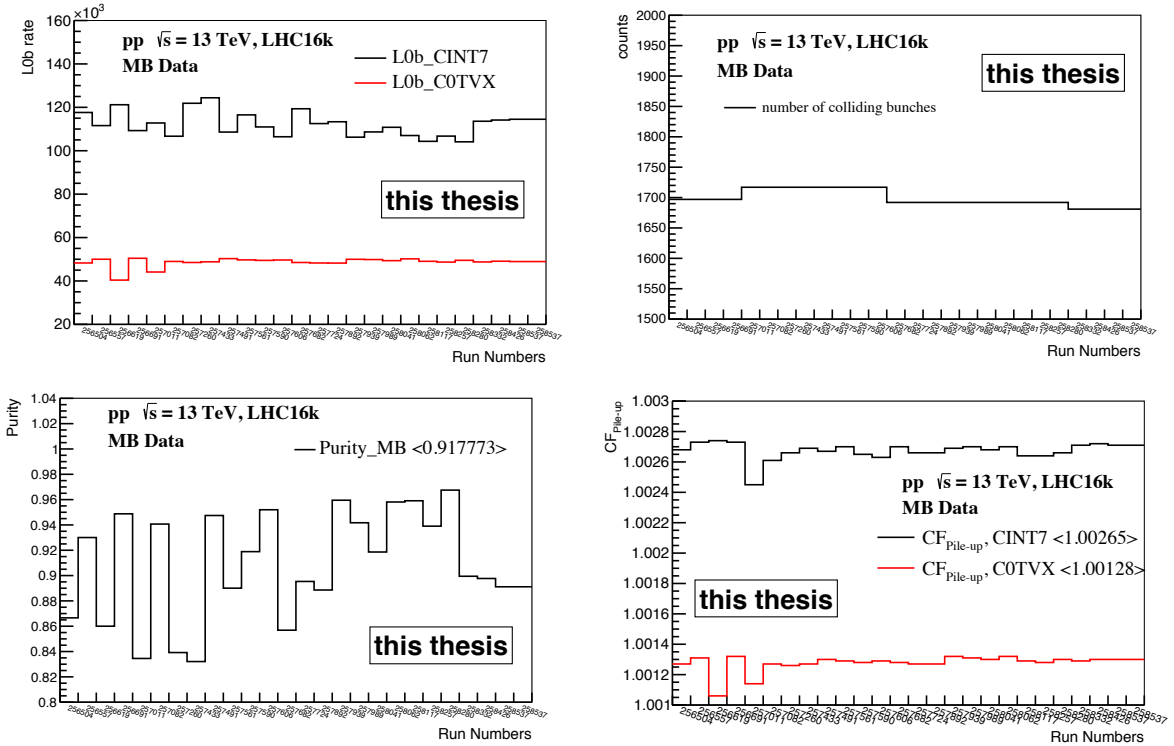


Figure 3.10: L0b trigger rates, number of colliding bunches ( $N_b$ ), purity factor (PF) and pile-up correction factor ( $CF_{pile-up}$ ) for the MB triggers (CINT & C0TVX) as a function of run numbers.

### 3.4.2 Offline method

The normalization factor for two muon triggers MSL ( $F_{norm}^{MSL}$ ) and MSH ( $F_{norm}^{MSH}$ ) are calculated run by run basis as follows:

$$F_{norm}^{i,Offline}(MSL) = \frac{N_{MB}^i \times CF_{Pile-up}^i}{N_{MB\&MSL}} \quad (3.10)$$

$$F_{norm}^{i,Offline}(MSH) = F_{norm}^{i,Offline}(MSL) \times \frac{N_{MSL}^i}{N_{MSL\&\&0MSH}} \quad (3.11)$$

where  $i$  stands for run number,  $CF_{Pile-up}$  is the pile-up correction factor,  $N_{MB}$  and  $N_{MSL}$  are the number of MB and MSL triggered events after offline selection.  $N_{MB\&\&0MSL}$  are the number of MB events satisfying a 0MSL input as well and  $N_{MSL\&\&0MSH}$  are the number of MSL triggered events containing 0MSH input.

The final value of the trigger normalization factor is obtained using the weighted average where the statistical uncertainty used as weight.

$$F_{norm}^{MSL(MSH)} = \frac{\sum_i F_{norm}^{i,MSL(MSH)} \times (\sigma_i^2)^{MSL(MSH)}}{\sum_i 1/(\sigma_i^2)^{MSL(MSH)}} \quad (3.12)$$

The statistical uncertainty in the measurement of  $F_{norm}^{MSL(MSH)}$  is given by

$$\left| \Delta F_{norm}^{MSL(MSH)} \right| = \sqrt{\frac{1}{\sum_i 1/(\sigma_i^2)^{MSL(MSH)}}} \quad (3.13)$$

### 3.4.3 Online method

Online (scalar) method is measured with the L0b trigger (Level 0 scalar inputs of MB trigger) rate taken from OCDB. Here, C0TVX trigger is used as minimum-bias (MB) trigger. The normalization factor in online method is measured as follows:

$$F_{norm}^{i,Online}(MSL/MSH) = \frac{L0b_{C0TVX}^i \times PF_{C0TVX}^i \times CF_{Pile-up}^i}{L0b_{MSL/MSH}^i \times PF_{MSL/MSH}^i} \quad (3.14)$$

where  $PF_{C0TVX}$ ,  $PF_{MSL}$  and  $PF_{MSH}$  are the purity factors corresponding to C0TVX, MSL and MSH triggers respectively.  $L0b_{C0TVX}$ ,  $L0b_{MSL}$  and  $L0b_{MSH}$  are the trigger rates at L0b level corresponding to C0TVX, MSL and MSH respectively. The final value is calculated by the weighted average and the statistical uncertainties are calculated same as in offline method.

### 3.4.4 Results on normalization procedure

The normalization factor ( $F_{norm}$ ) calculated with offline and online methods for MSL (left) and MSH (right) as a function of run numbers are shown in Figure 3.11. The final  $F_{norm}$  values and corresponding statistical uncertainties over all the run numbers for MSL and MSH are calculated using Eq. 3.12 and Eq. 3.13 respectively.

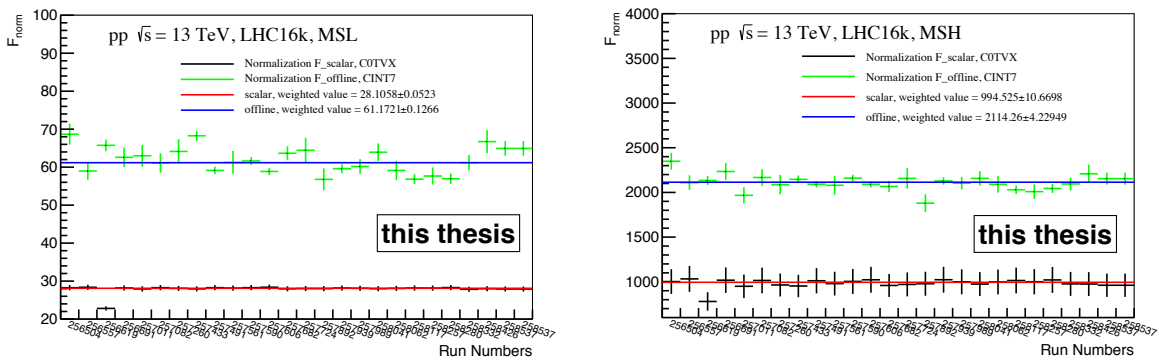


Figure 3.11: Normalization factor ( $F_{norm}$ ) for muon triggers MSL (left) and MSH (right) as a function of run number.

The cross-section ( $\sigma$ ) corresponding to MSL and MSH are also measured from the results based on offline and online method as following

$$\sigma_{MSL/MSH}^{Offline/Online} = \frac{\sigma_{VdM}^{V0/T0}}{F_{norm(Offline/Online)}^{MSL/MSH}} \quad (3.15)$$

$\sigma_{VdM}$  is the visible (reference) cross-section measured in van der Meer (VdM) scan in August 2015 based on particle detection in V0 and T0 detectors. The values of the visible cross-section measured by V0 and T0 detectors are  $\sigma_{VdM}^{V0} = (57.8 \pm 1.2)$  mb and  $\sigma_{VdM}^{T0} = (30.1 \pm 0.6)$  mb respectively [8]. To calculate the cross-section for the two muon triggers, the  $\sigma_{VdM}^{V0}$  is used for the offline method whereas  $\sigma_{VdM}^{T0}$  is used for the online method. Finally, the integrated luminosity ( $L_{int}$ ) for MSL and MSH can be calculated using  $\sigma_{VdM}^{T0}$  as given by

$$\begin{aligned}
 L_{int} &= \frac{N_{MSL/MSH}}{\frac{T_0}{\sigma_{VdM}}} \times F_{norm}^{MSL/MSH} \\
 &= \frac{N_{MSL/MSH}}{\sigma_{MSL/MSH}^{Online}}
 \end{aligned}
 \tag{3.16}$$

The calculated values of the integrated luminosity corresponding to MSL and MSH triggers are  $(176.85 \pm 3.54) \text{ nb}^{-1}$  and  $(2177.42 \pm 49.29) \text{ nb}^{-1}$  respectively. Finally, the production cross-section of muons decaying from heavy flavour hadrons is obtained using the cross-section calculated for the MSL and MSH triggers with the online method based on the C0TVX trigger.

The normalization factor ( $F_{norm}$ ), cross-section ( $\sigma$ ) for both the offline and online method and  $L_{int}$  corresponding to MSL and MSH triggers are reported in table 3.2.

Table 3.2: Normalization factor, cross-section and Integrated Luminosity for MSL and MSH data sample.

Trigger	$F_{norm}^{Offline}$	$F_{norm}^{Online}$	$\sigma^{Offline}$ (mb)	$\sigma^{Online}$ (mb)	$L_{int}(\text{nb}^{-1})$
MSL	$61.1721 \pm 0.1266$	$28.1058 \pm 0.0523$	$0.9449 \pm 2.09\%$	$1.071 \pm 2.0\%$	$176.85 \pm 3.54$
MSH	$2114.26 \pm 4.22949$	$994.525 \pm 10.6698$	$0.0273 \pm 2.09\%$	$0.0303 \pm 2.26\%$	$2177.42 \pm 49.29$

### 3.5 Acceptance times efficiency

The Acceptance times efficiency ( $A \times \epsilon$ ) as a function of  $p_T$  is estimated from a full realistic Monte-Carlo (MC) simulations. The  $p_T$ - and  $y$ -distribution of muons decaying from heavy flavour hadrons based on FONLL (Fixed Order + Next-to-Leading Logarithms) calculations. The GEANT3 transport package has been used to incorporate the detector descriptions and its responses. The  $A \times \epsilon$  calculations are done run by run and hence the evolution of the detector response over the time is taken into account. The parameterizations of the  $p_T$  (Eq. 3.17) and  $y$  (Eq. 3.18) distributions of muons from heavy flavour hadron decays are predicted by FONLL as follows:

$$\frac{a}{(b^2 + p_T^2)^c}
 \tag{3.17}$$

$$x^8 \cdot p_1 + x^6 \cdot p_2 + x^4 \cdot p_3 + x^2 \cdot p_4 + x \cdot p_5 + p_6 \quad (3.18)$$

where  $a, b, c$  and  $p_1, p_2, p_3, p_4, p_5, p_6$  are the free parameters for the given  $p_T$ - and  $y$ - distributions respectively. To measure the heavy flavour decay muon (HFM) contribution, both the  $c$  and  $b$ -quark hadronic contributions through their leptonic decay modes are considered using FONLL online tool [4]. The HFM have three contributions:  $\mu \leftarrow c$ ,  $\mu \leftarrow b$  and  $\mu \leftarrow D \leftarrow b$ . The CTEQ6.6 is used as a Parton Distribution Function (PDF). Considering the edge effect within the ALICE muon spectrometer acceptance, the rapidity range is broadened to  $-4.3 < y < -2.2$ . The  $p_T$ - and  $y$ - distributions are obtained according to the muon trigger conditions MSL ( $p_T \geq 1$  GeV/ $c$ ) and MSH ( $p_T \geq 4$  GeV/ $c$ ). The  $p_T$ - and  $y$ - distributions of HFM based on FONLL and their corresponding fits according to the Eq. 3.17 and Eq. 3.18 are shown in Figure 3.12 and Figure 3.13 respectively.

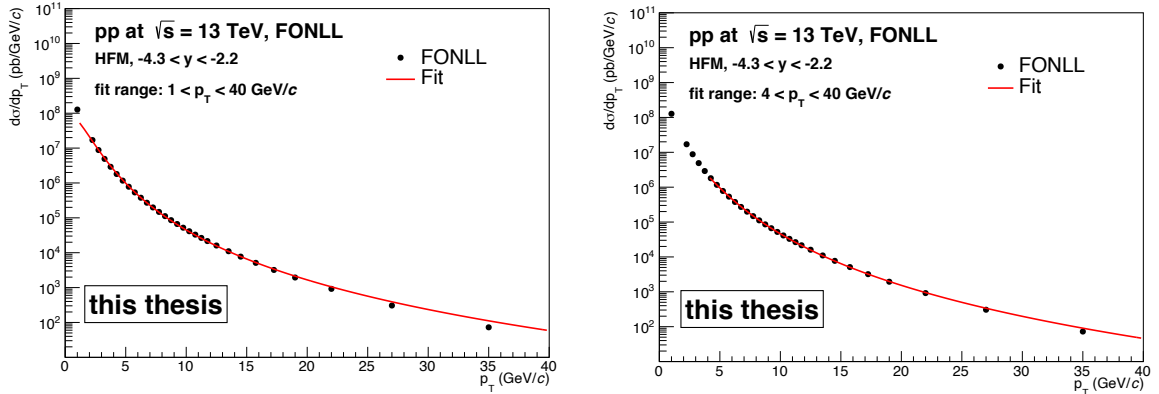


Figure 3.12:  $p_T$ -distribution in pp collisions at  $\sqrt{s} = 13$  TeV corresponding to MSL (left) and MSH (right) predicted by FONLL. The fit functions are also shown for  $p_T$  distribution.

The  $p_T$ -differential acceptance times efficiency ( $A \times \epsilon$ ) is calculated by:  $A \times \epsilon|_{MC}^i = N_{Tot}^{i,Rec} / N_{Tot}^{i,Gen}$ , where  $N_{Tot}^{i,Rec}$  and  $N_{Tot}^{i,Gen}$  are the total number of reconstructed and generated muons in the  $i$ th  $p_T$  bin. Large statistical fluctuation is visible towards the high  $p_T$ -region in  $A \times \epsilon$  for all the rapidity-intervals. These fluctuations are mitigated using an Error fitting function:

$$a \left[ b + Erf\left(\frac{p_T - c}{d}\right) \right] \quad (3.19)$$

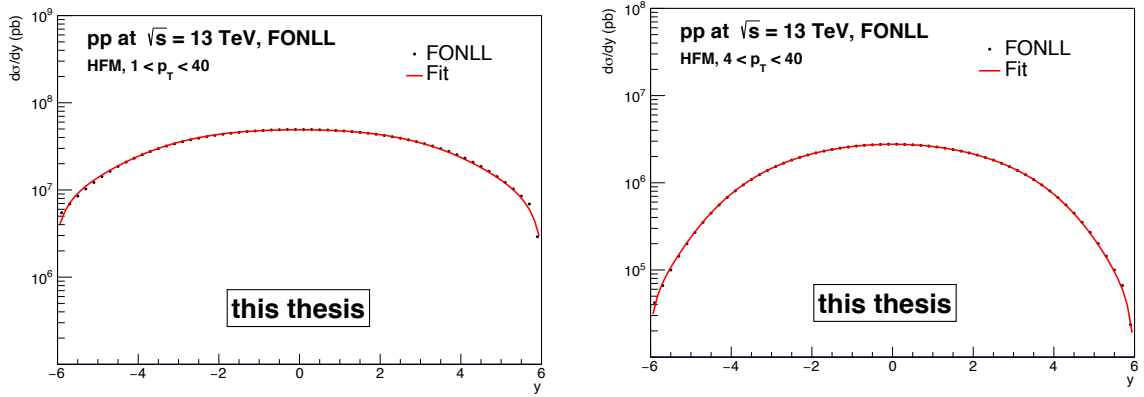


Figure 3.13:  $y$ -distribution in pp collisions at  $\sqrt{s} = 13$  TeV corresponding to MSL (left) and MSH (right) predicted by FONLL. The fit functions are also shown for  $y$  distribution.

where, a,b,c and d are the fitting parameters.

The  $A \times \epsilon$  as a function of  $p_T$  for MSL (left) and MSH (right) within the full acceptance  $-4. < \eta < -2.5$  are shown in Fig. 3.14. The  $p_T$ -differential  $A \times \epsilon$  at five different rapidity intervals are also shown for MSL and MSH in Fig. 3.15 and Fig. 3.16 respectively.

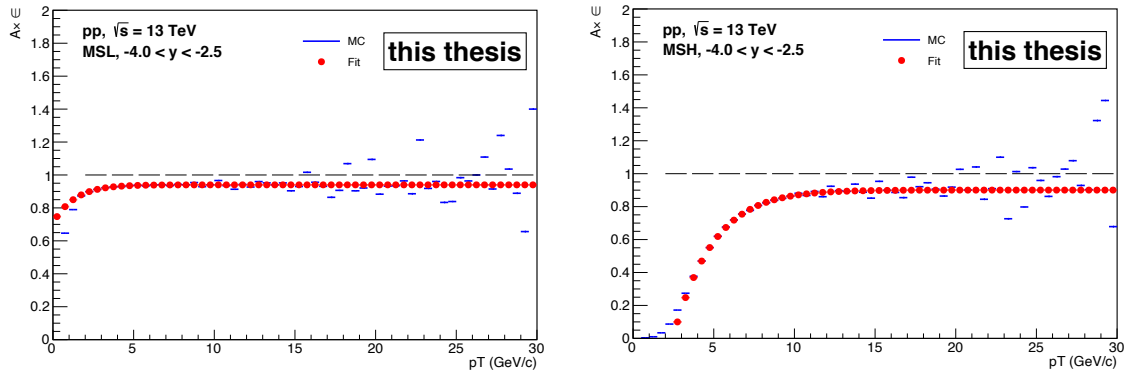


Figure 3.14: Acceptance times efficiency ( $A \times \epsilon$ ) as a function of  $p_T$  for two muon triggers MSL(left) and MSH (right) within the full acceptance ( $-4 < \eta < -2.5$ ) at  $\sqrt{s} = 13$  TeV.

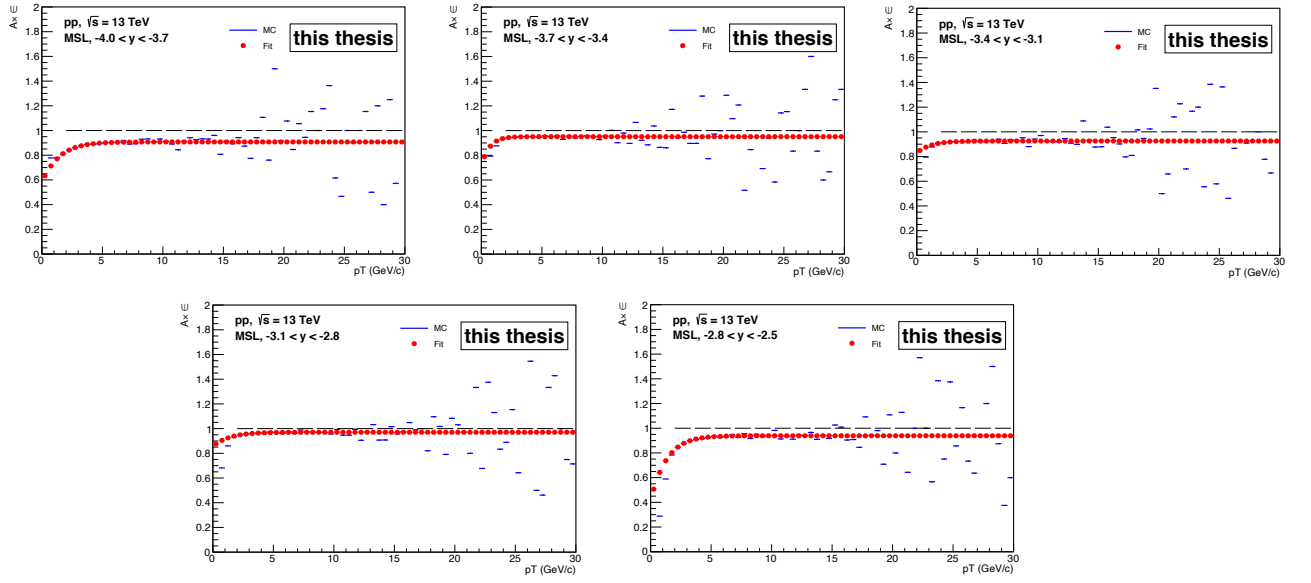


Figure 3.15: Acceptance times efficiency ( $A \times \epsilon$ ) as a function of  $p_T$  for MSL trigger at five rapidity intervals.

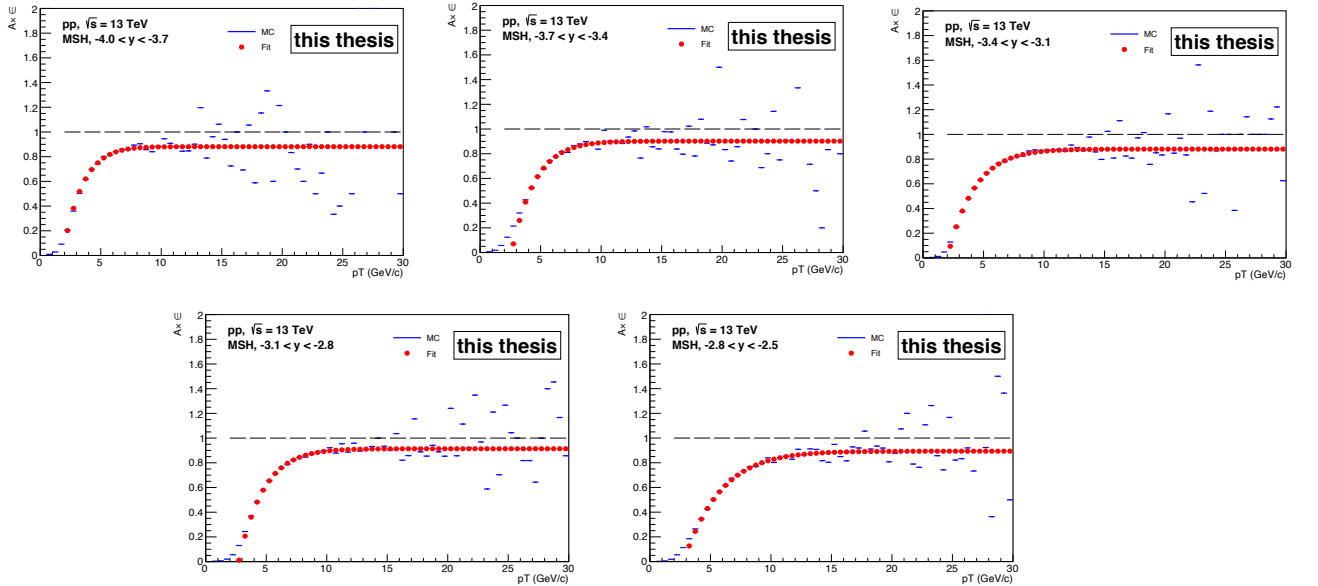


Figure 3.16: Acceptance times efficiency ( $A \times \epsilon$ ) as a function of  $p_T$  for MSH trigger at five rapidity intervals.

### 3.6 Correction of inclusive muon $p_T$ distribution.

In section. 3.3, the  $p_T$ -distributions of single muons are obtained using two single muon triggers MSL and MSH. The normalization of the single muon triggers MSL and MSH with the equivalent number of minimum-bias events are presented in section. 3.4. The  $A \times \epsilon$  for MSL and MSH triggered events are also obtained in section. 3.5. It is necessary to normalize the raw inclusive muons spectra to the equivalent number of MB events and then corrections for the  $A \times \epsilon$ . The  $p_T$  distribution of inclusive muons for MSL and MSH are normalized using the cross-sections of corresponding triggers as reported in Table. 3.2. Figure. 3.17 shows the  $p_T$ -distribution of inclusive muon within  $-4 < \eta < -2.5$  for MSL- and MSH-triggered events before and after the normalization correction. Furthermore, the normalized  $p_T$ -distributions of inclusive muons for MSL and MSH triggers are corrected with the  $A \times \epsilon$ . The results after the corrections with  $A \times \epsilon$  are shown in Figure. 3.18 for full acceptance and at different pseudo-rapidity intervals.

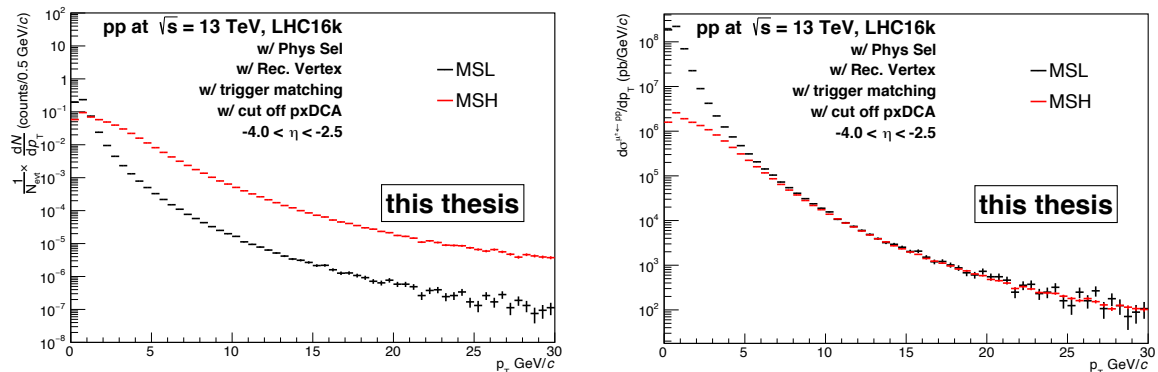


Figure 3.17: Inclusive muons  $p_T$ -distribution for MSL and MSH triggered events before (left) and after (right) normalization correction.

Figure 3.19 presents the ratio of the corrected  $p_T$ -distributions of MSH to that of MSL triggered events in the left panel and the same at different rapidity intervals in the right panel. It is observed that the maximum relative deviation between MSL and MSH triggered events is  $\sim 5\%$  for  $p_T > 6$  GeV/ $c$  within full acceptance ( $-4 < \eta < -2.5$ ) whereas at different sub-rapidity intervals it varies upto  $\sim 21\%$  for  $p_T$  range  $20 < p_T < 30$  GeV/ $c$ . The final  $p_T$ -spectra of inclusive muons are computed mixing the MSL and MSH triggered events in the  $p_T$  range  $2 < p_T < 7$  GeV/ $c$  and  $7 < p_T < 30$  GeV/ $c$  respectively. This mixed inclusive muon  $p_T$



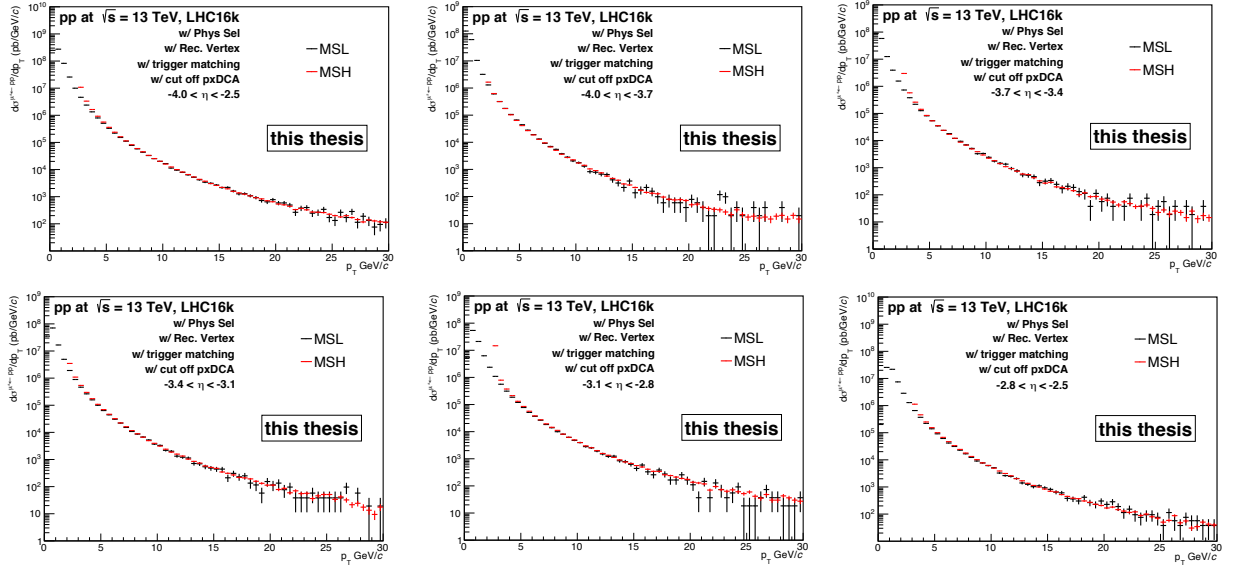


Figure 3.18: The comparison of normalized and  $A \times \epsilon$  corrected  $p_T$ -distributions of inclusive muons for MSL and MSH triggered events at different rapidity intervals.

distribution is used for the study of different background contributions and to obtain the HFM production cross-section after subtracting the total background muons. The final inclusive muons  $p_T$  distributions within the full acceptance and at various sub-rapidity intervals are shown in Figure 3.20.

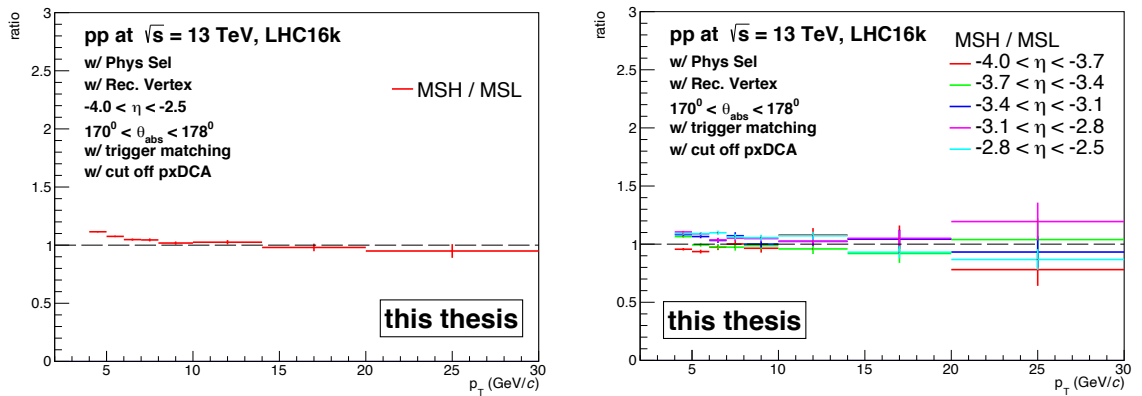


Figure 3.19: The ratio of the corrected (normalized and  $A \times \epsilon$ )  $p_T$  distributions of inclusive muons of MSH with respect to that of MSL triggered events for the full rapidity range (left) and various sub-rapidity intervals (right).

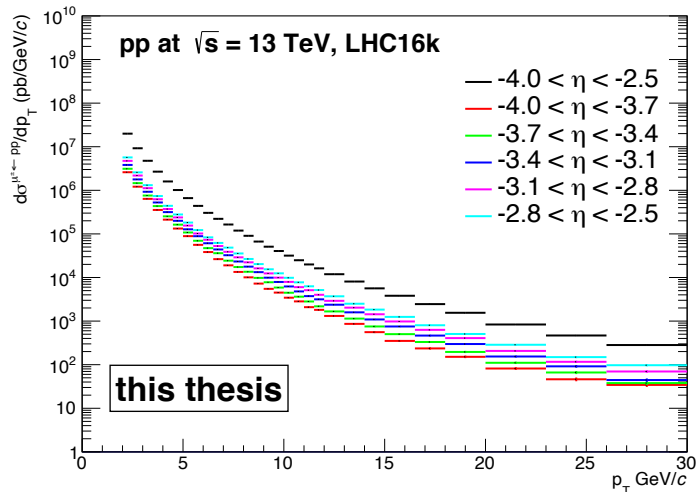


Figure 3.20: The  $p_T$  distributions of inclusive muons obtained by mixing MSL ( $2 < p_T < 7$  GeV/c) and MSH ( $7 < p_T < 30$  GeV/c) triggered events.

### 3.7 Estimation of background contributions

The contributions of muons from several background sources are to be subtracted from the corrected inclusive muons obtained in pp collisions at  $\sqrt{s} = 13$  TeV. Finally the  $p_T$ -differential production cross-section of heavy flavour decay muon (HFM) is measured as following:

$$\frac{dN_{pp}^{\mu\leftarrow HF}}{dp_T} = \frac{dN_{pp}^{incl \mu}}{dp_T} - \frac{dN_{pp}^{\mu\leftarrow \pi, K}}{dp_T} - \frac{dN_{pp}^{sec \mu}}{dp_T} - \frac{dN_{pp}^{\mu\leftarrow J/\psi}}{dp_T} - \frac{dN_{pp}^{\mu\leftarrow W/Z/\gamma^*}}{dp_T} \quad (3.20)$$

The contribution of secondary muon is very negligible ( $< 1\%$ ) for muon with  $p_T > 4$  GeV/c. However, the main background contribution towards low  $p_T$ -range (2-5 GeV/c) is from the muons decay from primary charged pion and kaon while at higher  $p_T$ -region ( $p_T > 14$  GeV/c) the contribution of muons from  $W/Z/\gamma^*$  decay is more prominent. At the intermediate  $p_T$ -region (5-14 GeV/c), the  $J/\psi$  decay muon component is found to be dominant. The contribution of upsilon ( $\Upsilon$ ) is not considered for this analysis because of its production cross-section is negligible when compares with the  $J/\psi$  production cross-section.

### 3.7.1 Primary charged pion and kaon decay muon

The procedure for the estimation of the background contribution due to the primary charged pion/kaon ( $\pi/K$ ) decay muons in this analysis is very similar to the strategy followed for the production of muons from heavy flavour hadron decays in previously done for pp collisions at  $\sqrt{s} = 5.02$  TeV [7].

All the steps for the estimation of muons decaying from primary  $\pi^\pm/K^\pm$  are discussed as following:

#### A. Extrapolation of charged pion and kaon transverse momentum spectra

To obtain the transverse momentum ( $p_T$ ) spectra of muons decaying from charged pion and kaon upto 30 GeV/ $c$  or even higher, it required the  $p_T$ -distribution of pion and kaon at least upto  $p_T = 40$  GeV/ $c$ . ALICE has measured the production of  $\pi^\pm$  and  $K^\pm$  in inelastic proton-proton (pp) collisions at a center-of-mass energy of  $\sqrt{s} = 13$  TeV at midrapidity ( $|y| < 0.5$ ) as a function of transverse momentum ( $p_T$ ) upto  $p_T = 20$  GeV/ $c$  [9]. Hence, the extrapolation is done for the measured  $\pi^\pm(K^\pm)$  from  $p_T = 20$  GeV/ $c$  to  $p_T = 40$  GeV/ $c$  to obtain the muon decaying from  $\pi^\pm$  and  $K^\pm$  upto  $p_T = 30$  GeV/ $c$ . The extrapolation is done by fitting the input  $\pi^\pm/K^\pm$  mid-rapidity  $p_T$ -spectra about 5000 times with Lavy-Tsallis distribution function (Eq. 3.21). The total uncertainties within the input  $p_T$ -distributions are quantified by adding the statistical and systematic errors in quadrature. The fit is performed in the range  $12 < p_T < 20$  GeV/ $c$  for both pion and kaon. For each fitting, the central values and the total errors ( $1\sigma$ ) at a given  $p_T$  bin are computed by generating random numbers according to the Gaussian distribution in the range  $p_T \leq 20$  GeV/ $c$ . Finally, the central values and the corresponding errors in the extrapolated region ( $20 < p_T < 40$  GeV/ $c$ ) are calculated by doing average and Root Mean Square (R.M.S) of all the fits at a given  $p_T$ -bin. The effect for varying the fit range towards a lower value at  $p_T = 7$  GeV/ $c$  has been checked also. This implementation can be found in Ref. [10]. The extrapolated  $p_T$ -distribution of charged  $\pi$  and  $K$  at mid-rapidity ( $|\eta| < 0.5$ ) are shown in Figure 3.21

$$f(p_T) = a \times p_T \times \left[ \frac{1 + (m_T - m_0)}{n \times T} \right]^{-n} \quad (3.21)$$

where,  $a$ ,  $n$ ,  $T$  are the free parameters,  $m_T = \sqrt{p_T^2 + m_0^2}$  and  $m_0$  is the rest mass of the particle.

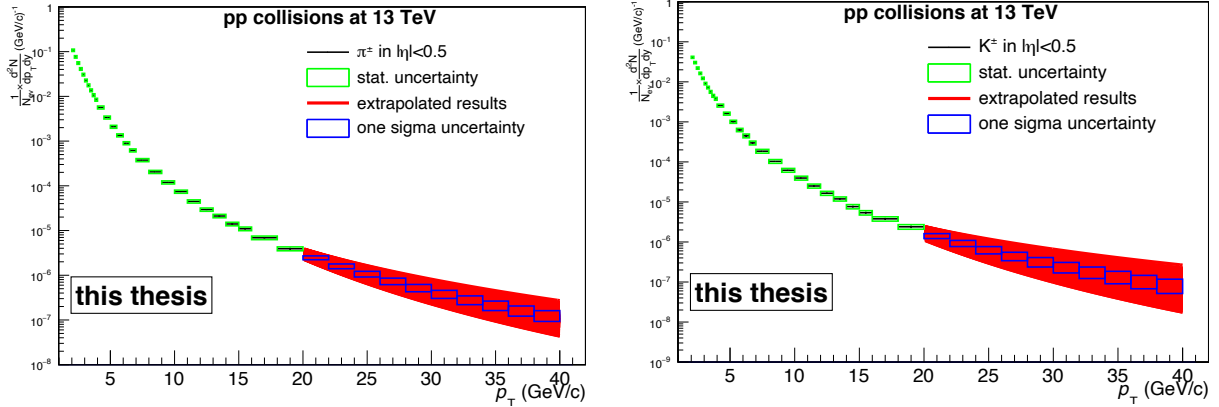


Figure 3.21: Extrapolated  $p_T$ -distribution of charged pion (left) and kaon (right) at mid-rapidity in pp collisions at  $\sqrt{s} = 13$  TeV.

To quantify any systematic error from the fitting with different functions, a power law function (Eq. 3.22) is used for this extrapolation towards higher  $p_T$  in addition to the Tsallis distribution.

$$f(p_T) = \frac{p_0}{(p_1^2 + p_T^2)^{p_2}} \quad (3.22)$$

where  $p_0$ ,  $p_1$ ,  $p_2$  are the fitting parameters.

The relative uncertainties obtained for extrapolating the pion (left) and kaon (right)  $p_T$  distribution towards higher  $p_T$  region using Tsallis distribution and power law function are shown in Figure 3.22. It is observed that smaller relative uncertainties are obtained while fitting with Tsallis distribution compared to the power law function. The maximum relative uncertainties are obtained for extrapolation of pion is  $\sim 27\%$  ( $\sim 37\%$ ) and for kaon is  $\sim 39\%$  ( $\sim 46\%$ ) from the fit with Tsallis distribution (power law function). The relative deviation in the uncertainties measured using these two fitting functions are considered as a source of systematic uncertainties for the  $p_T$  extrapolation of pion and kaon at mid-rapidity.

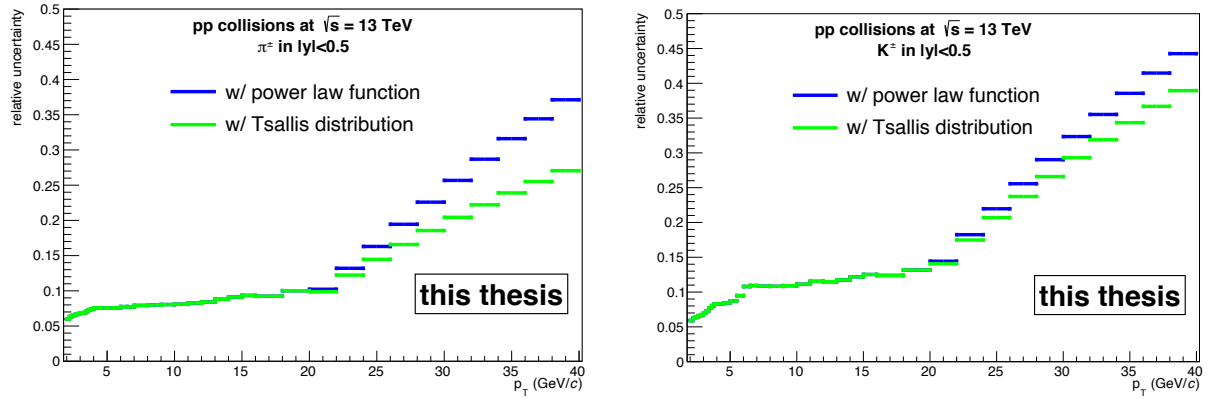


Figure 3.22: Relative uncertainties for extrapolated  $p_T$ -distribution of charged pion (left) and kaon (right) at mid-rapidity in pp collisions at  $\sqrt{s} = 13$  TeV using Tsallis distribution and power law function.

## B. Extrapolation of mid-rapidity charged pion and kaon towards forward rapidity.

In this analysis, the HFM will be measured in the forward rapidity ( $2.5 < y < 4$ ) in the acceptance of muon spectrometer. So, the background contribution of muon decaying from primary pion and kaon must be accounted in the forward rapidity  $2.5 < y < 4$ . Hence, the extrapolation of the midrapidity distribution of primary pion and kaon is to be done towards forward rapidity. This extrapolation from mid to forward rapidity can be expressed as:

$$\left[ \frac{d^2 N^{\pi^\pm(K^\pm)}}{dp_T dy} \right]_{fwd-y} = F_{extrap}(y, p_T) \cdot \left[ \frac{d^2 N^{\pi^\pm(K^\pm)}}{dp_T dy} \right]_{mid-y} \quad (3.23)$$

where  $F_{extrap}(y, p_T)$  is the  $p_T$ -dependent factor for the rapidity extrapolation. The rapidity distributions of primary  $\pi^\pm$  and  $K^\pm$  for  $p_T > 2$  GeV/ $c$  are obtained by means of Monte Carlo simulation with PYTHIA8 and PHOJET event generators. The simulated rapidity distributions ( $|y| < 6$ ) of pion and kaon is fitted using a polynomial function:  $x^8 \cdot p_1 + x^6 \cdot p_2 + x^4 \cdot p_3 + x^2 \cdot p_4 + x \cdot p_5 + p_6$ . The rapidity distributions obtained from PYTHIA8 (left) and PHOJET (right) along with the corresponding fit functions are shown in Figure 3.23. The ratios between the simulated rapidity distributions of charged pion and kaon and the corresponding fits for PYTHIA8 (left) and PHOJET (right) are shown in Figure 3.24 also. The uncertainties

for the rapidity extrapolation within  $|y| < 4.5$  are calculated by the relative deviation between PYTHIA8 and PHOJET results as shown in Figure 3.25. The relative uncertainties are measured upto 12% for pion and 18% for kaon respectively.

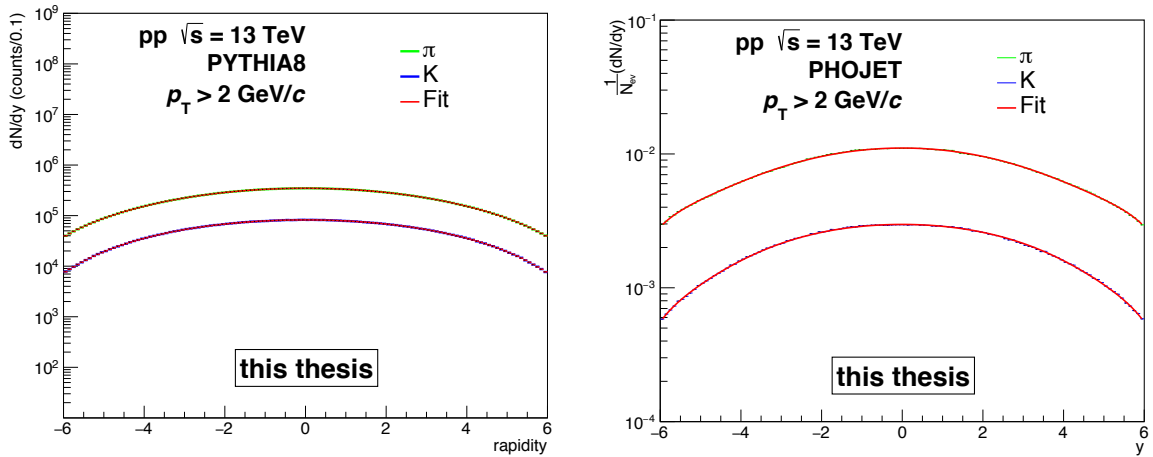


Figure 3.23: Rapidity distributions of charged pion and kaon with  $p_T > 2$  GeV/ $c$  obtained from PYTHIA8 (left panel) and PHOJET (right panel).

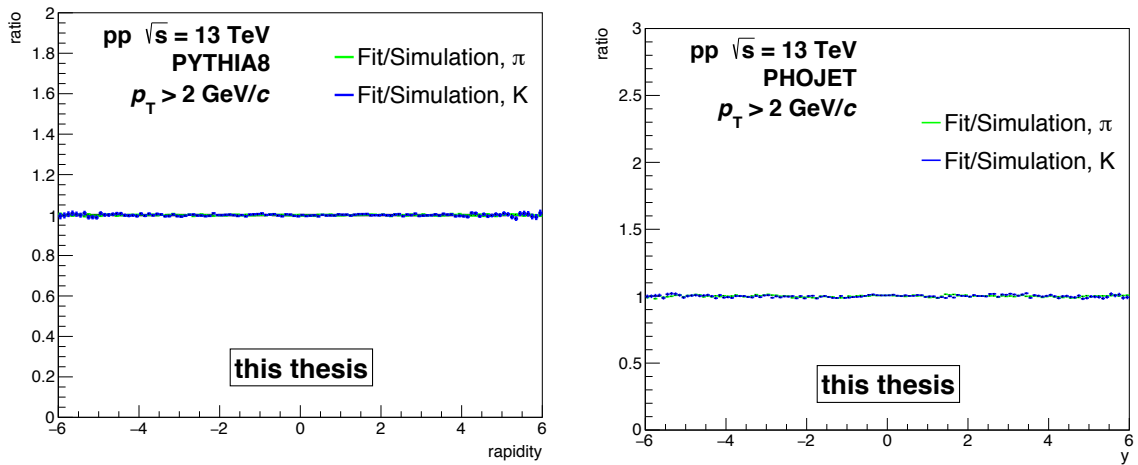


Figure 3.24: Ratio of the fitted function with that simulated rapidity distributions of charged pion and kaon with  $p_T > 2$  GeV/ $c$  obtained from PYTHIA8 (left panel) and PHOJET (right panel).

### C. $p_T$ -dependent rapidity extrapolation factor for charged pion and kaon.

In order to extrapolate the charged pion and kaon rapidity distribution, it must be introduced a  $p_T$ -dependent correction factor ( $F_{extrap}(y, p_T)$ ) in the extrapolation as given in Eq. 3.23. To

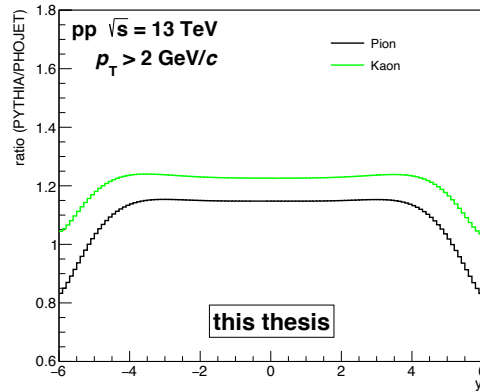


Figure 3.25: Ratio of the rapidity distributions of charged pion and kaon between PYTHIA8 and PHOJET.

calculate this correction factor, charged pion and kaon are generated using Monte Carlo (MC) simulation based on PYTHIA8 with large statistics upto  $p_T = 50$  GeV/ $c$ . This PYTHIA8 simulation is performed for two colour reconnection (CR) schemes based on Multi Parton Interaction (MPI) and new QCD model [11]. These two CR tunings are used to estimate the systematic errors corresponding to this  $p_T$ -dependent correction factor measurement. The correction factor ( $F_{extrap}(y, p_T)$ ) is weighted from the ratio of the  $p_T$ -distribution of charged pion (kaon) at different rapidity intervals relative to that measured at mid-rapidity ( $|y| < 0.5$ ) and then rescaled to the first  $p_T$  bin as shown in Fig 3.26. The  $p_T$ -dependency increases towards higher  $p_T$ -region and are more pronounced for CR=1 as compared with CR=0 towards forward rapidity.

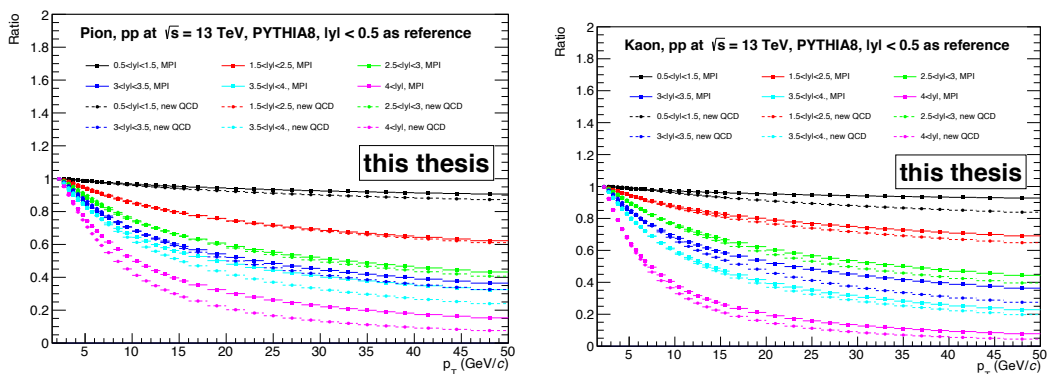


Figure 3.26: Generated  $p_T$ -distribution of  $\pi^\pm$  (left panel) and  $K^\pm$  (right panel) at different rapidity intervals with respect to that at mid-rapidity ( $|y| < 0.5$ ) and rescaled to that with first  $p_T$  bin for two colour reconnection schemes available in PYTHIA8.

One can also have a look in the comparison of  $p_T$ - dependent extrapolation between pion and kaon for a given model with MPI (CR = 0) and new QCD (CR = 1) as shown in Figure 3.27. It is observed from Figure 3.27 that kaon is more affected than pion towards forward rapidity region for any given colour reconnection scheme. The details of this  $p_T$ - dependent extrapolation implementation can be found in the Ref. [10, 12].

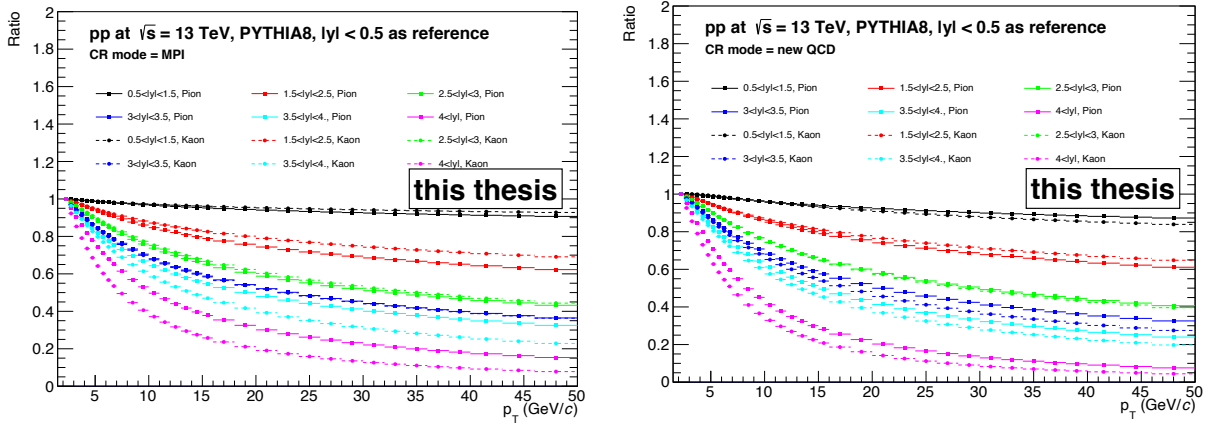


Figure 3.27: Generated  $p_T$ - distribution of  $\pi^\pm$  and  $K^\pm$  at different rapidity intervals with respect to that at mid-rapidity ( $|y| < 0.5$ ) and rescaled to that with first  $p_T$  bin for two colour reconnection schemes CR=0 (left panel) and CR=1 (right panel) available in PYTHIA8.

#### D. Fast simulation to generate muons decaying from charged pion and kaon

To estimate the contribution of muons decaying from charged pion and kaon, the effect of the front absorber in the muon spectrometer is to be taken into account. A fast simulation using the decay kinematics based on PYTHIA8 event generator is utilised to generate muons decaying from charged pion and kaon. In this fast simulation, charged pion and kaon are generated according to uniform  $p_T$ - and  $y$ - distribution and are then forced to decay into muon using PYTHIA decayer. Considering the absorber effect, the generated decay muon  $p_T$ - and  $y$ - distributions are weighted according to the input  $p_T$ - and  $y$ - distributions of  $\pi^\pm$  and  $K^\pm$ . The relative production probability of muons decaying from charged pion and kaon using the fast simulation is shown in Figure 3.28 for different  $p_T$  cut of hadrons ( $\pi^\pm$  and  $K^\pm$ ). It is found that the probability of muon production from a hadron is proportional to the position of the



production vertex ( $V_z$ ) with a cut of  $p_{T,hadron} > 2$  GeV/ $c$  as shown in Figure 3.28.

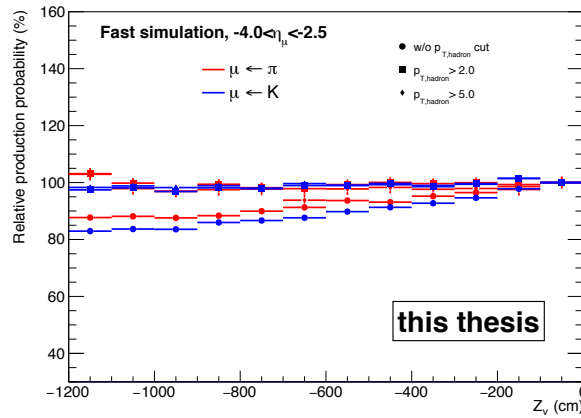


Figure 3.28: Relative production probability of muons from charged pion and kaon decay as a function of  $V_z$  in forward rapidity ( $-4 < \eta < -2.5$ ) with different  $p_{T,hadron}$  cuts.

The relative production probability of muons ( $p_{T,\mu} > 2$  GeV/ $c$ ) as a function of  $V_z$  and normalized to the bin content ( $-10 < V_z < 0$  cm) is obtained from the full simulation based on PYTHIA. This relative production probability of muons decaying from pion (left) and kaon (right) are shown in Figure 3.29.

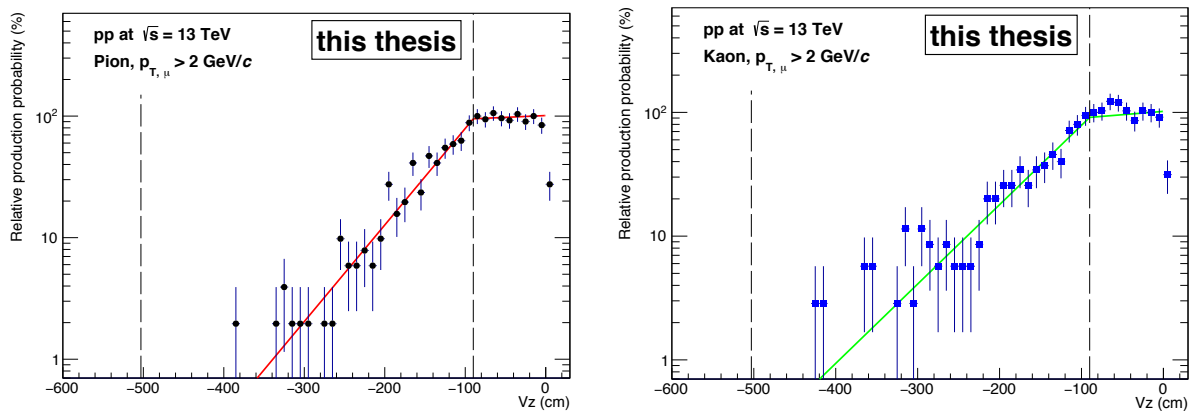


Figure 3.29: The relative production probability of muons from charged pion (left panel) and kaon (right panel) decay using full PYTHIA simulation. The corresponding fit functions are indicated (solid line) also.

Moreover, the decay vertex ( $V_z$ ) of pion and kaon decaying to muons can be described with a combination of two functions. These two functions depend on the position ( $|V_z|$ ) of the muon

production vertex and can be expressed as:

$$f_{decay}(V_z) = f_{free}(V_z) \times f_{abs}(V_z) \quad (3.24)$$

where,  $f_{free}(V_z) = 1$  if  $V_z \geq -90$  cm (before the front absorber) and  $f_{free}(V_z) = expo(V_z)$  if  $-503 \leq V_z < -90$  cm (inside the front absorber). However,  $f_{abs}(V_z) = expo(V_z)$  is used. The parametrization of the absorber effect for the muons decaying from charged pion and kaon has been estimated as shown in Figure 3.30.

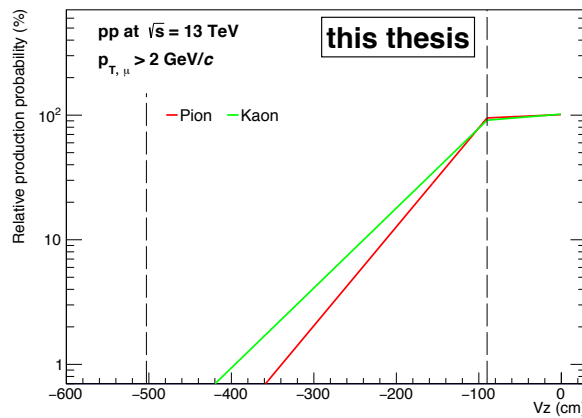


Figure 3.30: The parametrizaion for the relative production of muons from charged pion and kaon decay as a function of  $V_z$  in forward rapidity ( $2.5 < y < 4$ ) for muons with  $p_T > 2$  GeV/ $c$ .

### Results for the measurement of decay muon contribution

A fast simulation is performed to estimate the contribution of decay muons (muons decaying from primary charged pion and kaon) in forward rapidity ( $-4 < \eta < -2.5$ ). This fast simulation is used to obtain the  $p_T$  distribution of decay muons considering the weight according to the following steps:

- a)  $p_T$  extrapolation of midrapidity  $\pi^\pm$  and  $K^\pm$  towards high  $p_T$  region.
- b) Rapidity extrapolation.
- c)  $p_T$ - dependent rapidity extrapolation factor.

d) Parametrization of absorber effect.

The results obtained for decay muons and the corresponding systematic uncertainties from all the steps mentioned above have been discussed. A comparison of  $p_T$ - differential distribution of decay muons obtained using the rapidity extrapolation based on PYTHIA and PHOJET simulation is presented in Figure 3.31. This comparison is shown for decay muons from pion (left) and kaon (right). The bottom panel shows the ratio of the results obtained with PHOJET over PYTHIA. The relative error for the measurement of decay muons obtained from PYTHIA and PHOJET is almost constant and aggregate to  $\sim 0.3\%$  for pion and  $\sim 0.8\%$  for kaon respectively.

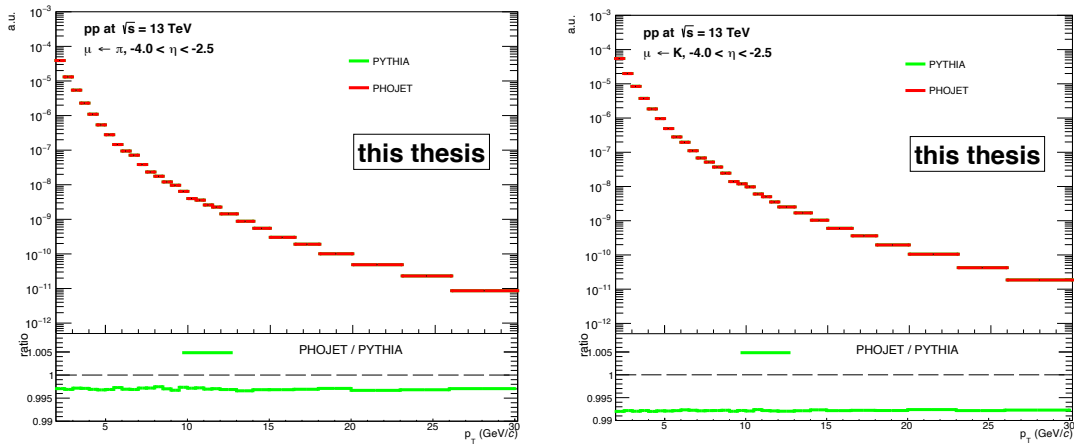


Figure 3.31: Comparison of  $p_T$ -distribution of muons decaying from charged pion (left) and kaon (right) obtained using rapidity extrapolation with PYTHIA and PHOJET.

Figure 3.32 displays a comparison in the production of muon decaying from charged pion (left panel) and kaon (right panel) at different conditions of  $p_T$ - dependent rapidity extrapolation. The bottom panels of Figure 3.32 show the ratios of the decay muons obtained with PYTHIA based on two CR (MPI and new QCD) schemes with respect to the results obtained without applying CR mechanism. A maximum relative uncertainty is obtained for the decay muons from pion (kaon) which is about 53% (54%) with MPI (CR=0) and is about 56% (59%) with new QCD (CR=1) with respect to the decay muons obtained without applying CR.

In Figure 3.33, muons decaying from charged pion (left panel) and kaon (right panel) for two CR schemes (MPI and new QCD) are also compared. The bottom panel shows the ratio of

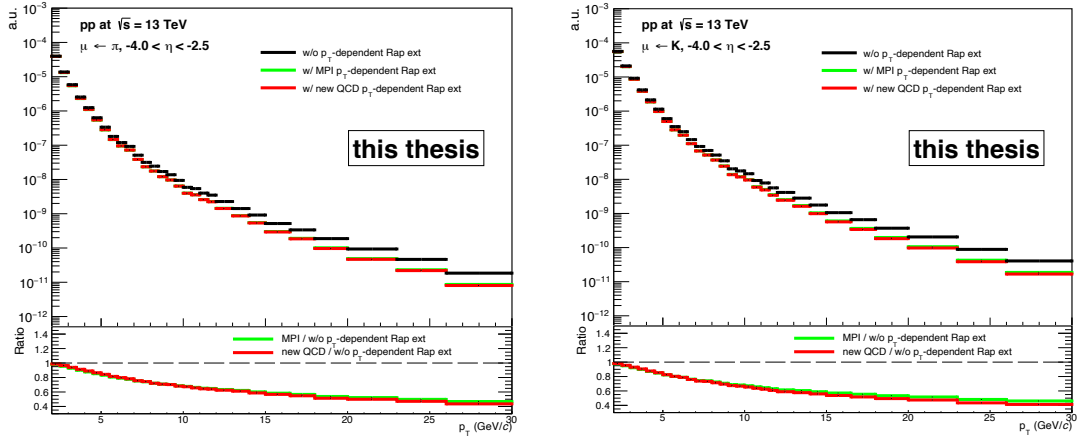


Figure 3.32:  $p_T$ -distribution of muons decaying from charged pion (left) and kaon (right) for different  $p_T$ -dependent rapidity extrapolation cases.

the results obtained with new QCD with respect to MPI. A maximum relative error of  $\sim 7\%$  ( $10\%$ ) is obtained for pion (kaon). These errors are used as a source of systematic uncertainties for measuring the decay muons obtained with  $p_T$ -dependent rapidity extrapolation.

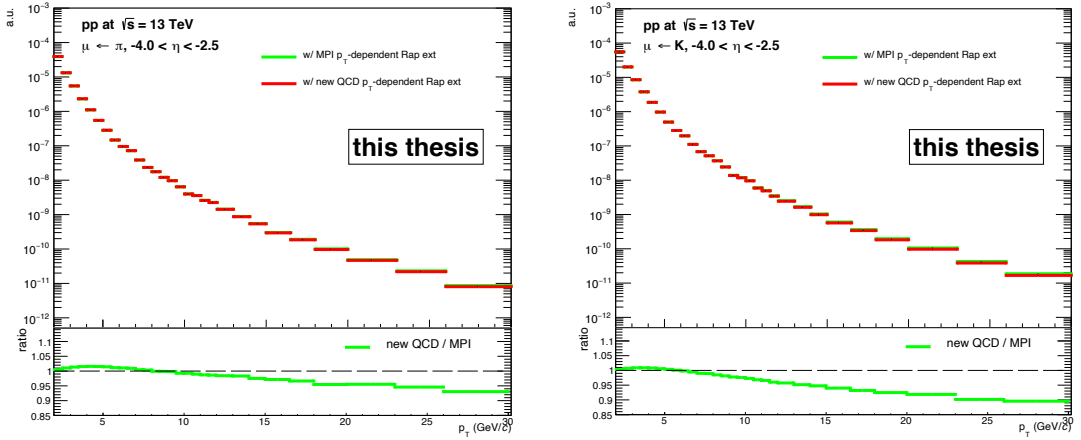


Figure 3.33: A comparison of  $p_T$ -distribution of muons decaying from charged pion (left) and kaon (right) with CR=0 (MPI) and CR=1 (new QCD) colour reconnection schemes.

A comparative study of muons decaying from charged pion (left) and kaon (kaon) obtained with the absorber parametrization (Eq. 3.24) and with a sharp cut on muon production vertex ( $V_z < 130$  cm) is shown in Figure 3.34. The bottom panel of Figure 3.34 shows a maximum relative error of  $\sim 20\%$ .

The decay muons from charged pion (left) and kaon (right) obtained with the input  $p_T$ -

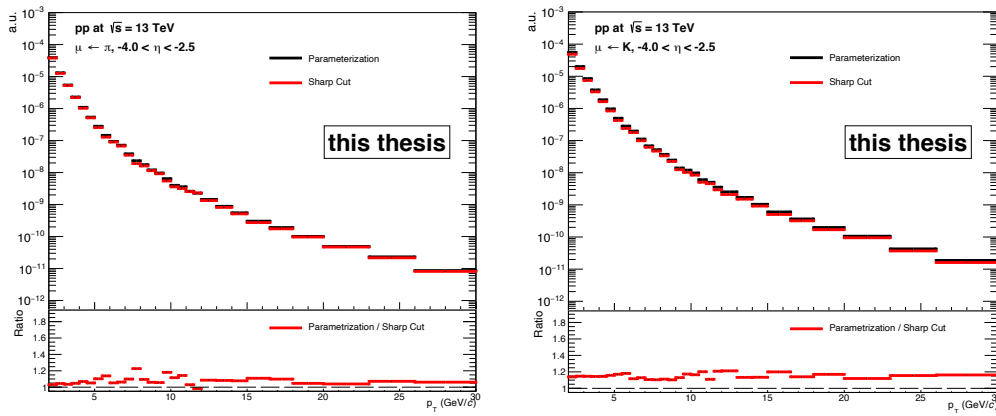


Figure 3.34: Comparative study of  $p_T$ -distribution of muons decaying from charged pion (left) and kaon (right) with the absorber parametrization and with vertex cut  $V_z < 130$  cm on muon production.

extrapolation at midrapidity using Tsallis distribution and a polynomial function are compared in Figure 3.35. A maximum relative difference in the measurement of muons decaying from pion and kaon using these two functions is  $\sim 10\%$  and  $\sim 7\%$  respectively. The relative error in the measurement of decay muons using these two functions is considered as a possible source of systematic uncertainty for the  $p_T$ -extrapolation. The total systematic uncertainty due to the  $p_T$ -extrapolation process has two contributions: i) the systematic uncertainty of the  $p_T$ -extrapolated input charged pion and kaon propagated to the muons and ii) systematic uncertainty to obtain decay muons due to the  $p_T$ -extrapolation using different functions. These two contributions are added in quadrature to calculate the total systematic uncertainty for the  $p_T$ -extrapolation process. The uncertainties for the measurement of decay muons due to the  $p_T$ -extrapolation of input pion/kaon spectra, extrapolation with various functions (Tsallis & power law) and the total systematic are shown for pion (left) and kaon (right) in Figure 3.36. A total systematic uncertainty of  $\sim 17\%$  for  $\pi \rightarrow \mu$  and  $\sim 21\%$  for  $K \rightarrow \mu$  respectively is calculated.

The estimated  $p_T$ -distributions of muons decaying from charged pion and kaon at forward rapidity ( $-4 < \eta < -2.5$ ) has been shown in the left panel of Figure 3.37. The open box is representing the total systematic uncertainty. The systematic uncertainties from various sources along with total uncertainty are presented in the right panel of Figure 3.37. The systematic uncertainties from different sources in the measurement of muons decaying from

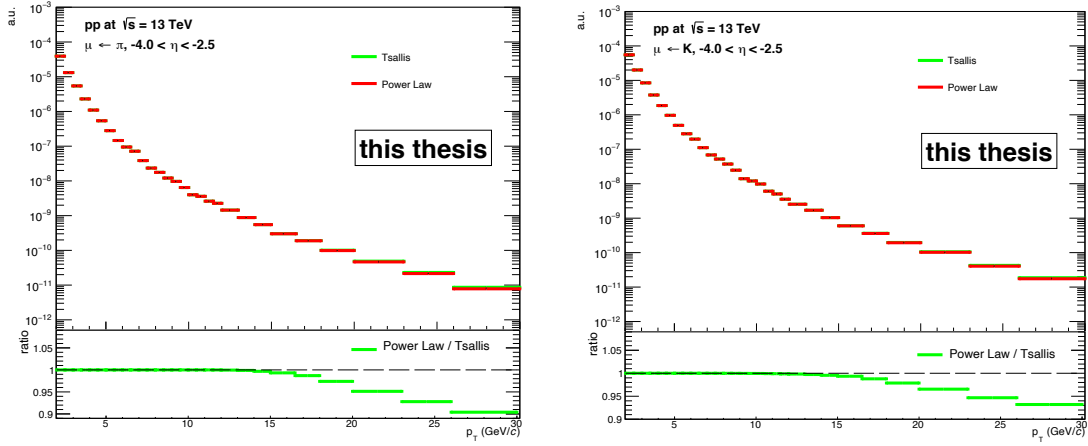


Figure 3.35: Comparison of decay muons  $p_T$ -distribution from charged pion (left) and kaon (right) is obtained with the  $p_T$ -extrapolation using Tsallis distribution and a polynomial function.

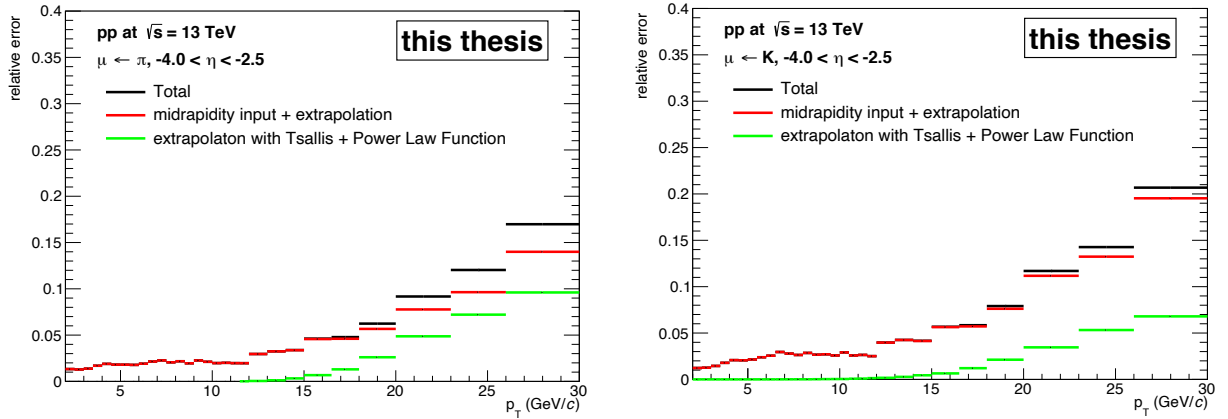


Figure 3.36: Systematic uncertainties for the measurement of decay muons during the  $p_T$ -extrapolation process for pion (left) and kaon (right).

charged pion and kaon amounts for i) charged pion and kaon  $p_T$ -spectra extrapolation towards high  $p_T$ -region: varies from  $<1\%$  to  $\sim 17\%$  and  $\sim 21\%$  for pion and kaon respectively, ii) mid to forward rapidity extrapolation:  $<1\%$  for both the pion and kaon, iii)  $p_T$ -dependent rapidity extrapolation: varies from  $<1\%$  to  $\sim 8.5\%$  and  $\sim 10.4\%$  for pion and kaon respectively, iv) Absorber effect: not implemented. All these systematic errors are added in quadrature to calculate the total systematic uncertainty. The total systematic uncertainty in the measurement of decay muons varies for pion (kaon) from  $\sim 1.5\%$  ( $1.5\%$ ) to  $\sim 18.5\%$  ( $23\%$ ) in the range  $2 \leq p_T \leq 30$  GeV/ $c$ . Finally, this estimated total systematic uncertainty is propagated to the

results obtained for the production cross-section of heavy flavour decay muons.

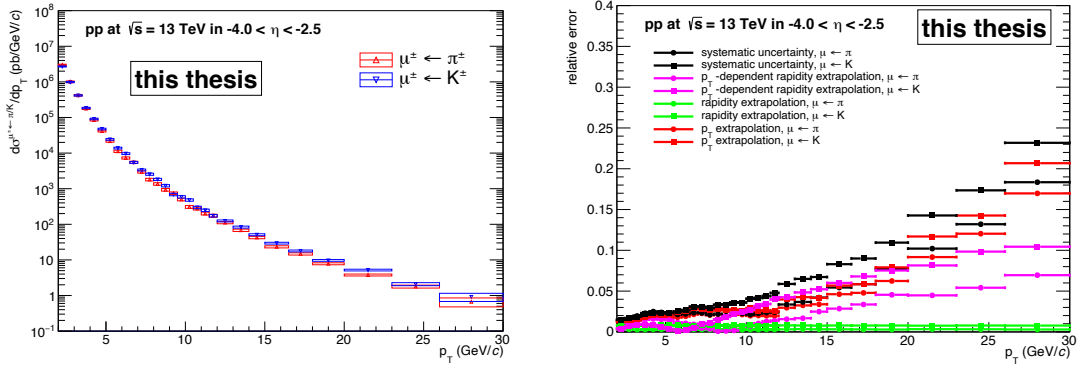


Figure 3.37:  $p_T$ -distribution of muons decaying from charged pion and kaon (left) in forward rapidity ( $-4 < \eta < -2.5$ ) and the corresponding systematic uncertainties (right).

The measurements of decay muons from charged pion (left panel) and kaon (right panel) with respect to the inclusive muons at different rapidity intervals are shown in Figure 3.38. The contributions are found to be very similar to both from pion and kaon. The fractional contribution of muons decaying from pion (kaon) relative to the inclusive muons in the full acceptance ( $-4 < \eta < -2.5$ ) varies from  $\sim 15\%$  ( $14\%$ ) to below  $1\%$  in the range of  $2 < p_T < 30$  GeV/ $c$ . The fractional contributions actually started to remain below  $1\%$  for pion (kaon) at  $p_T \approx 14$  ( $13$ ) GeV/ $c$ . It is evident from Figure 3.38 that the fraction of decay muons with reference to the inclusive muons at different sub-rapidity intervals decreases as one move towards more forward regions.

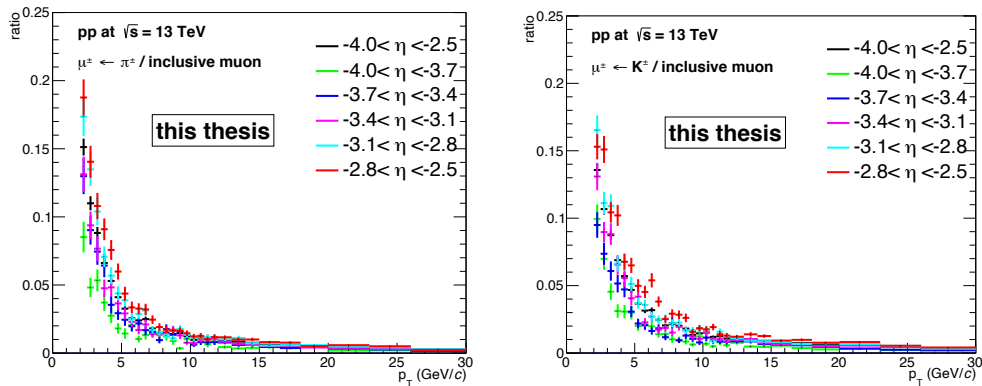


Figure 3.38: The ratio of decay muons  $p_T$ -distribution from charged pion (left) and kaon (right) with respect to the inclusive muons at different pseudorapidity intervals.

### 3.7.2 Secondary Muons

There is possibility of multiple scattering when the primary particles pass through the material of the front absorber. The secondary light hadrons are produced due to such multiple scattering and they decay further to muons are called as secondary muons. To estimate the contribution of secondary muons, a full simulation based on PYTHIA (LHC18f1\_extra) and PHOJET (LHC17h7b\_extra) have been used. The response of the detector effect is considered using the transport code with GEANT3. The  $p_T$ -distribution of muons decaying from various sources are shown in the left panel of Figure 3.39 using full PYTHIA8 simulation. The fractional contributions of secondary muons with respect to the inclusive muons are estimated within the full acceptance ( $-4 < \eta < -2.5$ ) and at different sub-rapidity intervals also. These fractional contributions are shown in the right panel of Figure 3.39. It is found that the contribution of secondary muons is  $\sim 3.2\%$  at  $p_T = 2$  GeV/ $c$  and less than 1% for  $p_T > 4$  GeV/ $c$  within the full acceptance. At different sub-rapidity intervals, it varies between 1.5% – 5% at  $p_T = 2$  GeV/ $c$ . It is also seen that the contribution of secondary muons decreases towards forward rapidity as well at high  $p_T$ -regions and negligible for  $p_T > 8$  GeV/ $c$  in the case of PYTHIA8 simulation.

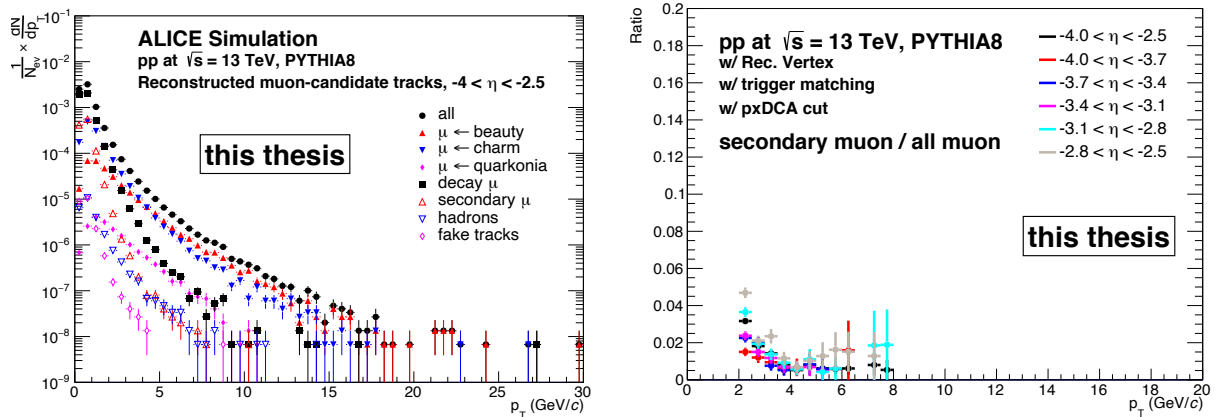


Figure 3.39:  $p_T$ -distribution of muons decaying from various sources using full MC PYTHIA8 simulation with GEANT3 in the range  $-4 < \eta < -2.5$  (left). The fractional contribution of secondary muons with respect to the inclusive muons at different rapidity intervals (right).

In the left panel of Figure 3.40, a comparison in the production of secondary muons between PYTHIA8 and PHOJET simulations with the transport code GEANT3 in the full ac-



ceptance ( $-4 < \eta < -2.5$ ) is shown. In addition, another simulation for PYTHIA8 using GEANT4 has been performed to check any systematic dependency in the transport codes. The same comparison between the two transport codes GEANT3 and GEANT4 using PYTHIA8 simulation has been presented as shown in the right panel of Figure 3.40. In the legend of Figure 3.40, “pythia8G3”, “pythia8G4” and “phojetG3” corresponds to the simulations with PYTHIA8+GEANT3, PYTHIA8+GEANT4 and PHOJET+GEANT3 respectively. A very similar contribution of the secondary muons from GEANT3 and GEANT4 simulations are obtained in the low  $p_T$  region ( $p_T < 4$  GeV/c). The relative difference in the  $p_T$  distributions of the secondary muons in the range  $2 < p_T < 8$  GeV/c is obtained and then used to calculate the systematic uncertainty associated to the transport codes. This leads to a systematic error of  $\sim 70\%$  in the measurement of secondary muons.

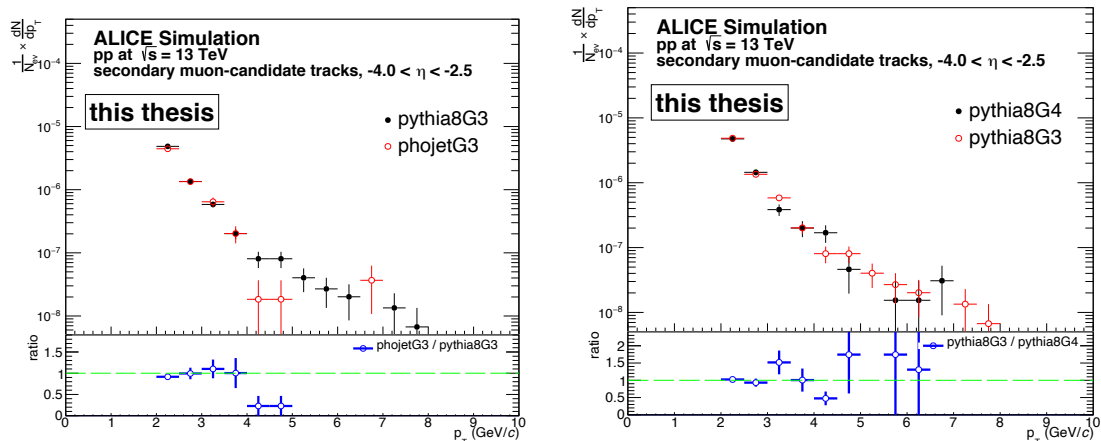


Figure 3.40: Comparison of  $p_T$ -distributions of secondary muons between PYTHIA8 and PHOJET simulation using GEANT3 in the range  $-4 < \eta < -2.5$  (left). The same comparison between GEANT3 and GEANT4 simulation with PYTHIA8 (right).

A comparison of the secondary muons and decay muons (muons decaying from primary charged pion and kaon) using PYTHIA8 and PHOJET simulations has been done also. In case of PYTHIA8, the results are presented with two transport codes GEANT3 and GEANT4. The fraction of secondary muons with respect to the decay muons for PHOJET with GEANT3 (top), PYTHIA8 with GEANT3 (bottom, left) and PYTHIA8 with GEANT4 (bottom, right) are shown in Figure 3.41 at the forward rapidity ( $-4 < \eta < -2.5$ ). These fractional contributions are very similar for all the cases upto  $p_T = 4$  GeV/c and does not depend much on the transport

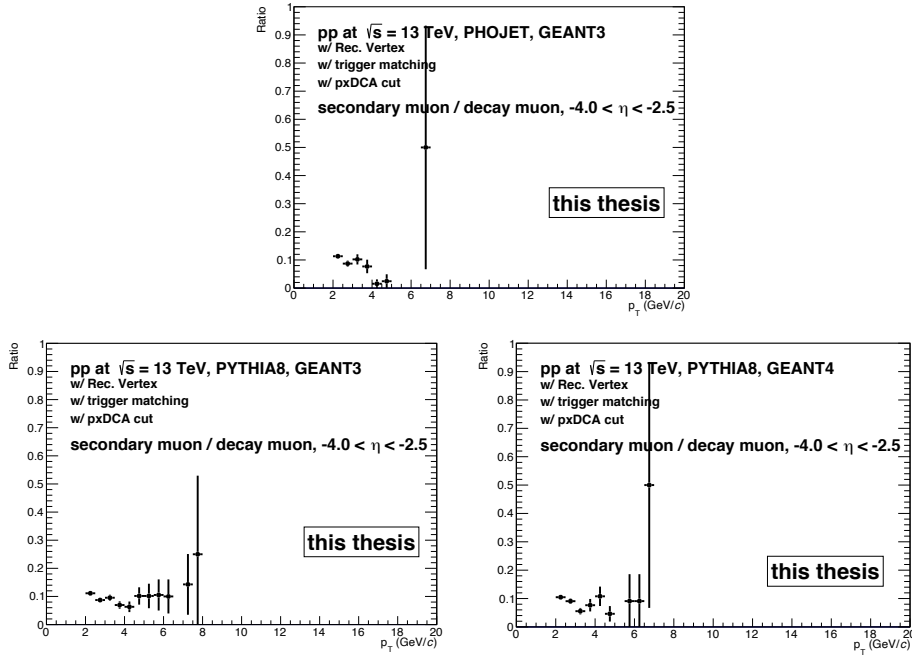


Figure 3.41: The ratio in the  $p_T$ -distribution of secondary muons with respect to the decay muons using the MC simulations of PHOJET with GEANT3 (top), PYTHIA8 with GEANT3 (bottom left) and PYTHIA8 with GEANT4 (bottom right) at the forward rapidity ( $-4 < \eta < -2.5$ ).

codes as well. The ratio shows the secondary muons is about 10% of decay muons and almost independent of  $p_T$  upto  $p_T = 4$  GeV/c.

### 3.7.3 Muons decaying from W and Z/ $\gamma^*$

The estimation of muons decaying from W and Z-boson/ $\gamma^*$  is done using a particle event generator called PPositive Weight Hardest Emission Generator (POWHEG) [13]. POWHEG is used to generate hard events for various processes involving heavy quarks, Higgs boson and the electroweak bosons ( $W^\pm$ , Z). In POWHEG, the calculation is upto NLO (Next-to-Leading Order) and the  $Z^0/\gamma^*$  interference is included. This hard event generator POWHEG is further interfaced with a shower Monte Carlo (MC) PYTHIA6 program adding the detector response using GEANT3 [14]. Two Parton Distribution Functions (PDF) CT10nlo and CTEQ6l are used to obtain the systematic uncertainties in the measurement of  $W^\pm$  & Z/ $\gamma^*$  decay muons. The transverse momentum (top) and rapidity (bottom) distributions of muons decaying from

$W^\pm$  and  $Z/\gamma^*$  using POWHEG simulation using these two PDFs CT10nlo (left) and CTEQ6l (right) are shown in Figure 3.42. This work is presented in Ref. [15].

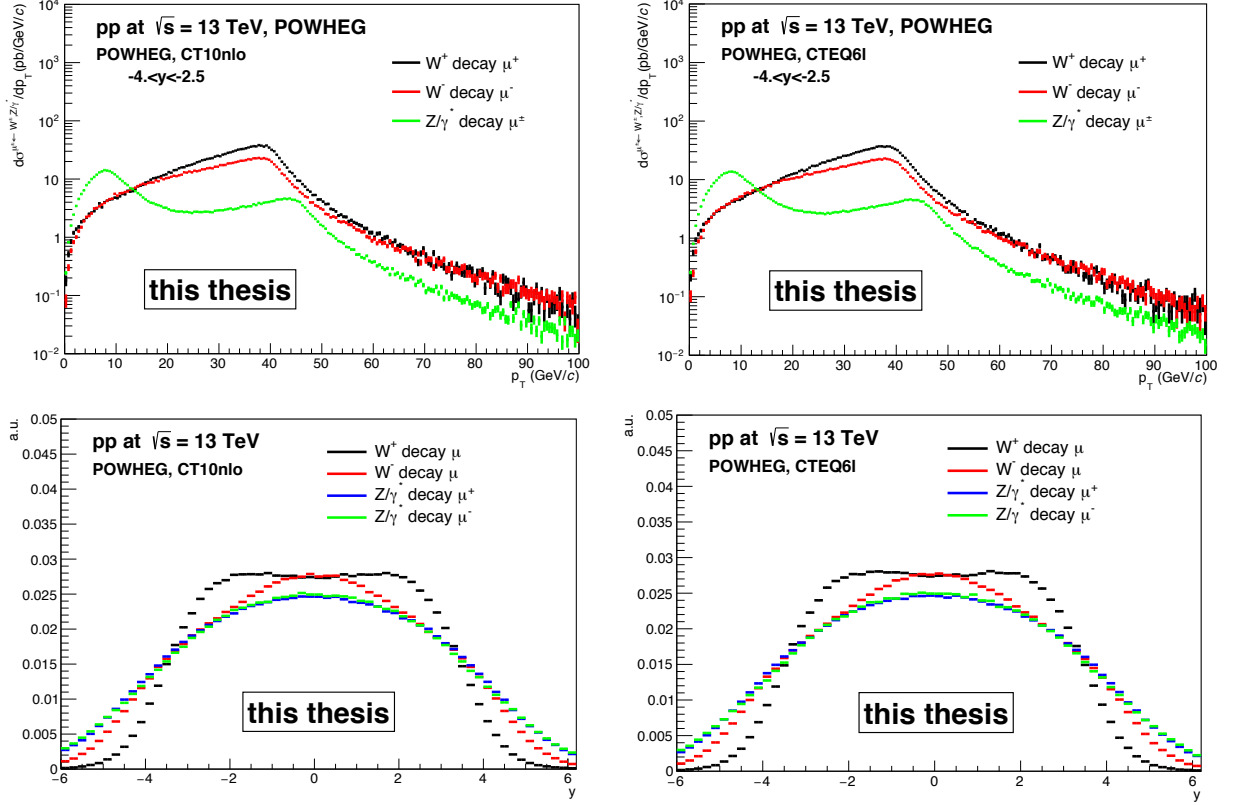


Figure 3.42:  $p_T$ - (top) and  $y$ - (bottom) distribution of muons decaying from  $W^\pm$  and  $Z/\gamma^*$  for two Parton Distribution Functions (PDF) CT10nlo (left) and CTEQ6l (right) respectively using POWHEG simulation.

A comparison in the ratio of  $W^\pm$  &  $Z/\gamma^*$  decay muons at different rapidity windows with respect to the mid-rapidity ( $|y| < 1$ ) between the two PDFs CT10nlo & CTEQ6l has been presented in the left panel of Figure 3.43. It is observed that the production of  $W^\pm$  &  $Z/\gamma^*$  decay muon decreases as one moves towards forward rapidity with reference to the mid-rapidity. A similar comparison in the ratio of  $W^\pm$  &  $Z/\gamma^*$  decay muons at different rapidity intervals is done between two center-of-mass energies  $\sqrt{s} = 5.02$  TeV and 13 TeV which is shown in the right panel of Figure 3.43. It is noticed that the production of  $W^\pm$  &  $Z/\gamma^*$  decay muons at forward rapidity with reference to the midrapidity ( $|y| < 1$ ) increases with energy.

The fraction of muons decaying from  $W^\pm$  &  $Z/\gamma^*$  relative to the inclusive muons in the range  $2 < p_T < 30$  GeV/ $c$  at different rapidity intervals are shown in Figure 3.44. It is seen

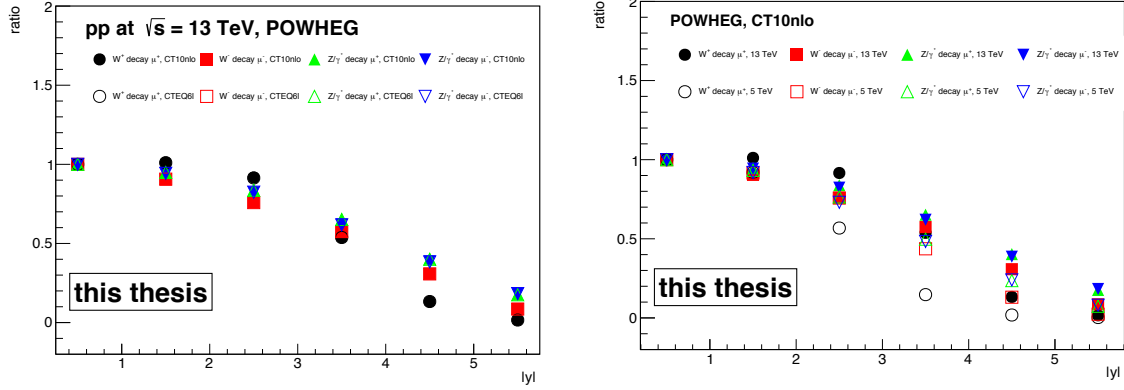


Figure 3.43: Comparison of  $W^\pm$  &  $Z/\gamma^*$  decay muons production at different rapidity intervals with respect to the mid-rapidity ( $|y| < 1$ ) for two Parton Distribution Functions (PDF) CT10nlo and CTEQ6l (left panel) and two center-of-mass energies  $\sqrt{s} = 5.02$  TeV and 13 TeV (right panel) respectively.

from the left panel of Figure 3.44 that the contribution of single muons decaying from  $W^\pm$  &  $Z/\gamma^*$  with respect to the inclusive muons is increasing with increase in  $p_T$  and also increases as one moves towards more forward rapidity regions. The same ratio within the full acceptance ( $-4 < \eta < -2.5$ ) is presented in the right panel of Figure 3.44. The fraction of  $W^\pm$  &  $Z/\gamma^*$ -decay muons to the inclusive single muons within  $-4 < \eta < -2.5$  is very negligible at lower  $p_T$ -regions, it becomes at least 1% at  $p_T = 15$  GeV/c, about 3.2% at  $p_T = 20$  GeV/c and then increased rapidly upto  $\sim 29\%$  at  $p_T = 30$  GeV/c. In different sub-rapidity regions, the fractional contribution varies from  $\sim 22\%$  to  $\sim 38\%$  at  $p_T = 30$  GeV/c.

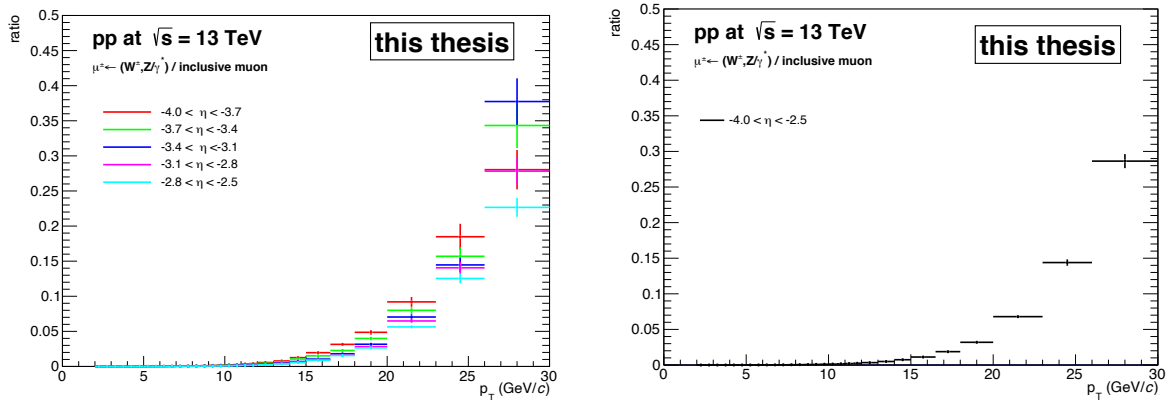


Figure 3.44: The ratio of  $W^\pm$  &  $Z/\gamma^*$  decay muons relative to the inclusive muons as a function of  $p_T$  at different intervals in the range  $-4 < \eta < -2.5$  (left). The same is for the full acceptance  $-4 < \eta < -2.5$  (right).

The estimation of systematic uncertainty for the measurement of muons decaying from  $W^\pm$  &  $Z/\gamma^*$  is done by considering the two PDFs CT10nlo and CTEQ6l using POWHEG simulation. This leads to systematic uncertainty of  $\sim 8.1\%$  for W decays and  $\sim 1.9\%$  for Z decays respectively. So, a total systematic uncertainty of  $\sim 8.3\%$  is estimated in the measurement of muons from  $W^\pm$  &  $Z/\gamma^*$  decays.

### 3.7.4 Jpsi decay muon background contribution

To measure the contribution of muons decaying from  $J/\psi$  to the inclusive single muons, a similar approach using fast simulation has been used as described in section 3.7.1. The muons from  $J/\psi$  decays are obtained according to a fast simulation using the steps as following:

- a) Generation of Jpsi with a uniform  $p_T$  and y distribution.
- b) Forced approach for  $J/\psi$  to decay into dimuon using PYTHIA decayer.
- c) Calculation of the weight factors for the muons decaying from  $J/\psi$  according to the  $p_T$  and y extrapolated distribution of  $J/\psi$ .
- d) Correction of the  $p_T$ -distribution of the muons with the branching fraction (5.96%) for the decay of  $J/\psi$  to dimuon.

In the estimation of single muons decaying from  $J/\psi$ , the transverse momentum ( $p_T$ ) and rapidity (y) distribution of inclusive  $J/\psi$  measured with ALICE detector at forward rapidity ( $2.5 < y < 4$ ) at center of mass energy  $\sqrt{s} = 13$  TeV are used as inputs [16]. The input  $p_T$ -distribution of inclusive  $J/\psi$  ranges from 0 to 30 GeV/c. In order to obtain the muons decaying from  $J/\psi$  upto  $p_T = 30$  GeV/c, the transverse momentum ( $p_T$ ) distribution of  $J/\psi$  is extrapolated upto 50 GeV/c. The extrapolated transverse momentum and rapidity distributions of  $J/\psi$  at  $\sqrt{s} = 13$  TeV are shown in left and right panels of Figure 3.45 respectively. The  $p_T$ - and y- extrapolation have been done using Lavy-Tsallis distribution (Eq. 3.21) and a polynomial function (Eq. 3.25) as following

$$f(y) = p_0 (1 + p_1 y^2) \quad (3.25)$$

where,  $p_0$  and  $p_1$  are the free parameters.

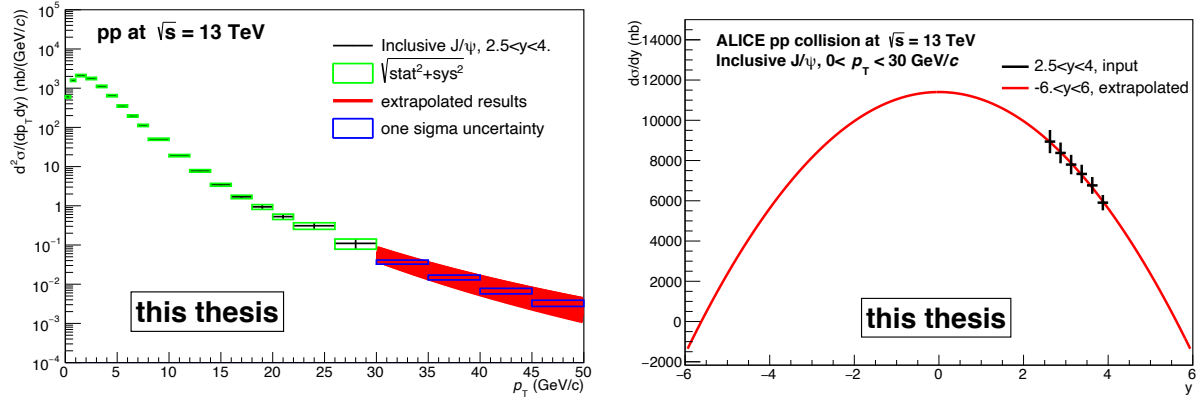


Figure 3.45: The extrapolated  $p_T$ - (left) and  $y$ - (right) differential production cross-section of  $J/\psi$  in pp collisions at  $\sqrt{s} = 13$  TeV.

The estimated  $p_T$ -distribution of muons decaying from  $J/\psi$  and the inclusive single muons within the full acceptance ( $-4 < \eta < -2.5$ ) are shown in Figure 3.46. Figure 3.47 presents the  $p_T$ -differential production cross-section of muons from  $J/\psi$  decay (left panel) and corresponding fraction with respect to the inclusive muons (right panel) at different pseudo-rapidity regions. The contribution of  $J/\psi$  decay muons with respect to the inclusive muons is maximum of about 7% in the  $p_T$  range between 5 - 14 GeV/ $c$  in the full acceptance ( $-4 < \eta < -2.5$ ). It is noticed that the  $J/\psi$  contribution decreases as one moves towards high  $p_T$  region for  $p_T > 14$  GeV/ $c$ . However, the fractional contribution of  $J/\psi$  at different sub-rapidity intervals varies between  $\sim 4.5\% - 9\%$  in the  $p_T$  range 5 - 14 GeV/ $c$ .

The left panel of Figure 3.48 presents a comparison in the  $p_T$ -distribution of  $J/\psi$ -decay muons obtained by  $p_T$ -extrapolation with Tsallis (Eq. 3.21), Polynomial function1 (Eq. 3.26) and Polynomial function2 (Eq. 3.27). The relative uncertainty between Tsallis and Polynomial 1 varies upto  $\sim 21\%$  while it varies upto  $\sim 39\%$  between Tsallis and Polynomial 2. The systematic uncertainty due to the input extrapolated  $p_T$ -spectra of  $J/\psi$  is propagated to the measurement of muons from  $J/\psi$  decay which contributes systematic uncertainty upto  $\sim 22\%$ . All these systematics are added in quadrature and the total uncertainties due to  $p_T$ -

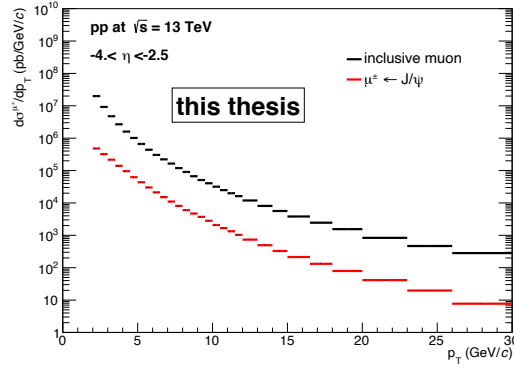


Figure 3.46: The estimated  $p_T$ -differential production cross-section of muons decaying from  $J/\psi$  (red line) and inclusive single muons (black line) in pp collisions at  $\sqrt{s} = 13$  TeV.

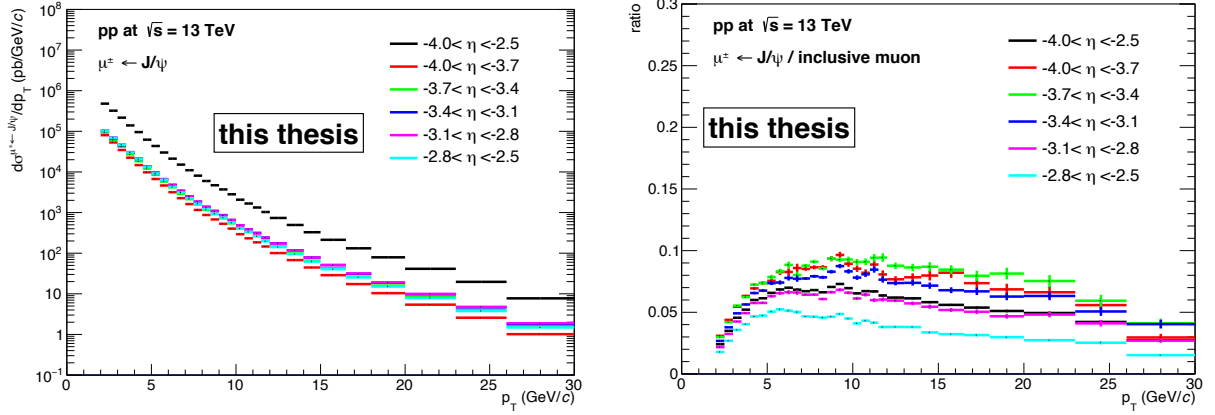


Figure 3.47: The  $p_T$ -distribution of muons decaying from  $J/\psi$  (left panel) and the corresponding fraction relative to the inclusive single muons (right) at different intervals in the range  $-4 < \eta < -2.5$ .

extrapolation is measured upto  $\sim 50\%$ . The various contributions of systematic uncertainties in the  $p_T$ -extrapolation process are shown in the right panel of Figure 3.48.

$$f(p_T) = C \times \frac{p_T}{\left(1 + \left(\frac{p_T}{p_0}\right)^2\right)^n} \quad (3.26)$$

$$f(p_T) = \frac{p_0}{(p_1^2 + p_T^2)^{p_2}} \quad (3.27)$$

where,  $C$ ,  $p_0$ ,  $p_1$ ,  $p_2$  and  $n$  are the free parameters.

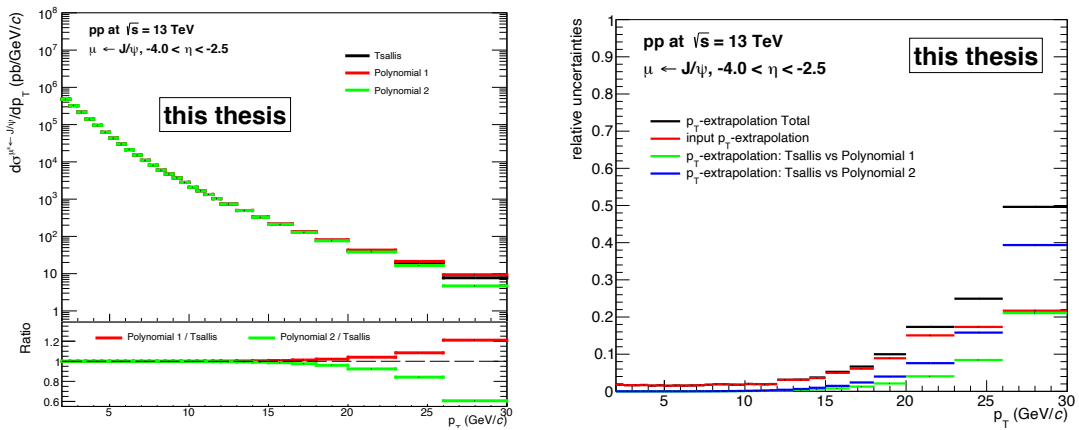


Figure 3.48: The  $p_T$ -distribution of muons decaying from  $J/\psi$  using  $p_T$ -extrapolation with Tsallis, Polynomial function1 and Polynomial function2 (left panel). The total systematic uncertainties with various contributions for  $p_T$ -extrapolation of  $J/\psi$  (right panel).

## 3.8 Systematic uncertainty

The various sources of systematic uncertainties are studied to obtain the differential production cross-section of heavy flavour decay muon as a function of transverse momentum ( $p_T$ ) and rapidity ( $y$ ). The sources of such systematic uncertainties are mainly from the measurement of inclusive muons and various background contributions. The systematic uncertainty on the yield of inclusive muons comes from the detector response generally.

### 3.8.1 Detector response

The systematic uncertainty on acceptance times efficiency ( $A \times \epsilon$ ) corrections includes the systematic uncertainties associated with muon tracking efficiency and muon trigger efficiency. A systematic uncertainty related to the matching efficiency due to the track reconstructed in muon tracking and trigger chambers is also considered. Finally, the systematic uncertainty on the track resolution and global alignment of the detector have been taken into account. The systematic uncertainties on muon tracking and trigger efficiency and also for matching the tracks between tracking chambers and trigger chambers are already measured for the production



of  $J/\psi$  in pp collisions at  $\sqrt{s} = 13$  TeV [16]. These published values are normalized by a factor of two to obtain the systematic uncertainties for single muons since  $J/\psi$  is reconstructed in dimuon channel. The following systematic uncertainties for this Heavy flavour decay muon production measurement in pp collisions at  $\sqrt{s} = 13$  TeV are discussed.

### Uncertainty on track efficiency

The systematic uncertainty in the measurement of single muons tracking efficiency is calculated by comparing the tracking efficiency obtained between data and MC simulation. The tracking efficiency measurements are done on MSL and MSH triggered events data sample and the corresponding tuned MC simulations. A systematic uncertainty of  $\sim 2\%$  is observed in average for single muons as discussed in Ref. [16].

### Uncertainty on trigger efficiency

To obtain the systematic uncertainty on trigger efficiency, two contributions have been considered: one, the difference in the trigger response between data and MC simulation, the other is the uncertainty from the intrinsic trigger chamber efficiency. The systematic uncertainty is estimated comparing the shape of trigger response distribution obtained from data and MC. The trigger responses have been measured for the single muon trigger Lpt ( $p_T$  threshold of 1 GeV/ $c$ ) with that of single muon MB trigger Apt ( $p_T$  threshold of 0.5 GeV/ $c$ ). A total 4% systematic uncertainty on the trigger efficiency is estimated by comparing the influence of the two single muon triggers (Lpt and Apt) of  $J/\psi$  [16]. This total uncertainty 4% includes the systematic uncertainty of 1.5% arising from the intrinsic trigger chamber efficiency. No systematic uncertainty measurement for the trigger response with Hpt ( $p_T$  threshold of 4 GeV/ $c$ ) trigger is done in the said  $J/\psi$  analysis. Therefore, the same value of systematic uncertainty arising from the trigger response with Lpt has been used for Hpt trigger in this HFM analysis. The systematic uncertainty of 4% on trigger efficiency is calculated for dimuon channel of  $J/\psi$ . So, 2% systematic uncertainty is considered for single muon triggers (Lpt and Hpt) in this single muon analysis.

## Uncertainty on track-trigger matching

A systematic uncertainty of 1% is reported for the precision measurement in the efficiency of matching the tracks in the muon tracking system and the tracks in the muon trigger system by means of simulations with respect to that data of  $J/\psi$  measurement [16]. This uncertainty measurement is based on the distribution of  $\chi^2$  used to perform this track-trigger matching condition. Finally, a value of 0.5% is considered as systematic uncertainty on track-trigger matching for this HFM analysis.

## Uncertainty on tracking resolution and misalignment of detector

The estimation of the systematic uncertainties on the cluster resolution for reconstructing muon tracks and a correction for the global misalignment of detector are done using a `AliMuonTrackSmearing` analysis task. The cluster resolution of the muon chamber is corrected by means of simulation in order to match the observed track resolution during data taking. A parametrization using Crystal Ball (CB) functions in the distribution of cluster and the reconstructed track positions on each chamber is applied. The parameters are obtained originally by tuning the CB on the data in pp collisions at  $\sqrt{s} = 5.02$  TeV. Since, the resolution is enough stable in Run 2, this parametrization in case of pp collisions at  $\sqrt{s} = 13$  TeV could be used. The following parameters used in the analysis task of Ref. [14] have been used further for this HFM analysis :

- **Data-tuned CB parameters:**

```
AliTaskMuonTrackSmearing *muonTrackSmearingTask = new AliTaskMuonTrackSmearing ("TaskMuonTrackSmearing", AliMuonTrackSmearing::kCrystalBall);
muonTrackSmearingTask->GetMuonTrackSmearing().SetSigmaxChSt1(0.000430);
muonTrackSmearingTask->GetMuonTrackSmearing().SetSigmayChSt1(0.000095);
muonTrackSmearingTask->GetMuonTrackSmearing().SetSigmayCh(0.000125);
muonTrackSmearingTask->GetMuonTrackSmearing().SetCrystalBallParams(1.907786,
1.846464, 1.587050, 1.750238, 1.331549, 1.941949);
```

The global misalignment shift is taken into account by measuring the  $\mu^+/\mu^-$  ratio in the  $p_T$  distribution of inclusive single muons. The measurement is done in the  $p_T$ -range where the contribution of heavy flavour decay muons is supposed to be maximum. For this, two  $p_T$  regions:  $10 < p_T < 20$  GeV/ $c$  and  $10 < p_T < 15$  GeV/ $c$  have been selected in the data sample. In this regard, a MC simulation is performed for the production of heavy flavour decay muon. The  $p_T$ - and  $y$ - differential production cross-section are obtained by the prediction of FONLL (Fixed-Order + Next-to-Leading Logarithms) calculations [4].

In order to match the  $\mu^+/\mu^-$  ratio obtained in data, the tuning of the smearing parameter ( $\sigma_{shift}$ ) is done in addition to the CB resolution parameters in the simulation. The  $\mu^+/\mu^-$  ratio is evaluated at various  $\sigma_{shift}$  values in the simulation which are listed in Table 3.3. A comparison in the  $\mu^+/\mu^-$  ratio for both the selected  $p_T$  ranges is done. Since both the selected  $p_T$  ranges are used for the MSH triggered data sample, the matching of this  $\mu^+/\mu^-$  ratio is done only for MSH triggered events. Table 3.3 summarizes the  $\mu^+/\mu^-$  ratios obtained in data and for various tuning of  $\sigma_{shift}$  used in simulation. The  $\sigma_{shift} = 3.25$  is found to be the best value to reproduce the  $\mu^+/\mu^-$  ratio obtained in data and does not differ in the two selected  $p_T$  ranges as indicated in Table 3.3.

Table 3.3: The comparison of  $\mu^+/\mu^-$  ratio obtained in data (LHC16k) and in FONLL based full MC simulation for various tuned values of  $\sigma_{shift}$  in two selected  $p_T$  ranges.

$\mu^+/\mu^-$	data	3.1	3.2	3.25	3.4	3.55	3.6
$10 < p_T < 20$ GeV/ $c$	0.787	0.794	0.79	0.787	0.778	0.775	0.773
$10 < p_T < 15$ GeV/ $c$	0.801	0.808	0.805	0.801	0.795	0.799	0.791

Finally, the systematic uncertainty due to the track resolution and misalignment is estimated from the difference of the muon  $p_T$  spectra based on simulations with  $\sigma_{shift}=0$  and  $\sigma_{shift} = 3.25$ . The ratio of the transverse momentum ( $p_T$ ) distribution of muons using simulation with  $\sigma_{shift} = 3.25$  with respect to that measured with  $\sigma_{shift} = 0$  is shown in Figure 3.49. This leads to systematic uncertainties vary from a small value ( $< 1\%$ ) to a maximum of  $\sim 7.7\%$  at  $p_T = 30$  GeV/ $c$  in the full acceptance ( $-4 < \eta < -2.5$ ). Whereas, at different sub-rapidity intervals, it varies from  $\sim 2.1\%$  to  $\sim 18.2\%$  at the highest  $p_T$  bin ( $p_T = 30$  GeV/ $c$ ).

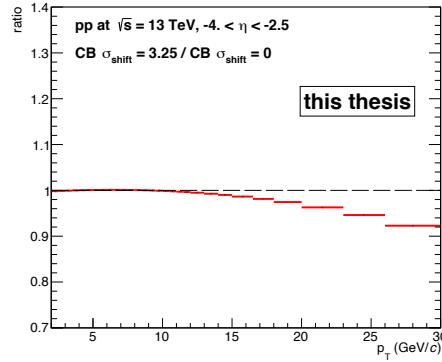


Figure 3.49: Ratio of the  $p_T$ -distribution of muons using  $\sigma_{shift} = 3.25$  with respect to  $\sigma_{shift} = 0$  at forward rapidity ( $-4 < \eta < -2.5$ ).

### 3.8.2 Systematic uncertainty from background sources

In section 3.7, the various sources of background contribution for the measurement of heavy flavour decay muon production in pp collisions at  $\sqrt{s} = 13$  TeV have been discussed. The estimated production cross-sections of muons decaying from various background sources (left) and their corresponding ratio with respect to the inclusive muons (right) as a function of transverse momentum at forward rapidity ( $-4 < \eta < -2.5$ ) have been presented in Figure 3.50. The vertical error bars and open boxes are representing the statistical and systematic uncertainties respectively.

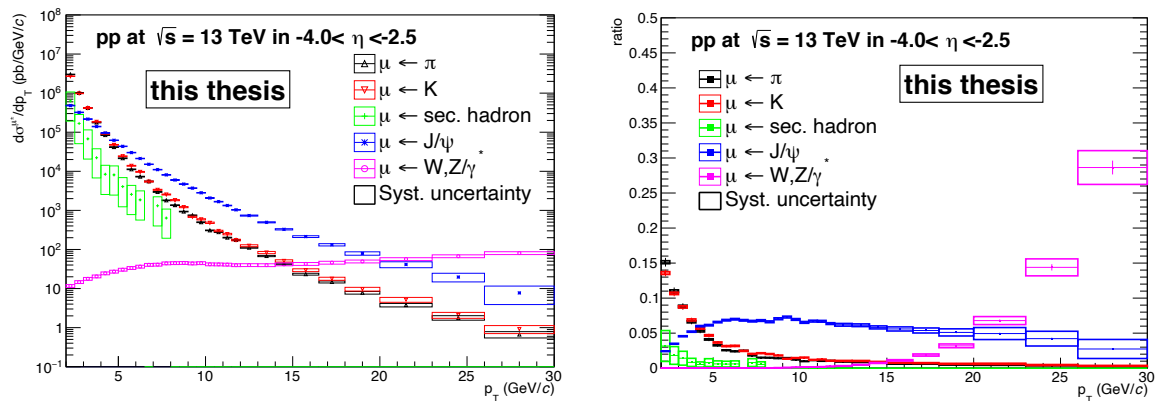


Figure 3.50: The estimated background contribution from various sources (left) and their corresponding ratio with respect to the inclusive muons (right) as a function of  $p_T$  at forward rapidity ( $-4 < \eta < -2.5$ ). The vertical error bars and open boxes are representing their corresponding statistical and systematic uncertainties respectively.

The systematic uncertainties associated with the various contributions in the measurement of the  $p_T$ -differential production cross-section of heavy flavour decay muons in  $-4 < \eta < -2.5$  are mentioned in table 3.4. The total systematic uncertainty is obtained by the quadratic sum of each of the systematic uncertainty from various sources as listed in table 3.4. The total systematic uncertainty along with the contributions from various sources are presented as a function of transverse momentum in Figure 3.51. The contribution of 2.1% systematic uncertainty on the integrated luminosity has been excluded from the total uncertainty measurement considering the fact that it is fully correlated with  $p_T$ . The total systematic uncertainty varies from a minimum value of  $\sim 3\%$  to maximum of  $\sim 9\%$  in the range  $2 < p_T < 30$  GeV/ $c$ . The maximum contribution in the high  $p_T$  region ( $26 < p_T < 30$  GeV/ $c$ ) is from the uncertainty measured due to track resolution and misalignment.

Table 3.4: Systematic uncertainties associated to the various sources in the measurement of  $p_T$ -differential production cross-section of heavy flavour decay muons at  $-4 < \eta < -2.5$  in pp collisions at  $\sqrt{s} = 13$  TeV.

Source	Uncertainty vs $p_T$
Tracking efficiency	2%
Trigger efficiency	0-2%
Matching efficiency	0.5%
Resolution & alignment	0-7.7%
$\pi \rightarrow \mu$	0-2.2%
$K \rightarrow \mu$	0-2%
Secondary $\pi, K$ decay muons	0-2.2%
$J/\psi \rightarrow \mu$	0-1.4%
$W/Z/\gamma^* \rightarrow \mu$	0-2.4%
Integrated luminosity	2.26%

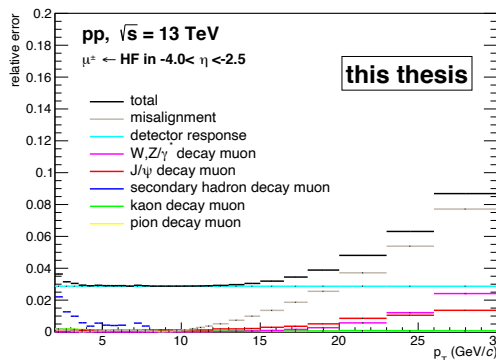


Figure 3.51: Contribution of systematic uncertainties from various sources as function of  $p_T$  in the full acceptance ( $-4 < \eta < -2.5$ ).

## 3.9 Results

In this section, the transverse momentum and rapidity differential production cross-sections of Heavy Flavour decay Muon (HFM) at forward rapidity in pp collisions at  $\sqrt{s} = 13$  TeV are presented. The results for the  $p_T$ -differential production cross-section of HFM are shown at different rapidity intervals also. The new measurement of  $p_T$ - and  $y$ - differential production cross-sections of HFM are compared with the FONLL calculations [4].

In FONLL calculations, the different contributions of HFM from heavy quarks (c and b) are considered as following:

1. muons decaying from charm quarks ( $c \rightarrow D \rightarrow \mu$ )
2. muons decaying from beauty quarks ( $b \rightarrow B \rightarrow \mu$ )
3. muons decaying indirectly from beauty quarks ( $b \rightarrow B \rightarrow D \rightarrow \mu$ )

The uncertainties at quark level are propagated at the lepton (muon) level and the additional uncertainty on the fragmentation process is included also. In the calculations, the uncertainties on quark masses ( $\sigma_Q$ ), QCD scales ( $\sigma_\mu$ ) and PDFs ( $\sigma_{PDFs}$ ) are considered. The upper ( $\sigma^{max}$ ) and lower ( $\sigma^{min}$ ) uncertainties on these parameters are obtained with different values of quark masses, QCD scales and PDFs. Finally, the uncertainties in production cross section of muons decaying from heavy flavour are obtained adding the uncertainties on quark masses, QCD scales and PDFs in quadrature.

The  $p_T$ -differential production cross-section of muons decaying from heavy flavour hadrons in the full acceptance of muon spectrometer ( $2.5 < y < 4$ ) is presented in Figure 3.52. The statistical and systematic uncertainties are represented by the vertical error bars and the open boxes respectively. The systematic uncertainty includes all the sources as described in Table 3.4 except the systematic uncertainty of 2.26% on trigger normalization. This analysis work in pp collisions at the highest center-of-mass energy  $\sqrt{s} = 13$  TeV allowed to extend the  $p_T$ -differential production cross-section of HFM towards high  $p_T$  region upto  $p_T = 30$  GeV/ $c$  with high precision measurement. A higher precision measurement on statistical and systematic

uncertainties is reached compared to the previous analysis performed at  $\sqrt{s} = 2.76$  and 7 TeV with Run 1 data and at  $\sqrt{s} = 5.02$  TeV with Run 2 data. The improvements in the results are coming from the precision measurement of muons decaying from light hadrons in high  $p_T$  region, high integrated luminosity and the uses of single muon triggers (MSL and MSH). The study of HFM is done from  $p_T = 2$  GeV/ $c$  to  $p_T = 30$  GeV/ $c$  and compared with the FONLL calculations. This FONLL calculations [17, 18] include the non-perturbative fragmentation of heavy quarks into open heavy flavour hadrons and their semi-leptonic decay into final-state leptons. At each  $p_T$ -bin, the central value of the FONLL prediction using the CTEQ6.6 PDF is shown by the black solid line and the corresponding systematic uncertainty by the shaded band. The systematic uncertainties are computed using the minimum and maximum uncertainties on quark masses, QCD scales (renormalization and factorization scales) and PDFs. The FONLL predictions for muons decaying from charm and beauty hadrons are displayed separately. The latter includes the muons from direct decay of B-hadron and indirect decays via D-hadrons. The bottom panel of Figure 3.52 presents the ratio of data with respect to the FONLL calculations. The new measurement with ALICE is well described by the FONLL prediction within uncertainties, although a smaller deviation from FONLL is observed at the highest  $p_T$ -bin ( $26 < p_T < 30$  GeV/ $c$ ). The ratio varies from  $\sim 1.08$  to  $\sim 1.2$  for  $2 < p_T < 20$  GeV/ $c$  and then increases upto  $\sim 1.37$  at the highest  $p_T$ -bin (26-30 GeV/ $c$ ).

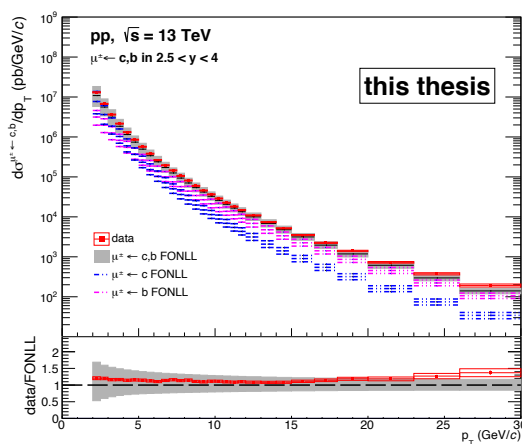


Figure 3.52: The  $p_T$ -differential production cross-section of muons decaying from heavy flavour hadrons at forward rapidity ( $2.5 < y < 4$ ) in pp collisions at  $\sqrt{s} = 13$  TeV and compared with FONLL calculations. The bottom panel presents the data to FONLL ratio.

The high statistics of muons using the two muon triggers allow to perform the measurement of  $p_T$ -differential production cross-section of HFM in five equal rapidity intervals in the full range of  $2.5 < y < 4$ . These results are presented in Figure 3.53 and compared with the FONLL predictions. The ratios between the data and FONLL calculations are shown in the bottom panels at each rapidity interval. A good agreement between the data and FONLL is observed within experimental and theoretical uncertainties where data exhibit some fluctuations at high  $p_T$ -region.

A study on the  $p_T$ -integrated production cross-section of muons from heavy flavour hadron decays as a function of rapidity is done. This study is performed for two  $p_T$ -ranges  $2 < p_T < 7$  GeV/ $c$  (left) and  $7 < p_T < 30$  GeV/ $c$  (right) as displayed in Figure 3.54. The measurement at these two  $p_T$  intervals are compatible with the FONLL predictions. In the lower  $p_T$  interval  $2 < p_T < 7$  GeV/ $c$ , the HFM predominantly comes from the charm hadron decays, while in the higher  $p_T$  region  $7 < p_T < 30$  GeV/ $c$ , the HFM from beauty hadron decays dominates over the charm hadron decays. The ratio of the data to FONLL predictions lies in the range of  $\sim 1.13$ - $1.25$  depending on the rapidity region.

Figure 3.55 displays the  $p_T$ -differential production cross-section of HFM in pp collisions at  $\sqrt{s} = 13$  TeV performed in this work. This result is compared with the results from the previous ALICE measurements at  $\sqrt{s} = 2.76$  TeV [1], 5.02 TeV [3] and 7 TeV [2] respectively. The result at  $\sqrt{s} = 13$  TeV has been extended upto  $p_T = 30$  GeV/ $c$  whereas the previous measurement at  $\sqrt{s} = 5.02$  TeV was upto  $p_T = 20$  GeV/ $c$ . The ratio of the heavy flavour production cross-section between different centre-of-mass energies is a powerful observable to test the sensitivity of pQCD calculations. The absolute production cross-section of heavy flavour predicted by FONLL is associated with large systematic uncertainties where the uncertainties from the QCD scale parameters are most dominating. The ratio of the production cross section of HFM at forward rapidity ( $2.5 < y < 4$ ) in pp collisions at  $\sqrt{s} = 13$  TeV with respect to that at  $\sqrt{s} = 5.02$  TeV (left) and at  $\sqrt{s} = 7$  TeV (right) are presented in Figure 3.56.

The systematic uncertainties between the measurements at two different center-of-mass energies are considered as uncorrelated when the ratio is computed. The calculation of ratio using FONLL is done considering the maximum and minimum uncertainties associated to the



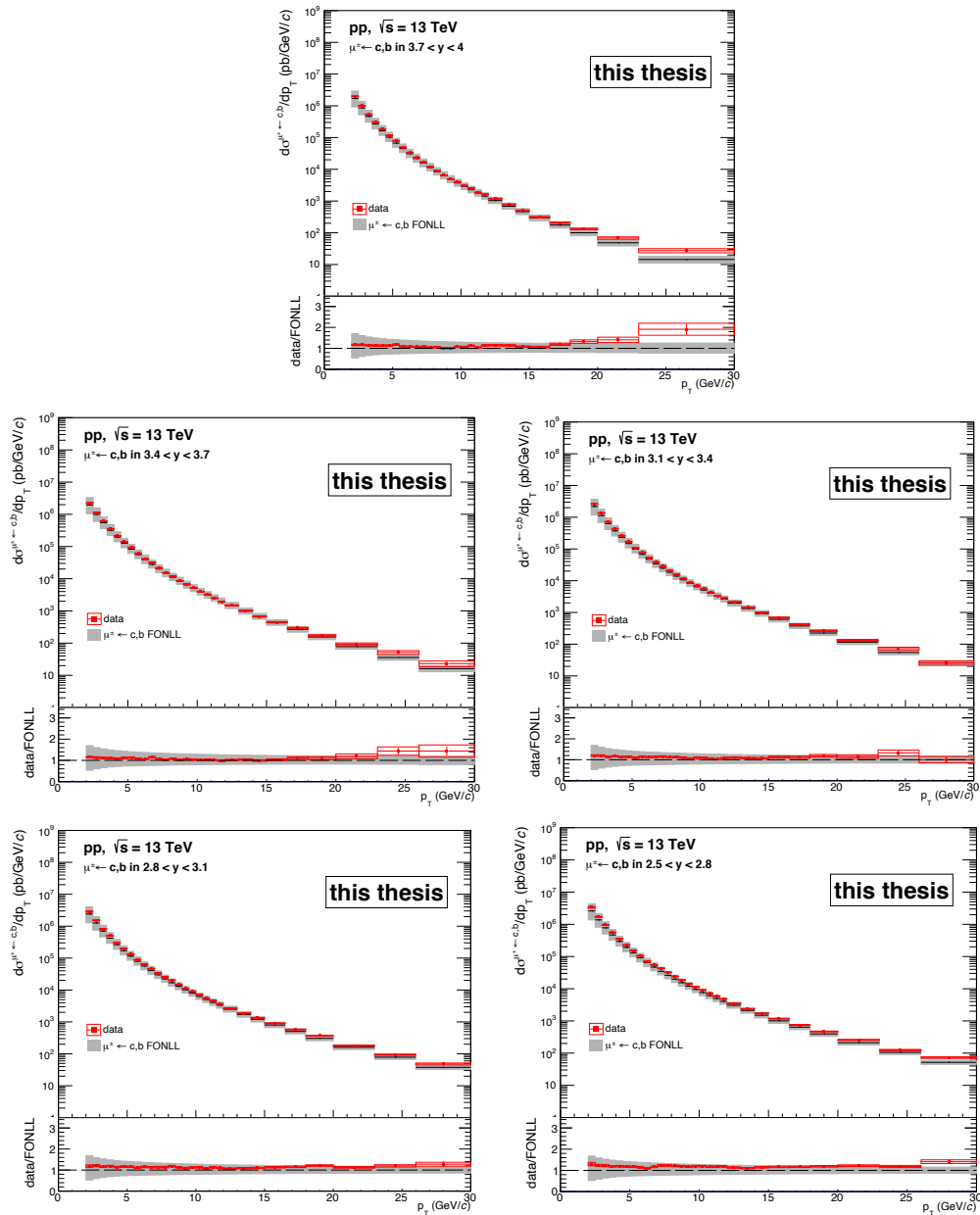


Figure 3.53: The  $p_T$ -differential production cross-section of muons decaying from heavy flavour hadrons for five rapidity intervals in the full range of  $2.5 < y < 4$ . The results are compared with FONLL calculations. The bottom panel presents the ratios of the data to FONLL.

QCD scales, PDFs and quark masses. Indeed, the predicted FONLL ratio could be computed assuming the correlation between the systematic uncertainties at different centre-of-mass energies. In Ref [18], the ratios of heavy flavour production cross-section at different centre-of-mass energies are predicted with high accuracy. In this ratio calculation, such correlation between

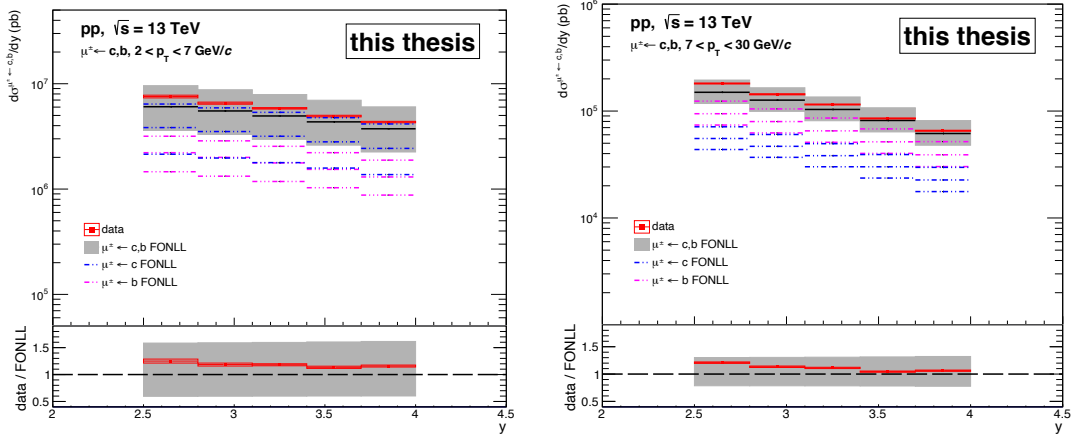


Figure 3.54: Production cross section of muons from heavy flavour hadron decays as a function of rapidity for the  $p_T$  intervals  $2 < p_T < 7$  GeV/ $c$  (left) and  $7 < p_T < 30$  GeV/ $c$  (right). Statistical and systematic uncertainties are represented by the vertical bars (smaller than symbols) and open boxes respectively. The production cross sections are compared with FONLL predictions (top). The ratios of the data to FONLL calculations are shown also (bottom).

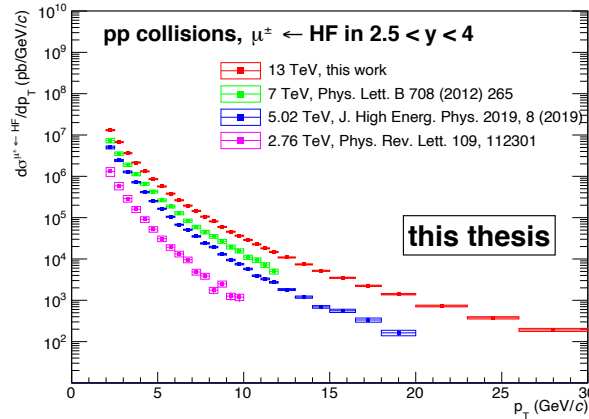


Figure 3.55: The production cross section of muons from heavy flavour hadron decays in forward rapidity ( $2.5 < y < 4$ ) at  $\sqrt{s} = 13$  TeV. The result is compared with the previous ALICE measurements at  $\sqrt{s} = 2.76$ , 5.02 and 7 TeV respectively. The statistical and systematic uncertainties are represented by the vertical bars and open boxes respectively.

the systematic uncertainties at different energies have not been implemented. When computing the ratio between the measurements at different centre-of-mass energies, the systematic uncertainty on the ratio of the HFM production cross-section (13 TeV/5.02 TeV & 13 TeV/7 TeV) from the measurements are increasing smoothly with increasing  $p_T$ .

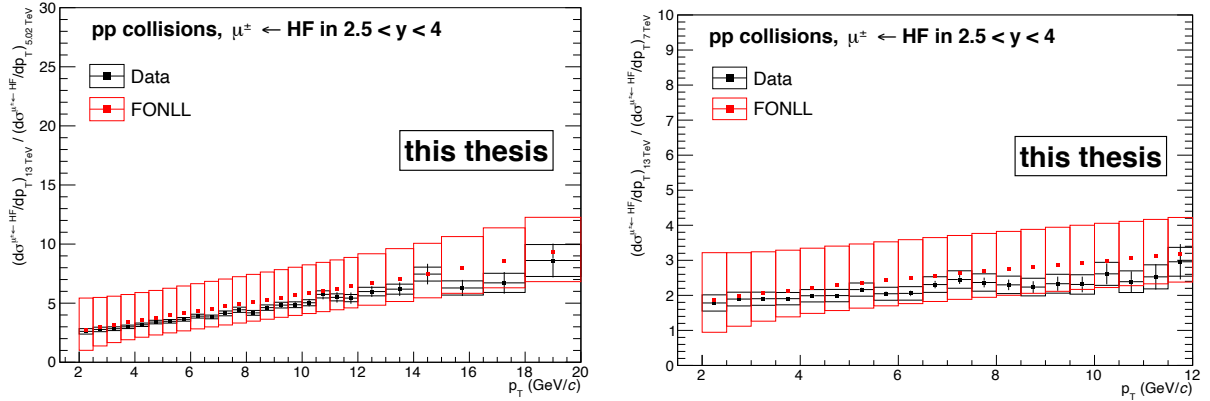


Figure 3.56: The ratio of production cross section of muons from heavy flavour hadron decays in forward rapidity in pp collision at  $\sqrt{s} = 13$  TeV with respect to that at  $\sqrt{s} = 5.02$  TeV (left) and at  $\sqrt{s} = 7$  TeV (right) respectively. The statistical (vertical bars) and systematic (open boxes) uncertainties are indicated. The results are compared with the FONLL calculations.

The ratio with respect to the  $\sqrt{s} = 5.02$  TeV ranges between  $\sim 2.6$ - $8.6$  in the  $2 < p_T < 20$  GeV/ $c$  and with respect to the  $\sqrt{s} = 7$  TeV, it is between  $\sim 1.8$ - $3$  in the  $2 < p_T < 12$  GeV/ $c$ . Both the measured ratios are well reproduced by FONLL predictions within uncertainties.

### 3.10 Summary

The new measurement of the production cross-section of muons from heavy flavour hadron decays in pp collisions at the highest available energy  $\sqrt{s} = 13$  TeV with the ALICE detector in Run 2 at LHC has been presented. The present result for the production cross-section of HFM as a function of  $p_T$  in the forward rapidity ( $2.5 < y < 4$ ) has an extended  $p_T$  coverage  $2 < p_T < 30$  GeV/ $c$  compared to the previously published measurements. The  $p_T$ -differential production cross-sections are also measured at five equal subrapidity intervals in the range  $2.5 < y < 4$ . The  $y$ -differential production cross-section of HFM is obtained at two different  $p_T$  region:  $2 < p_T < 7$  GeV/ $c$  and  $7 < p_T < 30$  GeV/ $c$  in the range  $2.5 < y < 4$ . The measurements of both the differential production cross-sections are compared with FONLL calculations and found to be in good agreement almost over the full  $p_T$  range. The central values of the HFM production cross-section using FONLL prediction seems to underestimate the ALICE data

over the whole  $p_T$  range. Comparisons for the production cross-section of HFM measured at  $\sqrt{s} = 13$  TeV are done with the previous ALICE measurements at  $\sqrt{s} = 2.76, 5.02$  and 7 TeV. The systematic uncertainty due to the track-resolution and misalignment will be updated in the near future and an improved modified uncertainty is expected especially at high  $p_T$ -region. An update in the measurement of systematic uncertainty for the trigger efficiency with Muon Single High (MSH) trigger could improve the overall systematic uncertainties to some extent. The addition of systematic uncertainty for the measurement of muons from primary pion and kaon decay due to the absorber effect parametrization, could improve the precision of measurement. All of these updates together are expected to improve the total systematic uncertainties and better results can be foreseen for comparison of this ALICE data at  $\sqrt{s} = 13$  TeV with theoretical model FONLL calculations within uncertainties in the whole  $p_T$  range.

---

# Bibliography

---

- [1] ALICE collaboration, *Production of muons from heavy flavour decays at forward rapidity in pp and Pb-Pb collisions at  $\sqrt{s_{NN}} = 2.76$  TeV*, *Phys. Rev. Lett.* **109** (2012) 112301 [[1205.6443](#)]. [75](#), [128](#)
- [2] ALICE collaboration, *Heavy flavour decay muon production at forward rapidity in proton-proton collisions at  $\sqrt{s} = 7$  TeV*, *Phys. Lett. B* **708** (2012) 265 [[1201.3791](#)]. [75](#), [81](#), [128](#)
- [3] ALICE collaboration, *Production of muons from heavy-flavour hadron decays in pp collisions at  $\sqrt{s} = 5.02$  TeV*, *JHEP* **09** (2019) 008 [[1905.07207](#)]. [75](#), [84](#), [128](#)
- [4] FONLL. <http://www.lpthe.jussieu.fr/~cacciari/fonll/fonllform.html>. [76](#), [93](#), [123](#), [126](#)
- [5] X. Zhang, *Study of Heavy Flavours from Muons Measured with the ALICE Detector in Proton-Proton and Heavy-Ion Collisions at the CERN-LHC*, Ph.D. thesis, Clermont-Ferrand U., 2012. [80](#)
- [6] J. Martin Blanco, *Study of  $J/\psi$  production dependence with the charged particle multiplicity in p-Pb collisions at  $\sqrt{s_{NN}} = 5.02$  TeV and pp collisions at  $\sqrt{s} = 8$  TeV with the ALICE experiment at the LHC*, Ph.D. thesis, Nantes U., 1, 2016. [87](#)
- [7] Z. Zhang, *Open heavy-flavour measurements via muons in proton-proton and nucleus-nucleus collisions with the ALICE detector at the CERN-LHC*, Ph.D. thesis, Clermont-Ferrand U., 2018. [87](#), [99](#)

- [8] ALICE collaboration, *ALICE luminosity determination for pp collisions at  $\sqrt{s} = 13$  TeV*, . 91
- [9] ALICE collaboration, *Production of light-flavor hadrons in pp collisions at  $\sqrt{s} = 7$  and  $\sqrt{s} = 13$  TeV*, *Eur. Phys. J. C* **81** (2021) 256 [2005.11120]. 99
- [10] M.S. Islam, “Update on HFM analysis in pp @ 13 TeV.”  
<https://indico.cern.ch/event/897577/>. 99, 104
- [11] PYTHIA8 online. <https://pythia.org/latest-manual/Welcome.html>. 103
- [12] M.S. Islam, “Update on HFM analysis in pp @ 13 TeV.”  
<https://indico.cern.ch/event/1123477/>. 104
- [13] S. Alioli, P. Nason, C. Oleari and E. Re, *A general framework for implementing NLO calculations in shower Monte Carlo programs: the POWHEG BOX*, *JHEP* **06** (2010) 043 [1002.2581]. 114
- [14] G. Taillepiéd, *Electroweak-boson production in p-Pb collisions at  $\sqrt{s_{NN}} = 8.16$  TeV with ALICE*, Ph.D. thesis, Clermont-Ferrand U., 2021. 114, 122
- [15] M.S. Islam, “Update on HFM analysis in pp @ 13 TeV.”  
<https://indico.cern.ch/event/966049/>. 115
- [16] ALICE collaboration, *Energy dependence of forward-rapidity J/ $\psi$  and  $\psi(2S)$  production in pp collisions at the LHC*, *Eur. Phys. J. C* **77** (2017) 392 [1702.00557]. 117, 121, 122
- [17] M. Cacciari, S. Frixione, N. Houdeau, M.L. Mangano, P. Nason and G. Ridolfi, *Theoretical predictions for charm and bottom production at the LHC*, *JHEP* **10** (2012) 137 [1205.6344]. 127
- [18] M. Cacciari, M.L. Mangano and P. Nason, *Gluon PDF constraints from the ratio of forward heavy-quark production at the LHC at  $\sqrt{S} = 7$  and 13 TeV*, *Eur. Phys. J. C* **75** (2015) 610 [1507.06197]. 127, 129

## CHAPTER 4

---

# Heavy Flavour decay muon and charged particles production using Angantyr model at LHC energies

---

In this chapter the discussion on the production of Heavy Flavour decay Muons (HFM) at forward rapidity ( $2.5 < y < 4$ ) and the charged particles in proton-proton (pp) and heavy-ion (A-A) collisions using Angantyr model in PYTHIA8 at LHC energies is done. These studies are done in small (pp), intermediate (Xe-Xe) and large (Pb-Pb) colliding systems. In pp collisions, the works have been performed with  $\sqrt{s} = 2.76, 5.02, 7.0$  and  $13$  TeV. These studies are also carried out in Xe-Xe collisions at  $\sqrt{s_{NN}} = 5.44$  TeV and in Pb-Pb collisions at  $\sqrt{s_{NN}} = 2.76$  and  $5.02$  TeV. For each case, the standard statistical uncertainty is calculated as  $\sqrt{N_{yield}}$  where  $N_{yield}$  is the yield of the particles. The production of HFM as a function of transverse momentum ( $p_T$ ) and rapidity ( $y$ ) at forward rapidity ( $2.5 < y < 4$ ) has been investigated. On the other hand, the production of charged particles is measured at mid-rapidity ( $|\eta| < 0.8$ ) as a function of  $p_T$ . The simulation results for both HFM and charged particle productions are contrasted with the available ALICE data. The study of  $p_T$ -differential productions of HFM and charged particles show agreement with the experimental ALICE data reasonably well for both pp and A-A collisions. In the case of HFM, the simulation results for  $y$ -distribution have been compared with ALICE data in pp collision at  $\sqrt{s} = 5.02$  and  $7.0$  TeV respectively. Apart

from the study of charged particles  $p_T$ -spectra, the results of average transverse momentum ( $\langle p_T \rangle$ ) as a function of charged-particle multiplicity ( $N_{ch}$ ) at mid-rapidity  $|\eta| < 0.3$  ( $0.15 < p_T < 10$  GeV/ $c$ ) are shown in both pp and A-A collisions. In addition to the particle spectra, the study of the observable  $R_{AA}$  is done, which can provide a more quantitative model-to-data comparison. So, the calculations of  $R_{AA}$  of HFM and charged particles at  $\sqrt{s_{NN}} = 2.76$  and 5.02 TeV are presented. Comparison of this simulated  $R_{AA}$  has been done with the experimental data measured by ALICE. In view of the foreseen O-O collisions during ALICE Run 3, predictions for the production of HFM and charged particles have been performed with Angantyr model in O-O collisions at  $\sqrt{s_{NN}} = 6.37$  TeV. The details of the results for HFM and charged particles are discussed in sections 4.3 and 4.4 respectively.

In high energy nucleon-nucleon and heavy-ion collisions, the heavy quarks (charm (c) and beauty (b)) are produced at the very early stage of the collisions. These heavy quarks are mostly produced by initial hard parton-parton scattering with high momentum transfer ( $Q^2$ ). In relativistic heavy-ion collisions, these heavy quarks are produced much before the formation of the deconfined medium (QGP). A QGP is phase of strongly interacting matters, consisting of quarks and gluons. Hence, the heavy quarks experience a full evolution while propagating through QGP and lose energy by successive collisions and gluon radiation. Thus, heavy quarks are very sensitive probes to study the parton energy loss mechanisms, hadronisation and the transport properties of the medium produced in high energy heavy-ion collisions. Whereas in pp collisions, we do not expect the formation of QGP medium and the production of heavy quarks can be described entirely via theoretical models based on perturbative Quantum ChromoDynamics (pQCD). Interestingly, many features are seen in high multiplicity proton-proton collisions at the LHC energies which are very common observables in heavy-ion collisions [1, 2]. The experimental measurements at relativistic heavy-ion collider (RHIC) and the LHC exhibit the evidence that the medium formed in these collisions undergoes collective expansion and it is comparable to a fluid flow [3, 4]. In general, the formation of QGP is not expected in small systems like proton-proton (pp) and proton-nucleus (p-A) collisions. Traditionally, the data collected from such collisions of small systems are utilized to construct a baseline reference to find the signature of the hot QGP medium produced in heavy-ion (HI) collisions. Hence, we must understand whether a HI collision is simply a collection of multiple nucleon-nucleon colli-



sions or there is a transition from a hadronic state to a new state of matter (QGP). Therefore, the observables used to investigate the existence of hot QGP medium in heavy-ion collisions may not be explained by a theoretical model which does not include the assumption of a hot thermalised medium.

## 4.1 Angantyr model

A heavy ion (nucleus) contains multiple number of protons and neutrons collectively known as nucleons. A nucleus-nucleus collision leads to many simultaneous sub-collisions. A substantial amount of energy involves in these sub-collisions and as a result, the number of particles produced in a HI collision is an order of magnitude higher than in a pp collisions. Usually, phenomenological models are based on the theoretical understanding. In addition, the free parameters of these models as predicted by the theories and are tuned by the experimental data. Thus, phenomenological models makes a link between theory and experiment. These models often provide information in terms of physics observables using random number generation. Phenomenological models based on such random generators are called Monte Carlo (MC) event generators. In our case, PYTHIA [5] is one such MC event generator.

In recent times, various theoretical models have been formulated and tested by the high-energy physics community to understand the collective behaviour in the small systems like pp and p-A collisions [6–9]. MC models which explain the flow like observations in HI collision experiments are based on the assumption of the hot thermalised medium. PYTHIA is a MC model committed for simulation of small systems like pp collision. The recent observations such as near side ridge [10] and strangeness enhancement [11] for high multiplicity pp events at LHC experiments show features like HI collisions. These new results may indicate for better understanding of phenomenological model. Moreover, PYTHIA or HI event generators are not good tools to explain these results. Generally, a PYTHIA event generator performs simulation without any assumption of thermalised medium, whereas a HI event generator is based on the QGP formation. The results of strangeness enhancement and near side ridge in pp collisions motivate for a common phenomenological approach to study both pp and heavy-ion

(HI) collision in a single framework. One such phenomenological model is Angantyr Model.

Angantyr model is an extrapolation of pp dynamics to HI collisions with PYTHIA. Therefore, this model makes a bridge between high energy phenomenology and heavy-ion collision studies. This model does not include any thermalised medium (QGP) creation in HI collision. Hence, Angantyr model is a non-thermal HI model similar to other conventional event generators for small (i.e. pp) collision system such as PYTHIA [5], HERWIG [12], SHERPA [13] etc. The pictorial view of conventional heavy-ion collision including the formation of QGP is shown on the right side of Figure 4.1 whereas QGP free Angantyr model is described on the left side of Figure 4.1. In hydrodynamical model of collision, the post-collision scenario passes various stages from QGP formation to hadronization. In Angantyr using PYTHIA, the event evolution is continuous with various stages but without any thermalised medium formation [14].

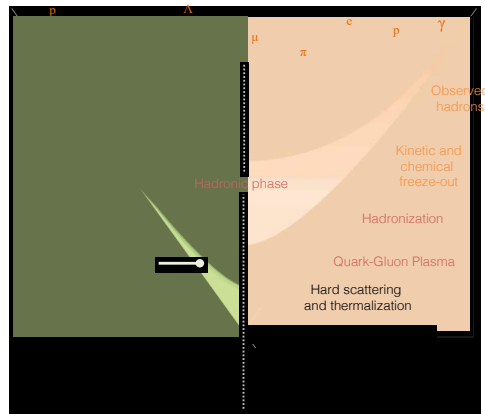


Figure 4.1: A Schematic representation of a heavy-ion collision using the hydrodynamical approach considering a thermalised medium creation (right side of the figure) and the PYTHIA/Angantyr model with no-QGP baseline method (left side of the figure) [14].

In this Angantyr model, the advanced PYTHIA8 package [5] is implemented as the underlying event generator. This model provides the facility to designate a nucleus instead of a hadron as projectile and/or target [15, 16]. It performs simulation to generate absolute final states of particles. Therefore, it provides a common platform to study pp, p-A and A-A collisions.

The aim of this phenomenological study is to see how well such extrapolation of pp dynamics can reproduce experimental data for HI collision. Here, the study of the production of heavy flavour decay muon (HFM) and charged particles is carried out. The study of charged-particle

multiplicity in small and heavy-ion collision systems has been done using Angantyr model before and compared the results with LHC experiments [15, 16]. The novelty of the present study is to explore the sensitivity of the approach using Angantyr model to study the production of HFM and how well the results obtained using the model explain the experimental ALICE data for both the collision systems (pp and A-A) in a single framework.

### 4.1.1 Physics processes in PYTHIA8

The Angantyr model is developed on the structure of PYTHIA8 which is the advanced version of PYTHIA6 adding Multiparton Interactions (MPI) effects. The details of the physics programs are available in online manual [17]. PYTHIA8 is suitable for high energy particle collisions of center of mass energy ( $\sqrt{s}$ ) ranges from 10 GeV to 100 TeV. The limitation in the lower value of center of mass energy ( $\sqrt{s} \leq 10$  GeV) is due to the unreliable results arising from the calculation of hadron-hadron cross-section in the hadronic resonance region. After the collision, the particles are produced in vacuum and the simulation does not include any interaction of the produced particles with the detector material. The PYTHIA simulation adds many physics processes internally. A brief discussion for a few of them is given below:

- **QCD process:** The QCD processes may govern by both soft and hard partonic scattering processes. A soft QCD subprocess may be classified as elastic ( $AB \rightarrow AB$ ), single diffractive ( $AB \rightarrow AX$  or  $AB \rightarrow XB$ ), double diffractive ( $AB \rightarrow X$ ) and non-diffractive. Whereas a hard QCD subprocess is generally  $2 \rightarrow 2$  processes available in PYTHIA. The hard QCD  $2 \rightarrow 2$  processes include  $g g \rightarrow g g$ ,  $g g \rightarrow q \bar{q}$ ,  $q g \rightarrow q g$ ,  $q q \rightarrow q q$ ,  $q \bar{q} \rightarrow g g$  etc, where  $q$  is by default a light quark (u, d, s). The heavy quarks (c and b) are also taken into account with their respective masses. In addition, there may also have contribution of three-parton final states ( $2 \rightarrow 3$  processes) generated by showers off two-parton processes.

The total cross-section in a hadronic collision is given by

$$\sigma_{tot} = \sigma_{elastic} + (\sigma_{SD} + \sigma_{DD} + \sigma_{ND}) \quad (4.1)$$

where  $\sigma_{elastic}$ ,  $\sigma_{SD}$ ,  $\sigma_{DD}$  and  $\sigma_{ND}$  are the elastic, single diffractive (SD), double diffractive (DD) and non-diffractive (ND) cross-sections respectively.

- **ISR and FSR:** The other physics processes such as initial state radiation (ISR) and final state radiation (FSR) were first introduced in PYTHIA 6.3 [18] and new features such as  $\gamma \rightarrow q\bar{q}$  and  $\gamma \rightarrow l^+l^-$  have been included in PYTHIA8 later.
- **MPI:** One of the important feature of PYTHIA is the multi-parton interactions (MPI) which are the direct consequence of the substructure of the colliding beam particles. In hadron-hadron collisions, it is possible to have multiple parton-parton interactions in the same event. The imposition of MPI in PYTHIA is very relevant to describe the underlying events. The MPI formalism is associated to both soft and hard multi-partonic interactions. Nucleon being an extended object, the nucleon-nucleon collisions may be defined as central to peripheral. This leads to MPI an impact-parameter dependence modeling. Therefore, if the impact parameter becomes smaller, the possibility arises for more central hadronic collision i.e, overlap between the colliding cloud of partons. One can expect larger average number of MPIs per collision for more central hadronic collisions.
- **Colour reconnection (CR):** In PYTHIA8, the primary technique for hadron production is the string fragmentation mechanism. The color string interaction is modified before hadronisation. The partons belonging to two different MPIs can be connected by color strings and then merged into one in such way that minimizes the total string length. Therefore, CR is the rearrangement of partons at the perterbative level just before hadronisation. After colour reconnection, the partons are connected with string and then fragment into hadrons via the Lund string model [19]. There are three different CR models available in PYTHIA8 as described below:
  - a) **MPI based model:** In this model, the partons of a lower- $p_T$  MPI system are merged with the partons of a higher- $p_T$  MPI. For each MPI system that undergoes a reconnection, minimizes the total string length. The reconnection probability for coloured partons from MPI with transverse momentum  $p_T$  is calculated in Ref. [20] and is given in Eq. 4.2.

$$P_{CR}(p_T) = \frac{(R_{CR} \cdot p_{T0})^2}{R_{CR} \cdot p_{T0} + p_T^2} \quad (4.2)$$

where,  $R_{CR}$  is the range parameter (ColourReconnection:range) and  $p_{T0}$  is the  $p_T$  regularisation parameter (MultipartonInteractions:pT0Ref). The higher value of  $R_{CR}$  means more reconnection probability. In PYTHIA8, its default value is set to  $R_{CR} = 1.8$  whereas the default value for MultipartonInteractions:pT0Ref is  $p_{T0}=2.15$ .

- b) **QCD based model:** In this model, the reconnection is based on the SU(3) QCD colour rules. According to the QCD colour rules, the probability to form a colour compatible singlet state from an uncorrelated triplet and anti-triplet is 1/9 times only. Using this model, the reconnections of dipoles can enhance the production of baryons.
- c) **Gluon-move model:** In this model, the reconnections are done in the same way as MPI based model, but only difference is that it considers only gluon for the reconnection. Here, each gluon is not only allowed to reconnect with the softer MPIs, but the reconnections are considered to all MPI systems.

### 4.1.2 Features of Angantyr model using PYTHIA8

The Angantyr model in PYTHIA8 is a generalization of high energy pp collision to HI collision to improve our understanding of the complete exclusive hadronic final states produced in such collisions without formation of any thermalised medium [15]. In this section, the essential features of the Angantyr model are summarized. In this model, the following aspects are considered to generalize the formulation of pp collision to p-A and A-A collisions for the simulation of an event generation:

- To determine the position of the nucleons within the colliding nuclei, the nuclear matter distribution is accounted from the Woods-Saxon (WS) density distribution.

- The geometric quantities like impact parameter ( $b$ ), the number of participant ( $N_{part}$ ) and nucleon-nucleon (NN) binary collisions ( $N_{coll}$ ) are calculated by means of MC simulations using Glauber formalism [21, 22]. The Glauber formalism is based on the eikonal approximation in the impact parameter space. So, the projectile nucleon(s) are assumed to travel along straight lines and undergo many sub-collisions with the nucleons in the target. Hence, a nucleon state in the projectile remains in the same state during its passage through the target nucleus and vice-versa. This non-diffractive interaction corresponds to the final state as a single pp event generated by PYTHIA8. Gribov made a point for the importance of diffractively excited nucleons which are the intermediate states in multiple NN sub-collisions [23]. The individual fluctuation in projectile and/or target nucleon is taken into account according to the Good-Walker formalism [24]. This diffractive excitation is a consequence of fluctuations in the substructure of projectile or target nucleons. To estimate the number of individual NN sub-collisions, Heiselberg et al. [25] and others studied the fluctuations in the projectile proton for p-A collisions. The cross-section and the number of wounded nucleons are calculated by taking the average over target nucleon states in p-A collisions. Angantyr is probably the first model to have this feature for the generalization to A-A collisions and takes into account the individual fluctuations for both the projectile and target nucleons.
- The Angantyr model is motivated by the old Fritiof model [26, 27] for p-A and A-A collisions and used to estimate the contribution to the final state from each interacting nucleon and the wounded nucleons (participants). In old Fritiof model, the event multiplicity is assumed to be proportional to the number of wounded nucleons calculated by Glauber Model [16]. According to Bialas *et al.* [28], the number of wounded nucleons is responsible for the production of soft particles, instead of individual NN sub-collisions. Moreover, the latter was seen to be correlated to hard processes. In the Fritiof model, the contribution from diffractive excitation for an interacting nucleon is close to the contribution from an average wounded nucleon. In that case, the mass distribution for diffractive excitation is given by  $dP \propto dM^2/M^2$ . So in the modified Fritiof model, it is possible to distinguish the wounded nucleons as diffractively and non-diffractively wounded nucleons. This modification is categorized the wounded nucleons involving in different types of

collision. In Angantyr model, an inelastic collision is described by non-diffractive (ND), single diffractive (SD) or double diffractive (DD) collision [29].

- In high energy collisions, the hard partonic sub-collisions play a major role which are scaled with NN sub-collisions instead of wounded nucleons. Therefore, it is important to account those events with multiple NN collisions which are basically associated with absorptive interaction of one projectile nucleon with several target nucleons (or vice versa). This leads to the idea of primary and secondary absorptive interactions in events with multiple non-diffractive (ND) interactions. In Angantyr model, the type of collisions between ND interacting nucleons is tagged according to the impact parameter. A primary non-diffractive (ND) interaction is defined with the smaller impact parameter for the collision between the projectile nucleon and the target nucleon. On the other hand, all other ND collisions are termed as secondary ND interaction.

The final state partons in nucleon–nucleon events are stacked together after generating all NN sub-collisions. The colour strings generated in a nucleon-nucleon collision are allowed to colour re-connection (CR) within the same sub-collision as described in PYTHIA8. The colour flow between any two different sub-collisions is restricted. After CR within the same sub-collision event, these strings hadronise by string fragmentation mechanism where each string breaks independently. Finally the hadrons are produced and travel freely without any interactions further. Moreover, the unstable hadrons decay and stable hadrons propagate further. In this present Angantyr model, the final state hadrons do not exhibit any long-range collectivity and no final state hadron-hadron interaction is considered.

The Angantyr model in PYTHIA8 is a direct extrapolation of high energy pp collisions to p-A and A-A collisions for describing the features of hadronic final states. This model provides a facility to combine many nucleon-nucleon collisions into one heavy-ion collision. Heavy nuclei such as He<sup>4</sup>, Li<sup>6</sup>, C<sup>12</sup>, O<sup>16</sup>, Cu<sup>63</sup>, Xe<sup>129</sup> and Pb<sup>208</sup> may be chosen using their respective PDG code in the form of 100ZZZAAAI. For example,  $Pb_{82}^{208}$  is of Z=82 and A=208. Hence, one can designate a Pb nucleus with a PDG number “1000822080” using the function `pythia.readString(“Beams:idA = 1000822080”)` to define a Pb beam (beam-A) for collision.

## 4.2 Centrality Class using Monte-Carlo Glauber (MCG) Model

In heavy-ion (HI) collisions, the two colliding nuclei are longitudinally Lorentz contracted. The impact parameter ( $b$ ) is the perpendicular distance between the centers of two nuclei at the time of collision. The overlap region of the two colliding nuclei is described by  $b$ . Therefore,  $b=0$  corresponds to a complete head-on collision while increasing value of  $b$  describes central to peripheral collision. A schematic representation of a HI collision is shown in Figure 4.2. In HI collision, the nucleons within the overlap region of two colliding nuclei are often participate in the collision. Whereas nucleons outside of that overlap region continue to move away in their respective beam directions and do not take part in the collisions. The nucleons which take part in the collisions are called participants and which do not are called spectators. In HI collisions, the initial geometric quantities such as impact parameter ( $b$ ), the number of participant ( $N_{part}$ ) and nucleon-nucleon binary collisions ( $N_{coll}$ ) are not directly determined from experiments. Rather these geometrical parameters are estimated from phenomenological models. The Monte Carlo Glauber (MCG) model is one of such model used for the calculation of these geometric quantities [30]. The MCG model is based on Eikonal approximation assuming straight-line trajectories of the nucleons along the beam axis from the two colliding nuclei [21, 22, 31]. However,  $N_{part}$  or  $N_{coll}$  calculated from MCG can be correlated with the event multiplicity in HI collisions. The event multiplicity distribution is described with centrality bins. Each of these centrality bins corresponds to certain interval of the impact parameter ( $b$ ) depending on the overlap region of the collision. In HI collision, the centrality is usually defined as a percentage of the overlap region (described by  $b$ ) to the total nuclear interaction cross-section as given below

$$c_i \simeq \frac{\pi b_i^2}{\sigma_{AA}}, \quad \text{for } b_i < R' \quad (4.3)$$

where  $c_i$  is the percentile of the centrality corresponding to impact parameter  $b_i$  for  $i$ -th bin.  $\sigma_{AA}$  is the inelastic nucleus-nucleus cross-section and  $R'$  is the sum of the radii of two colliding nuclei. In the calculation of centrality( $c$ ), a maximum value of impact parameter ( $b_{max}$ ) is



considered which is larger than twice the nuclear radius. The choice of  $b_{max}$  is large enough to simulate collisions until the interaction probability becomes zero. For each centrality class, the mean of these geometric quantities ( $N_{part}$  and  $N_{coll}$ ) are calculated over many events using MCG. Each centrality class corresponds to a certain interval of impact parameter with minimum ( $b_{min}$ ) and maximum ( $b_{min}$ ) values. In ALICE, there are two observables related to the collision geometry: one is the average charged-particle multiplicity ( $N_{ch}$ ) and another is  $E_{ZDC}$ , energy deposited in Zero-Degree Calorimeters (ZDC) by the particles close to the beam direction [32]. The average  $N_{ch}$  is assumed to increase with decreasing  $b$ . The  $E_{ZDC}$  is directly related to the number of spectator nucleons ( $N_{spec}$ ). The experimental results [33] describe that the rate of hard interactions is proportional to the  $N_{coll}$ , while the charged-particle multiplicity scales with  $N_{part}$ . In ALICE experiment, the ‘‘centrality’’ is defined as the percentile of the hadronic cross-section corresponding to particle multiplicity above a threshold ( $N_{ch}^{THR}$ ) or an energy deposited in the ZDC below a given threshold ( $E_{ZDC}^{THR}$ ) in the ZDC energy distribution  $d\sigma/dE'_{ZDC}$ .

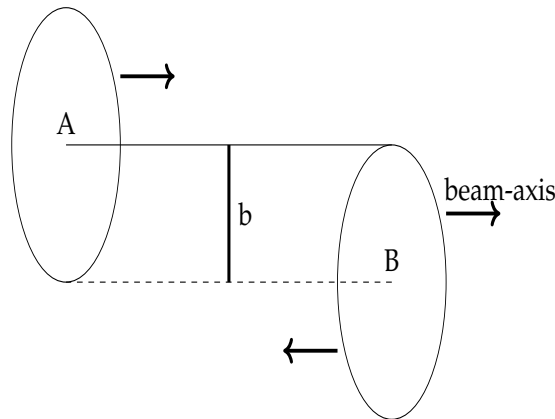


Figure 4.2: A schematic representation of a HI collision at an impact parameter ( $b$ ). The two colliding nuclei A and B are Lorentz contracted [29].

Following the Monte Carlo Glauber (MCG) model [21], the nucleons in each colliding nucleus are positioned stochastically by using the nuclear charge density function parameterized by the following Fermi distribution

$$\rho(r) = \rho_0 \frac{1 + \omega(r/\bar{R})^2}{1 + \exp(\frac{r-\bar{R}}{a})} \quad (4.4)$$

where  $\rho_0$  is the nucleon density,  $\bar{R}$  is nuclear radius,  $a$  is skin depth and  $\omega$  measures the deviations from spherical shape. In this phenomenological work, the results have been shown for Pb-Pb and Xe-Xe collisions. The nuclear radius ( $\bar{R}$ ) is  $6.62 \pm 0.06$  fm for  $^{208}\text{Pb}$  and is  $5.36 \pm 0.10$  fm for  $^{129}\text{Xe}$  [30]. The skin thickness parameter ( $a$ ) is  $0.546 \pm 0.010$  fm for  $^{208}\text{Pb}$  and is  $0.590 \pm 0.070$  fm for  $^{129}\text{Xe}$ . For this MCG calculation, a minimum inter-nucleon separation ( $d_{min}$ ) between the centers of the nucleons are used. The value of  $d_{min}$  for  $^{208}\text{Pb}$  and  $^{129}\text{Xe}$  nuclei have a default value of 0.4 fm. A maximum value of the impact parameter  $b_{max} \simeq 20$  fm  $> 2\bar{R}$  is selected, which is larger than twice the nuclear radius. The inelastic nucleon–nucleon cross section ( $\sigma_{NN}$ ) is obtained from pp collision and it depends only on the collision energy. A value of  $\sigma_{NN} = 61.8$  mb,  $\sigma_{NN} = 67.6$  mb and  $\sigma_{NN} = 68.4$  mb have been used for MCG calculation at  $\sqrt{s_{NN}} = 2.76$ , 5.02 and 5.44 TeV respectively. A more technical details for MCG calculations can be found in Ref [30, 34].

Table 4.1 and Table 4.2 present the values of geometric parameters ( $N_{part}$  and  $N_{coll}$ ) with their corresponding Root Mean Square (RMS) values for a given centrality class with a certain impact parameter interval ( $b_{min}$  to  $b_{max}$ ) for Pb-Pb collisions at  $\sqrt{s_{NN}} = 2.76$  TeV and 5.02 TeV respectively. These values are obtained from Monte Carlo Glauber (MCG) model calculation.

Table 4.1: Various geometric quantities in Pb-Pb collisions at  $\sqrt{s_{NN}} = 2.76$  TeV obtained with the MCG model for the centrality class used in this work.

centrality	$b_{min}$ (fm)	$b_{max}$ (fm)	$\langle N_{part} \rangle$	$\langle N_{coll} \rangle$
0 – 5%	0	3.49	381.18±17.14	1626.07±141.97
5 – 10%	3.49	4.93	327.84±17.93	1272.52±111.72
10 – 20%	4.93	6.97	258.55±26.93	892.05±139.08
20 – 30%	6.97	8.54	184.31±22.35	539.19±96.98
30 – 40%	8.54	9.86	127.18±18.83	310.27±68.32
40 – 50%	9.86	11.03	83.80±15.95	166.63±46.65
50 – 60%	11.03	12.08	51.80±13.30	82.39 ±30.03
60 – 70%	12.08	13.05	29.36±10.58	37.09±18.00
70 – 80%	13.05	13.95	15.18±7.65	15.46±9.99

Similarly, the geometric parameters  $N_{part}$  and  $N_{coll}$  with their corresponding RMS values

Table 4.2: Various geometric quantities in Pb-Pb collisions at  $\sqrt{s_{NN}}=5.02$  TeV obtained with the MCG model for the centrality class used in this work.

centrality	$b_{min}$ (fm)	$b_{max}$ (fm)	$\langle N_{part} \rangle$	$\langle N_{coll} \rangle$
0 – 5%	0	3.49	$383.85 \pm 16.52$	$1775.89 \pm 152.94$
5 – 10%	3.49	4.94	$331.70 \pm 17.81$	$1389.47 \pm 119.69$
10 – 20%	4.94	6.98	$262.70 \pm 27.00$	$973.40 \pm 150.73$
20 – 30%	6.98	8.55	$188.18 \pm 22.55$	$587.86 \pm 104.84$
30 – 40%	8.55	9.88	$130.50 \pm 19.06$	$337.93 \pm 73.71$
40 – 50%	9.88	11.04	$86.50 \pm 16.22$	$181.31 \pm 50.27$
50 – 60%	11.04	12.10	$53.85 \pm 13.59$	$89.64 \pm 32.31$
60 – 70%	12.10	13.06	$30.78 \pm 10.86$	$40.38 \pm 19.32$
70 – 80%	13.06	13.97	$16.02 \pm 7.94$	$16.79 \pm 10.72$

for a given centrality class in Xe-Xe collisions at  $\sqrt{s_{NN}} = 5.44$  TeV are obtained. These values are illustrated in Table 4.3.

Table 4.3: Various geometric quantities in Xe-Xe collisions at  $\sqrt{s_{NN}}=5.44$  TeV obtained with the MCG model for the centrality class used in this work.

centrality	$b_{min}$ (fm)	$b_{max}$ (fm)	$\langle N_{part} \rangle$	$\langle N_{coll} \rangle$
0 – 5%	0	2.997	$237.27 \pm 9.91$	$961.41 \pm 92.39$
5 – 10%	2.997	4.239	$206.98 \pm 11.59$	$746.57 \pm 73.74$
10 – 20%	4.239	5.995	$164.8 \pm 17.79$	$514.69 \pm 87.36$
20 – 30%	5.995	7.342	$117.84 \pm 15.6$	$302.55 \pm 60.62$
30 – 40%	7.342	8.478	$81.42 \pm 13.76$	$170.11 \pm 42.52$
40 – 50%	8.478	9.479	$53.75 \pm 12.1$	$90.84 \pm 29.18$
50 – 60%	9.479	10.384	$33.47 \pm 10.27$	$45.58 \pm 19.04$
60 – 70%	10.384	11.216	$19.45 \pm 8.27$	$21.69 \pm 11.94$
70 – 80%	11.216	13.989	$10.93 \pm 6.06$	$10.25 \pm 7.14$

The centrality of a given HI collision in Angantyr is assigned by applying a sharp cut on the  $N_{part}$  obtained from MCG and is used as input to the Angantyr simulation. Furthermore, the mean of  $N_{part}$ ,  $N_{coll}$  obtained from Angantyr simulation are compared with that obtained from MCG and the published ALICE data. It is to be noted that for a given centrality, the parameters  $\langle N_{part} \rangle$ ,  $\langle N_{coll} \rangle$  and  $\sigma_{AA}$  are important quantities to control the behavior of different collision systems in heavy-ions.

## 4.3 Production of Heavy Flavour decay muon using Angantyr model

### 4.3.1 Event generation for HFM simulation

Following the section 4.1.1 described above, the main processes of heavy quarks production (c, b) in PYTHIA8 are given below:

- i) Initial c or b quarks are produced via the hard  $2 \rightarrow 2$  partonic interactions (e.g.,  $q\bar{q} \rightarrow \bar{c}(\bar{b})c(b)$ ,  $g\bar{g} \rightarrow \bar{c}(\bar{b})c(b)$ ) and the same mechanism is used from the subsequent hard processes in MPI for the finite production probability.
- ii) The gluon splitting hard processes (e.g.,  $g \rightarrow \bar{c}(\bar{b})c(b)$ ) are used for heavy quark production [35].
- iii) These gluons may originate from the Initial State Radiation (ISR) and Final State Radiation (FSR).

The MPI model is one of the various models which can explain multiple parton-parton interactions in pp collisions at LHC energies. The MPI model influences light flavour production and it could also be applied in the Angantyr model for the understanding of the charged-particle multiplicity as well as the heavy flavour production [36, 37]. In this simulation work to study the HFM production, the following tuning has been done in Angantyr model using PYTHIA8 (version 8.235):

- a) **HardQCD:all=on** : the common switch for the group of all hard QCD processes including heavy flavour subset.
- b) **PhaseSpace:pTHatMin=5**: the base class for all hard-process phase-space generators for cuts in  $2 \rightarrow 2$  processes.
- c) **PhaseSpace:pTHatMinDiverge=0.5**: the extra  $p_T$  cut to avoid divergences of some QCD processes in the limit  $p_T \rightarrow 0$ .

- d) **Multi-Parton Interactions bProfile=3:** the inclusion of the varying impact parameter to allow all incoming partons to go through hard and semihard interactions.
- e) **Pythia8HeavyIons.h:** the inclusion of Heavy-ion class for the extension of pp analysis to heavy-ion study.
- f) **Tune:pp=5** Tune to pp data. The tuning is done mainly for the initial state radiation, multi-parton interactions and beam-remnants aspects of PYTHIA.
- g) **HeavyIon:modes=1:** Heavy-ion collision mode in Angantyr using PYTHIA8
- h) **HeavyIon:modes=2:** pp collision mode in Angantyr using PYTHIA8

### 4.3.2 Results on HFM simulations

In this work, we have studied the production of HFM as a function of transverse momentum ( $p_T$ ) in pp collisions. This study is also extended to heavy-ion (Xe-Xe and Pb-Pb) collisions in the forward rapidity ( $2.5 < y < 4$ ) domain. 1000 million events are generated both at centre-of-mass (cm) energies  $\sqrt{s} = 2.76$  TeV and 5.02 TeV in pp collision. However, 100 million events are simulated in pp collision at  $\sqrt{s} = 7$  TeV and 13 TeV respectively. Due to computational limit, it could only be possible to generate 15 million and 10 million events for Xe-Xe at  $\sqrt{s_{NN}} = 5.44$  TeV and for Pb-Pb collision at  $\sqrt{s_{NN}} = 2.76, 5.02$  TeV respectively. All the studies for the HFM production using Angantyr are compared with the published ALICE data in LHC energies. Note that the ALICE results for HFM at  $\sqrt{s} = 13$  TeV in pp collisions is not published yet.

In this section, the simulation results with Angantyr model are presented [38]. A comparative study has been done between the standalone PYTHIA8 and Angantyr results for pp collisions at LHC energies. The comparison for HFM  $p_T$  distribution in forward rapidity  $2.5 < y < 4$  at  $\sqrt{s} = 2.76, 5.02, 7$  and 13 TeV in pp collisions is shown in Figure 4.3. The results suggest that the HFM  $p_T$  distributions at forward rapidity in pp collision with default PYTHIA8 are well reproduced by HI collision model Angantyr. This comparison between default PYTHIA8 and Angantyr in pp collision allows to perform simulation for pp collision using

Angantyr model in addition to the default PYTHIA8. Hereafter, the Angantyr model is used irrespective of the size of the collision system in the analysis.

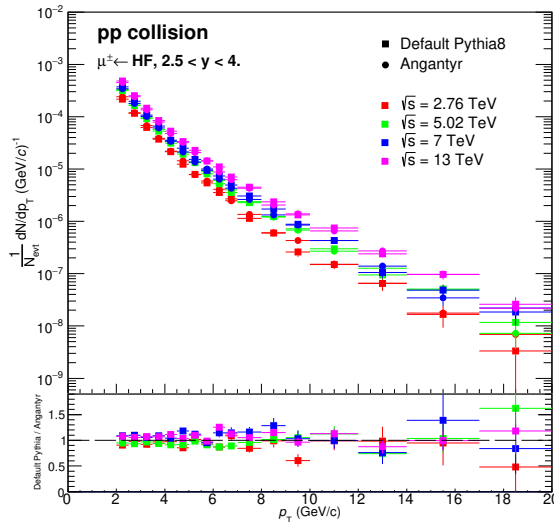


Figure 4.3: Comparison of the HFM  $p_T$ -spectra in p-p collisions at  $\sqrt{s} = 2.76, 5.02, 7$  and 13 TeV between default PYTHIA8 and Angantyr model calculations.

In Pythia8, PhaseSpace is a base class for all hard-processes either for  $2 \rightarrow 1$  or  $2 \rightarrow 2$  and also specialized for elastic and diffractive scattering. It is possible to constrain the kinematics of most of the hard subprocess. The cross section of a process in PYTHIA8 is adjusted only to the allowed phase space corresponding to the cuts applied. The more number of particles are generated in the final state for an application of more higher value in the PhaseSpace cut [5, 17]. Hence, the production of heavy flavour decay muon at forward rapidity ( $2.5 < y < 4$ ) is studied in pp collisions at  $\sqrt{s} = 5.02$  TeV with different PhaseSpace cuts using the function PhaseSpace:pTHatMin available in PYTHIA8. The results with the tuned PhaseSpace:pTHatMin are compared with the ALICE data[39] as shown in the left panel of Figure 4.4. A similar comparison is done for Pb-Pb at most central (0-10%) collisions with the tuning of pTHatMin values 5 and 20 at  $\sqrt{s_{NN}} = 5.02$  TeV as shown in Figure 4.4 (right panel). The left panel of Figure 4.4 suggests that PhaseSpace:pTHatMin=5 describes the ALICE result comparatively well in pp collision and also consistent with FONLL. However, Figure 4.4 (right panel) suggests no such dependency on PhaseSpace:pTHatMin for HI collisions. Therefore, the simulations are carried out for all collision systems with PhaseSpace:pTHatMin=5.

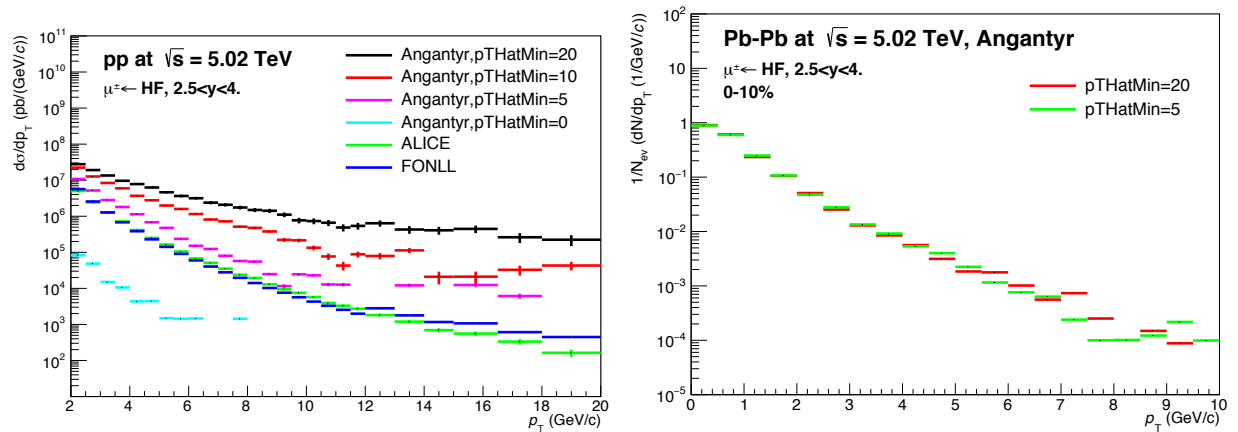


Figure 4.4: The  $p_T$ -distribution of heavy flavour decay muons at forward rapidity ( $2.5 < y < 4$ ) in pp collisions (left panel) and for most central (0-10%) Pb-Pb collisions (right panel) at  $\sqrt{s} = 5.02$  TeV respectively. The results with different PhaseSpace:pTHatMin cuts are compared.

Now the analysis program is described in more detail. The following two subsections are devoted for describing the production of HFM in three collision systems (pp, Xe-Xe and Pb-Pb). The productions of HFM are presented in the  $p_T$  range from 2 to 20 GeV/ $c$  and compared with the corresponding available ALICE data. The results obtained from Angantyr simulation are normalized with the yield obtained at  $p_T = 5$  GeV/ $c$ . In addition, a nominal average scale factor 0.4 at all energies is used for better visualization and in compliance to the slope of  $p_T$ -distributions with experimental data. These simulation results have been compared with the published ALICE measurements at their respective collision energies. The statistical errors are represented by vertical error bars in all the figures.

### pp collisions

The  $p_T$ -differential production cross-sections of HFM at forward rapidity ( $2.5 < y < 4$ ) in pp collisions at  $\sqrt{s} = 2.76$  TeV, 5.02 TeV, 7 TeV and 13 TeV are shown in Figure 4.5. The simulation results are compared with ALICE data [39–41] at their respective collision energies. The published ALICE data for HFM at  $\sqrt{s} = 13$  TeV is not available yet, so the simulated  $p_T$ -differential cross-section of HFM is compared with the Fixed Order + Next-to-Leading-Logarithms (FONLL) calculations at this  $\sqrt{s} = 13$  TeV. The prediction for the cross-section

of HFM is obtained from the heavy quark (charm ( $c$ ) and beauty ( $b$ )) decay into lepton. In this Monte Carlo (MC) simulation, heavy-quarks are produced via the elementary reactions:  $p + p \rightarrow charm + X$  and  $p + p \rightarrow bottom + X$  where the parton distribution function (PDF) CTEQ6.6 is used.

The simulation results are presented upto  $p_T = 20$  GeV/ $c$  for all the four energies as shown in Figure 4.5. However, the ALICE experimental data are available only upto  $p_T = 10$  GeV/ $c$  and  $p_T = 12$  GeV/ $c$  at  $\sqrt{s} = 2.76$  TeV and 7 TeV respectively. The ALICE measured the production cross-section of HFM at  $\sqrt{s} = 5.02$  TeV with more higher statistics at Run 2 compared to the Run 1. This allows to measure the HFM at  $\sqrt{s} = 5.02$  TeV upto  $p_T = 20$  GeV/ $c$ . It is to be noticed that the simulation results describe the ALICE data reasonably well. In the middle panel of Figure 4.5, the ratio of the simulation results with respect to the ALICE data are shown at  $\sqrt{s} = 2.76$  TeV, 5.02 TeV and 7 TeV respectively. The most bottom panel of Figure 4.5 shows the ratio of simulation with respect to FONLL at  $\sqrt{s} = 13$  TeV.

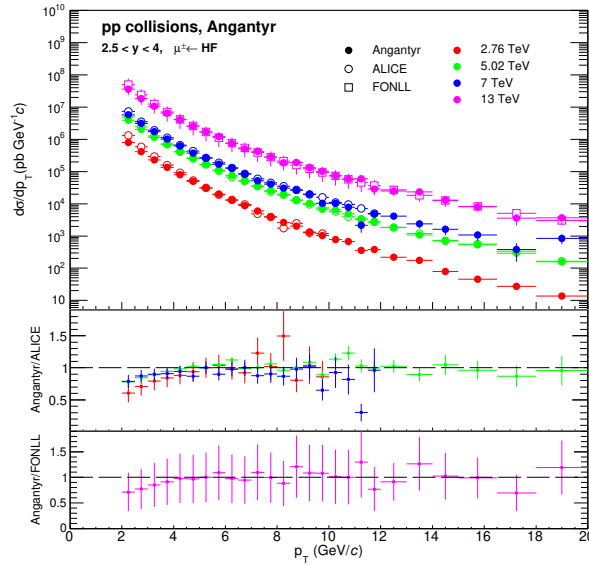


Figure 4.5: The simulated  $p_T$ -differential cross-section of muons from heavy flavour hadron decays in pp collisions are shown at  $\sqrt{s} = 2.76$  TeV, 5.02 TeV, 7 TeV and 13 TeV. Comparisons are done between simulation results and ALICE data [39–41]. At  $\sqrt{s} = 13$  TeV, the comparison is done with FONLL calculation.

In order to give a complete kinematic description, the HFM rapidity ( $y$ )-distribution is also presented in addition to the transverse momentum spectra at  $\sqrt{s} = 5.02$  and 7 TeV in



Figure 4.6. The HFM  $y$ -distributions at  $\sqrt{s} = 5.02$  TeV are obtained in two different  $p_T$  ranges:  $2 < p_T < 7$  GeV/ $c$  (top left panel) and  $7 < p_T < 20$  GeV/ $c$  (top right panel). Scaling factors 0.8 and 0.6 have been used for the said two  $p_T$  ranges respectively. Whereas, a scaling factor of 1.05 is used for the HFM  $y$ -spectrum obtained in the  $p_T$ -range  $2 < p_T < 12$  GeV/ $c$  at  $\sqrt{s} = 7$  TeV (bottom panel). This normalization is done for better comparison of simulation results with experimental data [39, 41]. It is to be noted that HFM  $y$ -distribution measured by ALICE exists only for pp collisions at  $\sqrt{s} = 5.02$  and 7 TeV.

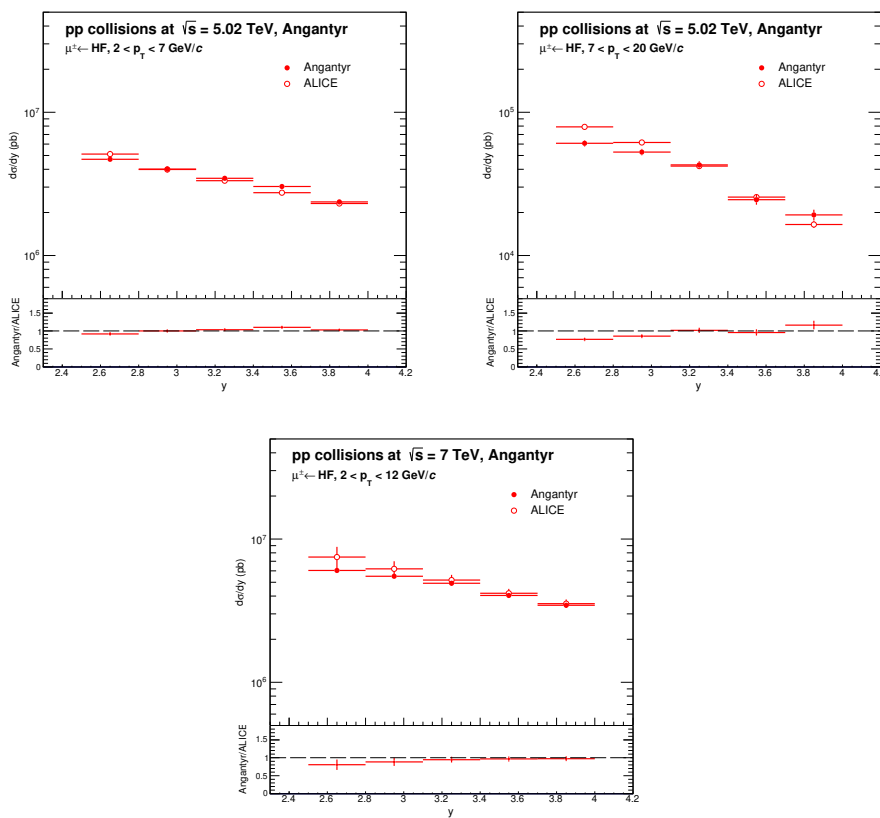


Figure 4.6: The simulated  $y$ -distribution of HFM in pp collisions at  $\sqrt{s} = 5.02$  TeV (top) and 7 TeV (bottom) are shown. The simulated results are compared with the corresponding ALICE data [39, 41]. The bottom panels describe the ratio of the simulation with respect to data.

## Heavy-ion collisions

After describing the production of HFM in pp collisions, the results obtained in heavy-ion (HI) collision using Angantyr model are presented. A sharp cut on  $\langle N_{part} \rangle$  is applied to

define the centrality classes in HI simulation. Table 4.4 presents a comparison of mean of  $N_{part}$  ( $\langle N_{part} \rangle$ ) and the corresponding standard deviation obtained from MCG model, Angantyr model (this work) and ALICE [42].

The  $p_T$ -differential yields of HFM at forward rapidity ( $2.5 < y < 4$ ) in Xe-Xe collisions at  $\sqrt{s_{NN}} = 5.44$  TeV are shown in Figure 4.7. This figure also shows a comparison of the simulation results with the ALICE data [43] in four different centrality classes: central (0–10%), semi-central (10–20% and 20–40%) and peripheral (40–60%). It is seen that the simulated HFM  $p_T$  spectra in Xe-Xe collisions describe the ALICE [43] data satisfactorily.

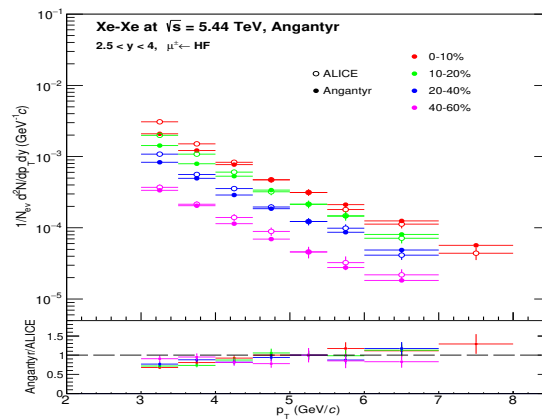


Figure 4.7: The  $p_T$ -differential yield of HFM with Angantyr simulation at forward rapidity ( $2.5 < y < 4$ ) and compared with the ALICE data [43] at various centrality classes (0–10%, 10–20%, 20–40% & 40–60%) in Xe-Xe collisions at  $\sqrt{s_{NN}} = 5.44$  TeV.

Figure 4.8 (left) displays the  $p_T$ -differential yields of muons produced from heavy flavour decay using Angantyr model at forward rapidity ( $2.5 < y < 4$ ) in Pb-Pb collision at  $\sqrt{s} = 2.76$  TeV. The simulation result for most central (0–10%) collision is compared with the ALICE data [44]. A similar observation for HFM production in Pb-Pb collision at  $\sqrt{s_{NN}} = 5.02$  TeV is presented in Figure 4.8 (right). The simulation results are obtained for three centrality classes (0–10%, 20–40% and 60–80%). ALICE has measured the production of HFM at forward rapidity in Pb-Pb collision at  $\sqrt{s_{NN}} = 5.02$  TeV in the same three centrality classes [44]. The simulation results are compared with the ALICE data as shown in Figure 4.8 (right). The bottom panel of Figure 4.8 shows ratio of the simulation with respect to ALICE data. The Angantyr model calculation reproduces the ALICE data nicely at both the energies.

Table 4.4: Comparison of mean of  $N_{part} (< N_{part} > \pm rms)$  in Pb-Pb collisions at  $\sqrt{s_{NN}} = 2.76$  TeV & 5.02 TeV and in Xe-Xe collisions at  $\sqrt{s_{NN}} = 5.44$  TeV obtained from MCG, ALICE and Angantyr (this work).

centrality	2.76 TeV			5.02 TeV			$< N_{part} >_{Pb-Pb}$			$< N_{part} >_{Xe-Xe}$ 5.44 TeV		
	MCG	ALICE	Angantyr	MCG	ALICE	Angantyr	MCG	ALICE	Angantyr	MCG	ALICE	Angantyr
0 – 5%	381.2±17.1	381.5 ± 18	380.3 ± 14.5	383.9 ± 16.5	383.4±17.8	383.6±14.0	237.3 ± 9.9	235.8±11	236.6±8.3	237.3 ± 9.9	235.8±11	236.6±8.3
5 – 10%	327.8±17.9	327.8 ± 20	327.9 ± 15.6	331.7± 17.8	331.2±19.6	331.9±15.6	207.0±11.6	206.7±13	206.2±9.2	207.0±11.6	206.7±13	206.2±9.2
10 – 20%	258.5±26.9	259.3 ± 27	258.0 ± 23.9	262.7±27.0	262±27.2	262.1±23.9	164.8±17.8	164.8±18	163.4±15.0	164.8±17.8	164.8±18	163.4±15.0
20 – 30%	184.3±22.4	186.5 ± 21	183.4 ± 19.3	188.2±22.6	187.9±21.6	186.9 ± 19.6	117.84±15.6	118.4±14	115.5±12.7	117.84±15.6	118.4±14	115.5±12.7
30 – 40%	127.2±18.8	130.1 ± 17	126.4 ± 13.8	130.5±19.1	130.8±17	129.4±13.8	81.4±13.8	82.2±11	78.8±8.7	81.4±13.8	82.2±11	78.8±8.7
40 – 50%	83.8±15.9	86.7 ± 13	82.4 ± 11.5	86.5±16.2	87.1±13.2	84.9±11.8	53.8±12.1	54.6±8.8	50.7±7.5	53.8±12.1	54.6±8.8	50.7±7.5
50 – 60%	51.8±13.3	54.3 ± 9.6	50.9 ± 6.9	53.8±13.6	54.3±9.9	52.3±7.2	33.5±10.3	34.1 ± 6.5	30.6±4.3	33.5±10.3	34.1 ± 6.5	30.6±4.3
60 – 70%	29.4±10.8	31 ± 6.9	28.7 ± 5.8	30.8±10.9	31±7	29.7±5.8	19.4±8.3	19.7±4.7	17.0±3.5	19.4±8.3	19.7±4.7	17.0±3.5
70 – 80%	15.2±7.7	15.8 ± 4.5	15.3 ± 2.3	16.0±7.9	15.7±4.6	16.3±2.3	10.9± 6.1	10.5±3.1	10.0±0.8	10.9± 6.1	10.5±3.1	10.0±0.8

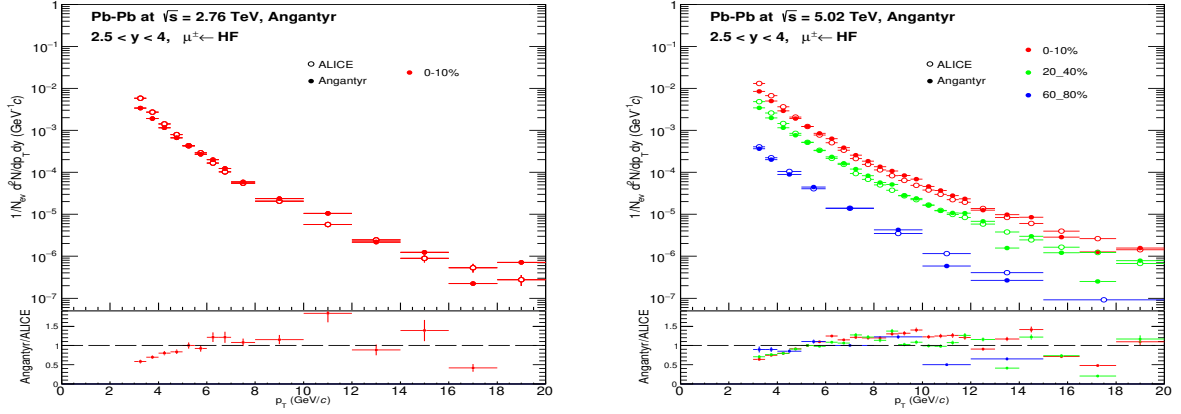


Figure 4.8: The  $p_T$ -differential yield of HFM at forward rapidity ( $2.5 < y < 4$ ) in Pb–Pb collisions at  $\sqrt{s_{NN}} = 2.76$  TeV (left) for most central collision (0–10%) and at  $\sqrt{s_{NN}} = 5.02$  TeV (right) for three centrality classes (0–10%, 20–40% and 60–80%) respectively. The simulated results are compared with the corresponding ALICE measurement [44].

### ALICE Run3 prediction for O-O collisions

It is worthwhile to mention that a prediction is given for the production of HFM in O-O collision at  $\sqrt{s_{NN}} = 6.37$  TeV with Angantyr model. ALICE has plan for a short period of O-O collision at  $\sqrt{s_{NN}} = 6.37$  TeV during Run 3 [45]. The study of HFM at forward rapidity ( $2.5 < y < 4$ ) in O-O system is done for both  $p_T$ - and  $y$ - distributions. 100 million events are generated at  $\sqrt{s_{NN}} = 6.37$  TeV using Angantyr for the simulation with O-O collision. It is to be noted that the Angantyr model does not incorporate any  $\alpha$ -cluster structure during the simulation with O-O collisions.

The  $p_T$ - differential production yield of HFM for central (0-10%) O-O collision is shown in Figure 4.9 (left). The result complies with the nature of other HFM  $p_T$ -distribution at comparatively higher mass collision system (Xe-Xe and Pb-Pb) done in this work. The right panel of Figure 4.9 shows the rapidity distribution of HFM in O-O collision within  $2 < p_T < 20$  GeV/ $c$  as complementary kinematic description.

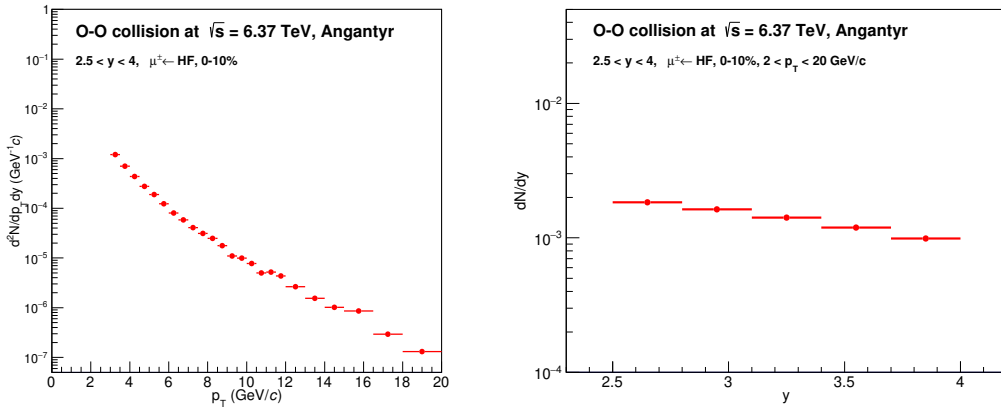


Figure 4.9: The  $p_T$  differential yield of HFM using Angantyr simulation at forward rapidity ( $2.5 < y < 4$ ) for 0–10% central O-O collisions at  $\sqrt{s_{NN}} = 6.37$  TeV (left). The rapidity distribution for 0–10% central collision within  $2 < p_T < 20$  GeV/c (right).

### Nuclear Modification Factor ( $R_{AA}$ ) of HFM

The profile of HFM  $p_T$  distributions between simulation results and the published ALICE measurement for both pp and HI collision have been compared so far. It has been discussed in section 4.1 that the present Angantyr model does not include any thermal medium formation in HI collision. This model excludes hadronic rescattering effects also [46]. In addition to the particle spectra, a more quantitative model-to-data comparison can be done by calculating the observable nuclear modification factor  $R_{AA}$ . Traditionally,  $R_{AA}$  is used as a probe to investigate the hadron production in HI collision compared to the pp collision. The  $R_{AA}$  is defined as the ratio of the yield in A-A collisions to that in pp collisions scaled by the corresponding average number of nucleon-nucleon collisions ( $\langle N_{coll} \rangle$ ). So, the transverse momentum ( $p_T$ ) dependent  $R_{AA}$  is given below by Eq. 4.5

$$R_{AA} = \frac{\frac{d^2 N_{AA}}{dp_T dy}}{\langle N_{coll} \rangle \frac{d^2 N_{pp}}{dp_T dy}} \quad (4.5)$$

In the previous section, results for Pb-Pb and Xe-Xe collisions have been presented assuming no creation of thermal medium in HI collisions. Here, an attempt is done to investigate the  $p_T$  dependence of  $R_{AA}$  for the production of HFM using Angantyr model. The  $p_T$  dependent

$R_{AA}$  calculations are performed in Pb-Pb collisions at the centre of mass energies 2.76 and 5.02 TeV respectively. The observations of  $R_{AA}$  in Pb-Pb collision are done only for most central (0–10%) collisions at both  $\sqrt{s} = 2.76$  TeV and 5.02 TeV.

To overcome small statistics specially at high  $p_T$  region ( $p_T > 12$  GeV/ $c$ ), the HFM  $p_T$ -spectra obtained with Angantyr simulation are fitted both in pp and Pb-Pb (0–10%) collisions. The fitting is performed with a polynomial function  $f(p_T)$  as given in Eq. 4.6.  $p_i$  ( $i = 0, 1, \dots, 7$ ) are the free parameters of the fit function. The HFM  $p_T$ -distribution is fitted in the  $p_T$  range from 2 to 20 GeV/ $c$  in pp collisions and within  $3 < p_T < 20$  GeV/ $c$  in Pb-Pb collisions (0–10%). Using this parameterized fit function for HFM  $p_T$ -spectra in pp and Pb-Pb collisions, we have evaluated the  $R_{AA}$  as given in Eq. 4.5.

$$f(p_T) = p_0 e^{p_T(p_1(1-e^{p_2 \cdot p_T}) + p_3)} \frac{1}{p_T^{p_4}} (p_5 + (p_6 \cdot p_T) + (p_7 \cdot p_T^2)) \quad (4.6)$$

Figure 4.10 presents the simulated  $R_{AA}$  as a function of  $p_T$  in 0–10% central Pb-Pb collisions at forward rapidity. The simulation results at  $\sqrt{s} = 2.76$  (left) and 5.02 (right) TeV are compared with the corresponding ALICE measurements. It is observed that the obtained  $R_{AA}$  in simulations overestimate the ALICE measurements but with values remain below unity. The simulated  $R_{AA}$  is found to be almost independent of  $p_T$  whereas ALICE has measured  $R_{AA}$  as a  $p_T$  dependent observable. The simulated  $R_{AA}$  is found close to unity at the lower energy  $\sqrt{s} = 2.76$  TeV (left panel of Figure 4.10) whereas it is substantially lower than unity at the higher energy  $\sqrt{s} = 5.02$  TeV (right panel of Figure 4.10).

Similar feature has also been observed in Ref. [14] for the  $R_{AA}$  of charged-particles using Angantyr+UrQMD model in the absence of any hadronic interactions in Pb-Pb collisions at  $\sqrt{s_{NN}} = 2.76$  TeV for two centrality classes 0–5% and 50–60%. It is reported that the Angantyr+UrQMD model overestimates the  $R_{AA}$  at mid- $p_T$  region ( $4 < p_T < 10$  GeV/ $c$ ) for peripheral collisions (50–60%) and in the range  $4 < p_T < 20$  GeV/ $c$  for central collisions (0–5%). In addition, Ref. [14] also shows that a cascade of hadronic interactions can significantly impact on  $R_{AA}$  causing more suppression up to 50%. These results put an agreement between simulation and experimental data only up to  $\sim 15$  GeV/ $c$ . In view of our present study

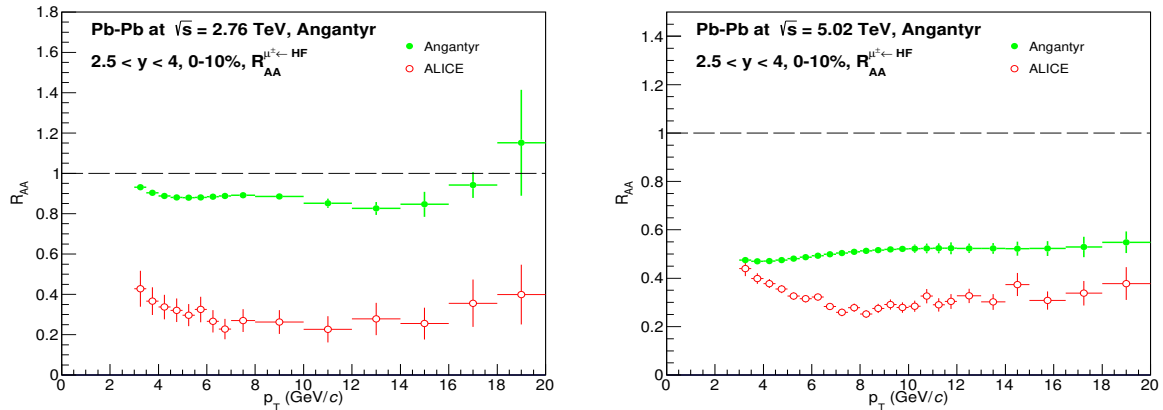


Figure 4.10: Angantyr simulation results for  $R_{AA}$  of Heavy Flavour decay Muons at forward rapidity ( $2.5 < y < 4$ ) in central (0–10%) Pb-Pb collisions at  $\sqrt{s_{NN}} = 2.76$  TeV (left) and 5.02 TeV (right). The simulated  $R_{AA}$  are compared with ALICE data [44].

of HFM and Ref. [14], it is noted that the simulated results on  $R_{AA}$  deviates from the typical results for particle production in experimental HI collision due to the non-inclusion of final state effects in the existing Angantyr model. The Angantyr simulation is based on the wounded nucleon model and does not incorporate any concept of binary  $N_{coll}$  scaling. The study of the simulated  $R_{AA}$  using Angantyr model suggests that a separation scale ( $p_{T,sep}$ ) between soft and hard components expected for  $N_{coll}$  scaling. However, the choice of the  $p_{T,sep}$ , would impact on the simulated  $R_{AA}$  results. A higher value of  $p_{T,sep}$  leads hard component to take over at higher  $p_T$  region. Note that, the normalisation on the  $p_T$ -spectra of HFM done in our analysis could impact on the suppression of  $R_{AA}$ . Regardless of the normalization, Figure 4.10 shows that the simulated  $R_{AA}$  is overestimated compared to the ALICE data and almost independent of transverse momentum over a large  $p_T$ -range (upto 20 GeV/c).

## 4.4 Charged particles production using Angantyr model

The study of charged particles in pp and A-A collisions using the default settings of Angantyr model in PYTHIA8 is done. The default settings in the model adds the colour reconnection (CR) mechanism based on multiple-parton interactions (MPI). In the default PYTHIA8, the colour strings only interact among themselves during the colour reconnection (CR) process and

hence a rearrangement of colour strings takes place just before the hadronisation. Recent LHC results in pp collisions show the signatures of near side ridge and strangeness enhancement similar to the features of HI collision [10, 11]. Therefore, the phenomenological understanding of hydrodynamics in HI collision experiments introduces new challenges. In the view of these new observations, an attempt to modify the colour string interactions is done in PYTHIA8. It is believed that a crowd of many colour strings due to high parton density environment in high multiplicity events can modify their effective string tension. The rope hadronisation [47, 48] and string shoving [49, 50] mechanisms have been implemented in PYTHIA8 for pp collisions to understand these flow-like effects observed in small systems. The rope hadronisation mechanism in PYTHIA modifies effective string tension with string density and affects the relative production probability of strange (s) quarks. On the other hand, string shoving mechanism allows PYTHIA8 to provide ridge like effects in pp collisions. However, these two new features of PYTHIA8 are not utilised for simulation in pp collisions rather the application of CR is done. In Angantyr model, the reconnection of colour is only allowed between the partons within the same nucleon-nucleon sub-collisions and is restricted between any two such sub-collisions. In this study of charged particle with Angantyr, the effect of CR mechanism has been demonstrated to test the qualitative evolution of the spectral shapes.

#### 4.4.1 Event generation for charged particle

For this study of charged particles, 1000 million events for pp, 10 million events for Xe-Xe and Pb-Pb collisions respectively are generated. The default settings of Angantyr model use the tuning “SoftQCD:all=on” with MPI which produces the inelastic, non-diffractive component of the total cross-section. The Colour Reconnection (ColourReconnection:mode=0) mechanism based on MPI is used here. The multiplicity distribution has dependency on MultiParton Interactions (MPI). In PYTHIA8, the average multiplicity distribution increases with the average number of MPI [51]. Colour Reconnection (CR) together with MPI in PYTHIA8 have special importance to describe underlying event (UE) observables [20]. A sharp cut is applied on the  $\langle N_{part} \rangle$  obtained by MCG as discussed in section 4.2 to define a centrality class for the simulation with HI collisions.



## 4.4.2 Results on charged particle

In this section, the results of the simulations for charged particles production using Angantyr model are presented. To begin with the Angantyr model for simulation in pp and HI collisions, a comparative study for charged particle production between the standalone PYTHIA8 and Angantyr model for pp collisions is needed. So, charged particle multiplicity ( $N_{ch}$ ) distribution in pp collision at  $\sqrt{s} = 2.76$  TeV has been compared between default PYTHIA8 and Angantyr model as shown in Figure 4.11. It is observed that the charged particles in pp collisions are qualitatively reproducible using the HI model (Angantyr) in PYTHIA8. Therefore, the simulation for charged particles using the default Angantyr model has been carried out irrespective of the collision systems.

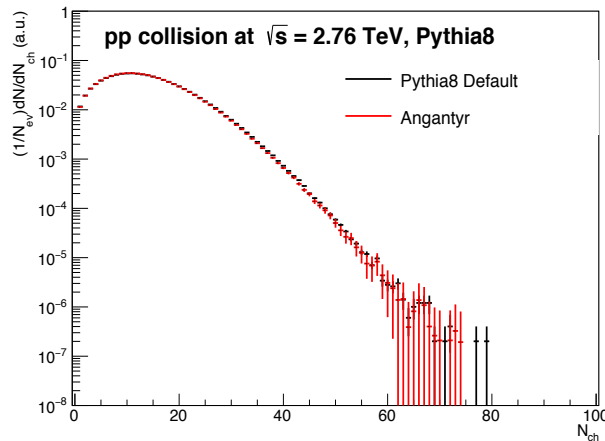


Figure 4.11: A comparison of charged-particle multiplicity distribution ( $N_{ch}$ ) at mid-rapidity ( $|y| < 0.5$ ) in pp collisions at  $\sqrt{s} = 2.76$  TeV between the standalone PYTHIA8 and Angantyr model.

### Transverse momentum spectra of charged particles

In Figure 4.12, the  $p_T$ -differential yields of charged particles in pp collisions at mid-rapidity  $|\eta| < 0.8$  in  $\sqrt{s} = 2.76, 5.02$  and 13 TeV using Angantyr model are presented upto  $p_T = 50$  GeV/ $c$ . The simulated results (full circle) are compared with the available ALICE data (open circle). The bottom panel of Figure 4.12 shows the ratio of the simulated results with the ALICE data. It is seen that the Angantyr result agrees well the ALICE data above  $p_T > 1$

GeV/ $c$ . The charged particles  $p_T$ -distribution in pp collision at  $\sqrt{s} = 7$  TeV using Angantyr model has been compared with ATLAS data in Ref [15]. No data is available for this energy in ALICE and the simulation result at  $\sqrt{s} = 7$  TeV is not shown in Figure 4.12. An arbitrary factor 0.84 is used to scale the simulated results in order to match the spectral shape with ALICE data. This scaling factor bears no physical significance and only shows the agreement of the spectral shape. It is to be noted that ALICE has measured the charged particle  $p_T$ -spectra upto  $p_T = 50$  GeV/ $c$  for both  $\sqrt{s} = 2.76$  and 5.02 TeV whereas it is only upto  $p_T = 20$  GeV/ $c$  at  $\sqrt{s} = 13$  TeV. Regardless of the ALICE measurement, the simulation is performed for the charged particle spectra upto  $p_T = 50$  GeV/ $c$  and ratios are shown upto  $p_T$  ranges measured by the ALICE at their respective center of mass energies.

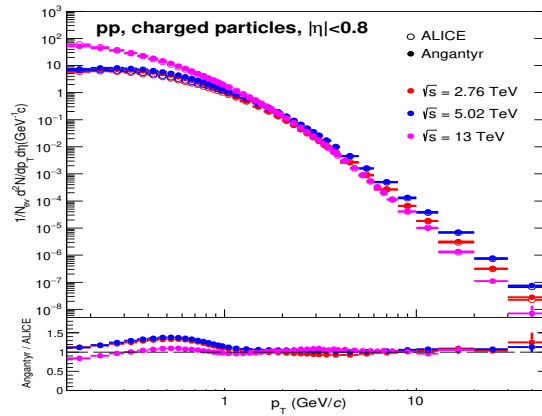


Figure 4.12: Transverse momentum spectra of charged-particle in pp collisions at  $\sqrt{s} = 2.76, 5.02$  and 13 TeV with Angantyr model. A comparison of model results (full circle) and ALICE data (open circle) [52] is done for  $\sqrt{s} = 2.76$  TeV (red), 5.02 TeV (blue) and 13 TeV (magenta).

Figure 4.13 shows the transverse momentum spectra of charged particles at mid-rapidity  $|\eta| < 0.8$  in Xe-Xe collisions at  $\sqrt{s_{NN}} = 5.44$  TeV. The simulation results are shown for nine different centrality classes from most central (0-5%) to peripheral (70-80%) with  $p_T$ -range upto 50 GeV/ $c$ . The simulation results are compared with the experimental data measured by ALICE [53]. The bottom panel of Figure 4.13 shows the ratio of the simulated results with the ALICE data. It can be seen that the Angantyr simulation describes the ALICE data better from peripheral to central collisions. Moreover, the model-to-data ratio shows humps around  $p_T = 7$  GeV/ $c$  and height of these humps increases towards more central collisions.

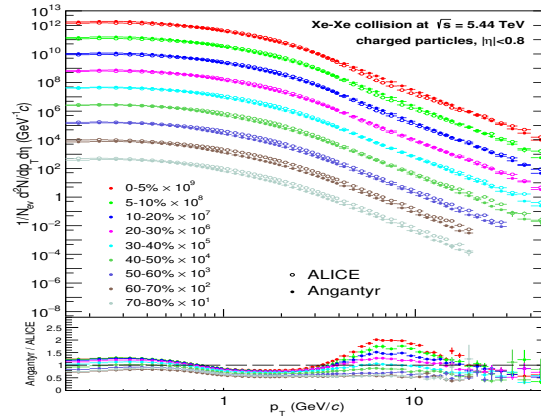


Figure 4.13: Transverse momentum of charged particles at mid-rapidity  $|\eta| < 0.8$  in Xe-Xe collisions at  $\sqrt{s_{NN}} = 5.44$  TeV for nine centrality classes. Comparisons are done between the simulation (full circle) and ALICE data (open circle). The centrality classes are described with different colors.

ALICE and ATLAS have measured the  $p_T$ -differential production yield of charged particles in Pb-Pb collisions at  $\sqrt{s_{NN}} = 2.76$  TeV. In Ref. [54], the comparisons between Angantyr simulation with ALICE data are shown for two centrality classes (0-20% and 40-60%). However, the comparisons with ATLAS data have been shown for four centrality classes (0-5%, 10-20%, 30-40%, 60-80%) in Ref. [15]. In this work, the simulation results are extended for nine different centrality classes from most central (0-5%) to peripheral (70-80%) collisions at  $\sqrt{s_{NN}} = 2.76$  and 5.02 TeV. In Figure 4.14, the transverse momentum spectra of charged particles at mid-rapidity ( $|\eta| < 0.8$ ) in Pb-Pb collisions at  $\sqrt{s_{NN}} = 2.76$  TeV (left panel) and 5.02 TeV (right panel) are shown. These simulation results are compared with the ALICE measurements for all nine centrality classes upto  $p_T = 50$  GeV/ $c$  at both the energies. The bottom panels of Figure 4.14 shows the model-to-data ratio. The results are similar as found in Xe-Xe collisions.

A study on the total charged particle multiplicity ( $N_{ch}^{tot}$ ) as a function of collision centrality in Xe-Xe and Pb-Pb collisions are performed. The collision centrality of a HI collision is described by the number of participating nucleons ( $N_{part}$ ) and the number of binary nucleon-nucleon collisions ( $N_{coll}$ ). Figure 4.15 represents the  $N_{ch}^{tot}$  per nucleon-nucleon pair as a function of  $N_{part}$  in Xe-Xe collisions at  $\sqrt{s_{NN}} = 5.44$  TeV and in Pb-Pb collisions at  $\sqrt{s_{NN}} = 2.76$  and 5.02 TeV respectively. The simulation result in Xe-Xe collision at  $\sqrt{s_{NN}} = 5.44$  TeV is

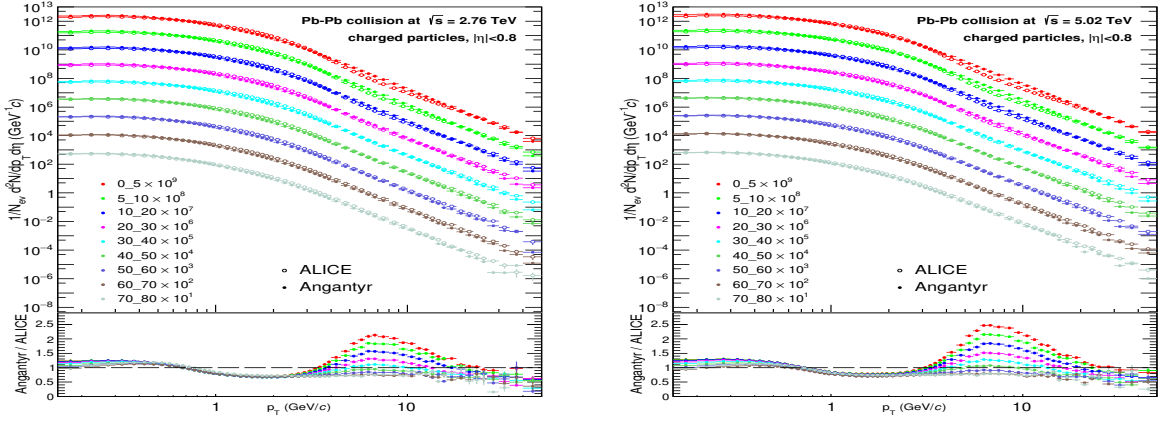


Figure 4.14: Transverse momentum of charged particles at mid-rapidity  $|\eta| < 0.8$  in Pb-Pb collisions at  $\sqrt{s_{NN}} = 2.76$  TeV (left) and 5.02 TeV (right) in nine centrality classes respectively. Comparisons are done between the simulation (full circle) and ALICE data (open circle). The centrality classes are described with different colors.

compared with the experimental data measured by ALICE [55]. For the comparison of the spectral shape, the simulated results are scaled by 1.07 for Xe-Xe and 1.29 and 1.08 for Pb-Pb collisions at  $\sqrt{s_{NN}} = 2.76$  and 5.02 TeV respectively. The simulation results describe the ALICE data reasonably well in Xe-Xe collisions for central collisions but deviates largely for peripheral collisions ( $N_{part} \lesssim 120$ ). The simulation results show the increasing trend of  $N_{ch}^{tot}$  per participants pair from peripheral to the most central collision as found in ALICE data. Figure 4.15 also indicates that  $N_{ch}^{tot}$  depends strongly on geometrical properties of the collision zone than on the size of the collision systems.

### Nuclear Modification Factor ( $R_{AA}$ ) of charged particles

In addition to the study of transverse momentum spectra of charged particles discussed in previous section, the study is extended for the nuclear modification factor ( $R_{AA}$ ) as a function of  $p_T$ . Figure 4.16 shows the  $p_T$ -dependent  $R_{AA}$  for the production of charged particles in Pb-Pb collisions at  $\sqrt{s_{NN}} = 2.76$  TeV (left) and 5.02 TeV (right). The simulated  $R_{AA}$  are shown for three centrality classes (0-10%, 10-20% and 50-60%). The simulated  $R_{AA}$  has been compared with the experimental results by ALICE [55]. Figure 4.16 indicates that the simulated  $R_{AA}$  of charged particles remain almost constant over the whole  $p_T$ -region after a sharp rise at lower

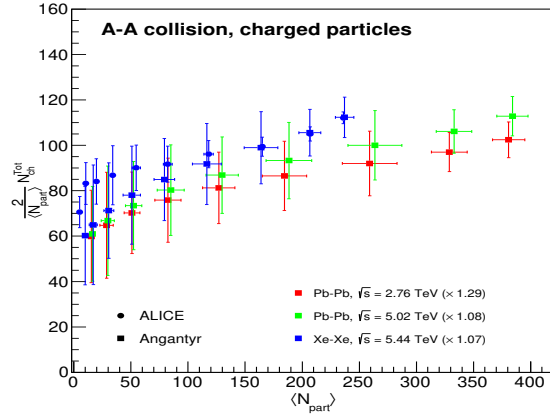


Figure 4.15: The  $\frac{2}{\langle N_{part} \rangle} N_{ch}^{tot}$  as a function of  $\langle N_{part} \rangle$  for Xe-Xe at  $\sqrt{s_{NN}} = 5.44$  TeV and Pb-Pb collisions at  $\sqrt{s_{NN}} = 2.76$  TeV and 5.02 TeV respectively. The comparison of Angantyr model calculation are done with ALICE data [55].

$p_T$  ( $p_T < 2$  GeV/c). However, it is noted that the simulation results overestimate the ALICE data upto  $p_T \lesssim 15$  GeV/c for the two central collisions but underestimate the ALICE data in the case of peripheral (50-60%) collision. The  $R_{AA}$  characteristics are similar for all the three centrality classes at both the center of mass energies except a slightly more suppression towards higher  $p_T$  region at  $\sqrt{s_{NN}} = 5.02$  TeV.

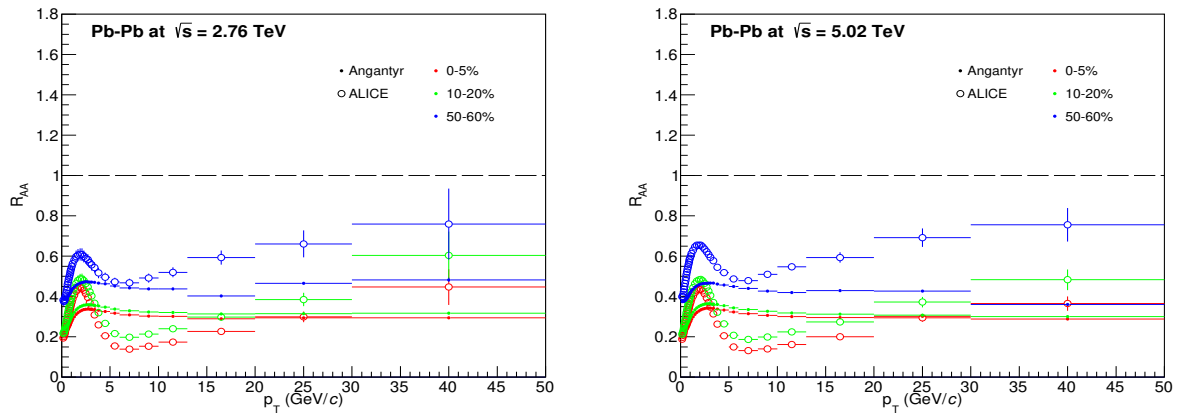


Figure 4.16:  $R_{AA}$  of charged-particles as a function of  $p_T$  at mid-rapidity ( $|\eta| < 0.8$ ) in Pb-Pb collisions at  $\sqrt{s_{NN}} = 2.76$  TeV (left) and 5.02 TeV (right) respectively. Comparison of simulated  $R_{AA}$  are done with ALICE data at three centrality classes (0-5%, 10-20% and 50-60%).

## Multiplicity dependence mean transverse momentum

In PYTHIA8, Colour Reconnection (CR) is a mechanism which reconnects the partons by colour strings just before the hadronisation. This can be attributed as a similar effect of flow where the partons are boosted just prior to the hadronisation in events with several multipartonic interactions (MPI). The CR is a microscopic process introduced in PYTHIA8 and does not need for a hot thermalised medium to be formed. The CR mechanism is very important ingredients in PYTHIA8 which could possibly explain the flow-like patterns observed in pp collisions [10, 11]. The inclusion of MPI in PYTHIA8 allows qualitative good description of the multiplicity distributions. The study of MPI in small system, provides the correlation between the number of MPI and the hardness/multiplicity of the event [56]. The other features like multiplicity dependence mean transverse momentum could be described by the colour reconnection. The modeling of CR is the probability of joining low and high  $p_T$  partons following the mechanism present in soft and hard QCD processes.

In this work, the CR effect in Angantyr model has been demonstrated in compliance with the observed experimental results. The simulation results are shown in Figure 4.17 for the mean transverse momentum ( $\langle p_T \rangle$ ) as a function of charged-particle multiplicity ( $N_{ch}$ ) at mid-rapidity  $|\eta| < 0.8$  ( $0.15 < p_T < 10$  GeV/ $c$ ) in both pp and HI (Xe-Xe and Pb-Pb) collisions. The comparison of these simulation results are also done with the ALICE data in pp collisions for energies at  $\sqrt{s} = 0.9, 2.76$  and 7 TeV and only at  $\sqrt{s} = 2.76$  TeV in Pb-Pb collisions.

Figure 4.17 (left) shows the comparative study of the mean  $p_T$  ( $\langle p_T \rangle$ ) with charged particle multiplicity ( $N_{ch}$ ) between Angantyr simulation and ALICE data [57] in pp collisions at three energies  $\sqrt{s} = 0.9, 2.76$  and 7 TeV respectively. The steep rise of  $\langle p_T \rangle$  with  $N_{ch}$  is observed for each energy. The bottom panel of Figure 4.17 (left) presents the ratio of simulation to data. It is seen that the simulation results are in compliance with the ALICE experimental data reasonably well in the multiplicity range of  $5 < N_{ch} < 20$  for all the three energies. A more qualitative study of this  $\langle p_T \rangle$  with  $N_{ch}$  has been performed for five LHC energies ( $\sqrt{s} = 0.9, 2.76, 5.02, 7$  and 13 TeV) as shown in Figure 4.17 (right). The bottom panel of Figure 4.17 (right) shows the ratio of the observables using the simulation at different energies

with respect to the highest energy  $\sqrt{s} = 13$  TeV. The results provide a knowledge of the energy dependency of  $\langle p_T \rangle$  in pp collision. It is noticed that a feeble effect on the  $\langle p_T \rangle$  induces by the collision energy. A maximum of 15% increment in the  $\langle p_T \rangle$  for the highest energy  $\sqrt{s} = 13$  TeV is observed with respect to the lowest energy  $\sqrt{s} = 0.9$  TeV. Figure 4.17 (right) also illustrates that the  $\langle p_T \rangle$  have the tendency to merge together towards higher multiplicity ( $N_{ch} \gtrsim 30$ ) irrespective of collision energy.

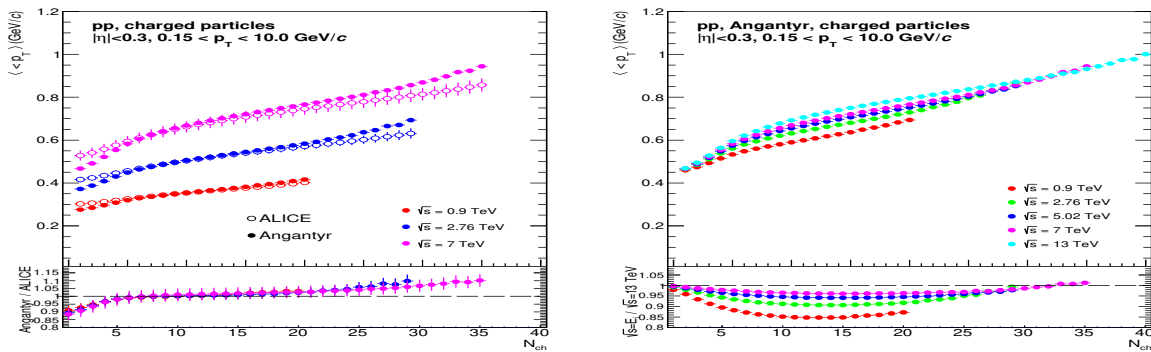


Figure 4.17: Mean transverse momentum ( $\langle p_T \rangle$ ) as function of charged particle multiplicity ( $N_{ch}$ ) in pp collisions at  $\sqrt{s} = 0.9, 2.76$  and  $7$  TeV. Comparison of simulations with ALICE data are done (left). Simulation results at  $\sqrt{s} = 0.9, 2.76, 5.02$  and  $7$  TeV are compared with respect to the result of  $13$  TeV (right).

The same study of  $\langle p_T \rangle$  with  $N_{ch}$  is done for Xe-Xe at  $\sqrt{s} = 5.44$  TeV and Pb-Pb collisions at  $\sqrt{s} = 2.76$  and  $5.02$  TeV respectively as shown in Figure 4.18. The simulation result for Pb-Pb at  $\sqrt{s} = 2.76$  TeV is compared to the corresponding ALICE data [57] and the bottom panel of this figure shows the ratio of simulation to the ALICE measurement. This comparison describes a qualitatively good agreement with experimental observation. Comparing the simulation results for Xe-Xe and Pb-Pb collisions from Figure 4.18, it seems there is no strong multiplicity dependence of  $\langle p_T \rangle$  above  $N_{ch} \gtrsim 10$ . Moreover, the  $\langle p_T \rangle$  is also found to be independent of the system of HI collisions at a comparable collision energy.

### ALICE Run3 prediction for O-O collisions

In view of the foreseen O-O collisions during ALICE Run 3, predictions for the transverse momentum distribution and mean transverse momentum as a function of charged particle

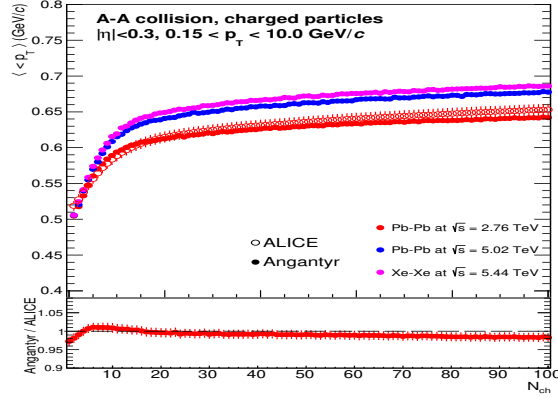


Figure 4.18: The mean transverse momentum ( $\langle p_T \rangle$ ) as function of charged particle multiplicity ( $N_{ch}$ ) in Xe-Xe at  $\sqrt{s_{NN}} = 5.44$  TeV and in Pb-Pb collisions at  $\sqrt{s_{NN}} = 2.76$  and 5.02 TeV respectively. Comparison of simulation with ALICE data [57] (Pb-Pb at  $\sqrt{s_{NN}} = 2.76$  TeV).

multiplicity are given in Figure 4.19. The left panel of Figure 4.19 presents the differential  $p_T$ -distribution of charged particles in O-O collisions at  $\sqrt{s} = 6.37$  TeV at mid-rapidity ( $|\eta| < 0.8$ ) for four centrality classes: 0-5%, 5-10%, 10-20% and 20-100%. The  $\langle p_T \rangle$  with  $N_{ch}$  at mid-rapidity ( $|\eta| < 0.3$ ) for integrated  $p_T$  range from 0.15 to 10 GeV/c is shown in Figure 4.19 (right). These results are very similar as obtained in the case of Xe-Xe and Pb-Pb collisions (Figure 4.18).

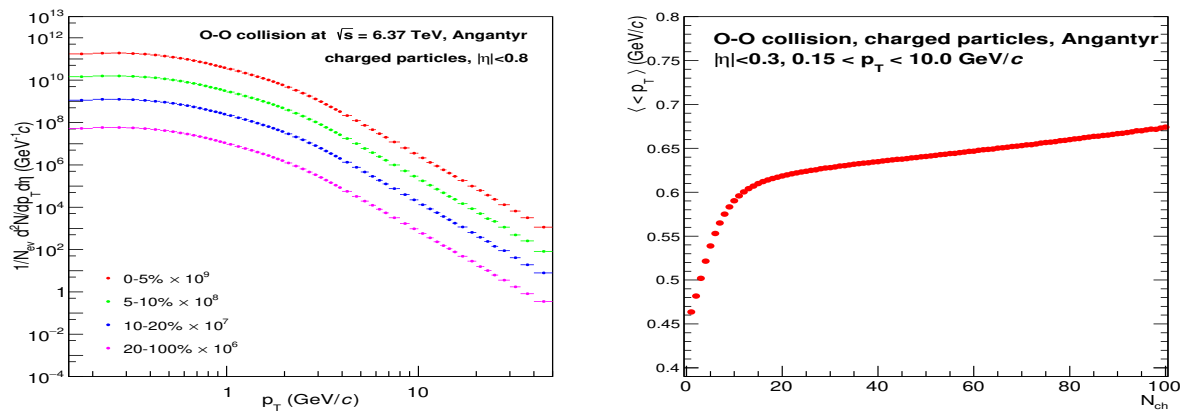


Figure 4.19: The profile of the charged-particles production at mid-rapidity ( $|\eta| < 0.8$ ) in O-O collisions at  $\sqrt{s_{NN}} = 6.37$  TeV for four centrality classes: 0-5%, 5-10%, 10-20% and 20-100% using Angantyr simulation (left). The  $\langle p_T \rangle$  as a function of  $N_{ch}$  ( $0.15 < p_T < 10$  GeV/c) at mid-rapidity  $|\eta| < 0.3$  (right).



## 4.5 Summary

In this simulation work, we have studied the production of HFM and charged particles in pp and HI collisions using the Angantyr model with PYTHIA8 event generator. For the first time, the production of HFM has been presented using a QGP free HI model such as Angantyr. The description of the HFM and charged particles productions using Angantyr Model agrees with the experimental ALICE data at various LHC energies fairly. The simulated  $R_{AA}$  for the production of HFM overestimates the ALICE data at  $\sqrt{s_{NN}} = 2.76$  and 5.02 TeV for the most central Pb-Pb collision. It is observed that the simulated  $R_{AA}$  in a QGP free HI collisions behave almost independent of  $p_T$  whereas the traditional results of HI experiment show  $p_T$ -dependent  $R_{AA}$ . An attempt may be done to investigate the HFM analysis using Angantyr with the new features of PYTHIA8 like CR mechanism to check any flow like effect and also an impact on  $R_{AA}$  measurement. On the other hand, the simulated  $R_{AA}$  of charged particles in Pb-Pb collisions overestimate the ALICE data for two central (0-5% and 10-20%) collisions but underestimate in the case of peripheral (50-60%) collision. The similar behaviour of  $R_{AA}$  (independent of  $p_T$ ) is seen for both HFM and charged particles.

The study of charged particles in pp and HI collisions using the Angantyr model with a combined configurations of multiparton interactions and colour reconnection is done. The effect of CR has been demonstrated to add any possible flow like effect with no thermal medium formation. The simulation results shown for  $p_T$  distribution of charged particles in pp collision agree with the experimental ALICE data almost over all  $p_T$  region. The discrepancy in the low  $p_T$  region ( $p_T < 1$  GeV/ $c$ ) could be originated from the differences of Angantyr and the default PYTHIA8 minimum bias machinery. All semi-inclusive cross-sections in hadron-hadron collisions could not be exactly reproducible using Angantyr model since there are basic operational differences in Angantyr from the default PYTHIA8. In default PYTHIA8, the choice of impact parameter is according to an exponentially falling overlap function, while it is determined by the fluctuations and opacity functions using Angantyr [15]. Therefore, the deviation towards low  $p_T$  region in Figure 4.12 is observed. In HI collision, the results for the charged particles are quite satisfactory for all centrality classes. However, we have seen

humps around  $p_T = 7 \text{ GeV}/c$  in the model-to-data ratio and these are getting stronger as we move towards more central collisions. This relates as an effect of CR and may indicate a sign of collectivity. The mean transverse momentum ( $\langle p_T \rangle$ ) as a function of charged-particle multiplicity ( $N_{ch}$ ) in pp and A-A (Pb-Pb & Xe-Xe) collisions have been presented. This study found in agreement with the ALICE data in the multiplicity range  $5 < N_{ch} < 20$  in case of pp collisions over wide range of LHC energies from  $\sqrt{s} = 0.9 \text{ TeV}$  to  $7 \text{ TeV}$ . It is also found in pp simulations that the  $\langle p_T \rangle$  as a function of  $N_{ch}$  has a very weak dependency on collision energy for  $N_{ch} < 30$ . The same study in case of HI collisions shows that the  $\langle p_T \rangle$  is independent of collision systems for a comparable collision energy.

The simulated results of  $R_{AA}$  for HFM and charged particles in Pb-Pb collisions are found to be independent of  $p_T$ . This could be an interesting feature of HI collision assuming no thermalised medium formation. Traditionally,  $R_{AA}$  value below unity may indicate the formation of QGP in HI collisions. Though the present Angantyr model does not assume any QGP formation but several other effects would contribute to describe the simulated  $R_{AA}$ . As explained before, the Angantyr model is based on the wounded nucleon model and does not scale binary collision  $N_{coll}$  accordingly. In Angantyr, the nucleon-nucleon interactions with different particle dynamics lead to an disagreement of  $R_{AA}$  below unity towards the high  $p_T$ .

It is to be noted that part of the discrepancy in the HI simulation results with data could originate from the implementation of different method centrality calculation with respect to experimental definition. Recently, the high energy physics community encourages for RIVET (Robust Independent Validation of Experiment and Theory) analysis [58] specially for HI collisions. RIVET is a framework to make direct comparison between Monte Carlo event generators and experimental results in pp, p-A and A-A collisions. RIVET is enable to provide calibration framework to define centrality classes based on the requirement of different experiments. Overall, the Angantyr model provides a common platform to exercise the phenomenology of high energy collisions in pp, p-A and A-A systems.

---

# Bibliography

---

- [1] C. Loizides, *Experimental overview on small collision systems at the LHC*, *Nucl. Phys. A* **956** (2016) 200 [[1602.09138](#)]. [136](#)
- [2] B. Schenke, *The smallest fluid on Earth*, *Rept. Prog. Phys.* **84** (2021) 082301 [[2102.11189](#)]. [136](#)
- [3] P. Christakoglou, *Experimental overview of collective flow with identified particles at RHIC and the LHC*, *EPJ Web Conf.* **90** (2015) 08004. [136](#)
- [4] U. Heinz and R. Snellings, *Collective flow and viscosity in relativistic heavy-ion collisions*, *Ann. Rev. Nucl. Part. Sci.* **63** (2013) 123 [[1301.2826](#)]. [136](#)
- [5] T. Sjöstrand, S. Ask, J.R. Christiansen, R. Corke, N. Desai, P. Ilten et al., *An introduction to PYTHIA 8.2*, *Comput. Phys. Commun.* **191** (2015) 159 [[1410.3012](#)]. [137](#), [138](#), [150](#)
- [6] Z. Khabanova, *Studies of collective effects in pp collisions at the LHC with the balance function for identified particles*, Ph.D. thesis, Utrecht U., 2020. 10.33540/286. [137](#)
- [7] CMS collaboration, *Evidence for Collective Multiparticle Correlations in p-Pb Collisions*, *Phys. Rev. Lett.* **115** (2015) 012301 [[1502.05382](#)].
- [8] A. Kisiel and T.J. Humanic, *Femtoscopic signatures of collective behavior as a probe of the thermal nature of relativistic heavy ion collisions*, [0908.3830](#).
- [9] A. Jaiswal et al., *Dynamics of QCD matter — current status*, *Int. J. Mod. Phys. E* **30** (2021) 2130001 [[2007.14959](#)]. [137](#)

- [10] CMS collaboration, *Evidence for collectivity in pp collisions at the LHC*, *Phys. Lett. B* **765** (2017) 193 [[1606.06198](#)]. 137, 160, 166
- [11] ALICE collaboration, *Enhanced production of multi-strange hadrons in high-multiplicity proton-proton collisions*, *Nature Phys.* **13** (2017) 535 [[1606.07424](#)]. 137, 160, 166
- [12] J. Bellm et al., *Herwig 7.0/Herwig++ 3.0 release note*, *Eur. Phys. J. C* **76** (2016) 196 [[1512.01178](#)]. 138
- [13] SHERPA collaboration, *Event Generation with Sherpa 2.2*, *SciPost Phys.* **7** (2019) 034 [[1905.09127](#)]. 138
- [14] A.V. da Silva, W.M. Serenone, D. Dobrigkeit Chinellato, J. Takahashi and C. Bierlich, *Studies of heavy-ion collisions using PYTHIA Angantyr and UrQMD*, [2002.10236](#). xxvii, 138, 158, 159
- [15] C. Bierlich, G. Gustafson, L. Lönnblad and H. Shah, *The Angantyr model for Heavy-Ion Collisions in PYTHIA8*, *JHEP* **10** (2018) 134 [[1806.10820](#)]. 138, 139, 141, 162, 163, 169
- [16] C. Bierlich, G. Gustafson and L. Lönnblad, *Diffraction and non-diffractive wounded nucleons and final states in pA collisions*, *JHEP* **10** (2016) 139 [[1607.04434](#)]. 138, 139, 142
- [17] PYTHIA8 online manual. <https://pythia.org/latest-manual/Welcome.html>. 139, 150
- [18] T. Sjostrand and P.Z. Skands, *Transverse-momentum-ordered showers and interleaved multiple interactions*, *Eur. Phys. J. C* **39** (2005) 129 [[hep-ph/0408302](#)]. 140
- [19] B. Andersson, G. Gustafson, G. Ingelman and T. Sjostrand, *Parton Fragmentation and String Dynamics*, *Phys. Rept.* **97** (1983) 31. 140
- [20] ATLAS collaboration, *A study of different colour reconnection settings for Pythia8 generator using underlying event observables*, . 140, 160
- [21] C. Loizides, J. Nagle and P. Steinberg, *Improved version of the PHOBOS Glauber Monte Carlo*, *SoftwareX* **1-2** (2015) 13 [[1408.2549](#)]. 142, 144, 145

- [22] M.L. Miller, K. Reygers, S.J. Sanders and P. Steinberg, *Glauber modeling in high energy nuclear collisions*, *Ann. Rev. Nucl. Part. Sci.* **57** (2007) 205 [[nucl-ex/0701025](#)]. [142](#), [144](#)
- [23] V.N. Gribov, *Glauber corrections and the interaction between high-energy hadrons and nuclei*, *Sov. Phys. JETP* **29** (1969) 483. [142](#)
- [24] M.L. Good and W.D. Walker, *Diffraction dissociation of beam particles*, *Phys. Rev.* **120** (1960) 1857. [142](#)
- [25] B. Blaettel, G. Baym, L.L. Frankfurt, H. Heiselberg and M. Strikman, *Hadronic cross-section fluctuations*, *Phys. Rev. D* **47** (1993) 2761. [142](#)
- [26] B. Andersson, G. Gustafson and B. Nilsson-Almqvist, *A Model for Low  $p(t)$  Hadronic Reactions, with Generalizations to Hadron - Nucleus and Nucleus-Nucleus Collisions*, *Nucl. Phys. B* **281** (1987) 289. [142](#)
- [27] H. Pi, *An Event generator for interactions between hadrons and nuclei: FRITIOF version 7.0*, *Comput. Phys. Commun.* **71** (1992) 173. [142](#)
- [28] A. Bialas, M. Bleszynski and W. Czyz, *Multiplicity Distributions in Nucleus-Nucleus Collisions at High-Energies*, *Nucl. Phys. B* **111** (1976) 461. [142](#)
- [29] H. Shah, *The Angantyr Model For Simulating Heavy-Ion Collisions*, bachelor thesis, Lund U., 2021. [xxvii](#), [143](#), [145](#)
- [30] C. Loizides, J. Kamin and D. d’Enterria, *Improved Monte Carlo Glauber predictions at present and future nuclear colliders*, *Phys. Rev. C* **97** (2018) 054910 [[1710.07098](#)]. [144](#), [146](#)
- [31] D. d’Enterria and C. Loizides, *Progress in the Glauber model at collider energies*, *Ann. Rev. Nucl. Part. Sci.* **71** (2021) 315 [[2011.14909](#)]. [144](#)
- [32] ALICE collaboration, *Centrality determination of Pb-Pb collisions at  $\sqrt{s_{NN}} = 2.76$  TeV with ALICE*, *Phys. Rev. C* **88** (2013) 044909 [[1301.4361](#)]. [145](#)

- [33] PHOBOS collaboration, *Phobos results on charged particle multiplicity and pseudorapidity distributions in Au+Au, Cu+Cu, d+Au, and p+p collisions at ultra-relativistic energies*, *Phys. Rev. C* **83** (2011) 024913 [[1011.1940](#)]. [145](#)
- [34] TGlauberMC on HepForge. <https://tglaubermc.hepforge.org/>. [146](#)
- [35] R. Singh, B. Sharma, R. Bala and S.S. Sambyal, *Simulation study of Open Charm production in proton-proton collisions at  $\sqrt{s} = 13$  TeV using Pythia 8*, [2108.09965](#). [148](#)
- [36] ALICE collaboration, *J/ $\psi$  Production as a Function of Charged Particle Multiplicity in pp Collisions at  $\sqrt{s} = 7$  TeV*, *Phys. Lett. B* **712** (2012) 165 [[1202.2816](#)]. [148](#)
- [37] ALICE collaboration, *Measurement of charm and beauty production at central rapidity versus charged-particle multiplicity in proton-proton collisions at  $\sqrt{s} = 7$  TeV*, *JHEP* **09** (2015) 148 [[1505.00664](#)]. [148](#)
- [38] M.S. Islam, T. Sinha, P. Roy and P.P. Bhaduri, *Study of heavy-flavor decay muon production in proton-proton and heavy-ion collisions using the Angantyr model at LHC energies*, *Int. J. Mod. Phys. E* **31** (2022) 2250007. [149](#)
- [39] ALICE collaboration, *Production of muons from heavy-flavour hadron decays in pp collisions at  $\sqrt{s} = 5.02$  TeV*, *JHEP* **09** (2019) 008 [[1905.07207](#)]. [xxviii](#), [150](#), [151](#), [152](#), [153](#)
- [40] ALICE collaboration, *Production of muons from heavy flavour decays at forward rapidity in pp and Pb-Pb collisions at  $\sqrt{s_{NN}} = 2.76$  TeV*, *Phys. Rev. Lett.* **109** (2012) 112301 [[1205.6443](#)].
- [41] ALICE collaboration, *Heavy flavour decay muon production at forward rapidity in proton-proton collisions at  $\sqrt{s} = 7$  TeV*, *Phys. Lett. B* **708** (2012) 265 [[1201.3791](#)]. [xxviii](#), [151](#), [152](#), [153](#)
- [42] ALICE collaboration, *Centrality determination in heavy ion collisions*, <https://inspirehep.net/literature/1821843>. [154](#)

- [43] ALICE collaboration, *Inclusive heavy-flavour production at central and forward rapidity in Xe–Xe collisions at  $s_{NN}=5.44$  TeV*, *Phys. Lett. B* **819** (2021) 136437 [[2011.06970](#)]. [xxviii](#), [154](#)
- [44] ALICE collaboration, *Production of muons from heavy-flavour hadron decays at high transverse momentum in Pb–Pb collisions at  $\sqrt{s_{NN}} = 5.02$  and 2.76 TeV*, [2011.05718](#). [xxviii](#), [154](#), [156](#), [159](#)
- [45] ALICE collaboration, *ALICE physics projections for a short oxygen-beam run at the LHC*, <https://inspirehep.net/literature/1945314>. [156](#)
- [46] S.A. Bass et al., *Microscopic models for ultrarelativistic heavy ion collisions*, *Prog. Part. Nucl. Phys.* **41** (1998) 255 [[nucl-th/9803035](#)]. [157](#)
- [47] C. Bierlich, G. Gustafson, L. Lönnblad and A. Tarasov, *Effects of Overlapping Strings in pp Collisions*, *JHEP* **03** (2015) 148 [[1412.6259](#)]. [160](#)
- [48] C. Bierlich, *Rope Hadronization and Strange Particle Production*, *EPJ Web Conf.* **171** (2018) 14003 [[1710.04464](#)]. [160](#)
- [49] C. Bierlich, G. Gustafson and L. Lönnblad, *A shoving model for collectivity in hadronic collisions*, [1612.05132](#). [160](#)
- [50] C. Bierlich, S. Chakraborty, G. Gustafson and L. Lönnblad, *Setting the string shoving picture in a new frame*, *JHEP* **03** (2021) 270 [[2010.07595](#)]. [160](#)
- [51] E. Cuautle, E. Dominguez and I. Maldonado, *Extraction of multiple parton interactions and color reconnection from forward-backward multiplicity correlations*, *Eur. Phys. J. C* **79** (2019) 626 [[1907.08706](#)]. [160](#)
- [52] ALICE collaboration, *Transverse momentum spectra and nuclear modification factors of charged particles in pp, p–Pb and Pb–Pb collisions at the LHC*, *JHEP* **11** (2018) 013 [[1802.09145](#)]. [xxix](#), [162](#)

- [53] ALICE collaboration, *Transverse momentum spectra and nuclear modification factors of charged particles in Xe-Xe collisions at  $\sqrt{s_{\text{NN}}} = 5.44$  TeV*, *Phys. Lett. B* **788** (2019) 166 [[1805.04399](#)]. 162
- [54] C. Bierlich, T. Sjöstrand and M. Uthm, *Hadronic rescattering in pA and AA collisions*, *Eur. Phys. J. A* **57** (2021) 227 [[2103.09665](#)]. 163
- [55] ALICE collaboration, *Centrality and pseudorapidity dependence of the charged-particle multiplicity density in Xe-Xe collisions at  $\sqrt{s_{\text{NN}}} = 5.44$  TeV*, *Phys. Lett. B* **790** (2019) 35 [[1805.04432](#)]. xxix, 164, 165
- [56] ALICE collaboration, *Charged-particle production as a function of multiplicity and transverse sphericity in pp collisions at  $\sqrt{s} = 5.02$  and 13 TeV*, *Eur. Phys. J. C* **79** (2019) 857 [[1905.07208](#)]. 166
- [57] ALICE collaboration, *Multiplicity dependence of the average transverse momentum in pp, p-Pb, and Pb-Pb collisions at the LHC*, *Phys. Lett. B* **727** (2013) 371 [[1307.1094](#)]. xxx, 166, 167, 168
- [58] Rivet — the particle-physics MC analysis toolkit. <https://rivet.hepforge.org/>. 170



# CHAPTER 5

---

## MFT-Ladder Assembly and Quality Assurance Test

---

In chapter 2, we have discussed the Muon Spectrometer (MS) of ALICE detector and the upgrade program of ALICE detector for Run 3. In the upgrade program of ALICE, the new Muon Forward Tracker (MFT) is installed upstream of the front absorber of Muon Spectrometer during the long shutdown 2 (LS2). The MFT has added to improve the vertexing capabilities of muon tracks to the existing muon spectrometer during Run 3 experiment. In this chapter, the assembly of MFT-ladders and their Quality Assurance (QA) tests are discussed. A detail description of the procedures of QA test for the qualification of ladders has been presented.

During Run 3, the ALICE will operate at higher integrated luminosity of  $L_{int} = 13 \text{ nb}^{-1}$  for Pb-Pb collision which is almost 10 times higher than the ALICE Run 2. It has planned to collect data with  $L_{int} = 200 \text{ pb}^{-1}$  in pp collision at  $\sqrt{s} = 13 \text{ TeV}$  also. Consequently, the electronics readout of ALICE detectors are upgraded to comply with high luminosity data responses. In Run 3, the data recording is 100 times more than the volume of data recorded by the Run 2 (2018). Therefore, the data-taking rate of ALICE detector has to be increased significantly to record this huge amount of data. The muon physics program with the existing Muon Spectrometer (MS) suffers several limitations, specially due to the multiple scattering experienced by the muon tracks inside hadron absorber [1]. So, the vertex region smears and it prevents to disentangle prompt and b-decay  $J/\psi$  as well as open charm and beauty

measurement. This smearing of vertex adds large systematic uncertainties which could not be explained well even with the available theoretical models. In addition, the limitation is also present in the rejection of muons coming from semimuonic decays of pions and kaons in the front absorber of MS and these create important background in the analyses using single muons and dimuon for the studies of low masses and low  $p_T$ . Finally, the hadron absorber is responsible for the degradation of kinematics to determine the mass resolution for resonances, especially for low masses. These limitations are to be overcome integrating a mere transparent detector between interaction point and the front (hadron) absorber of MS. This new detector Muon Forward Tracker (MFT) will put more pointing accuracy promising a reliable measurement of the offset with respect to the primary vertex of the interaction. This accuracy could be achieved by matching the extrapolated muon tracks coming from the muon tracking chambers after the front absorber with the clusters measured in MFT planes before this front absorber. So, this muons' offset could allow the limitations of muon physics such as (i) disentangle prompt (quarkonia, thermal photons) from displaced (open heavy flavour) dimuons, (ii) open charm and open beauty dimuons can be distinguished, (iii) extension of study of heavy flavour (HF) using single muons down to  $p_T \sim 1 \text{ GeV}/c$ , and the most interesting study beauty production down to zero  $p_T$  via  $J/\psi$  from b, a unique feature at the LHC in heavy-ion (A-A) collisions. Moreover, a possible improvement could be reached by rejecting a large fraction of background applying required cuts for matching the extrapolated muon tracks and the MFT clusters. This will allow a substantial reduction of background from semimuonic decays of primary and secondary pions and kaons, as well as punch-through hadrons arriving at the tracking chambers of MS escaping the front absorber.

## 5.1 The basic structure of MFT

The MFT consists of two identical conical halves placed coaxial to the beam pipe. Each of the conical structure is composed of five half disks with detection planes at both sides. A schematic layout of MFT integrated at the ALICE is shown in Figure 5.1. The MFT is placed upstream to the front absorber and inside the acceptance of Muon Spectrometer. The MFT

along with Muon Spectrometer will be a unique subset which allows a pseudo-rapidity coverage  $-3.6 < \eta < -2.45$ . The MFT is placed between the ITS (Inner Tracking System) inner barrel and the front absorber of MUON Spectrometer along the beam direction. The two conical halves of MFT surround the beam-pipe and is placed inside the ITS outer barrel.

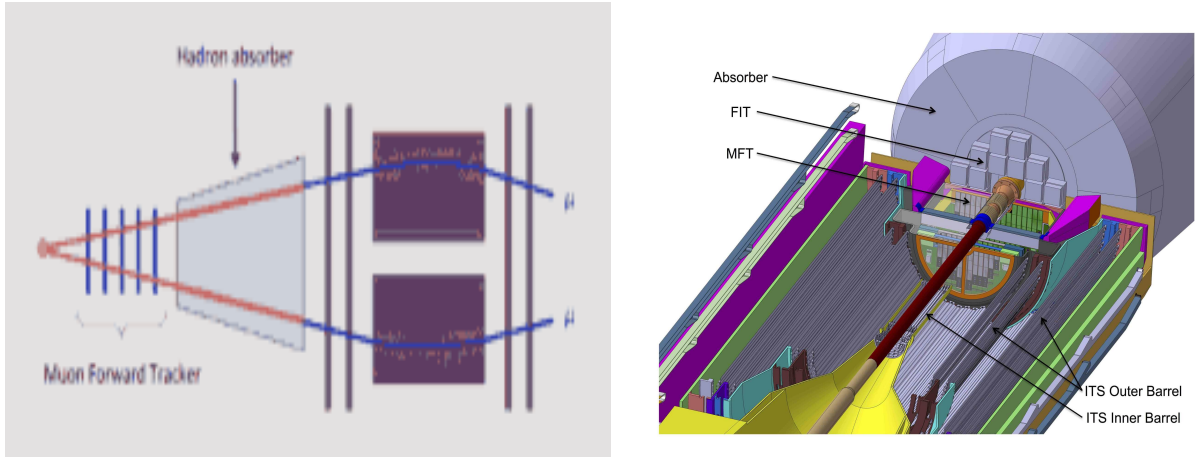


Figure 5.1: The schematic layout of MFT integrated with ALICE.

In Figure 5.2, a schematic view of the MFT detector is shown. The five half disks of each MFT half-cone are positioned at the distances 460 mm, 493 mm, 531 mm, 687 mm and 768 mm respectively from the interaction point (IP) along the beam direction. The top and bottom MFT half-cones are called as Top MFT (H1) and Bottom MFT (H0). The first two half-disks from the IP are identical (D0 & D1) while the remaining three are all different (D2, D3 & D4). The basic detection element of MFT is silicon pixel sensor which is integrated on a mechanical ladder structure. Each of the MFT half-disk is equipped with a specific number of ladders. However, a ladder may consist of 2 to 5 sensor chips bonded to a Flex Printed Circuit (FPC). The FPC is equipped with a connector and SMD (Surface Mounted Device) components such as decoupling capacitors and terminating resistors. The sensors in ladder are mounted on FPC using a glue of non-conducting type. The ultrasonic wire bonding is used for electrical inter-connection. In Table 5.1, the geometrical parameters of each half-disk are summarised.

The ladders are glued on each face of half disk. Each face of the half-disk is divided into 4 different zones called zone-0, zone-1, zone-2 and zone-3. The arrangement of ladders for each half-disk at different zones are shown in Figure 5.3.

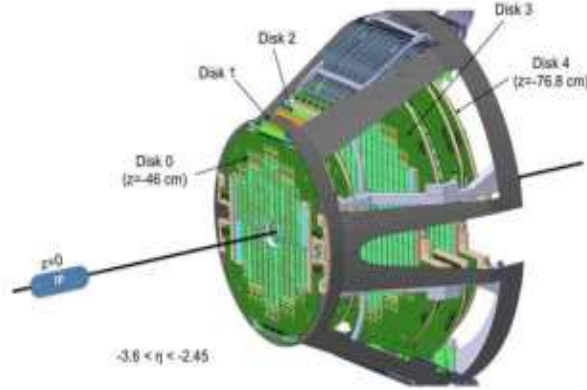


Figure 5.2: The schematic view of MFT detector [2].

Table 5.1: Various geometrical parameters of each half-disk of MFT [3, 4].

Half-disk	0	1	2	3	4	Full MFT
Inner radius (mm)	25.0	25.0	25.0	38.2	39.2	-
Outer radius (mm)	92.6	98.0	104.3	130.1	143.5	-
z-position (mm)	-460	-493	-531	-587	-768	-
No. of ladders	24	24	26	32	34	280
No. of ladders:						
2 sensor	6	6	4	0	0	32
3 sensor	18	18	14	10	8	136
4 sensor	0	0	8	22	18	96
5 sensor	0	0	0	0	8	16
No. of sensors	66	66	82	118	136	936

## 5.2 ALPIDE sensor

The basic detection element of the MFT is a silicon Monolithic Active Pixel Sensor (MAPS) and it is named as ALPIDE (ALice PIxel DEtector) [5, 6]. ALPIDE is developed by the ALICE Collaboration for both the MFT and the ITS. The TowerJazz 180 nm Complementary Metal Oxide Semiconductor (CMOS) imaging process [7] technology has been chosen to develop ALPIDE chip. This technology allows a maximum thickness of 50  $\mu\text{m}$  of a chip. Figure 5.4 shows a schematic view of a CMOS pixel sensor using TowerJazz technology. A pixel sensor consists of a  $p^-$  epitaxial layer which is used as sensitive volume and a highly p-doped ( $P^{++}$ ) substrate allows to integrate necessary circuitry on metal layer on the surface of chip.

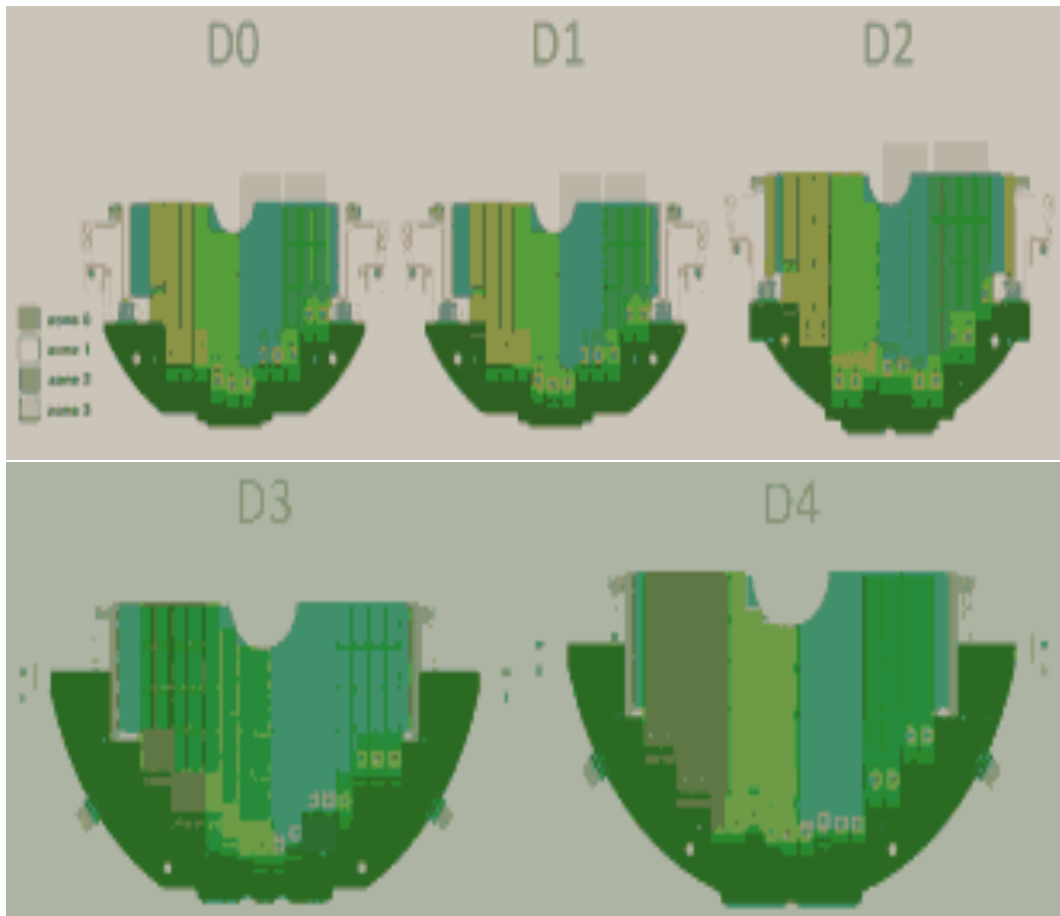


Figure 5.3: The arrangement of ladders and chips at different zones of MFT half-disks [4].

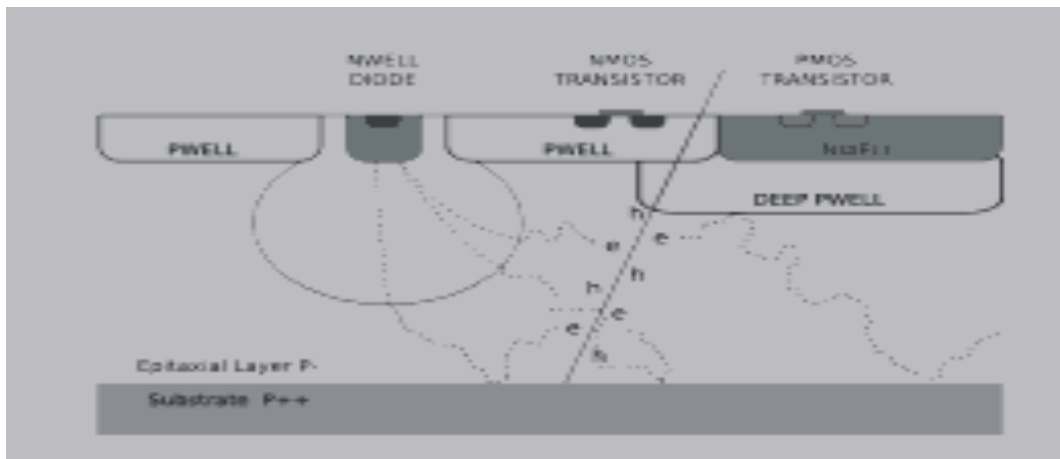


Figure 5.4: A Schematic cross-sectional view of a pixel of ALPIDE chip with TowerJazz CMOS technology.

When a charged particle passes through the sensitive volume, it creates electron-hole pairs

which drift towards the electrode due to the field generated in the depletion region (white region in Figure 5.4). After that, the electrode collects the part of the charges and registers this as a hit. The amount of charge deposition depends on the type and momentum of the particle passes through the detector. One of the main advantages of ALPIDE architecture is the digitization of signal produced inside the pixel and saving the hit information until the readout operation is performed.

A schematic of the ALPIDE chip architecture is described in Figure 5.5 (left). ALPIDE chip has a dimension of  $15 \times 30 \text{ mm}^2$  and a thickness of  $50 \mu\text{m}$ . An ALPIDE chip is organised by 512 rows and 1024 columns of pixel sensors and it comprises of total 524288 pixel sensors. Each pixel has the size of  $29.24 \mu\text{m} \times 26.88 \mu\text{m}$ . Figure 5.5 (right) describes a schematic of full pixel matrix block diagram of ALPIDE chip. The full pixel matrix is grouped in 32 different regions and hence each region is designated by a sub-matrix of  $512 \times 32$  pixels. The in-pixel multiple event memory reads using a priority encoder associated with each double column in each sub-matrix of 32 regions. The 32 Region Readout Units (RRU) in the chip periphery are connected with each sub-matrix which execute reading the response from each region. It is to be mentioned that the reading of the 16 double columns in each region are done sequentially while all the 32 region pixel-matrix are reading in parallel. The priority encoder logic ensures the reading only from the pixel when a signal generates.

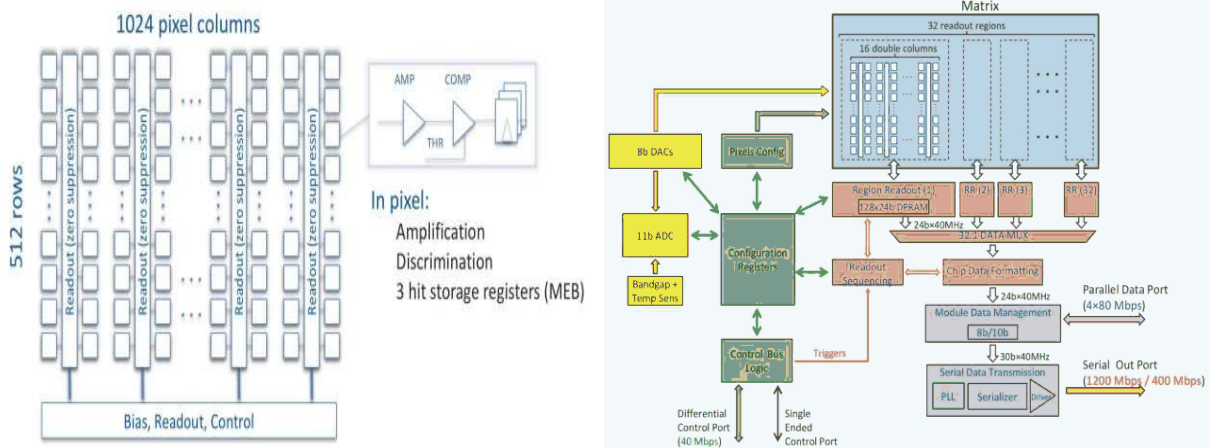


Figure 5.5: The Architecture of ALPIDE pixel-matrix (left) and ALPIDE readout block diagram (right).

## 5.3 Ladders Assembly

The ladders are the basic structures of MFT-disks and a composite unit of ALPIDE chips. These chips are placed in series along the length of the ladders. The ALPIDE chips are mounted on FPC using a non-conductive glue and allows the interconnection between the chips and the Front End Electronics (FEE). The FPC is made of aluminum foil of thickness  $25\ \mu\text{m}$  on a polyimide substrate of thickness  $75\ \mu\text{m}$ . Each FPC associated with a ladder has a constant width of  $16.7\ \text{mm}$  and its length changes depending on the number of chips mounted on the ladder. The FPCs were manufactured at CERN and then sent to Italy and Nantes in France for laser-drilling, cabling and connector installation. Thereafter, they are thoroughly inspected for quality check of the welding, positions of all the SMD components and to remove any unwanted substances. Then, a series of deep cleanings are followed by using ultrasonic baths based on alcohol, water with industrial detergent and demineralized water at the Department of Silicon Facility (DSF), CERN. After drying, the FPCs are again reinspected for any possible defects and contamination and also for flatness and size of the interconnection pads to the sensors.

Ladders of different lengths depending on the number of ALPIDE chips are assembled in a clean room of DSF at CERN. An automatic three-axis assembly machine called ALICIA (ALice Integrated Circuit Inspection and Assembly machine) is used to assemble the ladders in DSF. The ALICIA allows the positioning of the sensors with a high precision of the order of  $5\ \mu\text{m}$ . Each ALPIDE chip is positioned on Pre-Position Chuck (PPC) to test the quality and initial alignment of the chip. All the assembly operations for each ladder performed by ALICIA are recorded and/or photographed and assigned an unique identity number for future reference. After inspection, the chip on the PPC is placed on the HIC-Assembly Table (HAT) using gripper for the final assembly. The process is repeated for all the chips in the assembly process. All the chips placed on the HAT are mounted on the FPC with the help of glue (Araldite-2011) with a definite glue thickness of  $50\ \mu\text{m}$ . The volume of glue depends on the ladder size. The ladders under suction on the FPC jig are kept for 12 hours and then they are ready for the interconnection between the FPC and the chips. The interconnections are made by ultrasonic wire bonding on the metallic pads of the FPC. Soon after the bonding, a pull

test is carried out to measure the strength of the interconnections and hence it provides the information on the bonding quality.

In Figure 5.6 (top), a sample of ladder equipped with 4-chips after assembly along with the FPC side is shown. The opposite side of the same ladder equipped with the chips is shown in Figure 5.6 (bottom).

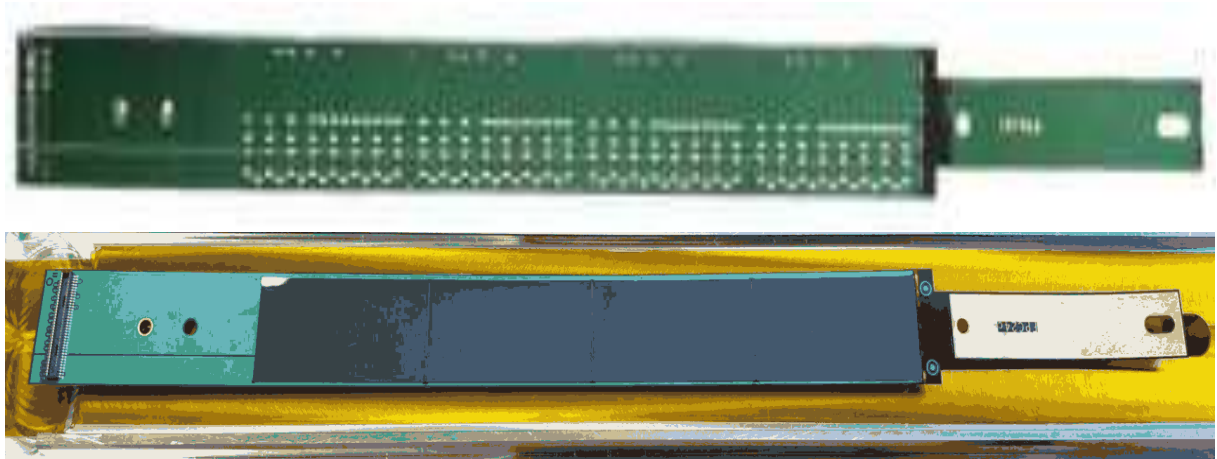


Figure 5.6: A view of ladders equipped with 4 chips along with FPC (top) and the back side of the same ladder with the integrated chips (bottom).

The wire bonding of the ALPIDE chips connected to the FPC is very fragile and may be broken for any irresponsible handling, touching or falling from any height. Therefore, the integrity of all wire bonds of a ladder should be preserved well so that they could function for a long period very reliably. Hence to avoid any damages, the ladder is placed inside a transportation box as shown in Figure 5.7. An ICL (Intermediate Card for Ladder) is mounted on the transportation box to perform the ladder qualification tests safely for multiple times (Figure 5.7 (bottom)). After the assembly at DSF, the ladders kept inside the transportation box are sent to the grey room of CEA Antenna building at CERN for the qualification tests.

## 5.4 Ladder Qualification Test

A series of different tests are carried out for the quality assurance (QA) of ladders at CEA Antenna building, CERN. The ladders which failed to qualify at any stage of these sequence





Figure 5.7: The Lid of a transportation box (upper). A ladder including an ICL board inside the transportation box (lower).

of tests are set aside and labeled as non-conformal ladders. I was involved in the ladder qualification activities at CERN for six months in two visits during April-June, 2019 and October-December, 2019 respectively. The workspace at the grey room of Antenna, is organised with two independent test benches for ladder qualification: Smoke Test and Functional Test. In the following sections, these two testing facilities are discussed.

### 5.4.1 Smoke Test

The first step for qualification test of a ladder is the smoke test. This test determines whether a ladder has adequate electrical connections with the nominal voltages applied to the analogue (AVDD), digital (DVDD), and back-bias (VBB) lines. This is done by gradually increasing the AVDD (Analog Voltage Drain-to-Drain), DVDD (Digital Voltage Drain-to-Drain) simultaneously upto the nominal value 1.80 V and then it is repeated with a VBB (Voltage in Back-Bias) ranging from 0 to -3.0V. In the following section 5.4.1, the basic arrangement for doing smoke test is described.

#### Arrangement for smoke test-bench

Figure 5.8 shows the basic arrangement for the smoke test bench. A HIROSE connector is used from FPC to the MFT-PCB to ensure a signal integrity at very high speed (1.2 Gb/s). However, the qualification of this HIROSE connector is limited for plug-in and plug-out only for 10 times. Hence, there is a possibility of a direct damage of the connector of the ladder which is under test. To avoid this, an ICL is connected to the ladder placed in a transportation

box. This ICL card can be used many times and hence no direct damage of the ladder during the test is expected. An ICL is equipped with decoupling capacitors of  $10\ \mu\text{F}$  and  $100\ \text{nF}$  compatible for AVDD, DVDD and VBB. The CAEN SY4527 low voltage power supply is used to provide all the voltages (AVDD, DVDD and VBB) to the ICL connected to the ladder via  $ICM_F$  (Intermediate Card for MOSAIC with FireFly connector). In this case, the jumpers on the  $ICM_F$  board are tuned in such a way that all the voltages from CAEN could be provided externally. Thus, the  $ICM_F$  board serves as a passive adaptor board between the CAEN & ICL during the test. The CAEN is connected with a PC which can control the power supply remotely.

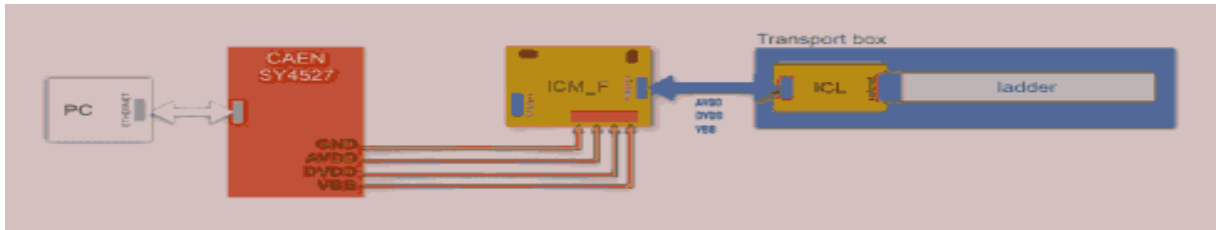


Figure 5.8: Basic arrangement of smoke test bench [8].

### Principle of smoke test

The whole smoke test process is fully automatic and controlled by the PC based on GUI (Graphical User Interface) software. The visualisation of the GUI based software to perform the smoke test is shown in Figure 5.9 (left).

During the smoke test, AVDD and DVDD simultaneously start ramping up from 0V to the nominal voltage 1.8 V. The current consumption for the AVDD and DVDD start to increase and reach different values after a certain voltage depending on the number of chips in the ladder. As soon as the AVDD and DVDD reach its nominal values, the VBB is supplied slowly in a decreasing mode down to -3.0V. During any stage of the test, if any over current flows through any of the lines, the test process stops automatically. A maximum of 10 mA current per chip is accepted during the back-bias voltage. Any over current flows through these lines can damage a chip permanently. However, there may be a transient high current due to the burning of contamination in the power lines which usually occurs before reaching the nominal value. Any



Figure 5.9: Visualisation of the GUI based software (left) and activity diagram (right) for smoke test [8].

over current on AVDD, DVDD or VBB during the smoke test operation is considered as a non-conformal (failed) test and the corresponding ladder is assigned to be a non-conformal ladder. In Figure 5.9 (right), the activity diagram for the process of smoke test is described.

## 5.4.2 Functional Test

Functional test is the next step for a ladder qualification after a successful smoke test. The functional test allows to check the performance of each constituent ALPIDE chips of a ladder when they are in active mode. During the test, the performance of the chips of a ladder can be checked simultaneously or one by one. The functional test is very crucial for a ladder qualification because this test describes the performance of the constituent chips when it will have a hit by charged particle passing through the pixel sensor. The ALICE-MFT group has designed various strategical steps for the functional test of a ladder qualification.

Functional test is performed with the AVDD and DVDD voltages of nominal value 1.8 V along with two back-bias conditions. First, the test is done without any back-bias voltage and then repeated for a reverse-bias of -3.0 V. A functional test of a ladder is said to be conformal if it qualifies both the back-bias conditions. In the following sections, the functional test without back-bias and with back-bias are discussed.

### 5.4.3 Basic Arrangement of Functional Test Bench

Figure 5.10 (top) shows the basic arrangement of functional test when no back-bias voltage is applied. The  $ICM_F$  board is organised as an active component during the functional test. An active ladder is required to feed a very stable and low noise voltages during operation. To do this, the  $ICM_F$  is powered with a lab power supply (5V) and the jumpers for AVDD and DVDD voltages are set on ‘on board’ which allow to generate low noise and stable AVDD and DVDD by the  $ICM_F$ . As the ladders on MFT-disks operate in a very high-hit rate environment, the MODular System for Acquisition Interface and Control (MOSAIC) is used for the ladder qualification tests. MOSAIC is a multi device testing platform based on a single Field Programmable Gate Array (FPGA) chip and used as a readout board dedicated to the ladder qualification tests. It is internally equipped with FPGA which is a generator of data and a pulser. MOSAIC is capable to read data at a high rate of 1.2 Gb/s through high speed serial links.

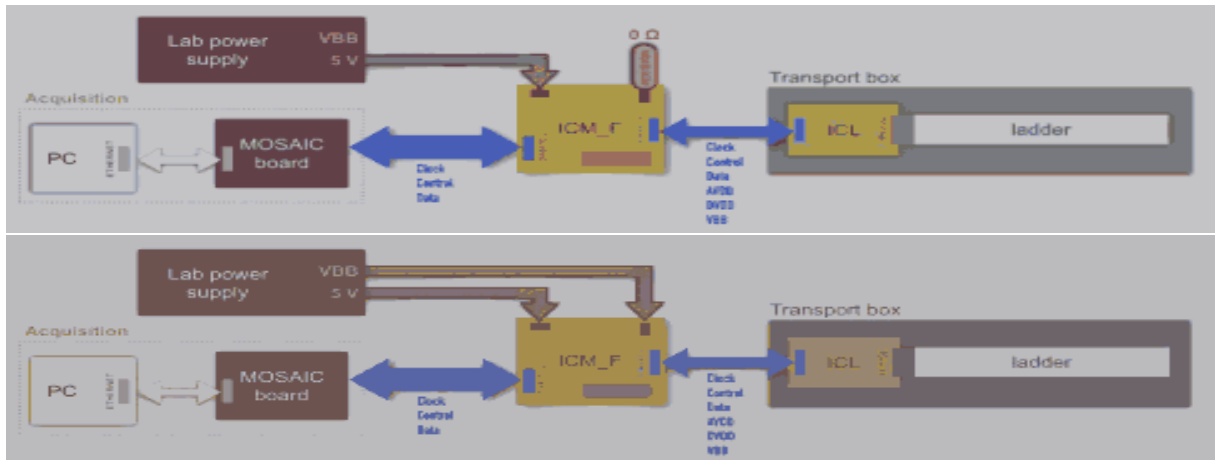


Figure 5.10: The basic arrangement of Functional Test without back-bias voltage (top) and with back-bias voltage (bottom).

During the functional test, MOSAIC plays an important role for sending clock, slow control and the data to the ladders through the  $ICM_F$  board. The ladders are powered on with the nominal voltages using lab power supply. The MOSAIC board sends the clock to the chips so that the chips remain in active mode. However, the slow control is bidirectional and used to write and then read the chip-registers. The MOSAIC is used to read the high speed (1.2

Gb/s) serial data sent by each chip on the ladder. There are one such data line for each chip on the ladder. The MOSAIC is connected with an Ethernet to provide the high speed data transmission, control of operation and also IP address configuration. The whole functional test is controlled by a Linux PC via the local network remotely. A LEMO resistor of  $0 \Omega$  is connected to the  $ICM_F$  board which ensures the reverse-bias is zero.

After a successful test without back-bias voltage, the ladder is tested through the same procedure with the nominal back-bias voltage of  $-3.0 \text{ V}$ . The basic arrangement for the functional test is shown in Figure 5.10 without back-bias voltage (top) and with back-bias voltage (bottom). In this case the LEMO resistor is removed and the  $ICM_F$  board is feeded by the required reverse-bias voltage provided by the lab power supply.

#### 5.4.4 Steps of Functional Test

A functional test is a process of several successive steps which are described as the following:

##### Electrical Test

Electrical test allows to check the electrical connections to all the components in the functional test bench. This is a set of observations in the power consumption for the ladder when it is powered on (test A), receives clock (test B) and is in active mode (test C). The power consumption of each ladder is proportional to the number of constituent chips. An adequate increment in the current ensures a proper functioning of the digital part of the chip when the clock is started. During the active mode of the ladder, a higher current is expected.

In Table 5.2, the nominal power consumption of ladders during the electrical test is illustrated.

Table 5.2: The nominal power consumption of ladders during electrical test.

Ladder	Current (in mA)	Current+Clock (in mA)	Current+Clock+Active mode(in mA)
2-chip	$\approx 82.5$	$\approx 155.0$	$\approx 245.0$
3-chip	$\approx 105.0$	$\approx 212.5$	$\approx 351.0$
4-chip	$\approx 136.5$	$\approx 279.5$	$\approx 461.0$
5-chip	$\approx 156.0$	$\approx 338.0$	$\approx 557.5$

## Readback Test

Readback test is done automatically by the software along with the electrical test. This test allows to check the functionality of slow control sent by MOSAIC. When the clock is on, the chips on the ladder start communicating via the slow control. The MOSAIC attempts to write in the chip-Configuration-Registers and then it is read back again by the MOSAIC. A Readback test is said to be successful if all the chips on the ladder are succeeded in this write and read operations.

At the end of a successful readback test, a complete investigation of all the chips with the performance of the full pixel-matrix of a chip are carried out. This is a set of observations automatically done step by step by a single click using the GUI software.

## FIFO scan

A FIFO (First In, First Out) scan is a quick process to test the functioning of all the DPRAMs (Dual Ported Random Access Memory) associated with each region of the ALPIDE-chip. FIFO uses an algorithm to organise and instruct a data buffer, in which the first entry in the chip-register is read first in a similar fashion to a queue with first come, first serve. There are four different patterns instructed consecutively by the MOSAIC to write into the DPRAM of each 32 RRU of a chip. Then they are read one by one with First In, First Out algorithm. A FIFO scan is successful if all these four instruction patterns are exactly read sequentially.

## Digital Scan

Digital scan is the follow up process after the completion of FIFO scan. During this scan, all the pixels in the matrix of a chip start their activities when receive clock sent by MOSAIC. Therefore, a digital scan is used to get the information about the number of bad pixels over the full matrix of each chip on the ladder. However, a bad pixel may be a dead pixel (DP), hot pixel (HP), inefficient pixel (IP) and stuck pixel (SP). The scan quality is classified for each individual chip depending on the number of bad pixels relative to the full pixel matrix.

## Threshold Scan

It is evident that the detection efficiency of a pixel sensor increases with the decreasing value in threshold, but due to this low threshold, the fake hit rate increases simultaneously. Moreover, the threshold value can change from pixel to pixel. During this step, a scan is organised over the whole pixel matrix and allows to optimize the threshold and noise of each pixel in unit of electrons or in DAC units. This scan provides the information of properties of each ALPIDE-chip such as mean and RMS value of threshold, number of dead pixels, pixels without threshold, noisy pixels and also the mean and RMS of noise.

## Noise Occupancy

A fake-hit rate ( or noise occupancy) is an important parameter for qualification test of an ALPIDE-chip. This is the probability for a pixel to register a hit when there is no ionizing particle passing through the pixel sensor. A Noise occupancy is a measure of the number of fake hits divided by the number of pixels times the number of triggered events for a given chip. A noise occupancy is expected to be less than  $10^{-5}$ /pixel/event for the MFT detector which designates as about 5 fake hits per event per chip.

### 5.4.5 Eye diagram scan

An eye diagram represents the average statistics of the high speed digital signal and provides the quality of serial digital signal transmission. The eye diagram scan is performed to check the transmission speed of the data in the MFT detector. During this measurement, the sensors are put in a specific test mode called PRBS (PseudoRandom Binary Sequence) mode where its Data Transmission Unit (DTU) sends a pseudo-random sequence of bits to the chip. The eye diagram scan is obtained by folding a digital waveform to each individual bit into a single graph and repeated this construction over many sample of the waveforms. The resultant graph represents the average statistics of the signal and shape of the graph looks like an eye.

The eye opening corresponds to one bit period also known as unit interval (UI). However, an ideal digital waveform of constant amplitude with sharp rise and fall edges should result an eye diagram as shown in Figure 5.11. But, in practice, the high speed digital signal suffers considerable impairments due to attenuation, noise, crosstalk, clock jitter etc. The eye diagram obtained for a typical high speed digital signal during the qualification test of a ladder is shown in Figure 5.12.

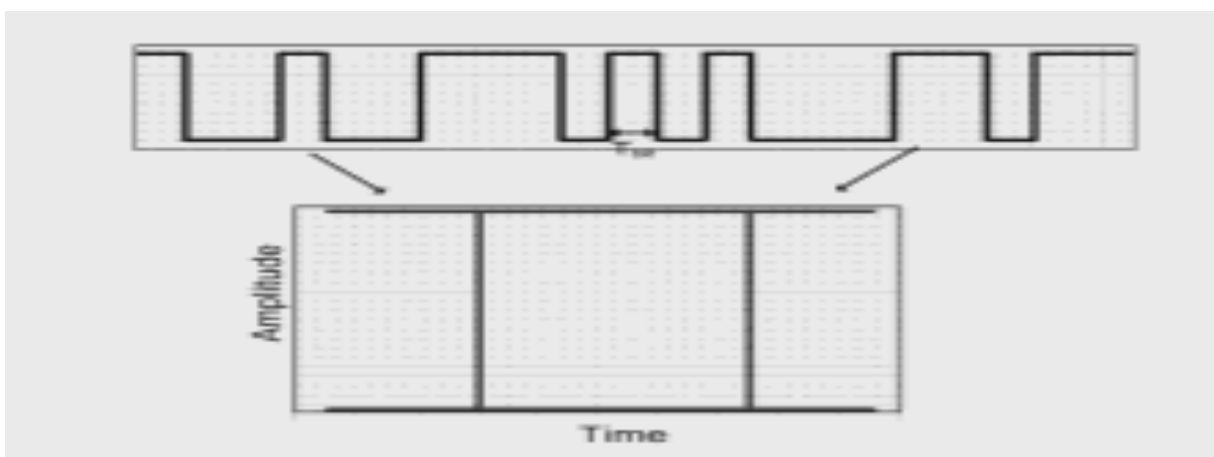


Figure 5.11: The Eye diagram for ideal high speed digital waveform signal.



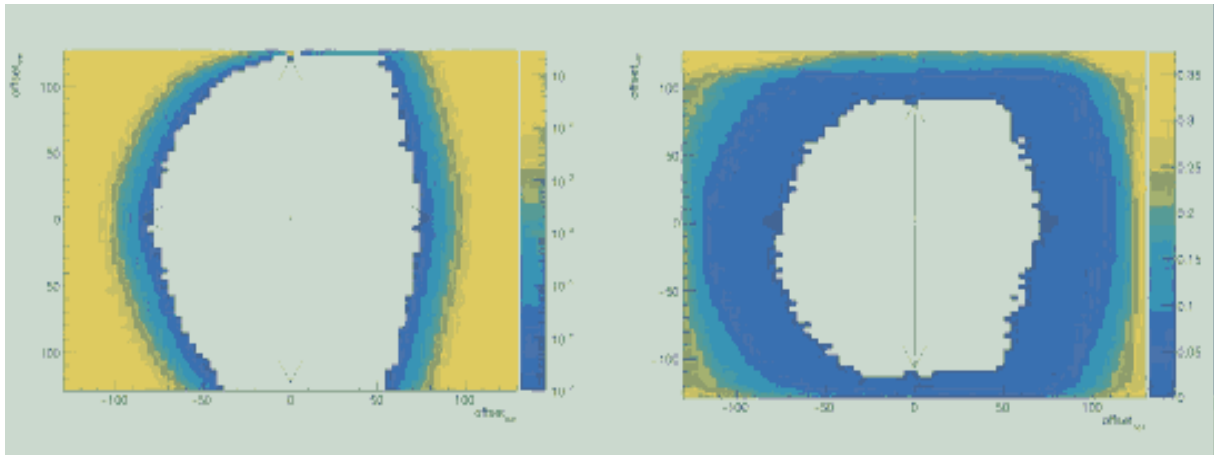


Figure 5.12: Two examples of Eye diagram obtained from the eye diagram scan of ladder.

## 5.5 Ladder qualification analysis

Each scan including eye diagram discussed above is assigned with a qualification grade based on the performances with respect to standard specifications of a chip. At the end of each scan, individual chip on the ladder is classified as gold, silver or bronze based on their performance during the scan. A good ladder is qualified in all the steps during the test processes and labelled as a conformal ladder. A bad ladder is the one which is failed for all or any constituent chip at any specific stage during the functional test and labelled as non-conformal ladder. However, a labelling of global classification of a ladder is done after the completion of the functional test based on the worst performed chip of the ladder. The classification parameters of a chip for all the scans during functional test are described in the Figure 5.13.

I have actively participated for the qualification tests of  $\sim 230$  ladders. The bonding lab were closed from mid-November to mid-December of 2019 due to renovation work. During this period, we investigated the non-conformal ladders available at Antenna building, CERN. Many of them were recovered and considered as conformal after performing specific qualification tests. Table 5.3 illustrates the summary of 472 number of assembled ladders which are undergone for the qualification tests at Antenna building, CERN. Moreover, a span of about two years took to manufacture 500 ladders for the MFT which are subsequently tested and qualified under the responsibility of the Irfu Antenna team at CERN. The qualification rate of ladders with gold

	cut on	gold	silver	bronze	non-conformal
Minimize	FIFO n errors	no error	0	0	the rest of the phase-space
	Digital scan (full matrix) n bad(**) pixels relative to full matrix	< 50 $1 / 10^4$	[ 50, 2100 [ $4 / 10^3$	[ 2100, 5243 [ 1 %	
	Threshold scan (full matrix) n dead pixels	< 50	[ 50, 2100 [	[ 2100, 5243 [	
	Noise occupancy (no power masked) noise	< 50	< 10	< 10	
	Noise occupancy (no power masked) n noisy(**) pixels	< 50	[ 50, 2100 [	[ 2100, 5243 [	
Maximize	Eye diagram width (horizontal opening)	> 80	[ 60, 80 [	[ 40, 60 [	
	Eye diagram height (vertical opening)	> 230	[ 200, 230 [	[ 170, 200 [	

Figure 5.13: Classification cuts during functional test.

and silver categories is around 91% which justifies the success for the project [9].

Table 5.3: Summary of the assembled and tested ladders.

Ladders	2-chip	3-chip	4-chip	5-chip
total	57	236	158	21
conformal	45	176	134	18
conformal yield	79%	75%	85%	86%

An online database for MFT ladder assembly modules is created to store all the information and the updates of ladder manufacture, assembly and test. The characteristic plots in the following sections are based on the conformal ladders as described in Table 5.3.

### 5.5.1 Electrical Test characteristics

In figure 5.14, the power consumption of the conformal ladders normalised to the number of chips are shown during electrical test. A contribution of 30 mA current consumption by the  $ICM_F$  is subtracted from all the results as described in Table 5.2. We observed few ladders with a current of 50-55 mA when clock was started during test B. This may come from the test of ladders with two MOSAICs in two different functional test benches.

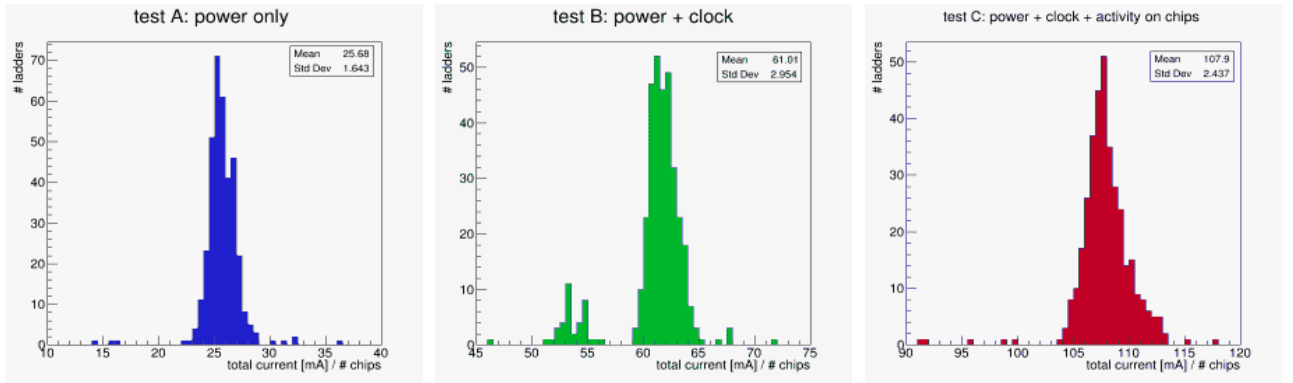


Figure 5.14: Power consumption of ladders per chip during electrical test A (left), B (middle), and C (right).

## 5.5.2 Threshold-Noise scan characteristics

It has been checked that the threshold and noise distributions for the chips on all ladder types (2,3,4,5 -chip ladders) are similar. Therefore, we present these two distributions by considering the results from all the chips irrespective of ladder type. In Figure 5.15, the mean (top) and rms (bottom) distributions are shown for no back-bias voltage (left) and with back-bias voltage of -3 V (right) respectively for threshold scan. In Figure 5.16, the mean (top) and rms (bottom) distributions are shown for no back-bias voltage (left) and with back-bias voltage of -3 V (right) respectively for noise scan. It is noticed from Figure 5.15 and Figure 5.16 that the application of back-bias voltage makes the threshold distribution more narrower and the average value of noise goes down to  $\sim 4$  electron from  $\sim 6$  electron compared to the case of no back-bias.

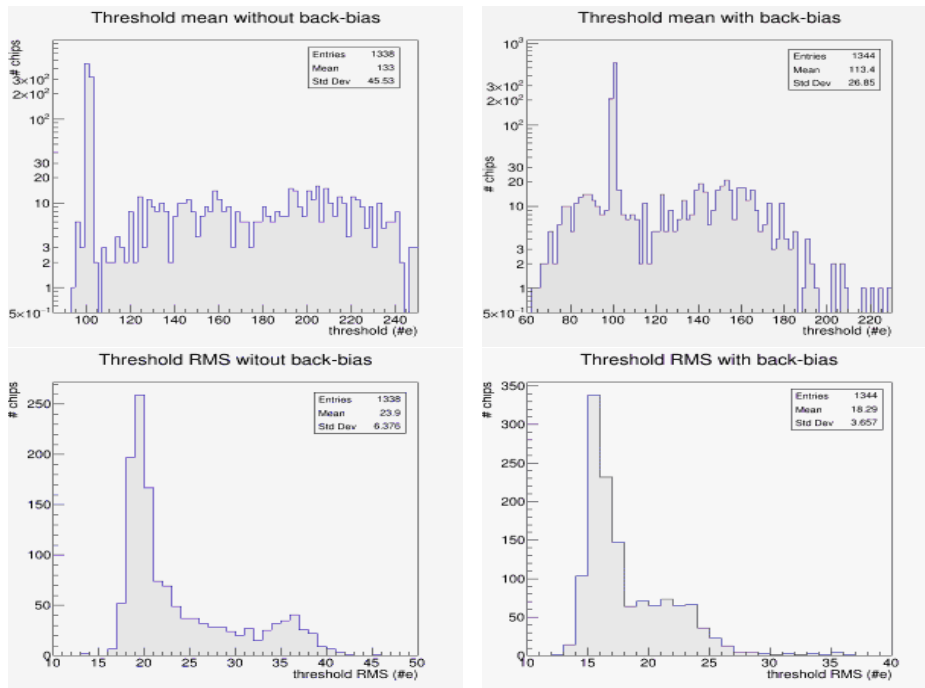


Figure 5.15: Statistics on threshold values: mean without back-bias (top left), mean with back-bias (top right), rms without back-bias (bottom left) and rms with back-bias (bottom right).

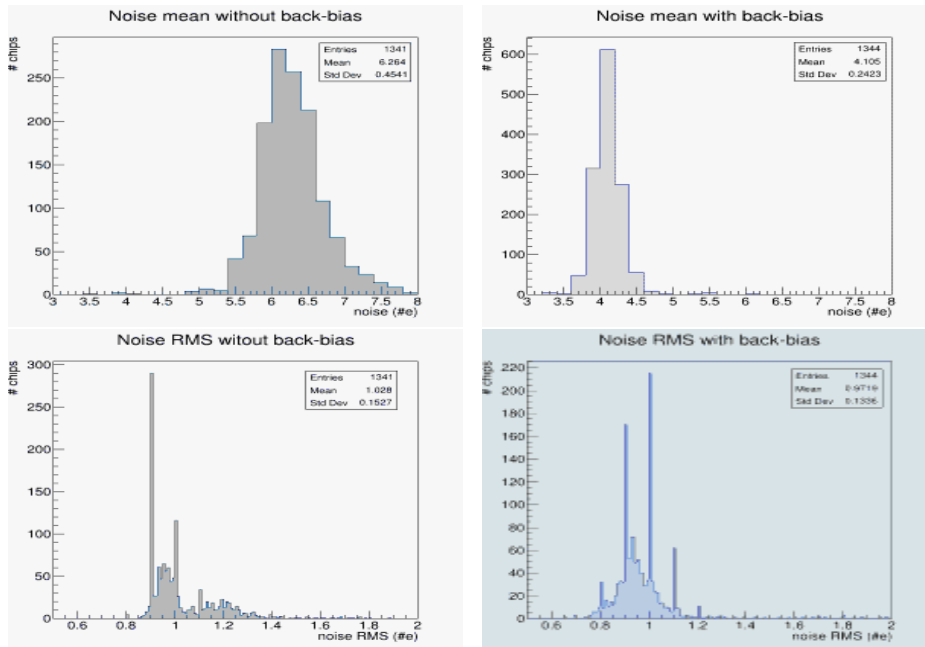


Figure 5.16: Statistics on noise values: mean without back-bias (top left), mean with back-bias (top right), rms without back-bias (bottom left) and rms with back-bias (bottom right).

### 5.5.3 Dead and noisy pixel

A detail analysis on the dead and noisy pixels are done in both digital scan and the threshold scan separately. During the digital scan, each pixel is pulsed for 50 times. Depending on the response from the digital part of each pixel, dead, inefficient and noisy pixel are detected. A dead pixel does not respond for any of the pulses. An inefficient pixel can not respond for 50 times. A noisy pixel responds for more than 50 times. During threshold scan, the analog part of each chip is tested using a pulse at a pixel while the rest of the pixels in the chip are masked. This is repeated for the full pixel matrix of a given chip. In this scan, a dead pixel corresponds to an unrealistically high threshold whereas a noisy pixel is with extremely low threshold.

## 5.6 Full MFT installation

Finally, the best 280 qualified ladders with 936 number of ALPIDE chips took part in the fabrication of 10 MFT half-disks for full MFT assembly. The installation and commissioning of full MFT in ALICE cavern was done in December 2020. Figure 5.17 (left) shows a rear view of the half-disks of the MFT detector in the MFT half-cone assembly and Figure 5.17 (right) shows the MFT detector in its final position after the installation in ALICE cavern (P2).

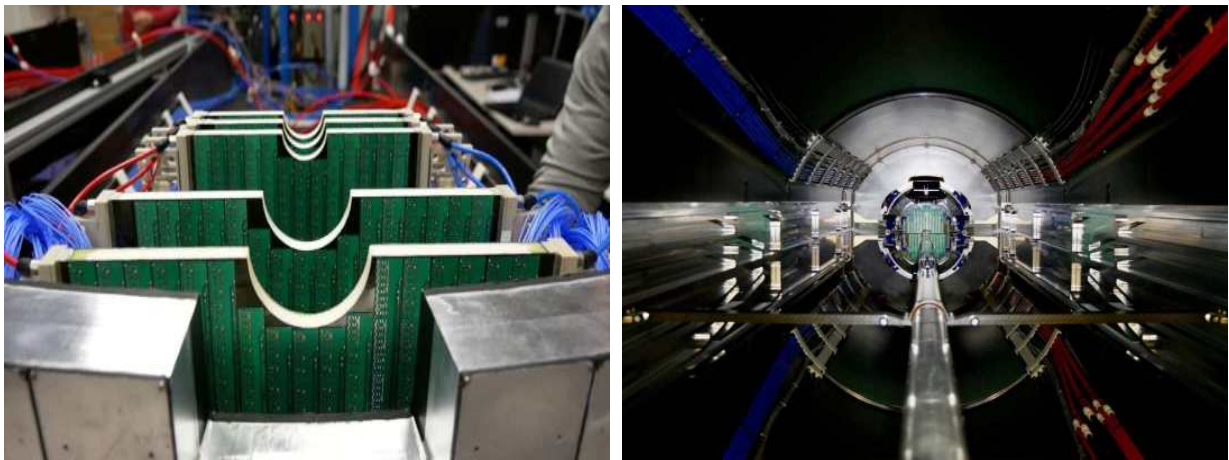


Figure 5.17: The rear view of MFT half-cone assembled inside the barrel (left). The MFT detector in at final position where the beam pipe goes in the center of MFT (right) [2].

## 5.7 Summary

The Muon Forward Tracker (MFT) is the new addition to the muon spectrometer of ALICE detector motivating from some interesting physics program expected to achieve during the Run 3 experiments. In this chapter the basic structural configuration of MFT-disk of ALICE detector has been discussed. Each face of the MFT half-disk has four different zones and consists of certain number of ALPIDE chips and ladders depending on the size of the disk. A brief description of the ALPIDE chip pixel-matrix architecture and the block diagram of ALPIDE readout have been discussed. The basic arrangements of the qualification test benches are described. The ladders assembly and the procedures for the quality assurance (QA) tests of the ladders conducted at the Antenna building of CERN have been given. The QA tests of the ladders at CERN was done by me as a part of the ALICE service task. Finally, few characteristic results based on the 472 number of conformal ladders after the successful qualification have been presented. The assembled full MFT detector is placed inside the ALICE cavern and then integrated with the ALICE detector. The MFT starts functioning to record physics data from 5th July, 2022 for the ALICE Run 3.

---

# Bibliography

---

- [1] ALICE MFT WORKING GROUP collaboration, *Performance Study for a Muon Forward Tracker in the ALICE Experiment*, in *13th ICATPP Conference on Astroparticle, Particle, Space Physics and Detectors for Physics Applications*, pp. 704–711, 2012, DOI [1201.0048]. 177
- [2] ALICE, MFT Collaboration, ALICE Muon Forward Tracker (MFT). <https://cds.cern.ch/record/2748310>. xxx, xxxi, 180, 197
- [3] MFTGeneral. <https://twiki.cern.ch/twiki/bin/viewauth/ALICE/MFTGeneral>. xxxiv, 180
- [4] ALICE MFT Operation Webpage. <https://twiki.cern.ch/twiki/bin/viewauth/ALICE/MFTGeneral>. xxx, xxxiv, 180, 181
- [5] ALICE collaboration, *The ALPIDE pixel sensor chip for the upgrade of the ALICE Inner Tracking System*, *Nucl. Instrum. Meth. A* **845** (2017) 583. 180
- [6] ALICE collaboration, *ALPIDE, the Monolithic Active Pixel Sensor for the ALICE ITS upgrade*, *Nucl. Instrum. Meth. A* **824** (2016) 434. 180
- [7] S. Senyukov, J. Baudot, A. Besson, G. Claus, L. Cousin, A. Dorokhov et al., *Charged particle detection performances of CMOS pixel sensors produced in a 0.18 $\mu$ m process with a high resistivity epitaxial layer*, *Nucl. Instrum. Meth. A* **730** (2013) 115 [1301.0515]. 180
- [8] Overview of the test benches for ladder qualification at CERN (production phase).

<https://twiki.cern.ch/twiki/bin/view/ALICE/LadderQualificationTestBench>.  
xxxi, 186, 187

[9] Ladder for ALICE-MFT. [https://irfu.cea.fr/en/Phoce/Vie\\_des\\_labos/Ast/ast.php?t=fait\\_marquant&id\\_ast=4799&fbclid=IwAR1eCuCks91rGehCYjkq-FTslT-X5RsYxDMoqfnWjEASuh8jYzCsA7MPbLE](https://irfu.cea.fr/en/Phoce/Vie_des_labos/Ast/ast.php?t=fait_marquant&id_ast=4799&fbclid=IwAR1eCuCks91rGehCYjkq-FTslT-X5RsYxDMoqfnWjEASuh8jYzCsA7MPbLE).

194



# CHAPTER 6

---

## Outlook

---

In high energy hadron-hadron and heavy-ion collisions, heavy quarks (charm and bottom) are copiously produced. These heavy quarks are produced in the very early stage of the collisions mainly through the hard parton-parton scattering with large momentum transfer ( $Q^2$ ). The study of heavy flavour production in proton-proton (pp) collisions at LHC energy regime provides an important test for perturbative Quantum Chromodynamics (pQCD). Furthermore, the measurement of heavy flavour production in pp collisions serves as a necessary baseline for the same measurement in proton-nucleus (p-A) and nucleus-nucleus (A-A) collisions.

The study of heavy flavour production in proton-proton and heavy-ion collisions by ALICE experiment have played a significant role to describe the theory of Quantum Chromodynamics. ALICE has measured the heavy flavour hadron decay muon (HFM) production cross-section at forward rapidity ( $-4 < \eta < -2.5$ ) in pp collisions at  $\sqrt{s} = 2.76$  TeV, 5.02 TeV and 7 TeV respectively. The new measurement of the production cross-section of HFM presented in this dissertation is crucial to describe the QCD at  $\sqrt{s} = 13$  TeV which is the highest center-of-mass energy in pp collision achieved by a particle accelerator till date.

The LHC started taking data for physics in Run 3 after an extensive upgrade program for about three years during the long shutdown 2. In ALICE Run 3, the presence of Muon Forward Tracker (MFT) at ALICE detector will significantly enhance the vertexing capabilities ( $5\mu m$ ) to the existing Muon Spectrometer (MS) and enable to separate the open charm and

beauty components. Very exciting and high-precision measurements such as separation of  $J/\psi$  from various sources, in medium charmonium dynamics, the medium density and the mass dependence of in-medium parton energy loss are expected with the addition of MFT with the Muon Spectrometer at ALICE during Run 3. As an extension to this work, the heavy flavour decay muon (HFM) production as a function of charged particle multiplicity ( $N_{ch}$ ) in pp collisions at LHC energies could be a very interesting study. This measurement of HFM as a function of  $N_{ch}$  could provide more insight of the interplay between the soft and hard physics and may help in understanding the phenomenological model to explain the underlying physics.

In chapter 4, the phenomenological study for the production of heavy flavour decay muons and charged particles in small to heavy-mass collision systems (pp, O-O, Xe-Xe, Pb-Pb) using Angantyr model have been investigated. The development of this model is based on the dynamics of pp collisions. The final state partons in nucleon-nucleon (NN) events are stacked together after generating all NN sub-collisions in a heavy-ion collision. The results presented in this dissertation suggest that the model reproduces transverse momentum ( $p_T$ ) distribution, mean  $p_T$  as a function of charged-particle multiplicity ( $N_{ch}$ ) in pp collisions very well. Although the model reproduces the mean  $p_T$  vs  $N_{ch}$  reasonably well in case of A-A collisions, it could only provide an overall description of the transverse momentum distributions at all centrality bins. The qualitative study of the nuclear modification factor of HFM and charged particles show the suppression of particle yields even in the absence of medium formation in the heavy-ion collisions. The disagreement of  $R_{AA}$  below unity could be from several effects such as different contributions to the particle dynamics at high  $p_T$  from different types of inelastic NN sub-collisions. Thus, at this stage the model can not reproduce the expected behaviour of  $R_{AA}$  about unity in the absence of thermal medium formation in the collision. The production of Heavy Flavour decay Lepton (HFL) as a function of charged particle multiplicity ( $N_{ch}$ ) in pp and heavy-ion collision systems may be a future scope to study using Angantyr model.

After the observation of the “flow-like” effect in small systems like pp collisions, it is being thought that there may be new kinds of hadronization mechanisms might exist when huge kinetic energy is involved in a collision irrespective of the colliding system sizes. So, interest has grown among the physics community to study the HI collisions without considering any

thermalised medium formation. Recently, the “string shoving” and “rope hadronisation” are introduced in PYTHIA8 to explain the “ridge like effects” and “strangeness enhancement” in high multiplicity pp events. This concept may also be applicable to the Angantyr model for HI events to explain similar observations while we approach for a model with a QGP free HI collision.

The ingredients like multiparton interactions (MPI) together with colour reconnection (CR) mechanism plays significant role to describe the final hadronic state of the underlying events (UE). In PYTHIA8, the colour reconnection occurs among the partons generated within the same NN sub-collision only and hence the same is for Angantyr model. The CR mechanism can not generate long-range collectivity among the produced hadrons. Therefore, a modification in the CR mechanism using Angantyr model is expected in such way that the colour reconnection occurs among the partons generated from all different sub-collisions in a HI events. This modification of colour flow among all the partons generated in a HI events could produce the effects similar to the collectivity in HI collisions.

It is seen that Angantyr provides an overall good description of general final state properties like multiplicity and transverse momentum distributions both in pp and A-A collisions. However, it is noted that the model description has large dependence on centrality and is very sensitive to the experimental definition of centrality. The measurement of centrality, trigger selection, primary particle definition etc. play major roles to improve the precision measurement by the current model. All these improvements are the key features of RIVET analyses. As RIVET provides a direct comparison between Monte-Carlo event generators (PYTHIA8, EPOS-LHC, Herwig, JEWEL, ThePEG) and experimental data, it is being used as a part of analysis and interpretation toolkit within LHC experiments. Therefore, the development of Monte Carlo event generators like Angantyr using RIVET is very crucial for the heavy ion physics to describe the experimental data.

Finally, the Angantyr model opens up a wide range of phenomenological understanding and explanation for QGP free HI collisions. The study of the collective effects from string-string interactions using Angantyr may allow to compare the hydrodynamic description of particle production and the transport mechanism in HI collisions. At present, the model should be

considered as a baseline for understanding the non-collective background to the observables sensitive to collective behaviour.

## Thesis Highlight

**Name of the Student:** Md. Samsul Islam

**Name of the CI/OCC:** Saha Institute Of Nuclear Physics **Enrolment No.:** PHYS05201604010

**Thesis Title:** Study of heavy flavour decay muons at forward rapidity in proton-proton and heavy-ion collisions at LHC energies

**Discipline:** Physical Sciences **Sub-Area of Discipline:** High Energy Nuclear & Particle Physics

**Date of Viva-Voce:** 07.10.2022

The new measurement of the production cross-section of single muons decaying from heavy flavour hadrons (HFM) in pp collisions at the highest available energy  $\sqrt{s} = 13$  TeV with the ALICE detector in Run 2 at LHC has been reported. The results are important to describe the theoretical pQCD calculations. The measurement of production cross-section of HFM has been presented with an extended transverse momentum ( $p_T$ ) upto 30 GeV/c with respect to the previous published ALICE results. The production cross-section of HFM as a function of rapidity ( $y$ ) at two different  $p_T$  regions:  $2 < p_T < 7$  GeV/c and  $7 < p_T < 30$  GeV/c are also shown. The measurements of  $p_T$ - and  $y$ - differential production cross-sections of HFM are compared with the theoretical model FONLL calculations. These comparisons are found to be in good agreement almost over the whole  $p_T$  range within the theoretical uncertainties. However, the central values of the experimental data for measuring the HFM-production cross-section with ALICE overestimate the theoretical FONLL predictions.

A phenomenological study of HFM and charged particles have been presented using Angantyr model in pp and A-A collisions at LHC energies. The features such as near side ridge and strangeness enhancement in heavy-ion (HI) collisions are observed in high multiplicity pp events at LHC energies recently which indicate for better understanding the phenomenology of hadronization mechanisms. The Angantyr model of HI collisions is the extrapolation of the pp dynamics into the HI collisions using PYTHIA event generator and does not include the assumption of QGP medium produced in high energy HI collisions. The study using Angantyr model could serve as reference of the non-collective background to the observables sensitive to the collective behaviours. The simulations are performed for pp, O-O, Xe-Xe and Pb-Pb collisions over a wide range of LHC-ALICE energies. The novelty of the present phenomenological study of HFM and charged particles production is to explore the results using Angantyr model that how well they describe the experimental ALICE data for various collision systems in a single framework. The transverse momentum distribution of HFM using Angantyr Model agrees fairly with the experimental ALICE data for various collision systems. The simulated  $R_{AA}$  as a function of  $p_T$  for the production of HFM overestimates the ALICE data at  $\sqrt{s} = 2.76$  and 5.02 TeV for the most central Pb-Pb collisions. The study of charged particles has been done applying the colour reconnection mechanism. The simulated  $p_T$  distribution of charged particles in pp collision agree with the experimental ALICE data almost over all  $p_T$  region. However, the  $p_T$  distribution of charged particles in HI collisions (Xe-Xe and Pb-Pb) describes the ALICE data fairly at nine different centrality classes. The mean  $p_T$  ( $\langle p_T \rangle$ ) as a function of charged-particle multiplicity ( $N_{ch}$ ) agrees the ALICE data well in the range of  $5 < N_{ch} < 20$  for pp collisions and also found to be dependent very weakly for  $N_{ch} < 30$ . The same study of  $\langle p_T \rangle$  in case of HI collisions is found to be almost independent of collision systems when the collision energies are in a comparative range. The simulated  $R_{AA}$  for the charged particles production overestimates the ALICE data for the central Pb-Pb collisions (0-10% and 10-20%) upto  $p_T \approx 15$  GeV/c but underestimate for the peripheral collision (50-60%). The simulated  $R_{AA}$  for both the HFM and charged particles production are found to be independent of  $p_T$  in Pb-Pb collisions.

The basic detection element of ALICE-MFT detector is the silicon pixel sensor and called as ALPIDE (ALice PIXel DEtector). These silicon sensors are integrated on a mechanical ladder structure. In this thesis, the assembly of MFT-ladders and their Quality Assurance (QA) tests are discussed. The basic arrangements of the qualification test benches for the QA of ladders are described.